MANIPULATION OF UNIFORMLY SHEARED TURBULENCE USING CURVATURE AND THIN RIBBONS

by

BRAHIM CHEBBI

Dissertation

presented to the University of Ottawa
in partial fulfillment of the
requirement for the degree of

DOCTOR of PHILOSOPHY

in

MECHANICAL ENGINEERING

OTTAWA-CARLETON INSTITUTE FOR MECHANICAL AND AEROSPACE ENGINEERING

ISBN 0-315-93566-9

Abstract

Part A

A nearly homogeneous uniformly sheared turbulent flow was subjected to curvature in the same direction as the mean shear and then to curvature reversal. The adjustment of the turbulence structure to a change of the value of the curvature parameter, $S = \frac{\overline{U}_c / R_c}{\partial \overline{U} / \partial n}$, is investigated. The structural parameter, $K_{uv} = \frac{\overline{uv}}{q^2}$, adjusts faster when the effects of curvature are stronger. For the small values of S obtained in the present investigation the adjustment of K_{uv} depends on both the original and new values of S as the flow is subjected to curvature reversal. Qualitative and quantitative similarities between the present flow and curved turbulent boundary layers are identified.

Part B

A thin ribbon is placed in rectilinear and curved nearly homogeneous uniformly sheared flows. The development of the wake of the thin ribbon is investigated. The mean flow characteristics of the wake of the thin ribbon developing in rectilinear

shear flow present a certain degree of self similarity and some resemblance to the characteristics of the wake of a LEBU in the outer part of turbulent boundary layers.

Acknowledgement

I am sincerely grateful to my supervisor Professor Stavros Tavoularis. His encouragement, guidance and permanent availability for discussions were a big asset for me to perform this work. What I learned from Professor Tavoularis goes far beyond Fluid Mechanics and Turbulence. He taught me the importance of detachment, objectivity, professionalism and intellectual honesty, in a researcher's career.

I must thank Dr. G. Holloway for sharing with me some of his thoughts about curvature and turbulence.

I wish to express my sincere appreciation to Sadok, Sonia, Amor, Limayem, Faouzi, Youssef, Ali, Chedly and Soufiène. Their friendship was very special to me and helpful during my timely studies in Ottawa.

To my family, and especially to my mother, I am greatly indebted for the support and understanding they have given me.

Financial support was provided by the Natural Sciences and Engineering Research Council of Canada.

Contents

List of Tables

List of Figures

Nomenclature

Part A

A	mean shear rate $= \frac{\partial \overline{U}}{\partial n}$, also constant in modified King's law
B	constant in modified King's law
d	wire diameter
$\mathbf{e}_s$	unit vector in the streamwise direction in (s,n,z) coordinates
$\mathbf{e}_n$	unit vector in the transverse direction in (s,n,z) coordinates
$\mathbf{e}_z$	unit vector in the apanwise direction in (s,n,z) coordinates
E	anemometer voltage
$E_{uu}, E_{vv}, \ldots$	wave number spectra
f	frequency
$F_{uu}, F_{vv}, \ldots$	frequency spectra
h^2	calibration constant for wire orientation
H	height of wind tunnel
$\mathbf{i}$	unit vector in streamwise direction in (x,y,z) coordinates
$\mathbf{j}$	unit vector in transverse direction in (x,y,z) coordinates

k	unit vector in spanwise direction in (x,y,z) coordinates
k_1	streamwise component of wave number vector
k_s	shear constant of wind tunnel $= \frac{1}{U_c}\frac{\partial \overline{U}}{\partial n}$
k^2	calibration constant for wire orientation
$K_{uu}, K_{vv}, \ldots$	Reynolds stresses tensor components
l	wire length
L	length scale $= \frac{q'}{\lvert\frac{\partial U}{\partial n}\rvert}$
$L_{uu}, L_{vv}, \ldots$	integral length scales
m^2	anisotropy scalar
n	transverse coordinate
$\aleph$	nondimensional parameter $= \frac{1}{1+\frac{n}{R_c}}$
p	fluctuating pressure
P	instantaneous pressure, also turbulent kinetic energy production
$\frac{q^2}{2}$	kinetic energy
R	radius of curvature or wire resistance
R_c	radius of curvature at centerline of section
Re	Reynolds number
$R_{uu}, R_{vv}, \ldots$	autocorrelations
S	ratio of extra rate of strain due to curvature to mean shear $= \frac{\frac{\overline{U}_c}{R_c}}{\frac{\partial U}{\partial n}}$, referred to as curvature parameter
s	streamwise coordinate
t	time
T	temperature, also time constant
$T_{uu}, T_{vv}, \ldots$	integral time scales

u	fluctuating velocity in streamwise direction
v	fluctuating velocity in transverse direction
w	fluctuating velocity in spanwise direction
U	instantaneous velocity in streamwise direction
$\mathbf{U}$	total velocity vector
$\mathcal{U}$	Fourier transform of u
V	instantaneous velocity in transverse direction
$\mathcal{V}$	Fourier transform of v
W	instantaneous velocity in spanwise direction
x	streamwise coordinate in (x,y,z) system of coordinates
y	transverse coordinate in (x,y,z) system of coordinates
z	spanwise coordinate in (x,y,z) and (s,n,z) systems of coordinates

Greek Letters

$\overline{\alpha}$	average coefficient of temperature of wires
β	roll angle
η	Kolmogoroff microscale
δ	boundar layer thickness
$\phi_{uu}, \phi_{vv}, \ldots$	pressure strain rate covariances
$\epsilon, \epsilon_{uu}, \epsilon_{vv}, \ldots$	viscous dissipation
κ_q	coefficient of growth of kinetic energy
λ_{uu}	Taylor microsacle in the streamwise direction
μ	dynamic viscosity of fluid
ν	kinematic viscosity of fluid
θ	orientation of wire with repect to probe axis

ρ	density of fluid
ρ_{uv}	correlation coefficient $= \frac{\lvert\overline{uv}\rvert}{u'v'}$
τ	time shift, $t_1 - t_2$, also total strain
ψ	yaw angle
v	Kolmogoroff velocity

Superscripts

$\overline{(\ )}$	average
$(\ )'$	root mean square

Part B

c	chord length of ribbon
C_f	skin friction coefficient
k_s	shear constant of wind tunnel $\frac{1}{U_c}\frac{\partial \overline{U}}{\partial n}$
l	wake half width
n	transverse coordinate
R	radius of curvature
R_c	radius of curvature at centerline of section
R_w	wall radius of curvature
Re	Reynolds number
Re_θ	Reynolds number based on boundary layer momentum thickness
Re_c	Reynolds number based on ribbon's chord length
s	streamwise coordinate
s_g	streamwise distance from shear generator
S	curvature parameter $= \frac{\frac{\overline{U}_c}{R_c}}{\frac{\partial \overline{U}}{\partial n}}$
t	thickness of ribbon
u	fluctuating velocity in streamwise direction
U	mean velocity in the streamwise direction
U_c	mean velocity in the streamwise direction at centerline of section
U_s	maximum velocity deficit in wake of ribbon
v	fluctuating velocity in transverse direction
w	fluctuating velocity in spanwise direction

x streamwise coordinate

y transverse coordinate

z spanwise coordinate

Greek symbols

δ boundary layer thickness

ν_T turbulent eddy viscosity

θ boundary layer momentum thickness

ξ nondimensional distance from wall $= \frac{n}{\delta}$

Chapter 1

General Introduction

1.1 Motivation

Drag reduction for external flows has been a challenging task for scientists and engineers for a long time, as evidenced for instance, in the review by Bushnell (1983). As knowledge on the origins of drag and on methods for its reduction improved, design of vehicles and machinery improved as well. For example, bluff cars and airplanes, having their wings and fuselage connected by multiple struts, were replaced by streamlined and more compact vehicles to reduce form drag. To further control form drag, different methods were used to delay separation of the boundary layer. Among the passive methods used is roughening of the wall surface to promote early transition to turbulence, as it is known that turbulence delays separation by increasing the rate of transfer of the free stream momentum to the wall. Some active methods involve suction of the boundary layer. Besides reducing form drag, efforts have also been made to reduce the other important type of drag, namely skin friction. This type of drag is higher in turbulent, than in laminar boundary layers. Attempts have been made to maintain an attached laminar flow over wings and other aerodynamic surfaces. Heating or cooling of the wall surface, depending on the type of fluid involved, have also been used for skin friction reduction. Maintaining laminar flow and suppressing turbulence is not always possible, especially in some practical cases for which the Reynolds numbers involved are very high. (A typical Reynolds number for flow over the fuselage of a commercial airplane is of the order of 10^8). For this reason, attention has been lately focussed on drag reduction by manipulation of the structure of the turbulent boundary layer. This can be achieved by active methods, such as mass injection in the flow (for example, polyethylene oxide injected in water has proved to reduce wall pressure fluctuations). It is obvious, however, that passive methods are preferable to active ones for their economic and technical advantages.

A method by which turbulence can be controlled is curvature of the wall. It has been well established that modest longitudinal convex curvature of the wall reduces turbulence intensity and skin friction. Wall shear stress on concave walls is higher and on convex walls it is lower than on flat walls. Although the instantaneous streamlines of all turbulent flows are highly curved and the majority of turbulent shear flows display curved mean streamlines, the effects of curvature have not yet been optimally accounted for in aerodynamic design.

Various devices have been proposed for skin friction reduction. Riblets, which are small grooves on the wall, aligned with the flow direction, are known to dampen the turbulence and reduce the skin friction under certain conditions. The riblets are also called internal manipulators, because they modify the wall sublayer of the boundary layer, in contrast to the external manipulators, mostly known as LEBU (Large Eddy

Break-Up devices), which act upon the outer sublayer. The latter devices are also known as BLADE (Boundary Layer Alteration Devices), OLD (Outer Layer Devices), RIOL (Ribbons In Outer Layer), Ribbons, Turbulence Manipulators, and Turbulence Moderators. They are placed in the outer region of the boundary layer and are known to cause skin friction reduction on the downstream wall. It is now believed that the wake of the ribbon plays a dominant role in the mechanisms of skin friction reduction.

The physical mechanisms controlling the structure of a turbulent boundary layer are very complex. The manipulation of boundary layers by using LEBU or by subjecting them to curvature adds more complexity. Moreover, experimental investigations in turbulent boundary layers are complicated by the difficulty of obtaining a good spatial resolution due to their relatively small size. In order to effectively use these methods for drag reduction, a good understanding of all physical phenomena involved is essential. This work is aimed at contributing to the understanding of the physical effects of curvature and thin manipulators on the structure of shear flows.

It is hoped that this work will provide more ideas in design considerations for drag reduction by turbulence structure manipulation and also contribute to the general understanding of the fundamentals of shear flows.

1.2 Objectives

Mean shear, wall effects and free stream entrainment are the main features affecting the structure of turbulent boundary layers. Mean shear plays a major role in the production and maintenance of turbulence. A simpler shear flow would be an unbounded one with a uniform mean shear and statistically homogeneous turbulence intensities. Laboratory realizations of flows resembling this idealized flow have been reported by many researchers, among them Rose (1966), Champagne, Harris and Corrsin (1970), Tavoularis and Corrsin (1981), Karnik and Tavoularis (1987) and Tavoularis and Karnik (1989), later referred to as TK. The experimental facility used by the latter authors was available for the present investigation. Tavoularis and Corrsin (1981) reported that these laboratory flows, termed "nearly homogeneous, uniformly sheared flows", had many similarities with the outer region of the turbulent boundary layer. Holloway and Tavoularis (1992a and 1992b), later referred to as HT1 and HT2 respectively, showed that uniformly sheared flows subjected to curvature behaved qualitatively similarly to curved turbulent boundary layers. Even though numerous successful investigations have been carried out on curved turbulent boundary layers and turbulent boundary layers manipulated by LEBU, more insight into these topics will be achieved by studying the behavior of the less complicated case of manipulation of the structure of the nearly homogeneous uniformly sheared flow. This will permit to bring into foreground the interaction between the shear and the curvature, and the shear and the manipulators, in the absence of wall and entrainment effects.

Two approaches are generally followed in the study of the manipulation of the structure of turbulent flows. The first is from an engineering point of view, and is concerned with the resulting effects from this manipulation on skin friction, heat transfer, noise etc., while the second is from a fundamental point of view, and is aimed at the study of the complex structure of turbulent flows and their response to disturbances. In this investigation, the second approach is adopted. The relative simplicity of the present flow (near homogeneity and absence of entrainment and wall effects) presents a tangible advantage to understand the response of the turbulence structure to manipulation.

The aims of the present investigation are to further study the effects of curvature on the turbulence structure of these flows and to investigate the development of the wake of a LEBU in these flows. Then connection will be made between the present experiments and the more complicated case of boundary layer flows.

The first part of this work is devoted to the investigation of the effect of curvature reversal and to the study of the rate of adjustment of the turbulence structure to curvature. The development of the wake of a manipulator placed in straight and curved shear flows is studied in the second part.

Part A:

Chapter 2

Introduction

Subjecting the streamlines of a shear flow to curvature amounts to the introduction of an extra rate of strain to the flow, in addition to its mean shear. The present flow, similar to curved boundary layer flows, is curved shear flow in which the streamline curvature is in the plane of the mean shear. This type of streamline curvature is probably the most common and important type of extra rates of strain. The effects of streamline curvature on the behavior of the flow have been studied extensively and are known to be significant. The variation of the angular momentum of the mean flow with respect to the radius of curvature of the mean streamlines is of primary importance in classifying curved shear flows. It is well established that when the angular momentum of the mean flow increases with increasing radius of curvature, the turbulent mixing is suppressed, and the flow is referred to as "stabilizing". On the other hand, when the angular momentum of the mean flow decreases with increasing radius of curvature, turbulent mixing is enhanced, and the flow is referred to as "destabilizing". According to the above classification, convex surfaces would have "stabilizing" effects, while concave surfaces would have "destabilizing" effects on turbulent boundary layers.

The introduction of convex wall curvature to reduce skin friction is a very attractive method of drag reduction due to its simplicity and effectiveness. Since in actual engineering applications, such as in the case of flows over airfoils or wings, the extent of curved regions is generally limited, the adjustment of turbulence structure to curvature is of high practical importance. Nevertheless, it is believed that this subject has not received enough attention. An attempt is made in the present investigation to study the adjustment of uniformly sheared flow to the introduction of curvature. As previously discussed, this flow presents some similarities with the outer region of turbulent boundary layers. Data from the present measurements and from those reported in the literature are used to investigate the possible dependence of the adjustment characteristics on the strength of curvature.

Moreover, streamlines subjected to curvature in one direction are frequently, in engineering applications, subjected to curvature reversal. For this reason, the behavior of the flow after curvature reversal is also examined.

Predictive methods for the effects of curvature, depending on its strength, are necessary for engineering design and calculations. In the investigation of HT1 the effects of curvature on a uniformly sheared flow were successfully described by a relation outlining the dependence of the Reynolds shear stress structural parameter on the relative strength of curvature to the mean shear of the flow. While the results of the latter investigation remain mostly academic, a quantitative comparison of the results obtained from experiments in curved turbulent boundary layers is very desirable. In the present investigation a step is made in this direction. The approach used by HT1 is extended to data collected from various experiments in curved turbulent boundary layers reported in the literature.

Chapter 3

Literature Review

The effects of wall curvature on turbulent flows were experimentally identified from mean flow measurements as early as the 1930's in Prandtl's laboratory in Göttingen, Germany, by Wilcken (1930), Wattendorf (1935) and Schmidbauer (1936). Wilcken (1930) observed that boundary layer growth is enhanced on concave surfaces and suppressed on convex ones. Wattendorf (1935) performed measurements of turbulent flows in curved ducts and identified the stabilizing effects of convex surfaces and the destabilizing effects of concave surfaces, using pressure, mean velocity and wall shear stress measurements. Schmidbauer (1936) concluded that convex boundary layers had lower skin friction compared to boundary layers on flat walls.

Bradshaw (1973) mentioned that the subject was virtually ignored after these experiments for nearly 20 years, and very few experiments were reported in the literature before the 1970 s, among which are those performed by Eskinazi and Yeh (1956) in a curved duct.

A growing interest was manifested in the 1970's. Ellis and Joubert (1974) performed detailed mean flow measurements in a curved duct and confirmed the increase of skin friction and of the rate of growth of the boundary layer on concave walls and their decrease on convex walls, compared to flat plate boundary layers. The above investigations established very well the response of the mean parameters of the boundary layer to the introduction of curvature. It has also been concluded by Ellis and Joubert (1974), Ramaprian and Shivaprasad (1978) and others that the extent of the logarithmic region of the boundary layer is decreased for convex turbulent boundary layers and increased for concave boundary layers.

Some turbulence measurements were also performed in this period, such as those by So and Mellor (1973), Meroney and Bradshaw (1975), Ramaprian and Shivaprasad (1978) and Shivaprasad and Ramaprian (1978). So and Mellor (1973) performed turbulence measurements in a turbulent boundary layer along a convex surface, with a boundary layer thickness to wall radius of curvature, $\frac{\delta}{R_w} \simeq 0.1$, and observed a reduction of the Reynolds stresses near the wall and their vanishing at a distance from the wall equal to about half the boundary layer thickness, δ. Meroney and Bradshaw (1975) performed turbulence measurements in curved convex and concave boundary layers ($\frac{\delta}{R_w} \simeq 0.01$). They observed a decrease in the shear stress near the wall and its vanishing at about 0.9δ from the wall for convex curved boundary layers, and its increase for concave curved boundary layers. Shivaprasad and Ramaprian (1978) conducted turbulence measurements including moments, autocorrelations, spectra and probability distributions in boundary layers along concave and convex walls with $\frac{\delta}{R_w} \simeq 0.01$. They found that the outer region of the turbulent boundary layer was affected by curvature more than the inner one is and that the velocity and length scales increased on concave surfaces and decreased on convex ones.

From the above investigations and from others it has been well established that convex curvature of the wall causes reduction of Reynolds stresses and length scales in boundary layers compared to those over a flat wall, while concave wall curvature causes the opposite effects: the outer region of the turbulent boundary layer is more affected by curvature than the inner one and curvature has a relatively stronger effect on the shear stress than on the normal stresses.

The strength of curvature is usually measured in the case of boundary layers by the ratio of the boundary layer thickness to the radius of curvature, $\frac{\delta}{R_w}$. The consensus is that curvature is considered mild for $\frac{\delta}{R_w} \simeq 0.01$ and strong for $\frac{\delta}{R_w} \simeq 0.1$. It has been concluded that while at mild curvatures the effect on boundary layers is noticeable, increasing the strength of curvature would not cause proportional increase of its effects (Ramaprian and Shivaprasad, 1978).

In the 1980's much more interest was taken in the subject and the literature was enriched with many measurements of curved turbulent boundary layers, including those of Gillis and Johnston (1980, 1983), Gibson, Verriopoulos and Vlachos (1984) and Muck, Hoffmann and Bradshaw (1985), for convex boundary layers, and those of Nakano et al. (1981), Shizawa and Honami (1983), Hoffmann, Muck and Bradshaw (1985), Jayaram, Taylor and Smits (1987) and Barlow and Johnston (1988a and 1988b) for concave boundary layers.

While concave and convex curvatures have opposite effects on boundary layers, contradicting conclusions were reached by different researchers on the relative importance of the turbulence parameter alteration by the two types of curvature. Ramaprian and Shivaprasad (1978) concluded that convex wall curvature seems to have stronger effects than concave wall curvature, for the same $\frac{\delta}{R_w}$, while Smits and Wood (1985) concluded from the results of Muck, Hoffman and Bradshaw (1985) that concave curvature had a stronger influence on turbulence structure than convex curvature did.

An important aspect of curved turbulent boundary layers is the adjustment of their turbulence structure to the introduction of wall curvature. An adjustment length of 10δ, suggested by Bradshaw (1973) has been frequently used; and some discussion on the subject has been included in the publications by Gillis and Johnston (1980 and 1983), Shizawa and Honami (1983 and 1985), Gibson, Verriopoulos and Vlachos (1984), Muck, Hoffmann and Bradshaw (1985), Hoffmann, Muck and Bradshaw (1985) and Barlow and Johnston (1988a).

Recovery from curvature and relaxation of the different turbulence quantities was also a point of interest and has been investigated by Smits, Young and Bradshaw (1979), who studied the relaxation of turbulent boundary layers subjected to short regions of strong convex and concave curvature, Gillis and Johnston (1980 and 1983), who examined the shear stress and wall shear recovery of a turbulent boundary layer subjected to a 90° convex curvature, and Alving and Smits (1986), who also studied the recovery of a turbulent boundary layer from a 90° strong convex curvature. Jayaram, Taylor and Smits (1987) studied the response of a compressible turbulent boundary layer to short regions of concave surface curvature and its relaxation.

Boundary layers subjected to curvature reversal have been studied by Baskaran, Smits and Joubert (1987 and 1991), who examined the development of a turbulent boundary layer subjected to a short region of concave curvature followed by a prolonged region of convex curvature. Gatski and Savill (1989) examined numerically the effects of curvature and its reversal on wall bounded shear flows. Their study included combinations of successive straight, stabilizing and destabilizing curvatures.

The present investigation is an extension of an experimental study by HT1 and HT2 on nearly homogeneous uniform shear flow subjected to prolonged uniform curvature. In their experiments, HT1 and HT2 used combinations of different curvatures and shear constants to get a wide range of the parameter $S = \frac{\frac{\overline{U}_c}{R_c}}{\frac{\partial U}{\partial n}}$, which represents a relative measure of the curvature magnitude with respect to the mean shear. While the previous investigations focussed on the effects of prolonged curvature on sheared flow, the present experiments deal with the effects of curvature reversal on the shear flow and the rate of adjustment of the flow structure to curvature.

Chapter 4

Analytical Considerations

4.1 Definitions of Turbulence Quantities

In this section, the relevant turbulence quantities to be used in this investigation are defined (Tavoularis, 1986).

The instantaneous velocity components in an (s,n,z) system of coordinates and the instantaneous pressure are decomposed into mean components, denoted by overbars, and fluctuating components, denoted by lower case letters, by using the Reynolds decomposition (Reynolds, 1894)

$$U = \overline{U} + u \tag{4.1}$$

$$V = \overline{V} + v \tag{4.2}$$

$$W = \overline{W} + w \tag{4.3}$$

$$P = \overline{P} + p \tag{4.4}$$

The Reynolds stresses are defined as the covariances (cross-correlations or double correlations) of the velocity fluctuations. The Reynolds stress tensor is then

$$\begin{pmatrix} \overline{u^2} & \overline{uv} & \overline{uw} \\ \overline{uv} & \overline{v^2} & \overline{vw} \\ \overline{uw} & \overline{vw} & \overline{w^2} \end{pmatrix} \tag{4.5}$$

(Note that the covariances should be multiplied by the negative density of the fluid to get the correct dimensions and sign for the stresses).

The non-vanishing structural parameters (or dimensionless Reynolds stresses) are obtained by nondimensionalizing the Reynolds stresses with the turbulent kinetic energy, $q^2 = \overline{u^2} + \overline{v^2} + \overline{w^2}$, as

$$K_{uu} = \frac{\overline{u^2}}{q^2} \tag{4.6}$$

$$K_{vv} = \frac{\overline{v^2}}{q^2} \tag{4.7}$$

$$K_{ww} = \frac{\overline{w^2}}{q^2} \tag{4.8}$$

$$K_{uv} = \frac{\overline{uv}}{q^2} \tag{4.9}$$

The correlation coefficient is another nondimensional representation of the Reynolds shear stresses, obtained by nondimensionalization with the product of corresponding rms values. For example, the correlation coefficient corresponding to the Reynolds shear stress $\overline{uv}$ is

$$\rho_{uv} = \frac{\overline{uv}}{u'v'} \tag{4.10}$$

where $u' = \sqrt{\overline{u^2}}$ and $v' = \sqrt{\overline{v^2}}$.

Temporal autocorrelations are measured by introducing a time delay, τ, into a signal, and then computing the averages of products of delayed and non-delayed quantities. For example, the autocorrelation coefficient in the streamwise direction is given as

$$R_{uu}(\tau) = \frac{\overline{u(t)u(t+\tau)}}{\overline{u^2}} \tag{4.11}$$

R_{vv} and R_{ww} corresponding to transverse and spanwise directions respectively are defined similarly. Integral time scales are defined as the integrals of the corresponding autocorrelation coefficients, for example as

$$T_{uu} = \int_0^\infty R_{uu}(\tau)d\tau \tag{4.12}$$

The Taylor time microscale in the streamwise direction is expressed as

$$\tau_{uu} = \left(\frac{\overline{u^2}}{\overline{(\partial u/\partial t)^2}}\right)^{1/2} \tag{4.13}$$

Length scales in the streamwise direction can be estimated using Taylor's hypothesis, so that

$$L_{uu} = \overline{U}T_{uu}, \quad L_{vv} = \overline{U}T_{vv}, \quad L_{ww} = \overline{U}T_{ww} \tag{4.14}$$

and

$$\lambda_{uu} = \overline{U}\tau_{uu} \tag{4.15}$$

The one-dimensional "frequency spectra" of a velocity component is defined as the Fourier transform of the corresponding autocorrelation function. For example, the streamwise one-dimensional "frequency spectra" is given as

$$F_{uu}(f) = \int_{-\infty}^{\infty} \overline{u(t)u(t+\tau)}e^{-j2\pi f\tau}d\tau \tag{4.16}$$

where $j = \sqrt{-1}$. The cross spectra $F_{uv}(f)$ of the two fluctuating velocity components $u(t)$ and $v(t)$ is defined as the Fourier transform of their cross correlation

$$F_{uv}(f) = \int_{-\infty}^{\infty} \overline{u(t)v(t+\tau)} e^{-j2\pi f\tau} d\tau \tag{4.17}$$

Alternative expressions for 4.16 and 4.17 are obtained by making use of the direct Fourier transforms, $\mathcal{U}$(f,T) and $\mathcal{V}$(f,T), of $u(t)$ and $v(t)$, respectively, in an interval (-T,T). $\mathcal{U}$(f,T) and $\mathcal{V}$(f,T) are given respectively as

$$\mathcal{U}(f,T) = \int_{-T}^{T} u(t) e^{-j2\pi ft} dt \tag{4.18}$$

$$\mathcal{V}(f,T) = \int_{-T}^{T} v(t) e^{-j2\pi ft} dt \tag{4.19}$$

The streamwise one-dimensional "frequency spectra" is then estimated as

$$F_{uu}(f) = \lim_{T\to\infty} \frac{1}{2T} |\mathcal{U}(f,T)|^2 \tag{4.20}$$

and the cross spectrum, $F_{uv}(f)$, as

$$F_{uv}(f) = \lim_{T\to\infty} \frac{1}{2T} (\mathcal{U}^*(f,T).\mathcal{V}(f,T)) \tag{4.21}$$

where $\mathcal{U}^*$ is the complex conjugate of $\mathcal{U}$. The coherence function is defined as

$$C_{uv}(f) = \frac{F_{uv}(f)}{(F_{uu}(f)F_{vv}(f))^{\frac{1}{2}}} \tag{4.22}$$

4.2 The (s,n,z) System of Coordinates

The (s,n,z) system of coordinates, shown in Figure 4.1, will be used to study the present type of curved shear flow which consists of consecutive sections, each with a constant curvature, thus exhibiting stepwise changes of curvature. In this system of coordinates, the coordinate s coincides with the geometric centerline of the test section. For a general curvilinear system of coordinates (q_1, q_2, q_3), the scale factors h_1, h_2 and h_3 relate the differential distances to the differentials of the coordinates. They are useful in determining the unit vectors of the system of coordinates and the different operators. They are equal to unity for a cartesian system of coordinates, and are given, for a general curvilinear system of coordinates with respect to the cartesian system of coordinates, (x,y,z), as (Karamcheti, 1966, p.140.)

$$h_m^2 = (\frac{\partial x}{\partial q_m})^2 + (\frac{\partial y}{\partial q_m})^2 + (\frac{\partial z}{\partial q_m})^2 \tag{4.23}$$

The unit vectors in a curvilinear coordinate system are given as

$$\mathbf{e}_m = \frac{1}{h_m}(\frac{\partial x}{\partial q_m}\mathbf{i} + \frac{\partial y}{\partial q_m}\mathbf{j} + \frac{\partial z}{\partial q_m}\mathbf{k}) \tag{4.24}$$

where m=1,2,3 and $\mathbf{i}$, $\mathbf{j}$ and $\mathbf{k}$ are the unit vectors of the (x,y,z) system of coordinates.

The (s,n,z) system of coordinates, shown in Figure 4.1, can be obtained from the cartesian system of coordinates, (x,y,z), also shown in the Figure, by the transformation

$$\begin{aligned} x &= x_{ci} + (R_{ci} + n)sin\frac{s - s_i}{R_{ci}} \\ y &= y_{ci} + (R_{ci} + n)cos\frac{s - s_i}{R_{ci}} \\ z &= z \end{aligned} \tag{4.25}$$

The values of s_i, x_{ci}, y_{ci} and R_{ci} are constant for every subsection and are shown in Figure 4.1. The convention used for the radius of curvature is that R_{ci} is positive if n is pointed away from the center of curvature and it is negative if n is pointed towards the center of curvature. Using equations 4.23, 4.24 and 4.25, the scale factors and the unit vectors of the (s,n,z) system of coordinates are obtained respectively as

$$\begin{aligned} h_s = h_1 &= 1 + \frac{n}{R_{ci}} \\ h_n = h_2 &= 1 \\ h_z = h_3 &= 1 \end{aligned} \tag{4.26}$$

$$\begin{aligned} \mathbf{e}_1 = \mathbf{e}_s &= cos\frac{s - s_i}{R_{ci}}\mathbf{i} - sin\frac{s - s_i}{R_{ci}}\mathbf{j} \\ \mathbf{e}_2 = \mathbf{e}_n &= sin\frac{s - s_i}{R_{ci}}\mathbf{i} + cos\frac{s - s_i}{R_{ci}}\mathbf{j} \\ \mathbf{e}_3 = \mathbf{e}_z &= \mathbf{k} \end{aligned} \tag{4.27}$$

A vector is given in the (s,n,z) system of coordinates by

$$\mathbf{A} = A_s\mathbf{e}_s + A_n\mathbf{e}_n + A_z\mathbf{e}_z \tag{4.28}$$

The velocity vector $\mathbf{U}$ is given in the (s,n,z) system of coordinates by

$$\mathbf{U} = U\mathbf{e}_s + V\mathbf{e}_n + W\mathbf{e}_z \tag{4.29}$$

In a general curvilinear coordinate system the del operator (Karamcheti, 1966, p.108) is given by

$$\nabla = \mathbf{e}_1\frac{1}{h_1}\frac{\partial}{\partial q_1} + \mathbf{e}_2\frac{1}{h_2}\frac{\partial}{\partial q_2} + \mathbf{e}_3\frac{1}{h_3}\frac{\partial}{\partial q_3} \tag{4.30}$$

By using the scale factors from equation 4.26, one gets

$$\nabla = \mathbf{e}_s\aleph\frac{\partial}{\partial s} + \mathbf{e}_n\frac{\partial}{\partial n} + \mathbf{e}_z\frac{\partial}{\partial z} \tag{4.31}$$

where $\aleph = (1 + \frac{n}{R_{ci}})^{-1}$. Then the gradient of a scalar ϕ is

$$\nabla\phi = \mathbf{e}_s\aleph\frac{\partial\phi}{\partial s} + \mathbf{e}_n\frac{\partial\phi}{\partial n} + \mathbf{e}_z\frac{\partial\phi}{\partial z} \tag{4.32}$$

and the gradient of a vector $\mathbf{A}$, which is a second order tensor, can be shown to be

$$\nabla \mathbf{A} = \begin{pmatrix} \aleph\frac{\partial A_s}{\partial s} + A_n\frac{\aleph}{R_{ci}} & \frac{\partial A_s}{\partial n} & \frac{\partial A_s}{\partial z} \\ \aleph\frac{\partial A_n}{\partial s} - A_s\frac{\aleph}{R_{ci}} & \frac{\partial A_n}{\partial n} & \frac{\partial A_n}{\partial z} \\ \aleph\frac{\partial A_z}{\partial s} & \frac{\partial A_z}{\partial n} & \frac{\partial A_z}{\partial z} \end{pmatrix} \tag{4.33}$$

The strain of $\mathbf{A}$ is then obtained from the components of $\nabla\mathbf{A}$ (Karamcheti, 1966, p.106) as

$$strain\mathbf{A} = \begin{pmatrix} \aleph\frac{\partial A_s}{\partial s} + A_n\frac{\aleph}{R_{ci}} & \frac{1}{2}\left(\frac{\partial A_s}{\partial n} + \aleph\frac{\partial A_n}{\partial s} - A_s\frac{\aleph}{R_{ci}}\right) & \frac{1}{2}\left(\frac{\partial A_s}{\partial z} + \aleph\frac{\partial A_z}{\partial s}\right) \\ \frac{1}{2}\left(\frac{\partial A_s}{\partial n} + \aleph\frac{\partial A_n}{\partial s} - A_s\frac{\aleph}{R_{ci}}\right) & \frac{\partial A_n}{\partial n} & \frac{1}{2}\left(\frac{\partial A_n}{\partial z} + \frac{\partial A_z}{\partial n}\right) \\ \frac{1}{2}\left(\frac{\partial A_s}{\partial z} + \aleph\frac{\partial A_z}{\partial s}\right) & \frac{1}{2}\left(\frac{\partial A_n}{\partial z} + \frac{\partial A_z}{\partial n}\right) & \frac{\partial A_z}{\partial z} \end{pmatrix} \tag{4.34}$$

The divergence of a vector $\mathbf{A}$ in the (s,n,z) system of coordinates is

$$\nabla.\mathbf{A} = \aleph\frac{\partial A_s}{\partial s} + \aleph\frac{\partial}{\partial n}\left(\frac{A_n}{\aleph}\right) + \frac{\partial A_z}{\partial z} \tag{4.35}$$

The curl of a vector $\mathbf{A}$ in the (s,n,z) system of coordinates is

$$\nabla\times\mathbf{A} = \left(\frac{\partial A_n}{\partial z} - \frac{\partial A_z}{\partial n}\right)\mathbf{e_s} + \left(\frac{\partial A_s}{\partial z} - \aleph\frac{\partial A_z}{\partial s}\right)\mathbf{e_n} + \left(\frac{\partial A_s}{\partial n} - \aleph\left(\frac{\partial A_n}{\partial s} - \frac{A_s}{R_{ci}}\right)\right)\mathbf{e_z} \tag{4.36}$$

The Laplacian of a scalar in (s,n,z) is derived to be

$$\nabla^2\phi = \nabla.(\nabla\phi) = \aleph^2\frac{\partial^2\phi}{\partial s^2} + \aleph\frac{\partial}{\partial n}\left(\frac{1}{\aleph}\frac{\partial\phi}{\partial n}\right) + \aleph\frac{\partial\phi}{\partial s}\frac{\partial\aleph}{\partial s} + \frac{\partial^2\phi}{\partial z^2} \tag{4.37}$$

It should be noted at this point that for the geometry of the section considered the radius of curvature changes from one subsection to the other. Since R_{ci} is not a continuous function along the section, the term $\frac{\partial\aleph}{\partial s}$ in the expression for the Laplacian operator does not exist at the points of change of curvature, if $n \neq 0$. Along the centerline, $n = 0$, $\aleph$ is equal to 1. Fortunately, as it will be shown in the next section, the terms involving Laplacians in the Reynolds stress equations may be neglected for the entire section.

The vector Laplacian is given as

$$\nabla^2 \mathbf{A} = \nabla(\nabla.\mathbf{A}) - \nabla \times (\nabla \times \mathbf{A}) \tag{4.38}$$

and, in an expanded form in the (s,n,z) system of coordinates, as

$$\nabla^2 \mathbf{A} = \left(\nabla^2 A_s + 2\frac{\aleph^2}{R_{ci}}\frac{\partial A_n}{\partial s} - \frac{\aleph^2}{R_{ci}^2}A_s\right)\mathbf{e}_s + \left(\nabla^2 A_n - 2\frac{\aleph^2}{R_{ci}}\frac{\partial A_s}{\partial s} - \frac{\aleph^2}{R_{ci}^2}A_n\right)\mathbf{e}_n + \left(\nabla^2 A_z\right)\mathbf{e}_z \tag{4.39}$$

4.3 Governing Equations of Curved Homogeneous Uniformly Sheared Flow

The Navier Stokes (momentum) and continuity equations for an incompressible fluid with constant properties are

$$\frac{\partial \mathbf{U}}{\partial t} + \mathbf{U}.\nabla\mathbf{U} = -\nabla\frac{P}{\rho} + \nu\nabla^2\mathbf{U} \tag{4.40}$$

$$\nabla.\mathbf{U} = 0 \tag{4.41}$$

The momentum equation can be written in the three directions of the (s,n,z) system of coordinates by using equations 4.32, 4.33 and 4.39, as

$$\frac{\partial U}{\partial t} + \aleph U\frac{\partial U}{\partial s} + V\frac{\partial U}{\partial n} + W\frac{\partial U}{\partial z} + \aleph\frac{UV}{R_{ci}} = -\frac{1}{\rho}\aleph\frac{\partial P}{\partial s} + \nu(\nabla^2 U + 2\frac{\aleph^2}{R_{ci}}\frac{\partial V}{\partial s} - \frac{\aleph^2}{R_{ci}^2}U) \tag{4.42}$$

$$\frac{\partial V}{\partial t} + \aleph U\frac{\partial V}{\partial s} + V\frac{\partial V}{\partial n} + W\frac{\partial V}{\partial z} - \aleph\frac{U^2}{R_{ci}} = -\frac{1}{\rho}\frac{\partial P}{\partial n} + \nu(\nabla^2 V - 2\frac{\aleph^2}{R_{ci}}\frac{\partial U}{\partial s} - \frac{\aleph^2}{R_{ci}^2}V) \tag{4.43}$$

$$\frac{\partial W}{\partial t} + \aleph U\frac{\partial W}{\partial s} + V\frac{\partial W}{\partial n} + W\frac{\partial W}{\partial z} = -\frac{1}{\rho}\frac{\partial P}{\partial z} + \nu(\nabla^2 W) \tag{4.44}$$

By using equation 4.35, the continuity equation can be written in the curvilinear coordinate system as

$$\aleph\frac{\partial U}{\partial s} + \aleph\frac{\partial}{\partial n}(\frac{V}{\aleph}) + \frac{\partial W}{\partial z} = 0 \tag{4.45}$$

By using the Reynolds decomposition and averaging the above equations, the mean flow equations are obtained as

$$\begin{aligned}\frac{\partial \overline{U}}{\partial t} + \aleph\overline{U}\frac{\partial \overline{U}}{\partial s} + \overline{V}\frac{\partial \overline{U}}{\partial n} + \overline{W}\frac{\partial \overline{U}}{\partial z} + \aleph\frac{\overline{U}\,\overline{V}}{R_{ci}} &= -\aleph\frac{1}{\rho}\frac{\partial \overline{P}}{\partial s} - \\ &\quad (\aleph\frac{\partial \overline{u^2}}{\partial s} + \aleph\frac{\partial}{\partial n}\frac{\overline{uv}}{\aleph} + \frac{\partial \overline{uw}}{\partial z} + \aleph\frac{\overline{uv}}{R_{ci}}) + \\ &\quad \nu(\nabla^2\overline{U} + 2\frac{\aleph^2}{R_{ci}}\frac{\partial \overline{V}}{\partial s} - \frac{\aleph^2}{R_{ci}^2}\overline{U})\end{aligned} \tag{4.46}$$

$$\begin{aligned}\frac{\partial \overline{V}}{\partial t} + \aleph\overline{U}\frac{\partial \overline{V}}{\partial s} + \overline{V}\frac{\partial \overline{V}}{\partial n} + \overline{W}\frac{\partial \overline{V}}{\partial z} - \aleph\frac{\overline{U}^2}{R_{ci}} &= -\frac{1}{\rho}\frac{\partial \overline{P}}{\partial n} - \\ &\quad (\aleph\frac{\partial \overline{uv}}{\partial s} + \aleph\frac{\partial}{\partial n}\frac{\overline{v^2}}{\aleph} + \frac{\partial \overline{vw}}{\partial z} - \aleph\frac{\overline{u^2}}{R_{ci}}) + \\ &\quad \nu(\nabla^2\overline{V} - 2\frac{\aleph^2}{R_{ci}}\frac{\partial \overline{U}}{\partial s} - \frac{\aleph^2}{R_{ci}^2}\overline{V})\end{aligned} \tag{4.47}$$

$$\begin{aligned}\frac{\partial \overline{W}}{\partial t} + \aleph\overline{U}\frac{\partial \overline{W}}{\partial s} + \overline{V}\frac{\partial \overline{W}}{\partial n} + \overline{W}\frac{\partial \overline{W}}{\partial z} &= -\frac{1}{\rho}\frac{\partial \overline{P}}{\partial z} - \\ &\quad (\aleph\frac{\partial \overline{uw}}{\partial s} + \aleph\frac{\partial}{\partial n}\frac{\overline{vw}}{\aleph} + \frac{\partial \overline{w^2}}{\partial z}) + \\ &\quad \nu(\nabla^2\overline{W})\end{aligned} \tag{4.48}$$

$$\aleph\frac{\partial \overline{U}}{\partial s} + \aleph\frac{\partial}{\partial n}\frac{\overline{V}}{\aleph} + \frac{\partial \overline{W}}{\partial z} = 0 \tag{4.49}$$

Equations of the fluctuating components can be obtained by subtracting the mean equations from the instantaneous equations. The fluctuating equations can be manipulated to obtain the equations of the different Reynolds stresses. For instance, the equation of the turbulent kinetic energy and the equation of the Reynolds shear stress in the (s,n) plane are given respectively as

$$\begin{aligned}
\frac{D}{Dt}\frac{q^2}{2} = & -[\aleph\overline{u^2}\frac{\partial \overline{U}}{\partial s} + \overline{uv}\frac{\partial \overline{U}}{\partial n} + \overline{uw}\frac{\partial \overline{U}}{\partial z} + \\
& \aleph\overline{uv}\frac{\partial \overline{V}}{\partial s} + \overline{v^2}\frac{\partial \overline{V}}{\partial n} + \overline{vw}\frac{\partial \overline{V}}{\partial z} + \\
& \aleph\overline{uw}\frac{\partial \overline{W}}{\partial s} + \overline{vw}\frac{\partial \overline{W}}{\partial n} + \overline{w^2}\frac{\partial \overline{W}}{\partial z} - \frac{\aleph}{R_{ci}}(\overline{uv}\overline{U} - \overline{u^2}\overline{V})] \qquad (4.50) \\
& -[\aleph\frac{\partial}{\partial s}(\frac{\overline{pu}}{\rho} + \frac{\overline{uq^2}}{2}) + \aleph\frac{\partial}{\partial n}(\frac{\overline{pv}}{\rho\aleph} + \frac{\overline{vq^2}}{2\aleph}) + \frac{\partial}{\partial z}(\frac{\overline{pw}}{\rho} + \frac{\overline{wq^2}}{2})] + \\
& \nu\nabla^2\frac{\overline{q^2}}{2} - \nu\overline{[(\frac{\partial u}{\partial n})^2 + \aleph^2(\frac{\partial u}{\partial s})^2 + (\frac{\partial u}{\partial z})^2 + (\frac{\partial v}{\partial n})^2 + \aleph^2(\frac{\partial v}{\partial s})^2 + (\frac{\partial v}{\partial z})^2 +} \\
& \overline{(\frac{\partial w}{\partial n})^2 + \aleph^2(\frac{\partial w}{\partial s})^2 + (\frac{\partial w}{\partial z})^2 + \frac{\aleph^2}{R_{ci}}(v\frac{\partial u}{\partial s} - u\frac{\partial v}{\partial s}) + \frac{\aleph^2}{R_{ci}^2}(u^2 + v^2)]}
\end{aligned}$$

$$\begin{aligned}
\frac{D}{Dt}\overline{uv} = & -[\aleph\overline{u^2}\frac{\partial \overline{V}}{\partial s} + \aleph\overline{uv}\frac{\partial \overline{U}}{\partial s} + \overline{uv}\frac{\partial \overline{V}}{\partial n} + \\
& \overline{v^2}\frac{\partial \overline{U}}{\partial n} + \overline{uw}\frac{\partial \overline{V}}{\partial z} + \overline{vw}\frac{\partial \overline{U}}{\partial z} - \frac{\aleph}{R_{ci}}(\overline{U}(2\overline{u^2} - \overline{v^2}) + \overline{uv}\overline{V})] + \\
& \aleph\overline{\frac{p}{\rho}(\frac{\partial v}{\partial s} + \aleph\frac{\partial}{\partial n}\frac{u}{\aleph})} - [\aleph\frac{\partial}{\partial s}(\frac{\overline{pv}}{\rho} + \overline{u^2 v}) + \qquad (4.51) \\
& \aleph\frac{\partial}{\partial n}(\frac{\overline{pu}}{\rho\aleph} + \frac{\overline{uv^2}}{\aleph}) + \frac{\partial}{\partial z}\overline{uvw} + \frac{\aleph}{R_{ci}}(\overline{uv^2} - \overline{u^3})] + \\
& \nu\nabla^2\overline{uv} - 2\nu\overline{[\frac{\partial u}{\partial n}\frac{\partial v}{\partial n} + \aleph^2\frac{\partial u}{\partial s}\frac{\partial v}{\partial s} + \frac{\partial u}{\partial z}\frac{\partial v}{\partial z} + 2\frac{\aleph^2}{R_{ci}}(u\frac{\partial u}{\partial s} - v\frac{\partial v}{\partial s}) + 2\frac{\aleph^2}{R_{ci}^2}uv]}
\end{aligned}$$

For curved homogeneous shear flow the following assumptions are made

a) The mean velocity is given by $(\overline{U}, \overline{V}, \overline{W}) = (\overline{U}_c + An, 0, 0)$, where $A = \frac{\partial U}{\partial n}$.

b) The flow is stationary so that $\frac{\partial}{\partial t}\overline{(\ )} = 0$.

c) The flow statistics are symmetric about the (s,n) plane, so that $\frac{\partial(\ )}{\partial z} = 0$ and $\overline{uw} = \overline{vw} = 0$.

Consequently, equations 4.50 and 4.51 may be simplified into

$$\aleph\overline{U}\frac{\partial}{\partial s}\frac{q^2}{2} = -\overline{uv}\frac{\partial \overline{U}}{\partial n} + \frac{\aleph}{R_{ci}}\overline{uv}\overline{U}$$

$$-[\aleph\frac{\partial}{\partial s}(\frac{\overline{pu}}{\rho}+\frac{\overline{uq^2}}{2})+\aleph\frac{\partial}{\partial n}(\frac{\overline{pv}}{\rho\aleph}+\frac{\overline{vq^2}}{2\aleph})+ \tag{4.52}$$
$$\nu\nabla^2\frac{\overline{q^2}}{2}-\nu[\overline{(\frac{\partial u}{\partial n})^2+\aleph^2(\frac{\partial u}{\partial s})^2+(\frac{\partial u}{\partial z})^2+(\frac{\partial v}{\partial n})^2+\aleph^2(\frac{\partial v}{\partial s})^2+(\frac{\partial v}{\partial z})^2}+$$
$$\overline{(\frac{\partial w}{\partial n})^2+\aleph^2(\frac{\partial w}{\partial s})^2+(\frac{\partial w}{\partial z})^2+\frac{\aleph^2}{R_{ci}}(v\frac{\partial u}{\partial s}-u\frac{\partial v}{\partial s})+\frac{\aleph^2}{R_{ci}^2}(u^2+v^2)}]$$

$$\aleph\overline{U}\frac{\partial}{\partial s}\overline{uv} = -\overline{v^2}\frac{\partial\overline{U}}{\partial n}+\frac{\aleph}{R_{ci}}\overline{U}(2\overline{u^2}-\overline{v^2})+\aleph\overline{\frac{p}{\rho}(\frac{\partial v}{\partial s}+\aleph\frac{\partial}{\partial n}\frac{u}{\aleph})}$$
$$-[\aleph\frac{\partial}{\partial s}(\frac{\overline{pv}}{\rho}+\overline{u^2v})+\aleph\frac{\partial}{\partial n}(\frac{\overline{pu}}{\rho\aleph}+\frac{\overline{uv^2}}{\aleph})+\frac{\aleph}{R_{ci}}(\overline{uv^2}-\overline{u^3})]+ \tag{4.53}$$
$$\nu\nabla^2\overline{uv}-2\nu[\overline{\frac{\partial u}{\partial n}\frac{\partial v}{\partial n}+\aleph^2\frac{\partial u}{\partial s}\frac{\partial v}{\partial s}+\frac{\partial u}{\partial z}\frac{\partial v}{\partial z}+2\frac{\aleph^2}{R_{ci}}(u\frac{\partial u}{\partial s}-v\frac{\partial v}{\partial s})+2\frac{\aleph^2}{R_{ci}^2}uv}]$$

The triple correlation terms, which represent turbulent diffusion, were neglected in straight nearly homogeneous flows by Harris, Graham and Corrsin (1977) and Tavoularis and Corrsin (1981) and in curved nearly homogeneous flows by HT1. These terms will also be dropped from the Reynolds stresses equations in the present case. Neglecting these terms makes the equations simpler but it will be kept in mind that the ratio of these terms to the convection terms is of the same order of magnitude as the turbulence intensity (for example $\frac{\frac{\aleph}{R_{c_1}}\overline{uv^2}}{\frac{\aleph}{R_{c_1}}\overline{U}\overline{v^2}} = O\left(\frac{u'}{\overline{U}}\right)$). The turbulence intensities vary from .08 to .16 along the section (as will be seen later in Figures 6.7, 6.8, 6.10 and 6.11). The molecular diffusion terms such as $\nu\nabla^2\frac{\overline{q^2}}{2}$ and $\nu\nabla^2\overline{uv}$ are much smaller than the turbulent diffusion terms, and are neglected for straight and curved shear flows. The sudden change of wall curvature from one subsection to the other should not affect this assumption. In fact, at the points of change of curvature the term $\frac{\partial\aleph}{\partial n}$ in equation 4.36, which is discontinuous, would be at worst equal to the maximum of the right and left hand side derivatives corresponding to the two subsections and therefore it would still be negligible. Along the centerline $\frac{\partial\aleph}{\partial n}=0$. It can be observed that $\aleph \simeq 1$, since $\frac{n}{R} < 3.5\%$ for the present section, and that the terms involving division by R_{ci} or R_{ci}^2 in the dissipation, such as $\overline{\frac{\aleph^2}{R_{ci}}(v\frac{\partial u}{\partial s} - u\frac{\partial v}{\partial s})}$, are negligible compared to other terms like $\overline{\aleph^2\left(\frac{\partial u}{\partial s}\right)^2}$. Finally, the parameter $S = \frac{\frac{\overline{U}_c}{R_{ci}}}{\frac{\partial \overline{U}}{\partial n}}$, frequently used to characterize curved shear flows is introduced. S represents the ratio of the extra rate of strain due to curvature to the mean shear of the flow. Only the rates of strain, $\frac{\overline{U}_c}{R_{ci}}$ and $\frac{\partial \overline{U}}{\partial n}$, appear in the expression of S. The other components of strainV, which can be obtained from equation 4.34, vanish for the assumed velocity profile of the present flow. Following the above assumptions, equations 4.52 and 4.53 reduce to

$$\begin{aligned}
\overline{U}\frac{\partial}{\partial s}\frac{\overline{q^2}}{2} &= -\overline{uv}\frac{\partial \overline{U}}{\partial n}(1-S) \\
&\quad -\nu\overline{[(\frac{\partial u}{\partial n})^2 + (\frac{\partial u}{\partial s})^2 + (\frac{\partial u}{\partial z})^2 + (\frac{\partial v}{\partial n})^2 + (\frac{\partial v}{\partial s})^2 + (\frac{\partial v}{\partial z})^2 +} \\
&\quad \overline{(\frac{\partial w}{\partial n})^2 + (\frac{\partial w}{\partial s})^2 + (\frac{\partial w}{\partial z})^2]}
\end{aligned} \tag{4.54}$$

$$\begin{aligned}
\overline{U}\frac{\partial}{\partial s}\overline{uv} &= -\overline{v^2}\frac{\partial \overline{U}}{\partial n}(1+S) + 2(\overline{u^2} - \overline{uv})\frac{\partial \overline{U}}{\partial n}S + \overline{\frac{p}{\rho}(\frac{\partial v}{\partial s} + \frac{\partial u}{\partial n})} \\
&\quad -2\nu\overline{[\frac{\partial u}{\partial n}\frac{\partial v}{\partial n} + \frac{\partial u}{\partial s}\frac{\partial v}{\partial s} + \frac{\partial u}{\partial z}\frac{\partial v}{\partial z}]}
\end{aligned} \tag{4.55}$$

By letting $R_{ci} \to \infty$ and thus $S = 0$, the equation of turbulent kinetic energy for straight uniform homogeneous shear flows (Tavoularis, 1985) and the equation of the Reynolds shear stress $\overline{uv}$ (Harris, Graham and Corrsin, 1977) are recovered.

Similar manipulations lead to the other Reynolds stress equations

$$\overline{U}\frac{\partial}{\partial s}\frac{\overline{u^2}}{2} = -\overline{uv}\frac{\partial \overline{U}}{\partial n}(1+S) + \overline{\frac{p}{\rho}\frac{\partial u}{\partial s}} - \nu\overline{[(\frac{\partial u}{\partial s})^2 + (\frac{\partial u}{\partial n})^2 + (\frac{\partial u}{\partial z})^2]} \tag{4.56}$$

$$\overline{U}\frac{\partial}{\partial s}\frac{\overline{v^2}}{2} = 2\overline{uv}\frac{\partial \overline{U}}{\partial n}S + \overline{\frac{p}{\rho}\frac{\partial v}{\partial n}} - \nu\overline{[(\frac{\partial v}{\partial s})^2 + (\frac{\partial v}{\partial n})^2 + (\frac{\partial v}{\partial z})^2]} \tag{4.57}$$

$$\overline{U}\frac{\partial}{\partial s}\frac{\overline{w^2}}{2} = \overline{\frac{p}{\rho}\frac{\partial w}{\partial z}} - \nu\overline{[(\frac{\partial w}{\partial s})^2 + (\frac{\partial w}{\partial n})^2 + (\frac{\partial w}{\partial z})^2]} \tag{4.58}$$

Equations 4.54 to 4.58 are identical to those derived by HT1 for uniform curvature, and consistent with those derived by Gatski and Savill (1989). The radius of curvature in the present case is allowed to vary in the streamwise direction. The difficulty induced from discontinuity of R_{ci} was overcome by neglecting the Laplacian term which contains $\frac{\partial}{\partial s}(\frac{1}{1+\frac{n}{R_{ci}}})$. Along the centerline the latter term is equal to zero, since $\aleph = 1$.

By identifying the production, P, dissipation, ϵ, ϵ_{uu}, etc., and pressure strain covariances terms, ϕ_{uu}, etc., the kinetic energy and Reynolds stress equations can be rewritten in a more compact form as

$$\overline{U}\frac{\partial}{\partial s}\frac{q^2}{2} = P - \epsilon \tag{4.59}$$

$$\overline{U}\frac{\partial}{\partial s}\overline{uv} = -\overline{v^2}\frac{\partial \overline{U}}{\partial n}(1+S) + 2\overline{u^2}\frac{\partial \overline{U}}{\partial n}S + \phi_{uv} + \epsilon_{uv} \tag{4.60}$$

$$\overline{U}\frac{\partial}{\partial s}\frac{\overline{u^2}}{2} = -\overline{uv}\frac{\partial \overline{U}}{\partial n}(1+S) + \phi_{uu} + \epsilon_{uu} \tag{4.61}$$

$$\overline{U}\frac{\partial}{\partial s}\frac{\overline{v^2}}{2} = 2\overline{uv}\frac{\partial \overline{U}}{\partial n}S + \phi_{vv} + \epsilon_{vv} \tag{4.62}$$

$$\overline{U}\frac{\partial}{\partial s}\frac{\overline{w^2}}{2} = \phi_{ww} + \epsilon_{ww} \tag{4.63}$$

Chapter 5

Experimental Apparatus and Instrumentation

5.1 The Wind Tunnel

The wind tunnel shown in Figure 5.1 (without the test section), built at the University of Ottawa and described in detail by Karnik and Tavoularis (1987), was used in the experiments of the present work. The original centrifugal fan was replaced by a mixed flow fan (Woods, model 63MX, 630mm diameter, powered by a 5 hp motor). A shear generator, comprising 12 separate channels 25.4mm high, separated by aluminium plates 150mm wide, was used. Sets of screens of different resistances were attached across the channels to create a uniformly sheared flow. A flow separator, 610mm long, consisting of 12 channels aligned with the shear generator channels, was inserted to improve the transverse homogeneity of the large scales. A nearly homogeneous shear flow was produced in this tunnel with $k_s = \frac{1}{U_c}\frac{\partial \overline{U}}{\partial n} \simeq 6.2m^{-1}$, for centerline speeds ranging from 5 to $15m/s$ (Karnik and Tavoularis, 1987). A curved section, shown in Figure 5.2, was built to study the adjustment of the turbulence structure of a homogeneous shear flow to curvature and its behavior following curvature reversal.

This section comprises a straight entrance section 203mm long, followed by a first curved section having a centerline arc length of 1017mm, followed by a second curved section of equal length but reversed curvature, after which a straight section 1245mm long follows. The centerline radius of curvature of both curved sections is 3500mm. For this radius the curvature parameter, $S = \frac{\frac{\overline{U}_c}{R_c}}{\frac{\partial U}{\partial n}}$, was equal to approximately ± 0.05 for a centerline velocity of 10m/s. The cross section of the entrance of the curved section was made smaller than that of the straight tunnel to permit removal of the boundary layers developed in the upstream straight section, and the side walls were also sharpened at the entrance to reduce the chance of separation. The width of the upstream test section is 480 mm. The distance between the side walls of the curved section was gradually increased from 413 mm at its begining to 430 mm at its end to compensate partly for boundary layer growth.

To align the curved section with the straight section, their centerlines were engraved on the side walls and adjusted to be tangent. The marked centerlines and radial lines, also engraved on the two side walls of the section, permitted the positioning of the probes by aligning their directions with the marked lines. The axis of the traversing mechanism screw (Figure 5.3) was offset so as to permit radial traversing of the tip of the probe.

5.2 Instrumentation and Accuracies

5.2.1 Hot wire response equation

In the present investigation hot wire anemometry is used as the main measurement technique. This technique has good spatial and temporal resolutions and is suitable for turbulent air flow measurements. The theory behind hot wire anemometry is based on the relationship between heat transfer from a cylindrical wire immersed in a flowing fluid and the velocity of the fluid.

The measurements were performed with a commercial cross wire probe (TSI model 1248 BJ-T1.5). It has two cylindrical sensors with diameters of $5\mu m$ and lengths of $1.2mm$. The wires are inclined 45° with respect to the probe axis and are separated by a distance of $0.5mm$. The wires were operated at constant temperature by two constant temperature bridges (TSI model 1050 A used in connection with a TSI 1051-2D monitor and power supply). The voltage E of the sensing wire operating at a constant temperature T_w in a flow stream with velocity **Q** and temperature T_f is given by the modified King's law as

$$\frac{E^2}{T_w - T_f} = A + BU_c^n \tag{5.1}$$

where A, B and n are calibration constants, depending on the wire and fluid properties, and U_c is the effective cooling velocity, defined as the velocity perpendicular to the wire that produces the same cooling as the velocity **Q** at an arbitrary orientation. The resistance and temperature of the wire can be correlated by a linear relationship over a narrow operating range,

$$R_w = R_f(1 + \bar{\alpha}(T_w - T_f)) \tag{5.2}$$

where R_f is the wire resistance at T_f and $\bar{\alpha}$ is the temperature coefficient of resistance, determined by measuring the resistance of the wire at different temperatures (Figure 5.4).

Figure 5.5-a shows two cylindrical wires mounted with their axes at angles θ_1 and θ_2 with respect to the probe body axis. In Figure 5.5-b, the probe of the body is at a yaw angle ψ and a roll angle β with respect to the velocity vector direction. A popular model provides the effective cooling velocity as

$$U_e^2 = Q_n^2 + k^2 Q_t^2 + h^2 Q_b^2 \tag{5.3}$$

where Q_n is the normal, Q_t is the tangential and Q_b is the binormal component of Q defined with respect to the wire axis. k^2 and h^2 are calibration constants depending on the probe geometry. By considering a reference frame attached to the probe body one may derive the expression

$$\begin{aligned} \frac{U_e}{Q} \;=\; & [(cos\psi cos\theta - cos\beta sin\psi sin\theta)^2 \\ & + k^2(cos\psi sin\theta + cos\beta sin\psi cos\theta)^2 \\ & + h^2(sin\beta \sin\psi)^2]^{\frac{1}{2}} \end{aligned} \tag{5.4}$$

Only the effect of change of the yaw will be investigated since its alignment is the most critical, especially in the curved section.

Changes in yaw angles can be introduced by geometric misalignment of the probe with the mean speed direction and by the presence of velocity fluctuations. Errors in positioning alignment were estimated to be around $\pm 3°$. The cross wire probe was calibrated in the wind tunnel with the shear generator removed, so that the turbulence intensity, $\frac{\sqrt{\overline{u^2}}}{U}$, was less than 0.5%. Referring to Figure 5.6, the maximum induced yaw, ψ_i, during calibration is estimated as

$$\psi_i = tg^{-1}\frac{v}{\sqrt{(U+u)^2+v^2}} = 0.3^\circ \tag{5.5}$$

A calibration jet with a swivelling mechanism, permitting positioning the probe at any desired yaw for a fixed roll, was used. The roll was set to zero, and readings from the two channels of the anemometer were taken for different yaws. By fitting curves corresponding to different values of k^2 to the anemometer's readings, the optimum value of k^2 was determined. The results are shown in Figure 5.7. From this Figure it is clear that for the present experiments, where yaw errors were less than 4°, one may use the approximation $k^2 = 0.0$. Then Equation 5.4 reduces to

$$\frac{U_e}{Q} = cos(\psi + \theta) \tag{5.6}$$

and, for a zero yaw,

$$\frac{U_e}{Q} = cos\theta \tag{5.7}$$

which is known as the Cosine law of Cooling.

5.2.2 The simultaneous measurement of two velocity components

The velocity output from the two anemometers is given by

$$\frac{E_1^2}{T_{w1} - T_f} = A_1 + B_1 U_{e1}^{n1} \tag{5.8}$$

$$\frac{E_2^2}{T_{w2} - T_f} = A_2 + B_2 U_{e2}^{n2} \tag{5.9}$$

As mentioned earlier, it can be assumed that the velocity component perpendicular to the wire provides all the cooling. Then, with reference to Figure 5.8, one gets

$$U_{e1} = \sqrt{(U sin\theta_1 + V cos\theta_1)^2 + W^2} \tag{5.10}$$

$$U_{e2} = \sqrt{(U sin\theta_2 - V cos\theta_2)^2 + W^2} \tag{5.11}$$

Since $W^2 << U^2$ for the present flow, one can further simplify the cross wire response, using $\theta_1 = \theta_2 = 45°$, as

$$U = \frac{1}{\sqrt{2}}(U_{e1} + U_{e2}) \tag{5.12}$$

$$V = \frac{1}{\sqrt{2}}(U_{e1} - U_{e2}) \tag{5.13}$$

Equations 5.12 and 5.13 give the instantaneous values of U and V in terms of the corresponding effective cooling velocities. When the probe is rotated by 90°, the U and W components are obtained. The average and fluctuating components can be obtained by using the Reynolds decomposition in equations 5.12 and 5.13.

5.3 Signal Processing and Data Acquisition

The signal output from the bridge of the hot wire anemometer was monitored on an oscilloscope. To digitize the signals, an analog to digital converter (Data Translation DT 2828) was used in connection with a microcomputer system (1800, IBM AT compatible). The DT 2828 contains four channels and operates on a simultaneous sample and hold mode, so that it can sample the four signals from the four channels simultaneously. It has a resolution of 12 bits, so the incoming analog signal is converted into a binary number which can assume 2^{12} or 4096 states. For the input range of $\pm$ 10V used, its analog resolution was about 5mV.

Sampling frequencies ranged from 0.5kHz to 40kHz for one channel used in continuous operation. If more channels are used, the sampling frequency is reduced in proportion. The ADC has a throughput frequency of 100kHz for one channel, but this precludes continuous operation.

Signals from the anemometer were conditioned in electronic circuits to make full use of the range of the ADC by offsetting and/or amplification. The electronic circuits also permit low pass filtering of the signals at frequencies equal to 1, 3 or 10kHz. The microcomputer has a 1Mb random access memory (RAM), an 80Mb hard disk drive and a 11MHz clock. Online computer programs processing the data were used to monitor the reliability of the measurements. Digitized samples of data were stored in a hard disk drive and later transferred to 60 Mb magnetic cassette tapes for later processing.

5.4 Resolution

Momentum and energy transfer in turbulent flows can be considered as due to the motion of eddies of different sizes, which coexist in the flow and range in size from the larger, energy containing eddies to the smaller, dissipative eddies. These eddies are characterized by their time and length scales. In an experimental investigation of turbulent flows the spatial and temporal resolutions of the probe should be investigated by comparing the characteristic length and time constants of the measuring system to the different time and length scales of the eddies which ought to be investigated.

5.4.1 Temporal resolution

In the following the different time constants of the probe (Corrsin, 1963) are estimated for a mean velocity of $10m/s$.
The convective constant of the wire is given by

$$\tau_1 = \frac{d}{\overline{U}} \approx 0.5\mu s \tag{5.14}$$

The time constant for a viscous shear disturbance to diffuse past the wire by using the kinematic viscosity of air at an ambient temperature of $20°C$ is

$$\tau_2 = \frac{d^2}{\nu} \approx 1.7\mu s \tag{5.15}$$

For heat transfer from the wire, the time constant is given by

$$\tau_3 = \frac{d^2}{\alpha} \approx 1.1\mu s \tag{5.16}$$

by using the thermal diffusivity of air α at $20°C$. The radial conduction is characterized by

$$\tau_4 = \frac{d^2}{\alpha_w} \approx 1.2\mu s \tag{5.17}$$

where α_w is the thermal diffusivity of tungsten. Since hot wire anemometry is based on the physics of fluid flow past the wire and heat transfer from it, the above calculations show that the wire has a good frequency response up to 0.5MHz.

The constant temperature bridge has a frequency response up to 100kHz. When using two channels simultaneously for measurements, the data acquisition system can be operated at frequencies up to 25kHz.

In the following, the time scales of eddies characterizing the present flow will be estimated using results from some preliminary measurements and from previous investigations.

The integral time scale in the streamwise direction had a typical value of

$$T_{uu} = \int_0^\infty R_{uu}(\tau)d\tau \approx 4000\mu s \tag{5.18}$$

The Taylor microscale in the streamwise direction had a typical value of

$$\tau_{uu} = \left(\frac{\overline{u^2}}{\overline{(\frac{\partial u}{\partial t})^2}} \right)^{0.5} \approx 600\mu s \tag{5.19}$$

The time required by eddies of the size of Kolmogoroff scales to pass through the sensing wire is estimated as

$$\tau = \frac{1}{\overline{U}}(\frac{\nu^3}{\epsilon})^{\frac{1}{4}} \approx 14\mu s \tag{5.20}$$

The above calculated time should not be confused with the Kolmogoroff time scale

$$\tau_k = (\frac{\nu}{\epsilon})^{\frac{1}{2}} \tag{5.21}$$

By using the Nyquist criterion, the minimum frequencies required to resolve the events described by the Taylor microscales and the Kolmogoroff microscales are given respectively as

$$f_{\tau_{uu}} = \frac{2.5}{\tau_{uu}} \approx 5kHz \tag{5.22}$$

$$f_\tau = \frac{2.5}{\tau} \approx 180kHz \tag{5.23}$$

From the above analysis it turns out that the frequency response of the wire and the bridge are a ` quate to resolve the passage of the energy containing eddies but only partly the passage of the dissipative eddies.

Figure 5.9 shows the streamwise frequency spectra measured in the tunnel with and without the shear generator inserted. The signal intensity in the wind tunnel with no shear was very low, and contained the effects of residual fan turbulence and electronic noise. At high frequencies the signal to noise ratio becomes very low. These parts of the spectrum can be removed by using low pass filtering at a cutoff frequency which should be high enough for the events characterized by Taylor's microscale not to be filtered. The required digitizing frequency for resolving the Taylor microscales was found to be around 5kHz. From the above considerations, a cutoff frequency of 10kHz seems adequate. The sampling frequency should also be high enough to avoid aliasing, i.e. erroneous transfer of energy from the high to low frequency range, and by the Nyquist criterion a sampling frequency of 25kHz was chosen.

In order to properly average events of duration comparable to the time scale of the energy containing eddies, the sampling interval should be long enough to contain many such events. A record of 2048 points taken at a sampling frequency of 2kHz is around 250 integral time scales long. 50 such records were taken 1 second apart to ensure convergence and independence. The statistics of each record were computed by time averaging and then ensemble averaging over 50 records was performed.

In summary, after the signal from the anemometer was low pass filtered at 10kHz, a record of 2048 points is taken at a sampling frequency of 25kHz, another record of

2048 points was taken at a frequency of 2kHz. for one second no data was taken and the procedure was repeated 50 times.

5.4.2 Spatial resolution

The Taylor's "Frozen Turbulence Hypothesis" is commonly used to determine the length scales from the time scales. This hypothesis gives the benefit of avoiding complicated instrumentation to measure spatial correlations. It is valid for turbulence intensities lower than 10% (Tavoularis, 1986) and, in the present case, resulted in

$$L_{uu} = \overline{U}T_{uu} \approx 40mm \tag{5.24}$$

$$\lambda_{uu} = \overline{U}\tau_{uu} \approx 6mm \tag{5.25}$$

The Kolmogoroff microscale can be estimated as

$$\eta = (\frac{\nu^3}{\epsilon})^{\frac{1}{4}} \approx 0.14mm \tag{5.26}$$

To have a good spatial resolution, the wire length should be small compared to the characteristic length of interest in the turbulent flow (Corrsin, 1963). For the probe used presently, having a wire length of $l = 1.5mm$, we have

$$\frac{l}{L_{uu}} \approx 0.0375 \quad , \frac{l}{\lambda_{uu}} \approx 0.25 \quad , \frac{l}{\eta_k} \approx 8.5 \tag{5.27}$$

From the above estimates it is clear that the wires are adequate for measuring the large scales of turbulence, marginally so for measuring the Taylor's microscales, and inadequate for the Kolmogoroff scales.

As an example, an estimate can be made of the error in measuring the Reynolds stresses in the streamwise direction, $\overline{u^2}$. By assuming negligible unsteady conduction along the wire, so that infinitesimal elements of the wire act as independent hot wires and contribute linearly to the overall wire response, the ratio of the apparent to the true velocity variance can be estimated as (Corrsin, 1963),

$$\frac{\overline{u_{app}^2}}{\overline{u^2}} = \frac{2\int_0^l (l-\tau)\rho(\tau)d\tau}{l^2} \tag{5.28}$$

where $\rho(\tau)$ is a correlation coefficient, approximated as

$$\rho(\tau) \approx 1 - \frac{\tau^2}{2\lambda_{uu}^2} \tag{5.29}$$

Substituting into equation 5.28, one gets

$$\frac{\overline{u_{app}^2}}{\overline{u^2}} = 1 - \frac{l^2}{24\lambda_{uu}^2} \approx 0.998 \tag{5.30}$$

5.5 Computational Procedures

To evaluate the various turbulence parameters defined in the previous chapter (section 4.1), discrete time histories, U_n^m, V_n^m and W_n^m, for the three velocity components were obtained, where m=1,2,...,M is the record number and n=1,2,...,N is the point number in one record. The discrete time histories of the fluctuating velocity components, u_n^m, v_n^m and w_n^m, were then obtained. For example

$$u_n^m = U_n^m - \frac{\sum_{n=1}^N U_n^m}{N} \tag{5.31}$$

The one point moments were calculated as

$$\overline{u^k} = \frac{\sum_{m=1}^M \sum_{n=1}^N (u_n^m)^k}{N \times M} \tag{5.32}$$

and the Reynolds shear stress was evaluated as

$$\overline{uv} = \frac{\sum_{m=1}^M \sum_{n=1}^N u_n^m v_n^m}{N \times M} \tag{5.33}$$

The autocorrelation coefficient $R_{uu}(\tau)$, where the time delay is $\tau = i \times \Delta t$ (Δt is the discretization time interval for the anemometer signal), was computed as

$$R_{uu}(\tau) = \frac{1}{M}\sum_{m=1}^{M}\left(\frac{\sum_{n=1}^{N-i} u_n^m u_{n+i}^m}{\sum_{n=1}^{N} u_n^m u_n^m}\left(\frac{N}{N-i}\right)\right) \tag{5.34}$$

Integral time scales were computed by integrating the corresponding autocorrelation coefficient to its first zero crossing.

The streamwise velocity derivatives were obtained as

$$\overline{\left(\frac{\partial u}{\partial t}\right)^2} = \frac{1}{(N-1)\times M}\sum_{m=1}^{M}\sum_{n=1}^{N-1}\frac{u_{n+1}^j - u_n^j}{\Delta t} \tag{5.35}$$

The Taylor time scale τ_{uu} was then evaluated from 4.13 (in the previous chapter). Length scales in the streamwise direction were estimated using Taylor's hypothesis so that

$$L_{uu} = \overline{U}T_{uu}, \quad L_{vv} = \overline{U}T_{vv}, \quad L_{ww} = \overline{U}T_{ww} \tag{5.36}$$

and

$$\lambda_{uu} = \overline{U}\tau_{uu} \tag{5.37}$$

To compute the spectra, a discrete Fourier transform of each record was computed. For example, for the streamwise velocity component,

$$\mathcal{U}_k^m = \sum_{n=1}^{N} u_n^m e^{-\frac{2\pi i k}{N}} \qquad k = 1, 2, \ldots \frac{N}{2} \tag{5.38}$$

which provides $\frac{N}{2}$ discrete values of the spectrum at frequencies

$$f_k = \frac{(k-1)}{N\Delta t} \tag{5.39}$$

The raw power spectral estimate was then computed as

$$F_{uu}(f_k) = \frac{1}{M\times N}\sum_{m=1}^{M}\mathcal{U}_k^m\mathcal{U}_k^{m*} \qquad k = 1, 2, \ldots, \frac{N}{2} \tag{5.40}$$

Smoothing was accomplished by averaging adjacent values of $F_{uu}(f_k)$. Spectra at frequencies ranging from 1.95 to 998 Hz were obtained from the 2 kHz records and spectra at frequencies ranging from 24.4 to 12476 Hz were obtained from the 25 kHz records. The values obtained overlapped at an intermediate range. The values at the higher frequencies from 2 kHz samples and at the lower ones from the 25 kHz samples were rejected. Spectra at frequencies above 3 kHz were also rejected, as subject to substantial noise and other errors.

It was previously mentioned that all signals were low-pass filtered at 10 kHz. While this caused no problems in calculating the stresses and length scales, using the 2 kHz samples for calculating the spectra would be subject to aliasing errors, as energy from the high frequencies would be fed into the lower frequencies. However, for this flow most of the energy was contained in the larger scales. To check the reliability of the calculated spectra, they were integrated to calculate the corresponding stresses, as for example,

$$\overline{u^2} = \int_{-\infty}^{+\infty} F_{uu}(f)df \tag{5.41}$$

A maximum difference of 5% was found between the values of the stresses obtained and those previously obtained.

Chapter 6

Measurements

The centerline velocity at the entrance to the section was set to about $10m/s$. In order to achieve the maximum possible value of mean shear rate, $A = \frac{\partial \overline{U}}{\partial n}$, screens were not inserted downstream of the shear generator. Two sets of flow configurations were obtained by inverting the shear generator. They will be referred to as NE and PE, depending on whether S was negative or positive at the entrance to the first curved section. These flow configurations are shown in Figure 6.1.

6.1 General Features of the Flow

The present study focuses mainly on the centerline measurements, away from the walls. In the following, only a brief qualitative evaluation of some important effects acting on the boundary layers developing on the duct walls will be made.

The boundary layers on the top and bottom walls are subjected to the stabilizing or destabilizing effects of curvature and to the mean shear of the free stream. In general, the growth of the boundary layer on the convex wall will be suppressed by the curvature of the wall, while the growth of the boundary layer on the concave wall will be enhanced. Irrespective of curvature effects, the boundary layer on the wall adjacent to the higher speed side of the "core" flow will tend to be thinner than that of the other side, due to Reynolds number effects. All things considered, wall curvature and mean shear direction effects on boundary layer thickness will tend to reinforce each other when $S < 0$ but oppose each other when $S > 0$.

The boundary layers on the side walls are subjected to many complicating effects, among which a spanwise variation of the free stream velocity due to shear of the flow, a spanwise pressure gradient due to curvature and a streamwise pressure gradient manifested in the streamwise variation of the centerline mean velocity in Figure 6.2. These effect act simultaneously on the boundary layers and might have enhancing or opposing effects on its growth depending on the sign of S. For example the difference in the free stream velocities due to the mean shear causes the boundary layer to decrease towards the region of higher velocities, while the spanwise pressure gradient is accompanied by a spanwise flow in the negative direction of the pressure gradient, causing a smaller boundary layer thickness in the region of higher pressure gradient.

The mean velocity was measured along the centerline of the section. Figure 6.2 shows the mean streamwise velocity component, $\overline{U}_c$, along the centerline for both cases NE and PE. $\overline{V}_c$ and $\overline{W}_c$ were less than 4% of $\overline{U}_c$ at most measuring points along the centerline. The variation of $\overline{U}_c$ along the centerline did not exceed 10%. A weak effect of the curvature on $\overline{U}_c$ is apparent in this figure.

Transverse velocity profiles were taken at different stations. Some of these profiles are shown in Figures 6.3 and 6.4 for cases NE and PE respectively. The variation of the slope of the profiles is believed to be due mainly to the presence of a transverse pressure gradient in the n direction as a result of the turning of the flow. Boundary layers and other wall effects might also have some effect on the slope of the profiles. The variation of the magnitude of the mean shear rate, $|A| = |\frac{\partial \overline{U}}{\partial n}|$, along the section centerline is shown in Figure 6.5. To evaluate A from transverse profiles, a straight line was fitted through the measured points. In the present investigation attention was focussed on the development of turbulence statistics along the centerline, so A was determined mainly from points closer to the center. The variation of the parameter $S = \frac{\overline{U}_c}{AR_c}$ along the centerline is shown in Figure 6.6. The variation of the parameter S within each curved subsection is very small compared to its jump due to reversal of sign from one curved subsection to the other. An average value of S will be considered for each subsection, shown in Figure 6.6 by a dashed line.

Transverse profiles of $\frac{u'}{U_c}$, $\frac{v'}{U_c}$ and $\rho_{uv} = \frac{|\overline{uv}|}{u'v'}$ are shown in Figures 6.7 to 6.9 for case NE, and in 6.10 to 6.12 for case PE, where U_c is the local centerline velocity. The transverse inhomogeneity was relatively mild and comparable to that in previous studies in straight sections (TK) and in curved sections (HT1).

Some typical spanwise measurements of $\frac{\overline{U}}{U_c}$, $\frac{u'}{U_c}$, $\frac{v'}{U_c}$ and $\rho_{uv} = \frac{|\overline{uv}|}{u'v'}$, where $\overline{U}_c$ is the local streamwise centerline velocity, are shown in Figures 6.13 to 6.16, and demonstrate a fairly good spanwise uniformity of the mean and turbulence fields. Even if streamwise vortices were formed due to curvature, their effects appear to be small and could be neglected compared to the primary turbulence.

It can be concluded that the uniformity of the shear, the homogeneity of turbulence intensities and the two-dimensionality of the mean flow generated in the present facility are acceptable for the present purposes.

6.2 Reynolds Stresses Development

The development of $\overline{u^2}$, $\overline{v^2}$, $\overline{w^2}$ and $|\,\overline{uv}\,|$ is shown in Figures 6.17 and 6.18 for cases NE and PE respectively. Similarly to what has been found by HT1, the growth of turbulent stresses was enhanced for $S < 0$ and suppressed for $S > 0$.

The comparative development of $\overline{u^2}$, $\overline{v^2}$, $\overline{w^2}$ is shown Figure 6.19 and that of q^2 and $|\,\overline{uv}\,|$ is shown in Figure 6.20 for both the NE and PE cases. The effect of change of sign of S is clearly shown in these figures. The values of $\overline{u^2}$, $\overline{v^2}$, $\overline{w^2}$ and q^2 for both cases essentially match at the end of the second curved subsection but these quantities grow differently in the final straight subsection. The values of $|\,\overline{uv}\,|$ for the two cases coincided at some position within the second curved subsection, after which the values in the PE case became larger than those in the NE case.

6.3 Integral Length Scales Development

The integral length scales were measured by integrating to the first zero crossing of the corresponding temporal autocorrelation coefficient, and by using the Taylor hypothesis. They are shown in Figures 6.21 and 6.22 for cases NE and PE respectively. Compatible with the findings of HT1, the growth of the integral length scales was enhanced for $S < 0$ and suppressed for $S > 0$.

An important observation from these measurements concerns the relative magnitude of these scales. In the initial straight subsection, L_{ww} was larger than L_{vv}. For the NE case, L_{vv} increased to larger values than L_{ww} within the first curved subsection ($S < 0$) but, when the curvature was reversed ($S > 0$), L_{vv} decreased dramatically to lower values than L_{ww}. For the PE case, L_{vv} actually decreased, in the first curved portion ($S > 0$), while L_{uu} and L_{ww} had only their rate of increase suppressed or they remained constant. When the curvature was reversed ($S < 0$), L_{vv} increased to larger values than L_{ww}.

The developments of the length scales for the cases NE and PE are compared in Figure 6.23. The values of the length scales for both cases coincided at some position before the end of the second curved subsection and they continued to grow at different rates. Curiously, the values of L_{vv} and L_{ww} approached each other again in the final straight subsection, while the values of L_{uu} remained distinct at the end of the test section.

6.4 Fine Structure Measurements

The Taylor microscales, determined from the Taylor timescales using Taylor's hypothesis, are shown in Figure 6.24. The streamwise microscales were only slightly affected by the introduction of curvature and its reversal.

6.5 Spectral Measurements

As an attempt to assess how continuous curvature and curvature reversal affected turbulent eddies of different sizes, the one dimensional spectra F_{uu}, F_{vv}, F_{ww} and F_{uv} at the selected positions specified in Figure 6.25 were measured and are shown in Figures 6.26 to 6.33.

The enhancement or suppression of the growth of the turbulent stresses in regions with negative or positive S is clear from the development of the spectra. These figures also show that, while all the scales are affected by curvature, the larger scales are clearly the most affected, in conformity with the length scale measurements, which showed a stronger effect felt by the integral length scales than by the Taylor microscales.

Chapter 7

Analysis and Discussion of Measurements

7.1 Total Strain of Turbulence Structure

In an unbounded, rectilinear, homogeneous shear flow, the only externally imposed scale is a characteristic time, equal to

$$\left| \frac{\partial \overline{U}}{\partial n} \right|^{-1} \tag{7.1}$$

(Harris, Graham and Corrsin, 1977). Then a dimensionless time for the development of turbulence, considered to be convected in a frame moving with the centerline mean speed, can be defined as

$$\tau = \frac{s}{\overline{U}_c} \left| \frac{\partial \overline{U}}{\partial n} \right| \tag{7.2}$$

τ can also be considered as representing a dimensionless distance from the flow origin and also as a total strain to which turbulence is subjected.

In a curved homogeneous shear flow with constant curvature the total strain is equal to

$$\tau = \frac{s}{\overline{U}_c} \mid \frac{\partial \overline{U}}{\partial n} \mid (1 - S) \tag{7.3}$$

(HT1). For $\mid S \mid \ll 1$, as it is in the present investigation, it seems reasonable to approximate τ by the rectilinear homogeneous shear flow expression (equation 7.2) in studying the development of turbulence quantities in the streamwise direction. A convenient velocity scale to be used for this type of flow (HT1) is the rms speed of the velocity fluctuations, $v = q'$. A length scale is then defined as $L = \frac{q'}{\mid \frac{\partial U}{\partial n} \mid}$. As mentioned in the previous Chapter, the mean shear in the present section varied somewhat, as a result of flow adjustment to curvature, among other effects. Because the variation of the parameter S within each subsection was relatively small, compared to its abrupt change from one subsection to another, a constant value of S was assumed for each subsection, which implied the assumption of a constant shear parameter, defined by

$$k_s = \frac{1}{\overline{U}_c} \mid \frac{d\overline{U}}{dn} \mid \tag{7.4}$$

within each subsection. As shown in Figure 7.1, the growth rates of τ, obtained by assuming constant k_s for each subsection, were somewhat lower in the NE than in the PE case.

7.2 Development of Turbulence Structure

According to Lumley and Newman (1977), the values of the second and third invariants (to be defined shortly) of the anisotropy tensor, $m_{ij} = K_{ij} - \frac{1}{3}\delta_{ij}$, of any turbulent flow must lie between the values of the invariants corresponding to two dimensional and axisymmetric turbulent flows. The state of turbulence of the present measurements was checked by calculating the second and third invariants, $II = m_{ij}m_{ij}$ and $III = m_{ij}m_{jk}m_{ki}$ respectively, and plotting them along with the curves corresponding to two dimensional and axisymmetric turbulence given by Lumley and Newman (1977). Figure 7.2-a shows that the present measurements lie well within the mentioned limits. In Figures 7.2-b and 7.2-c, the scales are modified to show more clearly the measurements corresponding to the NE and PE cases respectively.

The variation of the dimensionless stresses, K_{uu}, K_{vv}, K_{ww} and K_{uv}, along the curved section is shown in Figure 7.3. The effect of curvature on the isotropy of the Reynolds stress was that negative S increased the anisotropy of $\overline{uv}$ and positive S decreased it. The opposite effect was felt by $\overline{u^2}$, $\overline{v^2}$ and $\overline{w^2}$, especially in the adjustment regions of the curved subsections. In Figure 7.4-a, the angle of maximum normal stresses (on the (s,n) plane) obtained from

$$\theta = \frac{1}{2}tan^{-1}(-\frac{2K_{uv}}{K_{uu} - K_{vv}}) \tag{7.5}$$

is plotted for the NE and PE cases. $\theta = 0$ for an isotropic flow, where $K_{uv} = 0$. The magnitude of θ from 0 increased for negative S and decreased for positive S. The anisotropy scalar $m^2 = tr(m_{ij}m_{jk})$, where m_{ij} is the anisotropy tensor, is a measure of the total anisotropy. For the present case, the anisotropy is expressed as

$$m^2 = (K_{uu} - \frac{1}{3})^2 + 2K_{uv}^2 + (K_{vv} - \frac{1}{3})^2 + (K_{ww} - \frac{1}{3})^2 \tag{7.6}$$

and is plotted in Figure 7.4-b. The behaviors of m^2 and θ follow the behavior of K_{uv}, which shows the stronger effect of curvature on shear stress than on normal stresses. Since K_{uv} is more sensitive to curvature than the other stresses, flow development will be characterized mainly by the variation of K_{uv}. This identifies two regions within each subsection with constant curvature: an "entrance" region, where K_{uv} adjusts monotonically from its value in the previous subsection to a new value, and a "fully developed" region, where K_{uv} is essentially constant, thus pointing to a self-similar development of the turbulence structure. These two regions will be examined separately in the following, starting with the "fully developed" region, which can be compared readily with results of HT1.

7.3 Fully Developed Region

7.3.1 Reynolds shear stresses

It is clear from Figure 7.3, especially from the development of K_{uv}, that beyond a certain position within each subsection the structure becomes nearly independent of τ, consistently with the observations of HT1. The asymptotic values for K_{uv} for small values of $\mid S \mid$, measured by HT1, could be fitted by the empirical expression

$$K_{uv} = -0.14(1 - 3.0S)sgnA \tag{7.7}$$

where $A = \frac{\partial \overline{U}}{\partial n}$ and $sgnA = 1$ if $A > 0$ and $sgnA = -1$ if $A < 0$. Note that sgnS instead of sgnA was used by HT1 for cases where the curvature had always the same orientation with respect to the n-coordinate. However, this would lead to errors in the present coordinate convention, which permits the radius of curvature to change sign.

In Figure 7.5 the asymptotic values of $K_{uv}sgnA$, near the end of each subsection, obtained from the present measurements, are plotted versus S along with the measurements of HT1 and equation 7.7. The present results agree well with those of HT1.

7.3.2 Kinetic energy

In the experiments of HT1, the asymptotic growth of the turbulent kinetic energy was found to follow

$$\frac{q^2}{q_0^2} = e^{\kappa_q \Delta\tau} \tag{7.8}$$

where κ_q was empirically described by

$$\frac{\frac{1}{2}\kappa_q}{1-S} = 0.039(1 - 18.5S) \tag{7.9}$$

To compare the development of turbulent kinetic energy in the different subsections, the total strain was measured with reference to the start of the corresponding subsection. $\frac{q^2}{q_0^2}$ is plotted in Figure 7.6 versus $\Delta\tau = \tau - \tau_i$, where τ_i refers to the value of τ at the beginning of the considered subsection when measured with respect to the exit of the shear generator. Also shown in Figure 7.6 are lines having a slope κ_q, given by equation 7.9, corresponding to the different cases of flow development in each subsection. The lines were passed through the last measured point for each set to compare the kinetic energy growth rate reached for each subsection to the results of HT1.

From Figure 7.6 one could identify the "entrance" region and the "fully developed" region from the variation of the slope of the kinetic energy growth. In the "entrance" region the slope varies, while in the "fully developed" region the slope presents less variation and approaches the slope obtained from equation 7.9.

7.4 Entrance Region

7.4.1 Mean flow adjustment

In the present experiments the geometric curvature is changed in a stepwise manner. The flow first passes from a straight subsection to a curved one, next it enters a subsection of opposite curvature, and finally it passes into another straight subsection, where it tends to recover from curvature effects. However, it is not obvious that the mean streamlines would precisely follow the local geometric curvature. Shizawa and Honami (1983) estimated the curvature of the mean streamlines for a concave turbulent boundary layer by analyzing the velocity profiles in the free stream. They reported that the mean streamlines started to curve about 8 boundary layer thicknesses upstream of the onset of the wall curvature, and matched the wall curvature at about the same distance downstream of its start. An error function approximated the adjustment of the effective curvature of the mean streamlines to the wall curvature (curvature is defined as the inverse of the radius of curvature).

For the present measurements, the position of the mean streamline entering the curved section at its centerline was estimated roughly from continuity considerations, by using the transverse profiles measured at different positions along the section and neglecting boundary layer and three-dimensional effects. Figure 7.7 shows that any possible deviations of the streamline curvature from the geometric centerline curvature in the present flow could not be significant.

Furthermore, measurements of the mean shear, presented in the previous chapter (Figure 6.5), showed continuous change due to wall effects and to the radial pressure gradient induced by curvature, among other effects. As mentioned in the previous chapter the change of mean shear in each subsection (and consequently the change of S) will be disregarded by comparison to the abrupt change of S from one subsection to the other.

7.4.2 Normal stresses

The behavior of the normal dimensionless stresses is rather curious. K_{uu}, K_{vv} and K_{ww} enter the curved section with values comparable to those reported by TK and HT1, who suggested virtual independence of these parameters from S, at least for small values of $| S |$. K_{uu} increased at the start of each subsection for which $S > 0$ and decreased for $S < 0$, after which it regained its initial value at a distance comparable to the adjustment distance of K_{uv}. K_{ww} had the opposite behavior. K_{vv} quickly adjusted for every subsection to a slightly higher value for $S < 0$ and to a slightly lower value for $S > 0$.

Gatski and Savill (1989) and Gillis and Johnston (1983) reported that the anisotropy m^2, defined by equation 7.6, experienced an overshoot in recovering from a stabilizing curvature. No such behavior was experienced by m^2 at recovery from stabilizing curvature in the present measurements.

7.4.3 Reynolds shear stress

As Figure 7.3 shows, K_{uv} changes gradually from one asymptotic value, corresponding to a subsection with a certain value of S, to another asymptotic value, corresponding to the following subsection with a new value of S. This change can be approximated by the response of the first-order system type to a step change of its input, namely by the following equation

$$K_{uv} = (K_{uv})_{i-1} + [(K_{uv})_i - (K_{uv})_{i-1}]\,(1 - e^{-\frac{\Delta\tau}{T}}) \tag{7.10}$$

where T is a dimensionless time constant, the subscript i refers to the asymptotic value of the subsection under consideration and the subscript i-1 refers to the previous one. The curvature parameter is then denoted by S_i for the subsection under consideration and by S_{i-1} for the previous one. In Figures 7.8-a and 7.8-b, equation 7.10 is plotted for cases NE and PE respectively. The optimum value of T for each subsection was found by minimizing the difference between equation 7.10 and the measurement points using least square fitting.

Bradshaw (1973) reported that after prolonged application of a small extra rate of strain, e, (in the present case $e = \frac{\overline{U}_c}{Rc}$) the Reynolds stresses are observed to change as if their production changed by a factor

$$F = 1 + \alpha \frac{e}{\frac{\partial \overline{U}}{\partial n}} \tag{7.11}$$

where α is of the order of 10. Bradshaw reported also that when e changes suddenly from zero to a constant value, the value of α required to optimize agreement with results from experiments rises slowly to its asymptotic value of order 10. He defined an effective extra rate of strain $(\alpha e)_{eff}$, and suggested a first order system response equation of its change in the streamwise direction as

$$X\frac{d}{ds}(\alpha e)_{eff} = (\alpha e)_0 - (\alpha e)_{eff} \tag{7.12}$$

where the length X is a "time" constant, estimated from the ratio of the turbulent kinetic energy to the rate of production of turbulent kinetic energy as

$$X = \frac{\frac{1}{2}q^2\overline{U}}{-\overline{uv}\frac{\partial \overline{U}}{\partial n}} = \frac{\frac{1}{2}}{-K_{uv}\frac{1}{\overline{U}}\frac{\partial \overline{U}}{\partial n}} \tag{7.13}$$

The "time constant" defined in this manner represents the "life time" of the stress containing eddies, and is also referred to as the "spectral residence time" (Champagne, Harris and Corrsin, 1970). A value of $X = 10\delta$ was estimated by using values of the parameters in equation 7.13 corresponding to a typical straight turbulent boundary layer.

The approach adopted in the present investigation differs from that of Bradshaw (1973) in that the adjustment of a measured turbulence quantity, the structural parameter, is investigated instead of the "effective" extra rate of strain. An attempt is also made to investigate the dependence of the adjustment of K_{uv} on the strength of curvature applied to the shear flow, a matter which, to our knowledge, has not been given enough attention.

The present measurements correspond to small values of S and cannot provide a clear picture of possible dependence of T upon S. For this reason, it will be attempted to supplement this study with additional results. Although the measurements of HT1 were not originally intended to be used for investigating the adjustment of the flow to curvature, but rather the effects of prolonged constant curvature, they also contain measurements of K_{uv} near the entrance of their curved section, which could be used for estimating the time constant T, corresponding to different values of S. Unfortunately, in the HT1 experiments, the flow entered the curved section directly from the large upstream straight section and it was not permitted to settle as in the present experiment, a fact which adds some uncertainty to the HT1 results. Figure 7.9 shows the fitting of selected measurements of K_{uv} by HT1 by equation 7.10.

HT2 have speculated that curvature and shear act differently on eddies of different sizes. Extending HT2's speculation, we make the following assumptions. First, we assume that the parameter S is a measure of the strength of the "curved" eddies with respect to the "sheared" eddies. And, second, we assume that a flow originally subjected to a curvature parameter S_{i-1} and suddenly subjected to S_i contains both the original eddies corresponding to S_{i-1} and the newly generated eddies corresponding to S_i. Another useful concept was presented by Bradshaw (1973), who assumed that the rate of adjustment of a shear flow depends on the life time of the stress containing eddies. If one further extends this idea, one may assume that the rate of adjustment of curved shear flows depends on the "life time" of the "sheared eddies" and on the "life time" of the "curved eddies". The rate of adjustment of a curved shear flow would then, most likely, depend on both the local and the previous values of S, namely on S_i and S_{i-1}. An effective S parameter which is a combination of S_i and S_{i-1} might then be appropriate in scaling the time of adjustment. Many combinations of S_i and S_{i-1}, such as $(S_i - S_{i-1})$, $\frac{1}{(S_i - S_{i-1})}$ and $\frac{(S_i + S_{i-1})}{(S_i - S_{i-1})}$ have been tried. An average value of S, $S_{av} = \frac{(S_i + S_{i-1})}{2}$, resulted in better scaling of the cases considered. Unfortunately, S_{av} has the same value for some flows which are expected to have completely different rates of adjustment, as, for example, for a flow with unchanging

S ($S_{i-1} = S_i = S$) and an originally rectilinear shear flow subjected to a stepwise curvature ($S_{i-1} = 0$ *and* $S_i = 2S$). Both these flows have equal $S_{av} = S$ but are evidently likely to have quite different adjustment rates.

Six different cases of flow adjustment are obtained from the present measurements: two cases in which an originally rectilinear shear flow is subjected to either stabilizing or destabilizing curvature ($S_{av} = \frac{1}{2}S_i$), two cases of curvature reversal ($S_{av} = 0$) and two cases of recovery from stabilizing or destabilizing curvature ($S_{av} = \frac{1}{2}S_{i-1}$). The measurements of HT1 correspond all to an initially rectilinear shear flow subjected to curvature so that $S_{av} = \frac{1}{2}S_i$.

In Figure 7.11, $\frac{1}{T}$ is plotted versus S_{av} for all the cases mentioned above. It is clear from this figure that $\frac{1}{T}$ increases with $|S_{av}|$ for small values of S_{av} (ranging between ± 0.1). It is particularly interesting that all the different flows considered (rectilinear flows subjected to stepwise curvature, flows subjected to curvature reversal and flows recovering from curvature) scale with S_{av}. No premature generalization of this trend should be undertaken (such as for flows subjected to higher values of S or to flows subjected to curvature reversal with $S_{av} \neq 0$). We can however conclude that, for an originally rectilinear shear flow subjected to curvature, the adjustment is faster when the effects of curvature are stronger (higher S), and that, for a flow subjected to curvature reversal with small values of S, the adjustment depends on both the original and the new values of S.

In the following, some physical arguments will be used to attempt to predict the dependence of the rate of adjustment of curved shear flow on the strength of curvature applied to it. Only the cases in which the flow was originally rectilinear and curvature was applied to it or when a curved shear flow was recovering in a straight section will be considered.

As mentioned earlier we assume that the rate of adjustment of curved shear flows depends on the "life time" of the "sheared eddies", t_s, and on the "life time" of the "curved eddies", t_c.

A suitable estimate of the order of magnitude of t_s, obtained from the ratio of the turbulent kinetic energy to the rate of production of turbulent kinetic energy, in accordance with the procedure followed by Bradshaw (1973), would be

$$t_s \simeq \frac{\frac{1}{2}q^2}{|-\overline{uv}_s\frac{\partial \overline{U}}{\partial n}|} \tag{7.14}$$

A nondimensional time, T_s, can be obtained by dividing t_s by the time scale defined in 7.1, as

$$T_s = \frac{t_s}{|\frac{\partial \overline{U}}{\partial n}|^{-1}} \simeq \frac{\frac{1}{2}}{|(K_{uv})_s|} \tag{7.15}$$

Expressions similar expression to 7.14 and 7.15 can be used to estimate t_c and T_c. However, Bradshaw (1973) argued, as mentioned earlier, that the Reynolds stresses for shear flows subjected to prolonged curvature (or more generally to an additional rate of strain) are observed to change as predicted by a typical turbulence model, if the new production terms (corresponding to the extra rate of strain) are multiplied by a factor α. Following this hypothesis, one may use an expression similar expression to equation 7.14 to find t_c, but in which production by the curvature term would be multiplied by a factor α, as

$$T_c = \frac{t_c}{|\frac{\partial \overline{U}}{\partial n}|^{-1}} = \frac{\frac{1}{2}q^2}{|\alpha\overline{uv}_c S|} \simeq \frac{\frac{1}{2}}{|(K_{uv})_c\alpha S|} \tag{7.16}$$

In this expression, $(K_{uv})_c$ is the value of the shear stress structural parameter for the curved eddies. S could be equal to S_i or to S_{i-1}. If one further speculates that the time constant of adjustment to curvature would be equal to the harmonic average of the nondimensional "life time" of the "sheared eddies", T_s, and the nondimensional "life time" of the "curved eddies", T_c, then,

$$\frac{1}{T} = \frac{1}{T_s} + \frac{1}{T_c} \tag{7.17}$$

To justify the choice in equation 7.17, it can be seen from equation 7.15 and equation 7.16 that, for shear dominated flows (small value of S), $T \simeq T_s$, while for curvature dominated flows (large value of S), $T = T_c$. T_s is estimated from equation 7.15 by using the typical value of $|(K_{uv})_s| = 0.14$ for straight nearly homogeneous uniformly sheared flows. HT1 suggested that for curvature dominated flows ($S \to \infty$), the shear stress structural parameter tends to a value around 0.25. By using $|(K_{uv})_c| = 0.25$ and $\alpha \simeq 20$, T_c is estimated from equation 7.15. Furthermore, we note that, for the cases considered here, $S = 2S_{av}$. Equation 7.17 reduces then to a linear relationship between $\frac{1}{T}$ and S_{av}

$$\frac{1}{T} = a + b|S_{av}| \tag{7.18}$$

where $a = 0.28$ and $b = 20$. Equation 7.18 is plotted in Figure 7.10. It can be seen that the above arguments predict, at least qualitatively, reasonably well the variation of T with the strength of curvature for small values of S.

Other examples of flows subjected to curvature from the literature also show that these flows adjusted faster for higher values of S. From the study of Nakayama (1987) of curvature and pressure gradient effects on a small defect wake, the time constant T was estimated to be around 0.1 for $S \simeq 0.4$. Even though this value cannot be compared to the present estimates due to the high value of S and to the presence of a pressure gradient, it does document a large decrease of T at large S. Also, in the study of Ellis and Joubert (1974) of a turbulent shear flow in a curved duct, the development of the skin friction coefficient C_f was faster for the smaller radius of curvature and therefore for the larger value of S.

7.4.4 Kinetic energy

By using the time scale $\mid \frac{\partial \overline{U}}{\partial n} \mid^{-1}$ and the turbulent velocity scale $v = q'$, the turbulent kinetic energy (Chapter 4, equation 4.59) can be rewritten in a nondimensional form as

$$\frac{1}{q^2}\frac{d}{d\tau}\frac{q^2}{2} = -K_{uv}(1-S)sgnA - \frac{\epsilon}{q^2|A|} \tag{7.19}$$

The first term on the right hand side is the dimensionless production, P^* , and the second term is the dimensionless dissipation rate, ϵ^*.

Equation 7.19 can be used to estimate ϵ^* as the balance of the other terms, which are measurable. The development of the dimensionless dissipation, ϵ^*, based on equation 7.19, is shown in Figure 7.11-a and 7.11-b for the NE and PE cases respectively. A polynomial curve fitting to the kinetic energy development was undertaken to estimate the local kinetic energy derivatives in equation 7.19. Also shown in these figures is another estimate of the nondimensional dissipation rate, computed from direct measurements and with the use of the isotropic relation

$$\epsilon_i^* \simeq 30\mu\frac{K_{uu}}{|A|\lambda_{uu}^2} \tag{7.20}$$

In Figures 7.12-a and 7.12-b the dissipation to production ratio is plotted for the NE and PE cases respectively.

An average asymptotic value of ϵ^* for every subsection is estimated and compared in Figure 7.13 to the values estimated by HT1 for different values of S and to the following relation obtained by assuming exponential growth of kinetic energy (HT1)

$$\epsilon^* = 0.10(1+3.2S)(1-S) \tag{7.21}$$

The dissipation estimates are subjected to a lot of scatter, but they show a tendency to adjust to a certain value near the end of each subsection. To derive an expression for the evolution of the kinetic energy, one needs to model the evolution of ϵ^*. Two approaches will be explored here. At first, an average value of $\epsilon^* = 0.1$, which corresponds to $S = 0$ in equation 7.21, and is intermediate between the values of ϵ^* in the two curved subsections, will be assumed. Secondly, the average asymptotic values, corresponding to the value of S in each subsection, will be used, permitting ϵ^* to change abruptly from one subsection to the other. The actual variation of ϵ is expected to lie between these two limiting cases, and, in any case, ϵ^* was not found to be very sensitive to S for small values of $|S|$. A first-order system adjustment, with a time constant comparable to the time constant of adjustment of K_{uv}, seems also compatible with the data in Figure 7.11, but will not be further explored, as leading to unnecessary complications. The latter approach could, however, be beneficial for higher values of S, where a stronger variation of ϵ^* would be expected. Substituting for K_{uv} from equation 7.10, and solving the obtained differential equation, one gets

$$\begin{aligned} \frac{q^2}{q_0^2} &= exp\left\{(-2(1-S)sgnA(K_{uv})_\infty - 2\epsilon^*)\Delta\tau\right\} \\ &\times exp\left\{2(1-S)sgnA\left((K_{uv})_\infty - (K_{uv})_0\right)T(1-e^{-\frac{\Delta\tau}{T}})\right\} \end{aligned} \tag{7.22}$$

Equation 7.22 is plotted for each curved portion in Figure 7.14, along with the measurements. The first exponent, equal to κ_q, represents the asymptotic behavior. The second exponential represents the adjustment of the structure to curvature. As $\Delta\tau \to \infty$, the second exponential becomes negligible compared to the first one, and, for $\Delta\tau = 0$, q^2 is equal to q_0^2. The measurement points lie mostly between the two curves corresponding to constant ϵ^* and to the suddenly changing ϵ^*.

7.5 A First Order Model of Stepwise Introduction of Curvature

Based on the previous section, the change of the structural parameter, K_{uv}, of an originally straight shear flow subjected to stepwise curvature with a curvature parameter S can be described by a first-order system equation

$$T(S)\frac{dK_{uv}}{d\tau} + K_{uv} = -0.14(1-3.0S)sgnA \tag{7.23}$$

The time constant, T, was approximated as

$$\frac{1}{T} = a + b|S| \tag{7.24}$$

where $b' = \frac{b}{2}$ (b is the constant used in equation 7.18). Equation 7.23 then becomes

$$\frac{dK_{uv}}{d\tau} + (a + b'|S|)K_{uv} = -0.14(1-3.0S)sgnA(a + b'|S|) \tag{7.25}$$

For small values of S, a constant value of ϵ^* can be assumed. For higher values of S, within the range of applicability of this analysis, it may be assumed that the dissipation would adjust similarly to K_{uv}, with the same time constant, so that

$$\frac{d\epsilon^*}{d\tau} + (a + b'|S|)\epsilon^* = 0.10(1+3.2S)(1-S)(a + b'|S|) \tag{7.26}$$

7.6 Development of the Pressure Strain Rate Covariances

The pressure strain rate covariances, which appear in the Reynolds stress equations, are difficult to measure directly or to evaluate theoretically in terms of other parameters. They are often modeled and the overall success of turbulence prediction depends strongly on how well they are modeled (Tselepidakis, Gatski and Savill, 1991). Pressure strain covariances have been estimated from the Reynolds stress equations as the balance of the other terms by Champagne, Harris and Corrsin (1970) and TK for rectilinear nearly homogeneous flows and by HT1 for curved nearly homogeneous flows. As shown in a previous section, the dissipation rate, ϵ^*, can be estimated as the balance of other terms in the kinetic energy equation. Two approaches have often been used for estimating the partition of ϵ^* among its three components. The first approach, used among others, by Champagne, Harris and Corrsin (1970) assumes that the dissipation is isotropic, i.e.

$$\epsilon^*_{uu} = \frac{\epsilon^*}{3}, \qquad \epsilon^*_{vv} = \frac{\epsilon^*}{3}, \qquad \epsilon^*_{ww} = \frac{\epsilon^*}{3}, \qquad \epsilon^*_{uv} = 0 \qquad (7.27)$$

In the second approach, which was introduced by TK, the anisotropy of the dissipation was assumed to be equal to the anisotropy of the Reynolds stresses, so that

$$\epsilon^*_{uu} = K_{uu}\epsilon^*, \qquad \epsilon^*_{vv} = K_{vv}\epsilon^*, \qquad \epsilon^*_{ww} = K_{ww}\epsilon^*, \qquad \epsilon^*_{uv} = K_{uv}\epsilon^* \quad (7.28)$$

The above two approaches will be adapted to explore the adjustment of the pressure strain rate covariances to curvature and their response to curvature reversal.

By nondimensionalizing the Reynolds stress equations, the nondimensional pressure strain rate covariances are obtained as

$$\phi^*_{uu} = (2P^* - 2\epsilon^*)K_{uu} + \frac{\partial}{\partial\tau}K_{uu} + 2K_{uv}(1+S)sgnA + 2\epsilon^*_{uu} \qquad (7.29)$$

$$\phi^*_{vv} = (2P^* - 2\epsilon^*)K_{vv} + \frac{\partial}{\partial\tau}K_{vv} + 4K_{uv}SsgnA + 2\epsilon^*_{vv} \qquad (7.30)$$

$$\phi^*_{ww} = (2P^* - 2\epsilon^*)K_{ww} + \frac{\partial}{\partial\tau}K_{ww} + 2\epsilon^*_{ww} \qquad (7.31)$$

$$\phi^*_{uv} = (2P^* - 2\epsilon^*)K_{uv} + \frac{\partial}{\partial\tau}K_{uv} - (K_{vv}(1+S) + 2K_{uu}S)sgnA + 2\epsilon^*_{uv} \qquad (7.32)$$

The above equations differ from those of HT1 in that they permit a change of the various dimensionless parameters in the streamwise direction. Also, sgnS has been replaced by sgnA to accommodate curvature reversal. The first terms on the RHS of each equation appear because of the selected nondimensionalization with q; they do not appear in the equations of Gatski and Savill (1989), who nondimensionalized their equation with the initial kinetic energy, q_0^2.

HT1 assumed that the normal dimensionless stresses were essentially independent of S and had values close to those found for straight shear flow (TK), so that their derivatives with respect to τ were neglected. On the other hand, the terms containing K_{uv} in equations 7.29 and 7.30 exhibit a dramatic change when the value of S changes, particularly in the case of ϕ^*_{vv} . It was noted earlier that K_{vv} adjusts quickly to a new value in each subsection. So it is likely that the dramatic change in the parameter containing K_{uv}, when the curvature is changed suddenly, is partly balanced by a change in K_{vv}. In conclusion, neglecting $\frac{\partial K_{uu}}{\partial\tau}$, $\frac{\partial K_{vv}}{\partial\tau}$, etc would be justifiable for prolonged regions with constant curvature but, when the curvature changes suddenly, this assumption is unrealistic, because of the discontinuity of the terms containing S in ϕ^*_{vv}, and, to a lesser extent, in all pressure-strain covariances.

Following the above discussion, the local values of the different terms are used to compute the pressure strain covariances at each measuring point along the section. The derivatives of K_{uu}, K_{vv} and K_{ww} with respect to τ were estimated from the measurements and $\frac{\partial K_{uv}}{\partial \tau}$ was calculated from equation 7.10. The results are plotted in Figures 7.15 to 7.18. Even though the discontinuity in ϕ^*_{vv} and ϕ^*_{uv}, resulting from a sudden change of S was attenuated by taking into consideration the adjustments of K_{vv} and K_{uv}, changes in the values of these quantities occur relatively abruptly from one subsection to the other. This is most probably due to neglecting the higher order diffusion terms in the Reynolds stresses equations.

HT1 postulated that ϕ^*_{uu} is essentially an even function of S, ϕ^*_{vv} increases with S, while ϕ^*_{ww} and ϕ^*_{uv} decreases with S at least for small $| S |$. Figures 7.15 to 7.18 confirm these postulates.

7.7 Self-Similarity of the Flow

In self-preserving turbulent shear flows, such as wakes, jets, etc., an effective Reynolds number (Corrsin, 1957) can be defined as

$$Re_T = \frac{\Delta U l}{\nu_T} \tag{7.33}$$

where ΔU is a characteristic velocity difference, l is a characteristic transverse length scale and ν_T is the eddy viscosity. By analogy, an effective Reynolds number

$$Re_T = \frac{(\frac{\partial \overline{U}}{\partial n})^2 l^2}{-K_{uv} q^2} \tag{7.34}$$

can be defined for the nearly homogeneous uniformly turbulent shear flow (Tavoularis and Karnik, 1989). It has been stated by several investigators that no external length scale can be used for this flow, so one must resort to internal length scales. For example, the height of the channel is not appropriate since the boundary effects are neglected. The integral length scales have been used for this purpose in expressions similar or analogous to 7.34. Harris, Graham and Corrsin (1977) plotted $\frac{q^2}{L_{uu}^2(\frac{dU}{dn})^2}$ versus τ and found that it had a nearly constant value for large values of τ. Tavoularis and Karnik (1989) calculated R_T for their and other experiments and found small variations as τ changes. HT1 calculated $\frac{L_{uu}}{L}$, where $L = \frac{q'}{A}$, for curved nearly homogeneous turbulent shear flows. For high shear rates, close to the one in the present experiments, this ratio increased for negative S and decreased for positive S.

In Figures 7.19 and 7.20, R_T based on L_{uu} and L_{vv} are plotted versus τ for cases NE and PE respectively. R_T based on L_{uu} enters the curved section with values around 40, in conformity with those reported by TK. Because of the considerable scatter, no clear trend of the dependence of R_T on S can be discerned. It is remarkable, however, that when L_{vv} is used as the length scale for calculation of R_T, a much clearer trend is observed. This might imply that L_{vv} is more appropriate as the transverse length scale of self-preserving, uniformly sheared turbulence. Re_T increases for negative S and decreases for positive S. To make a comparison to the measurements of HT1, $\frac{L_{uu}}{L}$ was calculated and is shown in Figure 7.21. This ratio enters the curved section with a value around 2.5 and it increases for negative S and decreases for positive S, in conformity with the observations of HT1.

7.8 Study of Spectral Measurements

By using the Taylor approximation, the one-dimensional wave-number spectra can be obtained from frequency spectra. For example, the streamwise power spectral component is given as

$$E_{uu}(k_1) = \frac{\overline{U}}{2\pi} F_{uu}(f) \tag{7.35}$$

where k is the streamwise component of the wave number vector, given as

$$k_1 = \frac{2\pi f}{\overline{U}} \tag{7.36}$$

In Figures 7.22 to 7.27, E_{uu}, E_{vv} and E_{ww}, nondimensionalized by $\overline{u^2}L_{uu}$, are shown for the NE and PE cases, along with the spectra of isotropic turbulence obtained from von Karman's interpolation formula

$$\frac{E_{uu}(k_1)}{\overline{u^2}L_{uu}} = \frac{1}{\pi}[1 + (1.33 k_1 L_{uu})^2]^{-\frac{5}{6}} \tag{7.37}$$

where L_{uu} was estimated as

$$L_{uu} = \frac{\pi}{\overline{u^2}} \lim_{k_1 \to 0} E_{uu}(k_1) \tag{7.38}$$

In determining L_{uu}, the limit of E_{uu} at $k_1 = 0$ was taken to be equal to its value at the lowest wave number, because theoretically E_{uu} should approach a constant at low wave numbers (Tennekes and Lumley, 1973, p.255). The shape of $\frac{E_{uu}}{\overline{u^2}L_{uu}}$ was close to the shape of the isotropic spectra. It should be noted that the selected normalization procedure forces the measured spectra and the one obtained from equation 7.37 to collapse at the low wave numbers.

In an isotropic flow, E_{uu}, E_{vv} and E_{ww} would collapse on the curve described by 7.37. Figures 7.23, 7.24, 7.26 and 7.27 show that the effects of curvature on the

Reynolds stresses anisotropies are mostly felt by the large scales. In Figures 7.28 and 7.29, E_{uu}, nondimensionalized with the Kolmogoroff length scale and velocity, clearly shows also that the large scales were the most affected by curvature.

In Figures 7.30 and 7.31 the coherence function is shown for cases NE and PE respectively. By comparing the flows with comparable values of S but different flow histories (7.30-a to 7.31-b and 7.30-b to 7.31-a), it can be seen that the coherence of scales with $k_1 L_{uu} < 10$, while starting at different levels, reached comparable values, when subjected to comparable values of small S, over sufficient values of total strain. A close look at these figures also shows that the adjustment pattern of the large scales is different when the flow is subjected to positive or negative values of S. This observation becomes even more clear in Figure 7.32, where the value of $Re(C_{uv})$ at the smallest measured wave numbers is plotted versus τ for the NE and PE cases respectively. For negative S the adjustment resembles the behavior of a first order system, similar to the behavior of the correlation coefficient in Figure 6.25. For positive S, $Re(C_{uv})$ is still changing at the last measuring point of the considered subsection, even though the correlation coefficient reached an almost constant value within a certain distance from the start of the subsection. This suggests that the contributions of the large and small scales of the flow to the overall correlation was better established for negative than for positive S at the end of the considered subsection. Even though the uncertainty associated with the values of the coherence function at low wave numbers might cause some reservations towards the above observations, a close look at Figures 7.30 and 7.31 reveals that positive S causes stronger variations on the small scales (the cloud of coherence values at high wave numbers was thicker for positive S), which is another indication of the different response of turbulent eddies to positive and negative S.

Chapter 8

Comparison to Curved Turbulent Boundary Layers

In the present Chapter, a discussion of some measurements in curved turbulent boundary layers reported in the literature is undertaken and an attempt is being made for a quantitative comparison of curved boundary layers and curved nearly homogeneous flows.

8.1 Measure of the Additional Rate of Strain due to Curvature

The parameter $\frac{\delta}{R_w}$ (δ is the boundary layer thickness and R_w is the wall radius of curvature) is often used to characterize the strength of curvature for turbulent boundary layers. This parameter allows one to estimate the order of magnitude of the ratio of the extra rate of strain due to curvature, $e = \frac{\partial V_y}{\partial x}$ (where V_y is the transverse velocity in (x,y,z) coordinates) $\simeq \frac{\overline{U}}{R}$ (in (s,n,z) coordinates), to the main shear $\frac{\partial \overline{U}}{\partial n}$ to which the outer layer is subjected, by assuming that $\frac{\partial \overline{U}}{\partial n} = O(\frac{\overline{U}}{\delta})$. $\frac{\delta}{R_w}$

is also a measure of the pressure difference across a curved boundary layer, as can be verified from a momentum balance across the boundary layer, if one assumes a linear velocity profile. Clearly, even though $\frac{\delta}{R_w}$ is satisfactory for classifying curved turbulent boundary layers, a more realistic estimate for the rate of strain rate is needed for quantitative predictions and for comparison to curved uniformly sheared flows, as the mean shear varies strongly from the inner to the outer regions of the boundary layer.

8.1.1 Transverse variation of S

If for simplicity one assumes a power law velocity profile for the turbulent boundary layer

$$\frac{\overline{U}}{\overline{U}_\infty} = (\frac{n}{\delta})^{\frac{1}{p}} \tag{8.1}$$

where the value of p is usually taken equal to 7.0 for flat plate boundary layers, then the value of S at any position $\xi = \frac{n}{\delta}$ (n is the distance normal to the wall) in the boundary layer for convex and concave walls is given, respectively, as

$$S_{cv} = p\frac{\xi}{\frac{R_w}{\delta} + \xi} \tag{8.2}$$

$$S_{cc} = p\frac{\xi}{\frac{R_w}{\delta} - \xi} \tag{8.3}$$

The variations of S_{cv} and S_{cc} are drawn versus ξ for different values of $\frac{\delta}{R_w}$ in Figure 8.1-a. Only values of ξ up to 0.9 are shown because, as ξ approaches 1, the flow is strongly affected by intermittency effects and the mean shear of the flow goes to zero.

It is clear from this figure that curvature is relatively stronger in the outer region of the turbulent boundary layer. It is well known, however, that the power law becomes inaccurate in the inner layer and it is completely inappropriate in the viscous sublayer. By assuming a more realistic profile, based on the law of the wall, the following variations of S are obtained for convex and concave walls, respectively.

$$S_{cv} = C\frac{\xi}{\frac{R_w}{\delta} + \xi} \tag{8.4}$$

$$S_{cc} = C\frac{\xi}{\frac{R_w}{\delta} - \xi} \tag{8.5}$$

where the coefficient C is a function of the nondimensional distance from the wall, $n^+ = \frac{nu_\tau}{\nu}$ (u_τ being the shear velocity and ν the kinematic viscosity). Fot the laminar sublayer, the buffer layer and the outer region of a turbulent boundary layer, C is given respectively as

$$C = 1 \qquad n^+ < 4 \tag{8.6}$$

$$C = \frac{4.2 - 5.7ln(n^+) + 5.1(ln(n^+))^2 - 0.7(ln(n^+))^3}{-5.7 + 10.2ln(n^+) - 2.1(ln(n^+)^2} \qquad 4 < n^+ < 40 \tag{8.7}$$

$$C = \frac{5.45log_{10}(n^+) + 5.5}{\frac{5.45}{ln10}} \qquad n^+ > 40 \tag{8.8}$$

In Figure 8.1-b C is plotted for some typical limits of n^+, given in equations 8.6-8.8, corresponding to the three regions. The values obtained from the law of the wall are considerably less than the value of 7 obtained from the power law, showing a larger difference between S in the inner and outer layers.

The outer boundary layer presents a relatively small variation of the mean shear, $\frac{\partial \overline{U}}{\partial n}$, and an approximately constant structural parameter K_{uv}, between $\xi = 0.3$ and $\xi = 0.7$. In this layer, a typical value of the S parameter, defined as

$$S_{\xi=0.5} = \frac{\frac{\overline{U}_{\xi=0.5}}{R_{\xi=0.5}}}{\frac{\overline{U}_{\xi=0.7} - \overline{U}_{\xi=0.3}}{0.4\delta}} \tag{8.9}$$

will be used. In equation 8.9, $\overline{U}_{\xi=0.5}$ is the mean streamwise velocity at $\xi = 0.5$ and $R_{\xi=0.5}$ is the radius of curvature at $\xi = 0.5$. $R_{\xi=0.5}$ will be approximated by $R_w + \frac{\delta}{2}$ for convex walls and by $R_w - \frac{\delta}{2}$ for concave walls, R_w being the wall radius.

In the remaining of this Chapter, whenever S or K_{uv} are used, they will refer to the values at position $\xi = 0.5$ unless otherwise stated.

8.1.2 Streamwise variation of S

It is well known that the rate of growth of turbulent boundary layers is increased by concave curvature and decreased by convex curvature. Figures 8.2-a and 8.2-b show respectively the streamwise changes of δ and $\frac{\delta}{R_w}$ for various experiments reported in the literature. Conservation of vorticity in inviscid flows requires that concave curvature decrease the value of the mean shear in the outer layer, and that convex curvature increase it. Furthermore, as the boundary layer grows, the mean shear in the outer layer would be reduced. The inviscid and boundary layer growth effects will both tend to increase the S parameter in the streamwise distance for concave curvature, while the two effects will tend to cancel each other for convex curvature. Based on the above explanation, it may be expected that the S parameter would exhibit a stronger streamwise variation for concave walls than for convex walls. This is confirmed by Figure 8.2-c, where S, estimated from equation 8.9, is plotted versus the streamwise distance for different measurements reported in the literature. The average value of the ratio $\frac{S}{\frac{\delta}{R_w}}$, shown in Figure 8.2-d, was around 2.5 for convex boundary layers and presented more change in the streamwise direction for concave boundary layers.

8.2 Effect of Strength of Curvature on the Shear Stress Parameter

The change in turbulent stresses due to streamline curvature is fed back to the mean flow, as explained by Gibson, Verriopoulos and Vlachos (1984), and as can be seen from the momentum equation, which, written for rectilinear boundary layers is

$$\overline{U}\frac{\partial \overline{U}}{\partial s} + \overline{V}\frac{\partial \overline{U}}{\partial n} = -\frac{1}{\rho}\frac{\partial \overline{P}}{\partial s} + \frac{\partial}{\partial n}(-\overline{uv} + \nu\frac{\partial \overline{u}}{\partial n}) - \frac{\partial}{\partial s}(\overline{u^2} - \overline{v^2}) \tag{8.10}$$

To avoid the complexity of coupling the mean flow and the turbulence structure, only the effects of streamline curvature on the turbulence structure will be discussed in the following.

From the present measurements, those performed by HT1, and the measurements performed in curved turbulent boundary layers, it has been well established that curvature causes greater relative changes in $\overline{uv}$ than in q^2, resulting in a relatively stronger change of K_{uv} than of the normal dimensionless stresses. The structural parameter K_{uv}, which is a simple measure of the efficiency of turbulence in producing shear stress (Bradshaw, 1973), has a value around 0.15 for plane boundary layers, except close to the wall and near the outer edge. Because the outer region of turbulent boundary layers is affected by streamline curvature more than the inner layer, one would anticipate that K_{uv} would increase towards the outer edge in concave boundary layers, and decrease towards the outer edge in convex boundary layers. The change of K_{uv} between $\xi = 0.3$ and $\xi = 0.7$ is small compared to the change of the actual Reynolds shear stress, so that a representative value of K_{uv} taken at $\xi = 0.5$ will be selected to study the streamwise variation of K_{uv} with the strength of curvature for the outer layer.

The streamwise development of turbulent boundary layers is usually plotted versus the streamwise distances nondimensionalized by the boundary layer thickness, δ. $\frac{\Delta s}{\delta}$ can be regarded as analogous to the total strain, $\tau = \frac{s}{U}\frac{\partial \overline{U}}{\partial n}$, used for homogeneous uniformly sheared flow in the same manner that $\frac{\delta}{R_w}$ is analogous to $S = \frac{\frac{\overline{U}}{R}}{\frac{\partial U}{\partial n}}$. In Figure 8.3, K_{uv} is plotted versus $\frac{\Delta s}{\delta}$ for selected measurements from the literature. The deviation of K_{uv} from its flat plate value of 0.15 under the effect of curvature is clear from this Figure. The amount by which K_{uv} drops or increases for convex and concave turbulent boundary layers respectively is more pronounced for stronger curvature.

In estimating K_{uv} from the reported measurements, an average value was taken if the measurements presented spanwise variations (as in the case of Hoffmann, Muck and Bradshaw (1985)). When only the s and n components of the stresses were measured, the structural parameter was approximated by $K_{uv} \simeq \frac{\overline{uv}}{1.5(\overline{u^2}+\overline{v^2})}$ (experiments of Barlow and Johnston, 1988a).

In Tables 8.1 and 8.2 the conditions at which these experiments were performed are summarized for convex and concave turbulent boundary layers respectively. Despite the differences, most of the experiments show some quantitative consistency. An exception is the results of of Shivaprasad and Ramaprian (1978), which are not consistent with the other measurements, especially in the concave case. Gibson, Verriopoulos and Vlachos (1984) reported the comments of Hoffman and Bradshaw (1978) that the difference between these measurements and others is most probably due to the presence of strong secondary flow in the corners because of the low aspect ratio of their duct and to the inaccuracy of the nonlinearized constant-current anemometer used.

While K_{uv} gradually responded to the introduction of wall curvature, as can be seen from Figure 8.3, it did not attain asymptotic values in the measured ranges, particularly for concave boundary layers. Two features present in concave boundary layers seem to be strong factors in preventing the turbulence structure from reaching nearly asymptotic states. The first is the significant streamwise increase of S. The second is three-dimensionality: unlike convex turbulent boundary layers, which can be treated as two-dimensional flows, concave boundary layers may exhibit spanwise variations in mean flow and turbulence parameters, which makes them three-dimensional. The variation is due to the presence of quasi-steady longitudinal vortices, which are believed to be generated by a mechanism similar to the Rayleigh-Taylor-Görtler instability, present in concave laminar boundar layers. The magnitude and the importance of these spanwise variations varied from one investigation to the other. For example, Meroney and Bradshaw (1975) reported 50 to 100% spanwise variation in momentum thickness, Shizawa and Honami (1985) reported 16% variation in the same quantity, while Ramaprian and Shivaprasad (1978) did not find any evidence of the existence of the vortices. Barlow and Johnston (1988a) reviewed extensively the origin and behavior of these vortices, which are believed to be strongly dependant on upstream nonuniformities of the flow, such as screen misalignment. The variation of the importance of these spanwise variations from one investigation to the other has sometimes led to contradictory conclusions; for example, Shivaprasad and Ramaprian (1978) concluded that convex wall curvature appeared to have stronger effect on the behavior of the boundary layer than concave curvature of the same $\frac{\delta}{R_w}$, while Smits and Wood (1985) concluded from the results of Muck, Hoffman and Bradshaw (1985) that concave curvature had a stronger influence on turbulence structure than convex curvature did.

From Figure 8.3 it could be argued that, in convex boundary layers, some similarity had been attained at the last measuring stations, so that an asymptotic value of K_{uv} could be assumed for each case and a typical value of S could be defined, as this parameter did not vary significantly in the streamwise direction. Such asymptotic values of K_{uv} are plotted in Figure 8.4 versus the average values of S. Also shown in this Figure is the relation given by HT1 for the variation of K_{uv} versus S in nearly homogeneous curved flow. Using a linear least-squares fit, the variation of K_{uv} in convex boundary layers can be approximated by

$$K_{uv} = -0.144(1 - 3.9S)sngA \qquad for \quad 0 < S < 0.25 \tag{8.11}$$

which is only slightly different from the HT1 expression. It is more practical to give this relation in terms of $\frac{\delta}{R_w}$, so using $S \simeq 2.5\frac{\delta}{R_w}$, one gets

$$K_{uv} = -0.144(1 - 9.7\frac{\delta}{R_w})sgnA \qquad for \quad 0 < \frac{\delta}{R_w} < 0.1 \tag{8.12}$$

Despite quantitative differences between the responses of turbulence parameters to curvature in turbulent boundary layers and those in nearly homogeneous flow, the latter could be useful at least for rough estimates in curved turbulent boundary layers. For example, Gillis and Johnston (1980) found that the turbulence in the outer region of a turbulent boundary layer became quasi-isotropic after being subjected to 40° of convex curvature with strength $\frac{\delta}{R_w} \simeq 0.09$. To compute the streamwise variation of the kinetic energy, they used the following model for isotropic turbulence decay

$$\frac{q^2}{q_0^2} = (1 + \frac{5t\epsilon_0}{3q_0^2})^{-\frac{6}{5}} \tag{8.13}$$

where t is the time, equal to $\frac{\Delta s}{U}$, and ϵ_0 is the initial value of the turbulent dissipation. An attempt was made to compute the kinetic energy by using the exponential growth laws from TK and HT,

$$\frac{q^2}{q_0^2} = e^{\kappa_q \Delta \tau} \tag{8.14}$$

where κ_q is equal to 0.1 when the flow is straight and is given by equation 7.9 when the flow is curved. A much better agreement with the measurements is found as can be seen from Figure 8.5.

8.3 Adjustment of Turbulence Structure to a Step Change in Curvature

In engineering applications, such as flow over airfoils or wings, the extent of curved regions is generally limited. Therefore, prediction of the adjustment of the turbulence structure to curvature is of practical importance. Bradshaw (1973) suggested an adjustment length of 10δ for boundary layers subjected to a step change of an extra strain rate. It was shown earlier that for curved uniformly sheared nearly homogeneous flow the adjustment depended on the strength of curvature. A comparable behavior could be expected for curved turbulent boundary layers. Calculation methods for curved turbulent boundary layers could be improved by introducing an expression accounting for the adjustment of flow structure to curvature.

Bradshaw and his coauthors compared the behavior of convex and concave turbulent boundary layers. Hoffmann, Muck and Bradshaw (1985) and Muck, Hoffmann and Bradshaw (1985) argued that the speed of transient response to convex curvature is much greater than the speed of transient response to concave curvature, which was estimated to be one order of magnitude slower. The interpretation given was that the mechanisms involved in both cases are fundamentally different: convex curvature implies only attenuation of the eddy structure, while concave curvature implies its reorganization. It should, however, be mentioned that in their experiments in the concave boundary layers, these authors introduced artificial disturbances into the boundary layer to trigger a regular, steady vortex pattern, which was amplified by the unstable concave curvature. A contradicting conclusion was reached by Shizawa and Honami (1983), who reported a weaker spanwise variation and concluded that the mean flow and Reynolds stresses responded quickly to concave curvature. In curved homogeneous flow, for small values of S, the dependence of the time of adjustment on the sign of S could be ascertained, while for large values of S, the results of HT1 implied that the time of adjustment in stabilizing cases was slower than that in the destabilizing ones. The significant and continuous streamwise variation of S in concave boundary layers might be one of the fundamental reasons preventing these flows from attaining asymptotic states.

Another important point to make is that, as mentioned by Shizawa and Honami (1983), the turbulence structure starts adjusting to curvature before the start of the geometric curvature. Unfortunately no measurements at the start of curvature have been reported by other investigators so that it is not possible to confirm this point.

It is expected that near the wall the flow attains self-preservation much faster than in the outer layer, where S is much larger (Alving and Smits, 1986, and Smits and Wood, 1985). This led Alving and Smits (1986) to conclude that the response to curvature would be slow, where its effects are strong, which contradicts our finding (equation 7.18) for nearly homogeneous flows. In Figure 8.6-a, an estimated time constant T, is plotted versus ξ for different values of $\frac{\delta}{R_w}$, by using equation 7.18 and assuming a power law velocity profile.

A faster response of turbulence in the wall region than in the outer region does not contradict the proportionality of $\frac{1}{T}$ to $|S|$, if one observes that T is defined as the real response time multiplied by the mean shear, $\frac{\partial \overline{U}}{\partial n}$, and that near the wall the mean shear is many times higher than in the outer region. In Figure 8.6-b the time response to curvature, $t = \frac{T}{|\frac{\partial U}{\partial n}|^{-1}}$, is plotted versus ξ by assuming a power law profile. It should also be mentioned that one should expect differences in behavior of inner and outer regions of boundary layers, even if they were subjected to the same ratio of strain rate. For the outer regions of two boundary layers having similar mean shear and subjected to curvatures of different strengths, one would expect the one subjected to stronger curvature to respond faster. This is confirmed by Figure 8.6-b. Also, if one for example compares the measurements of Hoffmann, Muck and Bradshaw (1985) to those of Barlow and Johnston (1988a) from Figure 8.3, it can be seen that the latter ones, which were subjected to stronger curvature, seem to adjust faster than the former ones.

Chapter 9

Conclusions

9.1 Curved Nearly Homogeneous Uniformly Sheared Flow

The following conclusions can be drawn from analysis of the measurements of the present investigation

- Nearly asymptotic values of the shear stress structural parameter and the kinetic energy growth coefficient were reached for every subsection independently of the previous history of the flow and were in agreement with measurements of HT1. The curvature reversal does not seem to have a strong effect on the asymptotic structure of the flow.

- The adjustment of the shear stress structural parameter to curvature can be described by a first order system.

- The adjustment of the structure of a nearly homogeneous shear flow subjected to a stepwise change of curvature depends on both the initial and new values of S for low values of S.

- The structure of rectilinear nearly homogeneous shear flow subjected to stepwise curvature adjusts faster for stronger curvature.
- Spectral analysis showed that the large scales adjust at different rates for positive or negative S. For the values of S examined in the present investigation, the coherence function of the large eddies adjusts faster for negative S.

9.2 Comparison to Curved Turbulent Boundary Layers

The following conclusions can be drawn from the comparison to curved turbulent boundary layers:

- The transverse and streamwise variations of the ratio of the extra strain rate to the mean shear in curved turbulent boundary layers can be used to explain the differences in behavior between the inner and outer parts of the boundary layer and between convex and concave boundary layers.
- The discrepancies between measurements in concave boundary layers can be attributed mainly to the effect of longitudinal vortices, which depend strongly on upstream nonuniformities of the flow. It is felt that an experimental investigation on concave boundary layers, where the upstream nonuniformities are minimized to avoid the appearance of strong rod cell vortices and where the wall radius of curvature is varied in the streamwise direction to accommodate

the fast growth of the boundary layer thickness and to keep a nearly constant S, will be useful for quantitative comparison with the development of convex boundary layers and with the curved homogeneous flow.

- Similarly to the results of the curved homogeneous flow, the results of convex turbulent boundary layers were consolidated in a linear variation of K_{uv} versus S (or $\frac{\delta}{R_w}$) for weak and moderate curvatures.

- Similarly to the curved homogeneous flow, the measurements reported in the literature suggest that the stronger the wall curvature is, the faster the turbulence structure of the boundary layer would respond.

Part B:

Chapter 10

Introduction

Considerable attention was given by many researchers to the prospects of using a LEBU to alter the outer region of turbulent boundary layers for drag reduction purposes or other applications such as heat transfer, noise and reduction of wall pressure fluctuations. Understanding of the mechanisms responsible for skin friction reduction and other effects of the LEBU is essential for its potential use.

The effects of the wake of the LEBU are believed to be of primary importance. For instance, it is well established that maximum local skin friction reduction on the wall is located at the region where the wake boundary contacts the wall and that small eddies generated in the wake have the effect of reducing the energy of the large scales. The wake of the LEBU is also believed to cause isolation of the inner part of the boundary layer from the outer part. Finally, a pocket of velocity deficit in the wake is convected towards the wall as the wake grows, causing a reduction of the velocity gradient near the wall and, consequently, of wall shear stress.

Beside the "wake" effects, the other most commonly reported possible mechanisms responsible for downstream skin friction reduction on the wall are:

- Direct effects linked to the presence of the LEBU, such as the breakup of large eddies, which are responsible for momentum transfer to the wall, and the inhibition of their vertical velocity fluctuations.

- The so called "unwinding effect", described as being the phenomenon by which an eddy convected past the LEBU causes a counterrotating eddy to be generated at the trailing edge. The latter eddies are responsible for uplifting material from the wall, thus reducing the instantaneous velocity gradient, $\frac{\partial U}{\partial n}$, and consequently the wall shear stress.

In this investigation, an attempt was made to understand the structure and development of the wake of a LEBU in a boundary layer, by examining the behavior of the wake of a thin ribbon developing in a nearly homogeneous, uniformly sheared, turbulent flow. Detailed mean flow and turbulence measurements are performed. The possibility of self similarity of this wake is investigated and a comparison to the wake of a LEBU in a boundary layer is undertaken.

Engineering applications of LEBU's often involve placing them in curved turbulent boundary layers, as in flows over airfoils or wings. To investigate the development of the wake in curved free stream shear flows, the ribbon will be placed in the curved section of the facility described in Part A. Two opposite orientations of the mean shear with respect to curvature will be used to produce "stable" and "unstable" flows, which correspond to convex and concave boundary layers, respectively.

The use of a LEBU for drag reduction does not appear very promising, due to the difficulty in compensating for the device's drag. However, the use of LEBU's for reduction of noise pressure fluctuations and heat transfer still appears feasible, providing the present investigation with some practical justification. Besides, the development of a thin wake in uniformly sheared turbulence possesses some intrinsic interest on its own, as it is subject to the interaction of two distinct turbulence production mechanisms with different scales.

Chapter 11

Literature Review

The credit of inspiring the idea of wall skin friction reduction by manipulation of the outer region of the boundary layer is commonly attributed to Yajnik and Acharya (1977), who positioned wire-mesh screens within a turbulent boundary layer (parallel to the wall) and measured local skin friction reduction downstream of the screens.

Despite the excessive drag on the screens themselves, reported in the same study, this work motivated the research group of the High-Speed Aerodynamics Division of NASA Langley (Hefner, Weinstein and Bushnell, 1980) to seek out new methods for drag reduction based on the use of different devices. This group confirmed a reduction of local skin friction on the wall by using different devices, including fins mounted on the walls at different angles, parallel plates and spanwise grooves, and reported an up to 24% reduction in skin friction downstream of the devices. In the mean time, Corke, Guezennec and Nagib (1980) placed parallel stacked plates in a boundary layer with the idea of manipulating the turbulence structure for drag reduction purposes.

Following these attempts, the simpler, thin flat plate manipulators (ribbons), were favored because they generated lower added drag. Thin plates were tested by many investigators in different configurations inside the boundary layer in efforts to achieve the highest possible skin friction reduction. Among these investigations are those of Corke, Nagib and Guezennec (1982), Nguyen et al. (1984), Mumford and Savill (1984), Anders, Hefner and Bushnell (1984), Lemay et al. (1985), and Plesniak and Nagib (1985). The above investigations included parametric studies to determine the optimum configurations of LEBU in the outer boundary layer for maximum skin friction reduction. It was concluded that the ribbon should be thin to reduce the device's drag (around 0.1mm), it should have a chord length close to the boundary layer thickness ($\frac{c}{\delta} \simeq 0.8 - 1.2$), and that it should be placed at a distance from the wall, $\frac{h}{\delta} \simeq 0.3 - 0.8$. The tandem configuration was favored because the drag of the second ribbon was reduced as it was placed in the wake of the first one. The optimum distance between the two ribbons was reported to be between 6δ and 10δ.

After it was well established that LEBU's cause a reduction in local skin friction, attention was turned to the possibility of using other devices to avoid the technical problems associated with the use of thin flat ribbons. NACA airfoil-shaped manipulators were used by many researchers, among which are Anders and Watson (1985), Bandyopadhyay and Watson (1987), Bonnet, Delville and Lemay (1988) and Coustols, Cousteix and Belanger (1987), and proved to give, in general, a satisfactory performance. Although these airfoils were much thicker than flat ribbons (sometimes 10 times) and thus caused larger skin friction drag, they had the advantage of rigidity, which increased the feasibility of using them in actual flight conditions.

Positioning a manipulator at a small angle of attack with respect to the free stream was believed to improve its performance. This was discussed by Corke, Nagib and Guezennec (1982), Anders, Hefner and Bushnell (1984), Plesniak and Nagib (1985), Bandyopadhyay and Watson (1987) and Bonnet, Delville and Lemay (1988).

The literature has revealed several discrepancies among the reported results of skin friction measurements. Anders (1986) argued that the most important source of discrepancy was that, at the relatively low Reynolds numbers (40,000 to 100,000) at which most of the experiments were carried out, the performance of thin plates was inconsistent, due to unsteady separation and transition of the device's boundary layer, similar to the behavior of airfoils at this range of Reynolds numbers. He also argued that because at flight conditions the device's chord Reynolds number would normally be greater than 300,000, the applicability of the previous data would be limited. Additional errors have been attributed to the skin friction measurement techniques (Nguyen et al., 1984). Many researchers used the momentum balance method, which is known not to be very accurate. Others used the Preston tube method, which is based on the law of the wall, while Nguyen et al. (1984) found that the law of the wall may be inapplicable, at least close to the manipulator, where the boundary layer is not in equilibrium. In conclusion, it seems that the most reliable method would be the direct measurement of skin friction. The discrepancies in skin friction measurements led to contradicting conclusions regarding the possibility of achieving net drag reduction by use of LEBU. Early researchers have claimed the achievement of net drag reduction (Corke, Nagib and Guezennec (1982), Anders, Hefner and Bushnell (1984), Anders and Watson (1985), Plesniak and Nagib (1985) and may others). However, the above investigations inferred net drag reduction from a momentum balance, which as mentioned earlier is not a very accurate technique. Later studies used direct skin friction measurements. Nguyen, Savill and Westphal (1987) suggested that one should not expect significant net drag reduction from boundary layers manipulated by flat ribbons; Sahlin, Johansson and Alfredsson (1988) conducted measurements in a towing tank and reported no net drag reduction, while Poll and Westland (1987) studied the LEBU performance by direct total force measurements and did not record any net drag reduction.

Flight tests of LEBU were carried out by Berterlud (1984), who mounted ribbons on the wing of a SAAB A32 LANSEN airplane and reported a 10 to 15% local skin friction reduction. Berterlud and Watson (1987) reported that no serious technical problem, such as vibration or shock waves, would prevent the use of these devices in actual flight. Among the few high-speed studies of LEBU is the one by Bonnet, Delville and Lemay (1988), who used NACA profile manipulators in transonic boundary layers.

Besides skin friction reduction LEBU have other potential applications, such as heat transfer and noise reduction. Lindeman (1986) and Trigui and Guezennec (1992) reported skin friction and heat transfer reductions in manipulated turbulent boundary layers. The skin friction reduction was more important than heat transfer reduction, suggesting that the Reynolds analogy would not apply to manipulated boundary layers. Beeler (1986) and Coustols and Cousteix (1988) reported that skin friction reduction was accompanied by a reduction in the turbulent wall pressure fluctuations, which is beneficial for reducing fuselage vibration. In a theoretical investigation, Dowling (1989) also reported decay of pressure fluctuations and reduction of flow noise downstream of the LEBU.

The early investigations on manipulation of boundary layers by thin ribbons suggested that the main mechanism behind skin friction reduction is the break-up of the large eddies responsible for momentum transfer to the wall (Hefner, Weinstein and Bushnell (1980), among others), from which the name LEBU (Large Eddy Break-Up devices) is derived. Flow visualization by Mumford and Savill (1984) on the wake of the ribbon in a boundary layer gave detailed qualitative descriptions of the wake development and structure. These authors later suggested (Savill and Mumford, 1988) that the wake of the ribbon plays a major role in skin friction reduction and that the name LEBU should be substituted by a more meaningful name such as "manipulators". Even though it has by now been agreed that the wake plays a dominant role in skin friction reduction, the name LEBU is still frequently used. In recent years many investigations were carried out with the main objective to understand the physical structure of the wake of the LEBU. Such investigations, reporting flow visualization results and turbulence measurements, include those of Blackwelder and Chang (1986), Falco and Rashidnia (1987), Coustols, Cousteix and Belanger (1987), Coustols and Cousteix (1988 and 1989), Coustols, Tenaud and Cousteix (1989), Savory and Wisby (1989), Bonnet, Delville and Lemay (1987), Lemay (1989) and Lemay, Delville and Bonnet (1990).

The papers by of Blackwelder and Chang (1986), which report mean flow and length scales measurements, and those of Coustols, Coustei and Belanger (1987), Bonnet, Delville and Lemay (1987) and Lemay (1989), which report mean flow, Reynolds stresses and spectra measurements, will be used for comparison with the present measurements.

Some attempts have been made to study the effects of LEBU on boundary layers in the presence of a pressure gradient. Savill (1987) found that the maximum C_f reduction was delayed and increased with the presence of moderate adverse pressure gradients. Veuve, Truong and Ryhming (1987) found that the presence of an adverse pressure gradient did not alter qualitatively the mechanisms of C_f reduction, but played an amplification role on the long distance effects of the manipulator.

Bandyopadhyay (1985), Pineau, Nguyen and Dickinson (1987) and Nguyen et al. (1989) studied LEBU manipulated boundary layers over rough surfaces.

Finally, several attempts to model the manipulated boundary layers theoretically have been reported, among which one could mention those by Dowling (1985 and 1989), Balakumar and Widnall (1986), Klein and Friedrich (1989), Roach (1987a and 1987b), Savill (1987), Tenaud, Coustols and Cousteix (1987) and Coustols, Tenaud and Cousteix (1989).

Chapter 12

Experimental Apparatus and Instrumentation

12.1 The Wind Tunnel

The wind tunnel, the shear generator and the curved section used in this part were described in detail in Part A (section 5.1).

A nearly uniform, homogeneous shear flow was produced in this tunnel with $k_s = \frac{1}{U_c}\frac{d\overline{U}}{dn} \simeq 6.8m^{-1}$. The centerline speed was around $8.6m/s$ in the straight tunnel.

12.2 Choice and Mounting of the Ribbon

For a meaningful comparison of the present results to measurements in boundary layers, the dimensions of the ribbon to be used were chosen by analogy to those used in boundary layers. Parametric studies in the literature revealed that the chord length of the ribbon should have a value close to the boundary layer thickness. On the other hand it is believed that the break-up of the large eddies is an important factor in skin friction reduction caused by the LEBU. It is also known that the integral length scales in the boundary layer are of the same order of magnitude as the boundary layer thickness. So, for the present study, the chord length of the ribbon was scaled with the integral length scales characterizing the present flow. Lemay et al. (1989) showed that thin and thick ribbons exhibit the same effects on boundary layers, despite the fact that thicker ribbons are associated with larger device drag. In the present investigation no net drag is sought, so thicker ribbons will be favored to avoid technical complications, such as twisting of the ribbons, which might affect the flow. A flat ribbon of width 12.5mm compared to the streamwise integral length scale of $L_{uu} \simeq 10mm$ at the position of insertion of the ribbon in the straight section, and thickness 0.5mm was selected.

Figure 12.1 shows the mounting positions of the ribbon in the straight and curved sections of the wind tunnel. Also shown in this figure is the (s,n) system of coordinates, used in this investigation, in which the s coordinate coincides with the geometric centerline of the test section. The distance s_g is defined as the distance from the shear generator at which the ribbon is inserted.

When the ribbon is placed at the begining of the curved section ($s_g = 3433mm$), the wake develops in a "destabilizing" or "stabilizing" free stream, depending on whether the flow enters the curved section with positive or negative mean shear rate, $\frac{\partial U}{\partial n}$, respectively. The curvature parameter ($S = \frac{\frac{U}{R_c}}{\frac{\partial U}{\partial n}}$), which characterizes the strength of curvature with respect to mean shear, has a value around 0.05 or -0.05

for "stabilizing" or "destabilizing" flows, respectively. When the ribbon is placed at $s_g = 4093mm$, its wake develops in a reversing curved free stream flow.

For insertion in the straight section, the ribbon is fixed to a frame shown in Figure 12.2-a which permits the adjustment of angle of attack of the ribbon. Threaded mounts fastened on the side walls of the curved section (Figure 12.2-b) were designed to support the ribbon in the curved section.

12.3 Instrumentation

12.3.1 Hot wires

In the present investigation, hot wire anemometry is used as the main measurement technique. A commercial single wire probe was used for measurements in the near wake. The sensor has a diameter of $5\mu m$ and a length of $1.2mm$. A commercial cross wire probe was used for measurements further downstream. The sensors have a diameter of $5\mu m$ and a length of $0.6mm$, they are inclined 45^o with respect to the probe axis and they are $0.8mm$ apart.

12.3.2 Signal processing and data acquisition

The instrumentation used for signal conditioning and data acquisition has been described in Part A (section 5.3). The hot wires were operated at constant temperature by two constant temperature bridges (TSI model 1050 A, used in connection with a TSI 1051-2D monitor and power supply). A four channel analog to digital converter (Data Translation DT 2828) was used in connection with a microcomputer system (1800, IBM AT compatible).

The procedure adopted in Part A for signal conditioning and discretization was also used in Part B. Briefly, the signal from the anemometer was low pass filtered at 10kHz and digitized at two sampling frequencies, 25kHz and 2kHz. 50 records of 2048 samples were recorded at each position and for each frequency.

12.4 Computational Procedure

The different moments and length scales were computed from the discretized data as described in Part A (section 5.5). Only the data records digitized at 25kHz were used to compute the spectra. From previous investigations it is expected that small energetic eddies will be generated in the wake of the ribbon. Using the records digitized at 2kHz, which were not filtered at the proper Nyquist frequency, will result in contamination of the spectra at the low frequencies by energy fed from the high frequencies corresponding to the wake generated eddies.

Chapter 13

Measurements

13.1 Thin Wake in Rectilinear Shear Flow

13.1.1 Single wire measurements in the near wake

The centerline velocity before insertion of the ribbon was equal to about $8.6m/s$ and varied by less than 5% in the streamwise direction, while the shear constant, $k_s = \frac{1}{U}\frac{\partial \overline{U}}{\partial n}$, was around $6.8m^{-1}$.

Cross-wire anemometry has a relatively poor spatial resolution in the near wake of the ribbon. For this reason, single wire measurements of the streamwise mean velocity and fluctuations were conducted as best suited to the early stages of formation of the wake.

Transverse profiles of the streamwise mean velocity, taken above, below and at close distances downstream of the ribbon, placed at a distance $s_g = 1405mm$ from the shear generator, are shown in Figure 13.1-a along with the profiles taken at the same positions without the ribbon. These velocities are nondimensionalized with the nonmanipulated (without the ribbon) centerline mean velocity, U_{co}, at $\frac{x}{c} = 0$.

The profiles taken above and below the ribbon, corresponding to a distance $\frac{x}{c} = -0.4$ from the trailing edge, show that the flow accelerated towards the high velocity side. Such asymmetry in streamline displacement can be attributed to shear, as already observed in flows about pressure tubes (Tavoularis and Szymczak, 1989).

The downstream profiles in Figure 13.1-a show the velocity deficit due to the blockage of the flow by the ribbon. In Figure 13.1-b the streamwise Reynolds stresses corresponding to the profiles in Figure 13.1-a are presented; they show a high peak, associated with the turbulence in the boundary layers on the ribbon's surfaces. This peak was attenuated downstream and spread in the transverse direction, as the boundary layers from the two surfaces of the ribbon merged.

13.1.2 Cross wire measurements of mean velocity and Reynolds stresses

Transverse profiles of the streamwise mean velocity and the Reynolds stresses are shown in Figure 13.2. These quantities are nondimensionalized with U_{co}. The corresponding profiles in the absence of the ribbon are also shown in the same figures. The Reynolds stresses in the nonmanipulated profiles grew in the streamwise direction and presented a good degree of homogeneity in the transverse direction. The manipulated profiles show that, although the mean velocity deficit was practically invisible beyond a streamwise distance $\frac{x}{c} = 32$, the wake's effects on the turbulent stresses persisted up to at least $\frac{x}{c} = 80$.

The developments of the mean velocity and Reynolds stresses show that, near the ribbon, at $\frac{s}{c} = 4.6$ (and further upstream, if one considers single wire measurements), and towards the low velocity side, there was a region where the local mean shear direction was opposite to the free stream shear direction and where the shear stress reversed sign, in general conformity with gradient transport. Further downstream, the mean shear in the wake towards the low velocity side was lower than the mean shear in the free stream. The reduction of the shear is associated with lower production of turbulence, causing regions of Reynolds stress deficit. Towards the high velocity side, there was a region of higher mean shear and consequently higher production of turbulence. This created a peak of high turbulence intensity, in excess of the turbulence intensity of the nonmanipulated profiles. The peak of Reynolds shear stress disappeared at $\frac{s}{c} = 8.6$ and those of normal stresses became imperceptible at $\frac{s}{c} = 32$; however, the regions of deficit of all the stresses were still apparent at $\frac{s}{c} = 80$.

13.1.3 Measurements of integral and Taylor lengthscales

The developments of the transverse profiles of the integral length scales, L_{uu} and L_{vv}, and the streamwise Taylor microscale, λ_{uu}, are shown in Figure 13.3. The Taylor hypothesis was used to determine these length scales from the corresponding time scales. For the nonmanipulated profiles, the integral length scales grew in the streamwise direction and presented a good degree of transverse homogeneity, while the Taylor microscales remained almost constant, in agreement with the results of TK. All scales were reduced below their nonmanipulated values in the wake of the ribbon. The reduction in the integral length scales L_{uu} and L_{vv}, was visible up to the last measuring station at ($\frac{s}{c}$ = 80), while the Taylor microscales, λ_{uu} and λ_{vv}, practically regained their free stream values beyond $\frac{s}{c} = 32$.

13.1.4 Measurements with inclined ribbon

Transverse profiles of streamwise mean velocity and Reynolds stresses behind the ribbon, inclined at positive and negative angles of $\pm 3°$, with respect to the centerplane, are shown in Figures 13.4 and 13.5 respectively. Such inclinations did not seem to have a large effect on the mean flow or the Reynolds stresses in the present experiments.

13.2 Thin Wake in Curved Shear Flow

For measurements in the straight section, the ribbon was mounted on a fixed frame, which could easily be inserted in special slots of the tunnel. However, for measurements in the curved section, the ribbon had to be mounted at its two ends on the tunnel walls and then oriented as accurately as possible. Due to this requirement, the entire sets of measurements of manipulated profiles were first taken with the shear generator both in its upright and inverted orientations and then the ribbon was removed and measurements of the nonmanipulated profiles were performed. This resulted in considerable delay between sets of measurements and possibly caused minor differences in the tunnel speed and the mean shear. Thus, measurable discrepancies between the "free streams" of the manipulated and the corresponding nonmanipulated profiles were observed. To reduce these differences, the mean velocities and

Reynolds stresses of the manipulated profiles were nondimensionalized with U_c, a local centerline velocity interpolated from the values at the free stream, rather than with U_{co}, as was the case for the measurements in the straight section. The nonmanipulated profiles were nondimensionalized with the local centerline velocity at the considered station.

The development of transverse profiles of the mean velocity and the Reynolds stresses in the wake of the thin ribbon in "destabilized" and "stabilized" curved shear flows are shown in Figures 13.6 and 13.7 respectively. For these measurements, the ribbon was positioned at $s_g = 3433mm$ from the exit of the shear generator.

Curvature effects on the free stream and on the nonmanipulated profiles are clear from these figures, causing an enhancement of the turbulent stresses growth when the shear has a sign opposite to that of curvature, and its suppression when shear has the same sign as curvature, compared to the rectilinear shear flow.

Measurements of the mean velocity and the Reynolds stresses were also taken behind the ribbon placed at a distance $s_g = 4093mm$ from the exit of the shear generator. These are shown in Figures 13.8 and 13.9, nondimensionalized with the centerline mean velocity, U_{co}, at $\frac{z}{c} = 0$, corresponding to the nonmanipulated flow. At this position, it was established from part A that the flow had reached its nearly asymptotic structure. The first set of profiles (closest to the ribbon) in Figures 13.8 and 13.9 can be compared to corresponding profiles in Figures 13.6 and 13.7, in order to assess the effect of the degree of development of "free stream" turbulence structure upon the wake. The two other profiles correspond to positions where the curvature reversed direction and could be analyzed to document that effect.

13.3 Spectral Measurements of Wake in Rectilinear Shear Flow

Figures 13.10, 13.11 and 13.12 present measurements of the streamwise and transverse one-dimensional frequency spectra at selected positions across the wake, at the streamwise positions $\frac{x}{c}$ = 4.6, 8.6 and 32, respectively. As was discussed previously, only signals digitized at 25 kHz were used to calculate these spectra, which caused considerable uncertainty of the measurements in the lower frequency range. Figure 13.10 shows that at $\frac{x}{c} = 4.6$, the energy corresponding to the large scales in the wake was lower than the corresponding values in the nonmanipulated flow, while a peak of high energy at the small scales was observed in the wake only. Figure 13.11 shows that the energy peak associated with the small scales was considerably attenuated at $\frac{x}{c} = 8.6$. At $\frac{x}{c} = 32$, as can be seen from Figure 13.12, it is remarkable that the attenuation of the large scales persisted, while the energy peak of the small scales was imperceptible.

Chapter 14

Analysis and Discussion of Measurements

14.1 Thin Wake in Rectilinear Shear Flow

The behavior of the mean flow and the Reynolds stresses in the wake of the ribbon, developing in a rectilinear shear flow, is in general qualitative agreement with the behavior of these quantities in the wakes of LEBU in manipulated turbulent boundary layers, presented by Lemay (1989), Blackwelder and Chang (1986) and Coustols, Cousteix and Belanger (1987), among others. The present wake, similar to wakes of LEBU in turbulent boundary layers, presents a faster growth towards the low velocity side. This behavior can be attributed in part to the higher molecular diffusion at the lower velocities. Furthermore, based on an examination of the momentum equation in the streamwise direction, Lemay (1989) argued that the strong negative gradient of $-\overline{uv}$, present on the low-speed side of the wake, induces a pumping effect on the velocity deficit towards the wall.

In accordance with measurements in manipulated boundary layers, peaks of normal stresses, having values higher than the corresponding values of the non-manipulated profiles, were present at stations close to the ribbon, where also the shear stress profiles showed some asymmetry, with high values towards the high velocity side and low values towards the low velocity side. The excesses of normal and shear stresses disappeared quickly downstream, while the deficits of these quantities persisted at further distances. This behavior is most probably due to the different sizes of the eddies involved in these processes and will be further discussed in the spectral analysis (section 14.4).

The behavior of the integral length scales shows some differences from those in manipulated boundary layers. Lemay (1989) found that the values of L_{uu} were reduced in the near wake, grew rapidly to match the nonmanipulated values at an intermediate stage of the wake and then they showed a reduction compared to their values in the nonmanipulated profiles further downstream. Blackwelder and Chang (1986) also found that the values of L_{uu} were reduced downstream of the LEBU, showed some increase over those of the nonmanipulated values at an intermediate stage of the wake development close to the wall and then their values were reduced further downstream. While in the latter two studies L_{uu} shows some increase over the corresponding values in the nonmanipulated flow at a certain stage in the development of the wake of the LEBU, persistent decrease of the values of L_{uu} below the nonmanipulated values was observed for the present wake. The difference might be due to the presence of the wall for the manipulated boundary layers. Similar to what has been reported for manipulated turbulent boundary layers (Blackwelder and Chang, 1986), the integral length scales deficit has a slower rate of decay in the streamwise direction, compared to the mean velocity and Taylor microscale deficits.

In the following section, a quantitative comparison between the mean flow development in the wake of the ribbon in uniformly sheared flow and that in the outer region of turbulent boundary layers will be attempted.

14.2 Test of Self Similarity of the Wake

The development of two-dimensional, symmetric wakes in a uniform, non-turbulent free stream has been well documented. A self similar solution for the flow is available and appears to describe the wake development well. In this solution, it is assumed that the streamwise mean velocity $\overline{U}$ and the Reynolds shear stress $-\overline{uv}$ can be expressed, respectively, as

$$\frac{\overline{U}_\infty - \overline{U}}{\overline{U}_s} = f(\frac{n}{l}) \tag{14.1}$$

$$-\frac{\overline{uv}}{\overline{U}_s^2} = g(\frac{n}{l}) \tag{14.2}$$

where $\overline{U}_\infty$ is the free stream velocity and $\overline{U}_s$ is the maximum velocity deficit in the wake; the functions f and g are assumed to depend only on the ratio of the transverse position in the wake n to its half width l which is assumed to be a function of the streamwise position, s, only. In addition, the gradient transport assumption

$$-\overline{uv} = \nu_T \frac{\partial \overline{U}}{\partial n} \tag{14.3}$$

is used, and the eddy viscosity, ν_T, is assumed to be constant across the wake. Solutions for the maximum velocity deficit, $\overline{U}_s$, and the wake half width, l, are obtained as

$$U_s = as^{-\frac{1}{2}} \tag{14.4}$$

$$l = bs^{\frac{1}{2}} \tag{14.5}$$

where a and b are constants.

The effect of free stream turbulence on the wake development and its self similarity have been investigated, among others, by Pal and Raj (1981), who found that free stream turbulence increases the wake recovery and growth rates. A self similar solution was obtained by modifying equation 14.1 with the introduction of two parameters, ϕ_1 and ϕ_2, which depend on the turbulence level of the free stream and on the streamwise distance s as

$$\frac{\overline{U}_\infty - \overline{U}}{\overline{U}_s \phi_1} = f(\frac{n}{l\phi_2}) \tag{14.6}$$

The effect of low free stream shear on the wake self similarity has also been investigated. Ahmad, Luxton and Antonia (1975) performed measurements of the development of the wake of a flat plate in weakly sheared flow ($k_s = \frac{1}{U_c}\frac{\partial \overline{U}}{\partial n} \simeq 1.25m^{-1}$), and concluded that the low shear used did not affect seriously the self similarity of the wake. These authors also reported that for the low value of shear they used in their experiments the wake exhibited a faster growth towards the high velocity side, contrary to what has been observed in the present wake.

The present wake is a complicated one, where no self-similar solution can be expected, because there is a continuous change in the turbulence of the free stream, unrelated to the wake development. An attempt has been made by Roach (1989a and 1989b) to calculate the mean flow characteristics of manipulated boundary layers by superimposing a symmetric wake and uniform shear. The gradient transport assumption was used and good agreement with experimental results was reported.

The present measurements are suitable for checking such calculation methods. In the following, the evolution laws of the maximum velocity deficit, $\overline{U}_s$, and the wake half width, l, in the present measurements will be compared with corresponding expressions based on thee experiments of Blackwelder and Chang (1986), Lemay (1989) and Coustols, Cousteix and Belanger (1987).

Some characteristic parameters of the ribbons and flows in the different experiments to be compared are listed in Table 14.1.

In order to consolidate the present results and those in manipulated turbulent boundary layers, a proper scale for the streamwise development is required. In Figures 14.1-a and 14.1-b, the maximum velocity deficit is plotted versus the streamwise distance s nondimensionalized respectively by the chord length c of the ribbon and twice the momentum thickness θ, of the boundary layer at the trailing edge of the ribbon. The momentum thickness θ has been recommended as a length scale for low deficit wakes (Wygnanski, Champagne and Marasli, 1986), and Figure 14.1-b shows that the differences between the different sets of data were reduced when this parameter was used for nondimensionalization. To estimate θ, the boundary layers on the ribbon were assumed to be laminar. From Figure 14.1-b, an average decay exponent of -0.67 was estimated using all data presented, collected in flows with free stream turbulence intensities between 5% and 7% at the trailing edge of the ribbon. Compared to the typical value of -0.5 in low-turbulence flows, this shows, in accordance with the results of Pal and Raj (1981), that free stream turbulence enhances the decay rate of the maximum velocity deficit. These authors reported an exponent of -0.62 for a free stream turbulence intensity of 4% at the trailing edge of their flat plate. It should be noted, however, that in the experiments of Pal and Raj (1981) the free stream turbulence was decaying, and grid-generated, while the free stream turbulence in the present experiments was growing as a result of continuous production by the mean shear.

As was discussed earlier, the wake grew deeper into the low velocity side. This introduces a difficulty in defining the half width of the wake. An attempt was made to determine l by measuring the distance between the two locations at which the velocity deficit was equal to 50% of its maximum value. The results from the present measurements and those of Lemay (1989) and Coustols, Cousteix and Belanger (1987) are shown in Figure 14.2. The wake growth rates for the present measurements and for the two boundary layer experiments were comparable. The data points close to the ribbon were not used as they are more likely to be dependent on the ribbon geometry. Close to the ribbon, the relatively high values of l for the measurements of Coustols, Cousteix and Belanger (1987) are likely to be due to the much larger thickness of the airfoil they used, compared to the present ribbon and the one used by Lemay (1989).

An average exponent of 0.53 is estimated for the rate of growth of the presented data. This is compatible with the conclusion of Pal and Raj (1981) that free stream turbulence causes the wake to grow faster.

The Reynolds stresses are more difficult to scale, first because they reach their asymptotic development laws (if such exist) much slower than the mean velocity (Tennekes and Lumley, 1973, p. 115), and second because of the strong asymmetry in the stress profiles of the present wake. It can also be seen from Figure 13.2 that the alteration of the Reynolds stresses extends further in the transverse direction than the region of visible mean velocity deficit.

14.3 Test of Gradient Transport in the Wake of the Ribbon

A condition for the applicability of gradient transport models (GTM) to a shear flow is that the characteristic scale of the turbulent transporting mechanism be small compared with the characteristic dimension of the inhomogeneity of the mean transported quantity (Sreenivasan, Tavoularis and Corrsin, 1981). Strongly inhomogeneous flows generally violate this condition, although in certain inhomogeneous flows that exhibit geometrical symmetry GTM show some degree of success. Roach (1989a and 1989b) employed the gradient transport assumption to calculate the mean flow characteristics of manipulated boundary layers by superposition of a wake and uniformly sheared flow, and found a good agreement with experimental results. Therefore, it seems worthwhile to check the applicability of GTM to the present wake. To pursue this objective, the Reynolds shear stress, $-\overline{uv}$, has been plotted in Figures 14.3 to 14.8 at different stations downstream of the ribbon, versus the mean velocity gradient, $\frac{\partial \overline{U}}{\partial n}$, obtained by fitting polynomial curves through the measured mean velocity profiles. Also shown in these figures are the corresponding profiles of $\overline{U}$, $-\overline{uv}$ and $\frac{\partial \overline{U}}{\partial n}$. For the GTM to apply, plots of the shear stress vs the mean gradient should collapse on a curve passing through the origin. If this curve were a straight line, the eddy viscosity would be a constant. Figure 14.3, corresponding to $\frac{s}{c} = 4.6$, shows the inadequacy of the gradient transport assumption at this station. The curve forms a loop, which starts at points corresponding to the free stream towards the low velocity side, and then closes again towards the high velocity side. This curve suggests that there are two regions, one towards the low velocity side and the other towards the high velocity side of the wake, in which momentum is transported in a direction opposite to that of the mean shear (regions where $\frac{\partial \overline{U}}{\partial n}$ and $-\overline{uv}$ are of opposite sign). Another characteristic of the loop, more clear at $\frac{s}{c} = 8.6$ as can be seen from Figure 14.4, is that it crosses itself, thus bringing its two sides closer to each other. Figures 14.3 to 14.8 show that the loop gets smaller at further distances downstream and opens up as the wake expands in the transverse direction. At the last measuring stations, the curve approaches a straight line, which can be extrapolated to cross the origin, implying a better applicability of the GTM. An average line, passing through the origin has been fitted casually (namely without the use of a fitting algorithm, which may have introduced bias towards locations in which more measurements are available) to each set of data of $-\overline{uv}$ vs $\frac{\partial \overline{U}}{\partial n}$, in Figures 14.3 to 14.8. Average values of the eddy viscosity ν_T obtained from the slopes of the drawn lines, are plotted in Figure 14.9 versus the streamwise distance. Also shown in this Figure is ν_T obtained from the nonmanipulated flow. TK (1989) showed that, for the nearly homogeneous uniformly sheared flow, nondimensionalization with the integral length scale and the rms value of the turbulent kinetic energy results in a merely constant value of ν_T. Figure 14.9 shows that ν_T in the near wake was substantially lower than the value in the nonmanipulated flow, consistent with the fact that eddies in the wake are much smaller, on the average, than the "free stream" eddies. As the wake decays, however, ν_T approaches its "free stream" value.

14.4 Spectral Analysis

The measurements of the statistical moments of the velocity provided a good description of the extent and the strength of the wake; however, they cannot reveal the complexity of its turbulence structure or identify the relative strengths and differences in sizes and structures of the different eddies present in the flow. Spectral measurements are more suited for such investigations.

The sets of F_{uu} and F_{vv} spectra from Figures 13.10, 13.11 and 13.12 in the previous chapter reveal the coexistence of two distinct types of eddies, apparently with very different energy containing ranges : a) larger eddies, produced by the "free stream " mean shear, surviving to a certain degree in the wake, and b) small eddies, produced by the velocity deficit in the wake.

The measurements show a reduction in the energy level and scales of the " free stream " eddies, that could be attributed to their "break-up" as they cross the ribbon and their enhanced viscous damping caused by the finer eddies in the boundary layers on the two sides of the ribbon and in the wake. It may also be deduced that the energy-containing range of the wake-generated eddies overlaps with the inertial and viscous subranges of the " free stream" eddies, thus precluding the appearance of a universal equilibrium range, which has been observed in self similar flows. By comparing F_{uu} and F_{vv}, it can be seen that the distortion of the nonmanipulated spectra due to the wake is stronger for F_{vv}. The measurements show that the energy peaks at high frequencies are considerably attenuated at $\frac{s}{c} = 8.6$ and invisible at $\frac{s}{c} = 32$, while the reduction in the energy levels at the low frequencies is still present at $\frac{s}{c} = 32$. This is consistent with the behavior of the integral length scales, which were reduced from their "free stream" values up to the last measuring station. It was also noted earlier that peaks of normal stresses present close to the ribbon were suppressed quickly, while pockets of Reynolds stress deficit persisted further downstream. The peaks are associated with the small eddies, which have a shorter "life time" than the large eddies associated with the Reynolds stresses deficit.

The above observations are in agreement with those of Coustols and Cousteix (1989) and Bonnet, Delville and Lemay (1987) using spectra in manipulated boundary layers. To make a quantitative comparison with the results of the latter authors, we attempted to correlate the frequency of peak spectral energy and the half width of the wake. Bonnet, Delville and Lemay (1987) found an energy peak at 9 kHz, which corresponds to an eddy size of 2.4 mm for the local mean velocity of 22 m/s. By slightly heating the ribbon, these authors used the temperature excess as a tracer to determine the wake characteristics. The total width of the wake at the same location was reported to have a value close to the eddy size of 2.4 mm. In the present case, at location $\frac{s}{c} = 4.6$, the spectral peak was at a frequency of 1130 Hz (Figure 13.10) at $\frac{n}{c} = -\frac{3}{20}$, which is on the low velocity side of the wake; the local velocity at this point was $8.3 m/s$, giving an eddy size of 7.3 mm. The total width of the wake at this location was estimated to be around 7 mm. Therefore in both cases, the energy containing eddies produced in the wake had a size close to the wake's half width.

The coherence function, shown in Figure 14.10, uncovers further subtleties in the wake's structure. Although the general variation of the coherence is compatible with the variation of the shear stress correlation coefficient, one can also identify regions of coexistence of eddies with opposing shear stresses. For example, by examining Figure 14.10-a and the corresponding correlation coefficient and mean velocity profiles in Figure 14.11-a, it can be seen that at point (c), although the overall shear stress is nearly zero, there are large " free stream " eddies with negative shear stress and small " wake " eddies with positive shear stress. In contrast, at point (e), where the shear stress is also near zero, all scales appear to be nearly uncorrelated. These observations can be easily explained by considering that location (c) is at a local mean velocity maximum, at the edge of the wake, while location (e) is at a local velocity minimum, at the center of the wake, and thus more likely to contain wake-produced eddies than the former case is. Also, examination of points (b) and (f), which lie on the opposite edges of the wake, reveals that they have comparable correlation coefficients, but different eddy structures. At point (f), located on the high velocity side of the wake, the small, wake-generated eddies have considerably higher values of shear stress. The above observations about the pairs of points ((c),(e)) and ((b),(f)) at position $\frac{s}{c} = 4.6$ can also be extended to the same points at $\frac{s}{c} = 8.6$, as can be seen from Figures 14.10-b and 15.10-b, although the strength of the wake-generated eddies is reduced (note that these points at this position are shifted towards the low velocity side). Figures 14.10-c and 14.11-c show that, further downstream, at station $\frac{s}{c} = 32$, the strength of the wake-generated eddies closely approached the strength of the corresponding eddies in the nonmanipulated flow.

14.5 Effect of Ribbon Inclination

Shear stress profiles at $\frac{s}{c} = 8.6$ and 32 for zero, positive and negative angles of attack of the ribbon, are presented in Figures 14.12. It can be seen that, at positive inclination, the minimum shear stress was somewhat higher than that at no inclination, but its location was shifted towards the low velocity side; negative inclination caused the opposite effects. It may be possible that in proximity to the wall, streamline displacement towards the wall causes the wake to approach the wall at a closer distance. As it is known that the maximum reduction of C_f by a LEBU coincides with the location at which the wake contacts the wall (Lemay, 1989), this displacement effect might cause larger overall skin friction reduction.

14.6 Effect of Curvature

The identification of the direct effects of curvature on the development of a thin wake would require the insertion of the ribbon in flows with different values of the parameter S but identical free stream turbulence energy and structure. Unfortunately this is not possible in the present configurations, because the free stream turbulence is also affected by curvature. Another problem is created by the fact that, at the position of the ribbon in the straight section (which was substantially upstream of those in the curved section), the kinetic energy and the length scales of the free stream turbulence were much smaller than those in the curved section, thus causing a slower diffusion of the wake. As clearly seen from Figure 14.13, the wake in the straight section appears to be stronger than those in the curved section, but this is hardly due to curvature effects. A more reliable test of these effects can be made by comparing wakes in the two curved sections with opposite values of S, because differences between the free stream turbulence properties in these two cases were not as severe. To further reduce discrepancies, the local shear stresses were normalized by the corresponding free stream values. Note that the horizontal axis in Figure 14.13 was defined such that positive n always pointed towards the mean shear direction, and therefore towards the center of curvature, when $S < 0$, and away from the center of curvature, when $S > 0$. It may be observed from this figure that, for the present experimental conditions, curvature has a negligible effect on the relative strength of the wake. This observation is consistent with rough predictions based on an algebraic Reynolds stress model (Coustols and Savill, 1989). It may be argued that, unlike eddies produced by the mean shear, which are large enough to be affected by curvature, eddies produced by the wake are sufficiently small to follow the mean streamlines without substantial distortion by centrifugal actions. On the other hand, it is also obvious that, in all cases, the wake axis was shifting towards the center of curvature, in conformity with the hypothesis that centrifugal actions tend to divert slower fluid towards the center and faster fluid away from the center. It may be speculated that the wake of a LEBU placed in the outer layer over a convex wall would tend to shift closer to the wall than that produced by the same LEBU inserted in a plane boundary layer with the same turbulence properties, thus causing a larger wall shear stress reduction in the convex wall case; the reverse would happen in concave boundary layers.

The Reynolds shear stress $-\overline{uv}$ has been plotted versus the mean velocity gradient, $\frac{\partial \overline{U}}{\partial n}$, at different stations downstream of the ribbon in Figures 14.14 to 14.17 for

$S < 0$ and in Figures 14.18 to 14.21 for $S > 0$. Similarly to what has been observed for the wake in straight shear flows, the data form loops which start in the free stream on the low velocity side and close in the free stream on the high velocity side. As the wake develops downstream and grows in the transverse direction, these loops get smaller and open up. The loops cross themselves at the stations closer to the ribbon, where a region of negative production is observed. Furthermore, one can see clearly that curvature further reduces the accuracy of the GTM by increasing the extent of the region with countergradient transport.

Chapter 15

Conclusions

The following conclusions can be drawn from the measurements and analysis of the wake of a thin ribbon in uniformly sheared flow.

- The wake of the thin ribbon in uniformly sheared flow behaves qualitatively similarly to the wake of a LEBU in the outer part of a turbulent boundary layer.

- The relaxation of the maximum velocity deficit of the present wake and its growth rate are comparable to those in the wake of a LEBU in the outer regions of turbulent boundary layers and presents some self similarity.

- Spectral analysis illustrates the coexistence of the wake-generated smaller eddies and the free stream mean shear generated larger eddies.

- For the present experimental conditions, curvature of the free stream had a negligible effect on the relative strength of the wake; it however caused the wake axis to shift towards the center of curvature.

Chapter 16

General Conclusion

The present investigation has shown that the nearly homogeneous uniformly, sheared flow is in many respects qualitatively similar to the outer region of turbulent boundary layers. It has also be seen that measurements and analyses of curved, nearly homogeneous, uniformly sheared flow could be used for quantitative predictions of the behavior of curved turbulent boundary layers. Finally, the wake of a thin ribbon in nearly homogeneous uniformly sheared flow can be considered as closely related to the wake of LEBU in the outer region of turbulent boundary layers.

References

General

BUSHNELL, D.M. 1983 Turbulent drag reduction for external flows. *AIAA-83-0227*.

CHAMPAGNE, F.H., HARRIS, V.G. & CORRSIN, S. 1970 Experiments on nearly homogeneous turbulent shear flow. *J. Fluid Mech.* **41**, 81-139.

HOLLOWAY, A.G.L & TAVOULARIS S. 1992 The effects of curvature on sheared turbulence. *J. Fluid Mech.* **237**, 569-603 (referred to herein as HT1).

HOLLOWAY, A.G.L & TAVOULARIS S. 1992 Effects of curvature on the spectra of sheared turbulence. *Turbulent Shear Flows* 8, (ed. Durst, F. et al.), 383-401, Springer (referred to herein as HT2).

KARNIK, U., & TAVOULARIS, S. 1987 Generation and manipulation of uniform shear with the use of screens. *Exps Fluids* **5**, 247-254.

ROSE, W.G. 1966 Results of an attempt to generate a homogeneous turbulent shear flow. *J. Fluid Mech.* **25**, 97-120.

TAVOULARIS, S. & CORRSIN, S. 1981 Experiments in a nearly homogeneous shear flow with a uniform mean temperature gradient. Part 1. *J. Fluid Mech.* **104**, 311-347.

TAVOULARIS, S. & KARNIK, U. 1989 Further experiments on the evolution of turbulent stresses and scales in uniformly sheared turbulence. *J. Fluid Mech.* **204**, 457-478 (referred to herein as TK).

Part A

ALVING, A.E. & SMITS, A.J. 1986 The recovery of a turbulent boundary layer from longitudinal curvature. *AIAA-86-0435.*

BARLOW, R.S. & JOHNSTON, J.P. 1988a Structure of a turbulent boundary layer on a concave surface. *J. Fluid Mech.* **191**, 137-176.

BARLOW, R.S. & JOHNSTON, J.P. 1988b Local effects of large-scale eddies on bursting in a concave boundary layer. *J. Fluid Mech.* **191**, 177-195.

BASKARAN, V., SMITS, A.J. & JOUBERT, P.N. 1987 A turbulent flow over a curved hill. Part 1. Growth of an internal boundary layer. *J. Fluid Mech.* **182**, 47-83.

BASKARAN, V., SMITS, A.J. & JOUBERT, P.N. 1991 A turbulent flow over a curved hill. Part 2. Effects of streamline curvature and streamwise pressure gradient. *J. Fluid Mech.* **232**, 377-402.

BRADSHAW, P. 1973 Effects of streamline curvature on turbulent flow. AGARDograph no. 169.

CHAMPAGNE, F.H., HARRIS, V.G. & CORRSIN, S. 1970 Experiments on nearly homogeneous turbulent shear flow. *J. Fluid Mech.* **41**, 81-139.

CORRSIN, S. 1957 Some current problems in turbulent shear flows. In *Proc. 1st Naval Hydr. Symp. Nat. Acad. Sci./Nat. Rec. Counc.*, publ. no. 515, Washington, DC.

CORRSIN, S. 1963 Turbulence: Experimental Methods. *Hanbuch der Physik* 8, 523-590.

ELLIS, L.B. & JOUBERT, P.N. 1974 Turbulent shear flow in in a curved duct. *J. Fluid Mech.* **62**, 65-84.

ESKINAZI, S. & YEH, H. 1956 Fully developed turbulent flow in a curved channel. *J. Aero. Sci.* **23**, 65-84.

GATSKI, T.B. & SAVILL A.M. 1989 An analysis of curvature effects for the control of wall-bounded shear flows. *AIAA-89-1014*.

GIBSON, M.M. VERRIOPOULOS, C.A. & VLACHOS, N.S. 1984 Turbulent boundary layer on a mildly curved convex surface : Part 1, Mean flow and Turbulence measurements. *Exps. Fluids* **2**, 17-24.

GILLIS, J.C. & JOHNSTON, J.P. 1980 Experiments on the turbulent boundary layer over convex walls and its recovery to flat-wall conditions. In *Turbulent Shear Flows*, **2**, (ed. Bradbury, L.J.S. et al.), 116-128, Springer.

GILLIS, J.C. & JOHNSTON, J.P. 1983 Turbulent boundary-layer flow and structure on a convex wall and its redevelopment on a falt wall. *J. Fluid Mech.* **135**, 123-153.

HARRIS, V.G., GRAHAM & CORRSIN, S. 1977 Further experiments in nearly homogeneous turbulent shear flow. *J. Fluid Mech.* **81**, 657-687.

HOFFMANN, P.H., MUCK, K.C. & BRADSHAW, P. 1985 The effects of concave surface curvature on turbulent boundary layers. *J. Fluid Mech.* **161**, 371-403.

HOFFMANN, P.H. & BRADSHAW, P. 1978 Turbulent boundary layers on surfaces of mild longitudinal curvature. *Imperial Coll. Aero. Rep. 78-04*, London.

HOLLOWAY, A.G.L & TAVOULARIS S. 1992 The effects of curvature on sheared turbulence. *J. Fluid Mech.* **237**, 569-603. (referred to herein as HT1).

HOLLOWAY, A.G.L & TAVOULARIS S. 1992 Effects of curvature on the spectra of sheared turbulence. *Turbulent Shear Flows* 8, (ed. Durst, F. et al.), 383-401, Springer (referred to herein as HT2).

JAYARAM, M., TAYLOR, M.W. & SMITS, A.J. 1987 The response of compressible turbulent boundary layer to short regions of concave surface curvature. *J. Fluid Mech.* **175**, 343-362.

KARAMCHETI, K. 1966 Principles of Ideal-Fluid Aerodynamics. John Wiley and Sons Inc., New York.

KARNIK, U., & TAVOULARIS, S. 1987 Generation and manipulation of uniform mean shear with the use of screens. *Exps Fluids* **5**, 247-254.

LUMLEY, J.L., & NEWMAN, G.R. 1977 The return to isotropy of homogeneous turbulence. *J. Fluid Mech.* **82**, 161-178.

MERONEY, R.N. & BRADSHAW, P. 1975 Turbulent boundary-layer growth over a longitudinally curved surface. *AIAA J.* **13**, 1448-1453.

MUCK, K.C., HOFFMANN, P.H. & BRADSHAW, P. 1985 The effect of convex surfaces curvature on turbulent boundary layers. *J. Fluid Mech.* **161**, 347-369.

NAKANO, S., TAKAHASHI, A., SHIZAWA, T., & HONAMI, S. 1981 Effects of stable and unstable free streams on a turbulent flow over a concave surface. In *Proc. 3rd Symp. Turbulent Shear Flows*, pp. 4.1-4.23.

NAKAYAMA, A. 1987 Curvature and pressure-gradient effects on a small defect-wake. *J. Fluid Mech.* **175**, 215-246.

RAMAPRIAN, B.R. & SHIVAPRASAD, B.G. 1977 Mean flow measurements in turbulent boundary layers along mildly curved surfaces. *AIAA J.* **15**, 189-196.

RAMAPRIAN, B.R. & SHIVAPRASAD, B.G. 1978 The structure of turbulent boundary layers along mildly curved surfaces. *J. Fluid Mech.* **85**, 273-303.

REYNOLDS, O. 1894 On the dynamical theory of incompressible fluids and the determination of the criterion. *Phil. Trans. Roy. Soc.* vol. 186 p. 123, London.

SCHMIDBAUER, H. 1936 Turbulent friction layer on convex surfaces. *NASA Tech. Memo 791 and ARC no. 2608, Translations of Luftfahrtforsch.*, vol. 13, p. 160.

SHIZAWA, T. & HONAMI, S. 1983 Experiment on turbulent boundary layer over a concave surface - effects of introduction of curvature-. In *Proc. 4th Symp. Turbulent Shear Flows*, pp. 6.38-6.43.

SHIVAPRASAD, B.G. & RAMAPRIAN, B.G. 1978 Turbulence measurements in boundary layers along mildly curved surfaces. *J. Fluid Eng.* **100**, 37-46.

SMITS, A.J., & WOOD, D.H. 1985 The response of turbulent boundary layers to sudden perturbations. *Ann. Rev. Fluid Mech.* **17**, 321-358.

SMITS, A.J., YOUNG, S.T.B & BRADSHAW, P. 1979 The effect of short regions of high surface curvature on turbulent boundary layers. *J. Fluid Mech.* **94**, 209-242.

SO, R.M.C. & MELLOR, G.L. 1973 Experiments on convex curvature effects in turbulent boundary layers. *J. Fluid Mech.* **60**, 43-62.

SREENIVASAN, K.R. 1985 The effect of contraction on a homogeneous turbulent shear flow. *J. Fluid Mech.* **154**, 187-213.

TAVOULARIS, S. & CORRSIN, S. 1981 Experiments in a nearly homogeneous shear flow with a uniform mean temperature gradient. Part 1. *J. Fluid Mech.* **104**, 311-347.

TAVOULARIS, S. 1985 Asymptotic laws for homogeneous turbulent shear flows. *Phys. Fluids* **28**, 999-1001.

TAVOULARIS, S. 1986 Techniques for turbulence measurement. *Encyclopedia of Fluid Mechanics* **1**, ch. 36, (Editor Cheremisinoff, N.P.) Gulf Publishing Company, Houston.

TAVOULARIS, S. & KARNIK, U. 1989 Further experiments on the evolution of turbulent stresses and scales in uniformly sheared turbulence. *J. Fluid Mech.* **204**, 457-478.

TENNEKES, H. & LUMLEY, J.L. 1972 A first course in turbulence. The MIT Press, Cambridge, Massachusetts.

TSELEPIDAKIS, D.P., GATSKI, T.B. & SAVILL, A.M. 1991 A comparison of turbulence models for homogeneous shear flows with longitudinal curvature. *ICASE/LaRC*

Workshop on Transition and Turbulence, NASA Langley Research Center, Hampton, VA. 23665-5225.

WATTENDORF, F.L. 1935 A study of the effect of curvature on fully developed turbulent flow. *Proc. Roy. Soc. Lond.* A148, 565-598.

WILCKEN, H. 1930 Effect of curved surfaces on turbulent boundary layers. *NASA TT F-11421.*

Part B

AHMAD, Q.A., LUXTON, R.E. & ANTONIA, R.A. 1975 The behavior of two-dimensional wake in a uniformly sheared turbulent flow. *J. Appl. Mech.*, June, 1975. pp. 283-288.

ANDERS, J.B. 1986 Large eddy breakup devices as low Reynolds number airfoils. *SAE Tech. Paper 861769.*

ANDERS, J.B.; HEFNER, J.N. & BUSHNELL, D.M. 1984 Performance of large-eddy breakup devices at post-transitional Reynolds numbers. *AIAA-84-0345.*

ANDERS, J.B. & WATSON, R.D. 1985 Airfoil large-eddy break-up devices for turbulent drag reduction. *AIAA-85-0520.*

BANDYOPADHYAY, P.R. 1985 The performance of smooth-wall drag reducing outer-layer devices in rough-wall boundary layers. *AIAA-85-0558.*

BANDYOPADHYAY, P.R. & WATSON, R.D. 1987 Pressure field due to drag reducing outer layer devices in turbulent boundary layers. *Exps. Fluids* **5**, 393-400.

BALAKUMAR, P. & WIDNALL , S.E. 1986 Application of unsteady aerodynamics to large-eddy breakup devices in a turbulent flow. *Phys. Fluids* **29**, 1779-1787.

BEELER, G.B. 1986 Turbulent boundary-layer wall pressure fluctuations downstream of a tandem LEBU. *AIAA J.* **24**, 689-691.

BERTERLUD, A. 1984 Full scale experiments into the use of large-eddy-breakup devices for drag reduction on aircraft. In *AGARD Conf. Proc. Improvement of Aerodynamic Performance Through Boundary Layer Control and High Lift Systems.* vol. 365, pp. 5.1.10-5.1.25.

BERTERLUD, A. & WATSON R.D. 1987 Use of LEBU-devices for drag reduction at flight conditions. In *Proc. Turbulent Drag Reduction by Passive Means*, R. Aero. Soc.

BLACKWELDER, R.F. & CHANG, S.I. 1986 Length scales and correlations in a LEBU modifided turbulent boundary layer. *AIAA-86-0287.*

BONNET , J.P., DELVILLE, J. & LEMAY J. 1987 Study of LEBUs in modified turbulent boundary layer by use of passive temperature contamination. In *Proc. Turbulent Drag Reduction by Passive Means*, R. Aero. Soc.

BONNET , J.P., DELVILLE, J. & LEMAY J. 1988 Experimental study of the behavior of NACA 0009 profile in a transonic LEBU configuration. In *Proc. 16th ICAS Congress, Jerusalem,* pp. 987-998.

CORKE, T.C., GUEZZENNEC Y. & NAGIB, H.M. 1980 Modification in drag of turbulent boundary layers resulting from manipulation of large scale structures. *Prog. Astronaut. Aeronaut.* **72**, 128-143.

CORKE, T.C., NAGIB, H.M., & GUEZZENEC; Y.G. 1982 A new view on origin , role and manipulation of large scales in turbulent boundary layers. *NASA CR-165861.*

COUSTOLS, E., COUSTEIX, J., & BELANGER, J. 1987 Drag reduction performance on Riblet surfaces and through outer layer manipulators. In *Proc. Turbulent Drag Reduction by Passive Means*, R. Aero. Soc.

COUSTOLS, E. & COUSTEIX, J. 1988 Turbulent boundary layer manipulation in zero-pressure gradient. In *Proc. 16th ICAS Congress, Jerusalem*, pp. 999-1013.

COUSTOLS, E. & COUSTEIX, J. 1989 Experimental manipulation of turbulent boundary layers in zero pressure gradient flows through external and internal devices. In *Proc. 7th Symp. Turbulent Shear Flows, Stanford University*, pp. 25.3.1-25.3.6.

COUSTOLS, E. & SAVILL, A.M. 1989 Résumé of important results presented at the third turbulent drag reduction working party. *Appl. Sci. Res.* **46**, 183-196.

COUSTOLS, E., TENAUD, C. & COUSTEIX, J. 1989 Manipulation of turbulent boudary layers in zero pressure gradient flows: detailed experiments and modelling. *Turbulent Shear Flows* **6**, (ed. Andre, J.-C. et al.), 164-178, Springer.

DOWLING, A.P. 1985 The effect of large-eddy breakup devices on oncoming vorticity. *J. Fluid Mech.* **160**, 447-463.

DOWLING, A.P. 1989 The effect of large-eddy breakup devices on flow noise. *J. Fluid Mech.* **208**, 193-223.

FALCO, R.E. & RASHIDNIA, N. 1987 What happens to the large eddies when drag reduction is achieved by outer flow manipulators?. In *Proc. Turbulent Drag Reduction by Passive Means*, R. Aero. Soc.

GUEZENNEC, Y.G. & NAGIB, H.M. 1985 Documentation of mechanisms leading to net drag reduction in manipulated turbulent boundary layers. *AIAA-85-0519.*

HEFNER, J.N., WEINSTEIN, L.M. & BUSHNELL, D.M. 1980 Large-eddy breakup scheme for turbulent viscous drag reduction. *Prog. in Astronaut. and Aeronaut.* vol. 72, pp. 110-127.

KLEIN, H. & FRIEDRICH, R. 1989 Manipulating large-scale turbulence in a channel and a boundary layer. In *Proc. 7th Symp. Turbulent Shear Flows, Stanford University*, pp. 25.4.1-25.4.6.

LEMAY, J., PROVENÇAL, D., GOURDEAU, R., NGUYEN, V.D. & DICKINSON, J. 1985 More detailed measurements behind turbulence manipulators including tandem devices using servo-controlled balances. *AIAA-85-0521.*

LEMAY, J. 1989 Etude expérimentale du comportement de la turbulence dans une couche limite incompressible en présence d'un manipulateur externe. Ph.D. Dissertation, Laval University, Quebec, Canada.

LEMAY, J., DELVILLE, J. & BONNET, J.P. 1990 Turbulent kinetic energy balance in a LEBU modified turbulent boundary layer. *J. Exps. Fluids* 9, 301-308.

LEMAY, J., SAVILL, A.M., BONNET, J.P. & DELVILLE, J. 1989 Some similarities between turbulent boundary layers manipulated by thin and thick flat plate manipulators. *Turbulent Shear Flows*, 6, (ed. Andre, J.-C. et al.), 179-193, Springer.

LINDEMANN, A.M. 1986 Turbulent Reynolds analogy factors of stacked large-eddy

Breakup devices. *J. Spacecraft* **23**, 348-350.

MUMFORD, J.C. & SAVILL, A.M. 1984 Parametric studies of flat plate, turbulence manipulators including direct drag results and laser flow visualization. In *Laminar Turbulent Boundary Layers, Their Control and Flow Over Compliant and Other Surfaces*, vol. 11, pp. 41-45. Fluids Eng. Div. ASME.

NGUYEN, V.D., DICKINSON, J., JEAN, Y., CHALIFOUR, Y., ANDERSON, J., LEMAY, J., HAEBERLE, D., & LAROSE, G. 1984 Some experimental observations of the law of the wall behind large-eddy breakup devices using servo-controlled skin friction balances. *AIAA-84-0346.*

NGUYEN, V.D., SAVILL, A.M. & WESTPHAL, R.V. 1987 Skin friction measurements following manipulation of a turbulent boundary layer. *AIAA J.* 25, 498-500.

NGUYEN, V.D. 1988 Sur les techniques de la réduction de la trainée de frottement par la manipulation de la couche limite. *56ième Congrès de l'ACFAS, Moncton, N.B., Canada.*

NGUYEN, V.D., DICKINSON, J., BÉLANGER, J. & PINEAU, F. 1989 Re-examination of the scaling roughness function for k-type rough walls using a servo-controlled wall drag balance. *Exps Fluids* 8, 111-113.

PAL, S. & RAJ, R. 1981 Wake behavior in the presence of free stream turbulence. *Transactions of the ASME* vol.103, pp. 490-498.

PINEAU, F., NGUYEN, V.D., DICKINSON, J. & BELANGER, J. 1987 Study of flow over a rough surface with passive boundary layer monipulators and direct wall drag measurements. *AIAA-87-0357*.

Plesniak, M.W. & Nagib, H.M. 1985 Net drag reduction in turbulent boundary layers resulting from optimized manipulation. *AIAA-85-0518*.

Poll, D.I.A. & Westland, P.G. 1987 A study of LEBU performance by direct total-force measurements. In *Proc. Turbulent Drag Reduction by Passive Means*, R. Aero. Soc.

Roach, P.E. 1987a A new method of calculating the boundary layer characteristics downstream of manipulators. Part I: Boundary layer integral parameters. In *Proc. Turbulent Drag Reduction by Passive Means*, R. Aero. Soc.

Roach, P.E. 1987b A new method of calculating the boundary layer characteristics downstream of manipulators. Part II: Skin friction and net drag reduction. In *Proc. Turbulent Drag Reduction by Passive Means*, R. Aero. Soc.

Savill, A.M. 1987 Algebraic and Reynolds stress modelling of manipulated boundary layer including effect of free-stream turbulence. In *Proc. Turbulent Drag Reduction by Passive Means*, R. Aero. Soc.

Savill, A.M. & Mumford, J.C. 1988 Manipulation of turbulent boundary layers by outer-layer devices: skin friction and flow visualization results. *J. Fluid Mech.*. **191**, 389-418.

Savory, E., Toy, N. & Wisby, C. 1989 Visualisation of the wakes of LEBU manipulators. *Forum of turbulent flows. 3rd joint ASCE/ASME Mechanics conference, San Diago, California, U.S.A.* pp. 115-120.

SAHLIN, A., JOHANSSON, A.V. & ALFREDSSON, P.H. 1988 The possibility of drag reduction by outer layer manipulators in turbulent boundary layers. *Phys. Fluids* **31**, 2814-2820.

SREENIVASAN, K.R., TAVOULARIS, S. & CORRSIN, S. 1981 A test of gradient transport and its generalizations. In Turbulent Shear Flows **3** 96-112. (Editors Bradbury, L. J.S. et al.) Springer.

TAVOULARIS, S. & KARNIK, U. 1989 Further experiments on the evolution of turbulent stresses and scales in uniformly sheared turbulence. *J. Fluid Mech.* **204**, 457-478 (referred to herein as TK).

TAVOULARIS, S. & SZYMCZAK, M. 1989 Displacement effect of square-ended pitot tubes in shear flows. *Expts. Fluids* 7, 33-37.

TENNEKES, H. & LUMLEY, J.L. 1973 A first course in turbulence. The MIT Press, Cambridge, Massachusetts.

TENAUD, C., COUSTOLS, E. & COUSTEIX, J. 1987 Modelling of turbulent boundary layers manipulated with thin outer layer devices. In *Proc. Turbulent Drag Reduction by Passive Means*, R. Aero. Soc.

TRIGUI, N. & GUEZENNEC, Y.G. 1990 Heat transfer reduction in manipulated turbulent boundary layers. *Int. J. Heat and Fluid Flow.* **11**, 214-219.

YAJNIK, K.S. & ACHARYA, M. 1977 Nonequilibrium effects in a turbulent boundary layer due to the destruction of large eddies. In *Structure and Mechanics of Turbulence*, Lecture Notes in Physics, vol. 76, pp. 249-260, Springer.

VEUVE, M., TRUONG, T.V. & RYHMING, I.L. 1987 Detailed measurements of a tandem manipulator in pressure gradients. In *Proc. Turbulent Drag Reduction by Passive Means*, R. Aero. Soc.

WYGNANSKI, I., CHAMPAGNE, F. & MARASLI, B. 1986 On the large-scale structures in two-dimensional, small-deficit, turbulent wakes. *J. Fluid Mech.* **168**, 31-71.

	initial boundary layer thickness δ_0(mm)	wall radius of curvature R_w (mm)	boundary layer thickness to wall radius of curvature ratio δ_0/R_w	momentum thickness Reynolds number R_θ	longitudinal pressure variation
So and Mellor (1973)	24	varied from 254 to 352	.09	3100	constant pressure
Ramaprian and Shivaprasad (1977) and Shivaprasad and Ramaprian (1978)	22.5	2490	.01	2400	slight favorable pressure gradient
Muck, Hoffmann and Bradshaw (1985)	22	2410	.01	5000	slight favorable pressure gradient
Gibson, Verriopoulos and Vlachos (1984)	19.5	2440	.008	3300	pressure gradient removed
Gillis and Johnston (1980)	38	450	09	4700	negligible pressure gradient
Gillis and Johnston (1983)	39 19.5	450 450	.09 .05		negligible pressure gradient

Table 8.1: Convex turbulent boundary layers.

	initial boundary layer thickness δ_θ (mm)	wall radius of curvature R_w (mm)	boundary layer thickness to wall radius of curvature δ_θ/R_w	momentum thickness Reynolds number R_θ	longitu-dinal pessure variation	spanwise variation
Barlow and Johnston (1988a)	65	1360	0.05	1300	pressue gradient minimized	20 % variation in C_f
Shivaprasad and Ramaprian (1977) and Ramaprian and Shivaprasad (1978)	23	2590	0.01	2400	strong favorable pressure gradient	negligible variation
Shizawa and Honami (1983 and 1985)	27	600	0.045	2900	constant pressure	16 % variation in θ
Hoffmann, Muck and Bradshaw (1985)	22	2540	0.01	5000	slight favorable pressure gradient	30 % variation in C_f

Table 8.2: Concave turbulent boundary layers.

	c (mm)	t (mm)	c/δ_o	h/δ_o	$\overline{U}_o$ (m/s)	$\overline{U}_c$ (m/s)	$u'/\overline{U}_c$ %	Re_c	θ (mm)	δ_0 (mm)	L_{ex} (mm)	comments
present measurements	12.5	0.5	NA	NA	NA	8.6	5	7000	0.11	NA	10	
Blackwelder and Chang (1986)	38	0.1	0.63	0.75	5	4.5	6	11200	0.26	-	26	two ribbons placed in tandem, data downstream of first ribbon
Lemay (1989)	25	0.1	1.1	0.43	25	21	7	36000	0.1	23.5	8	
Coustols, Cousteix and Belanger (1988)	20	1.8	1.2	0.3	32	-	6	35500	0.08	16.7	4	two NACA009 airfoils placed in tandem, data downstream of first airfoil

Table 14.1: Ribbon and flow characteristics for present flow and manipulated boundary layers.

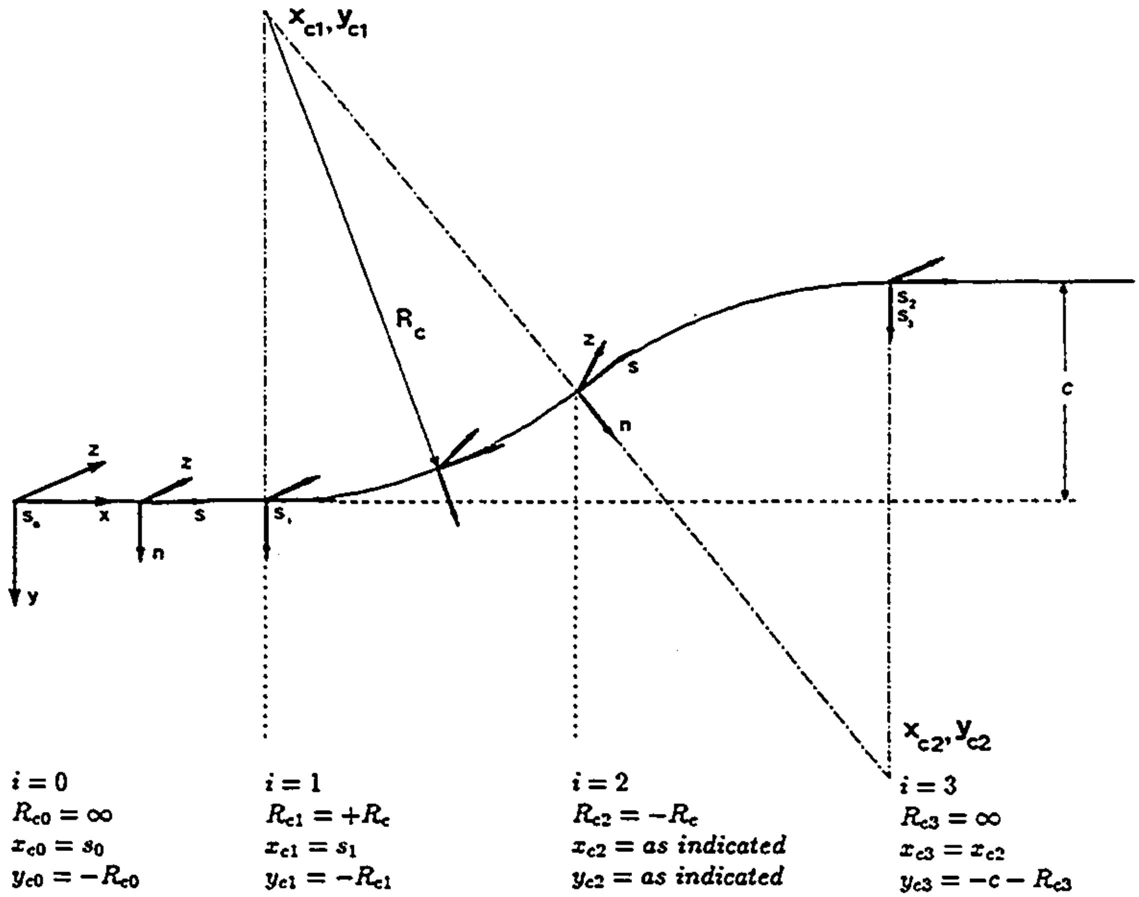

Figure 4.1: The (s,n,z) system of coordinates.

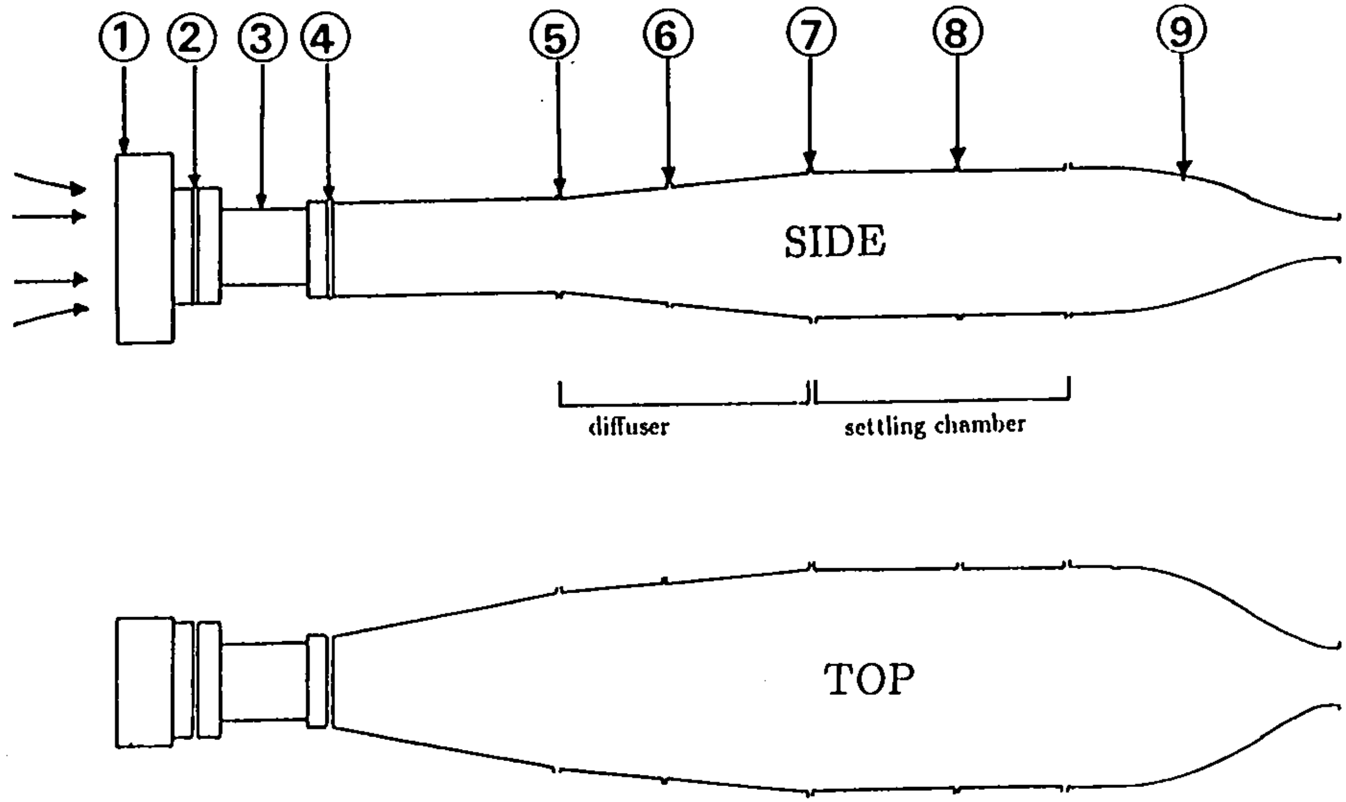

Figure 5.1: The Wind Tunnel; 1, filters; 2,4, flexible coupling; 3, axial fan; 5,6, screen M6-4; 7, acreen M3-2; 8, screen M1-6; 9, 16:1 contraction.

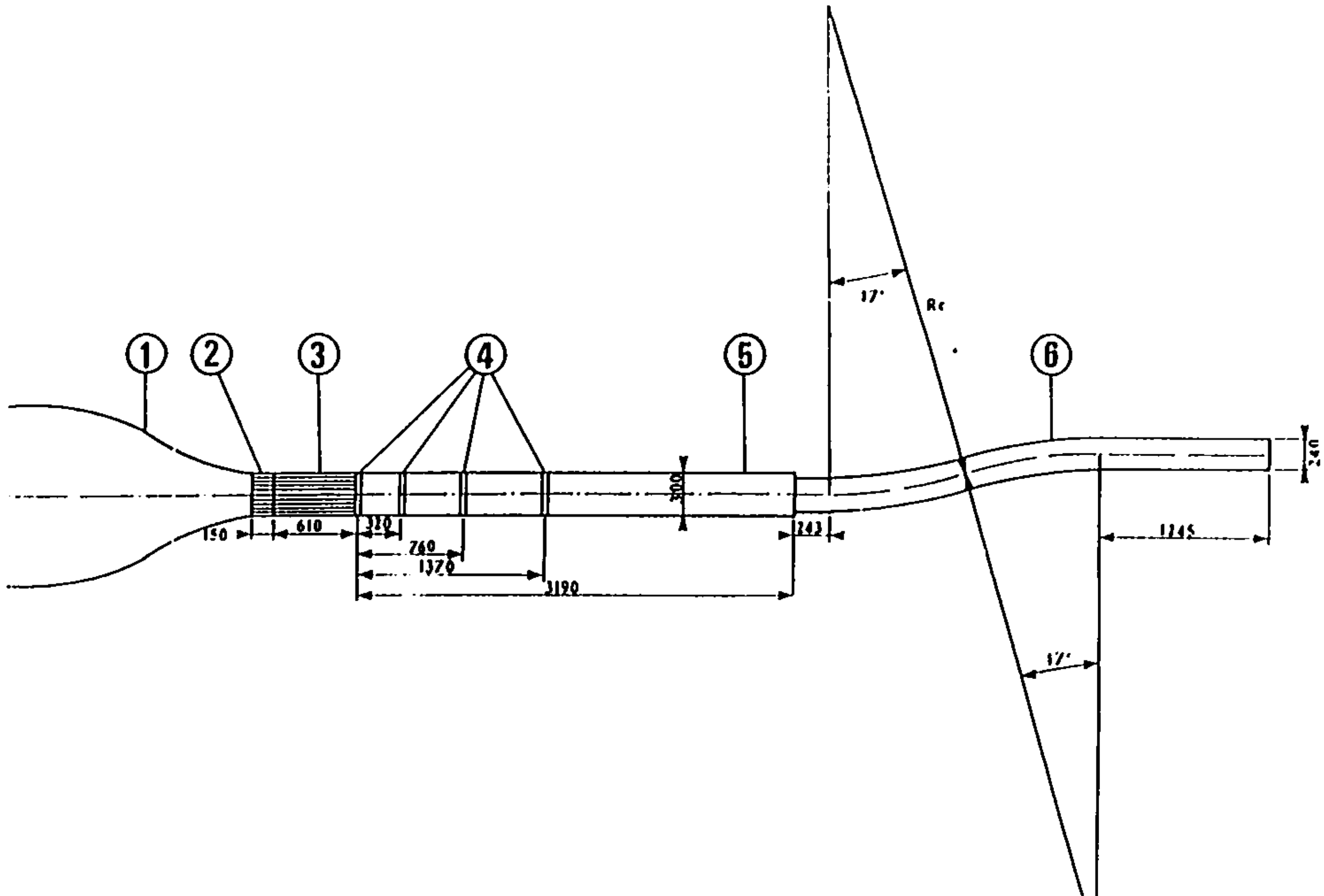

Figure 5.2: The straight and curved sections of the wind tunnel; 1, contraction 16:1; 2, shear generator; 3, flow separator; 4, screens for shear reduction 5, straight section; 6, curved section.

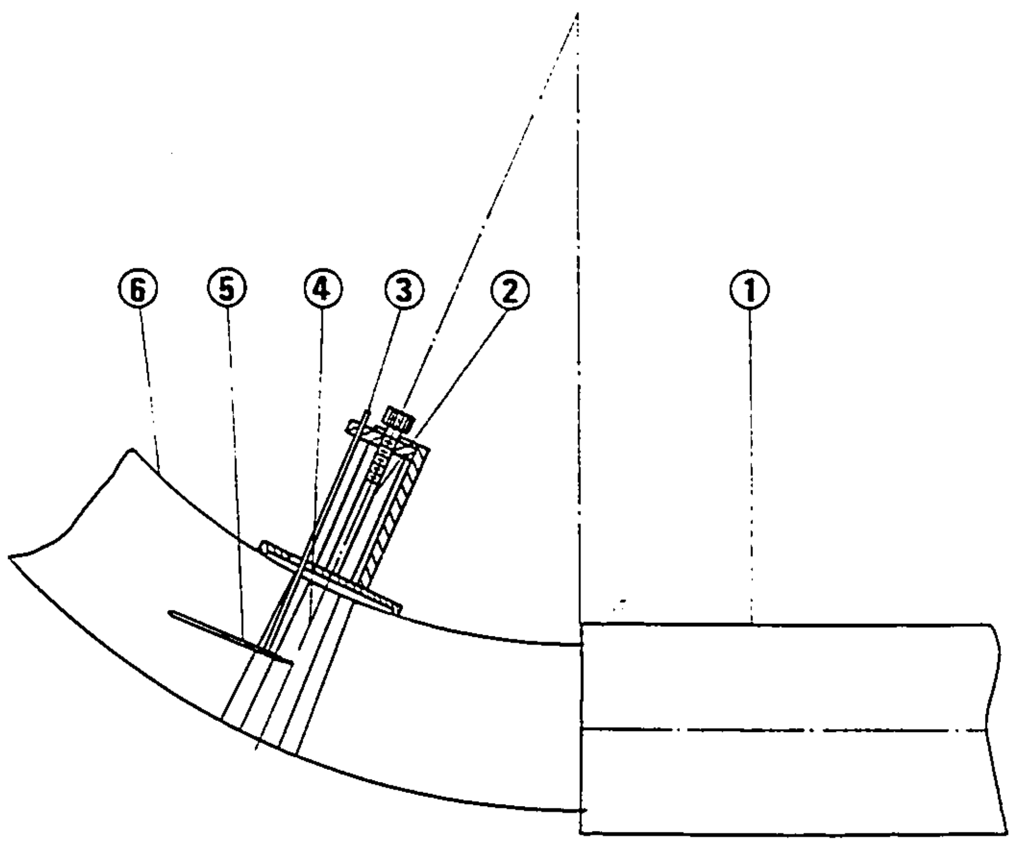

Figure 5.3: The traversing system; 1, straight test section; 2, traversing mechanism screw; 3, probe holder; 4, engraved radial lines; 5, probe; 6, curved section.

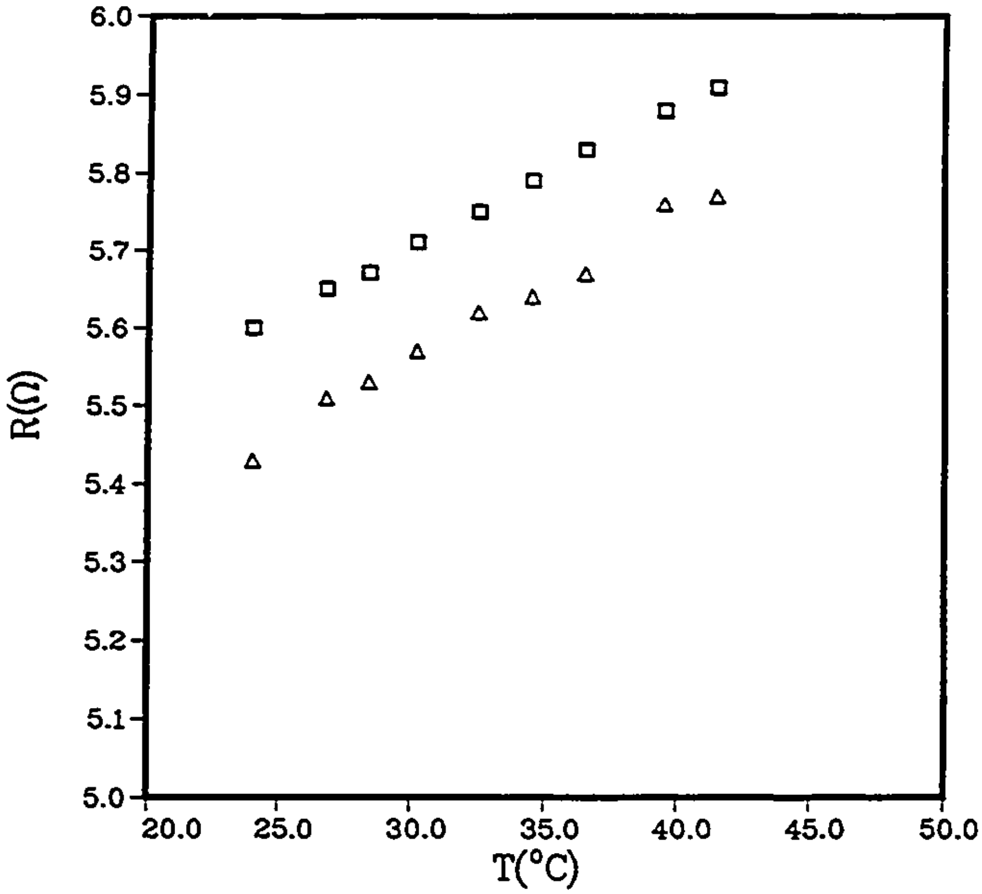

Figure 5.4: Variation of wire resistance with temperature; □, *wire* 1; △, *wire* 2

(a)

(b)

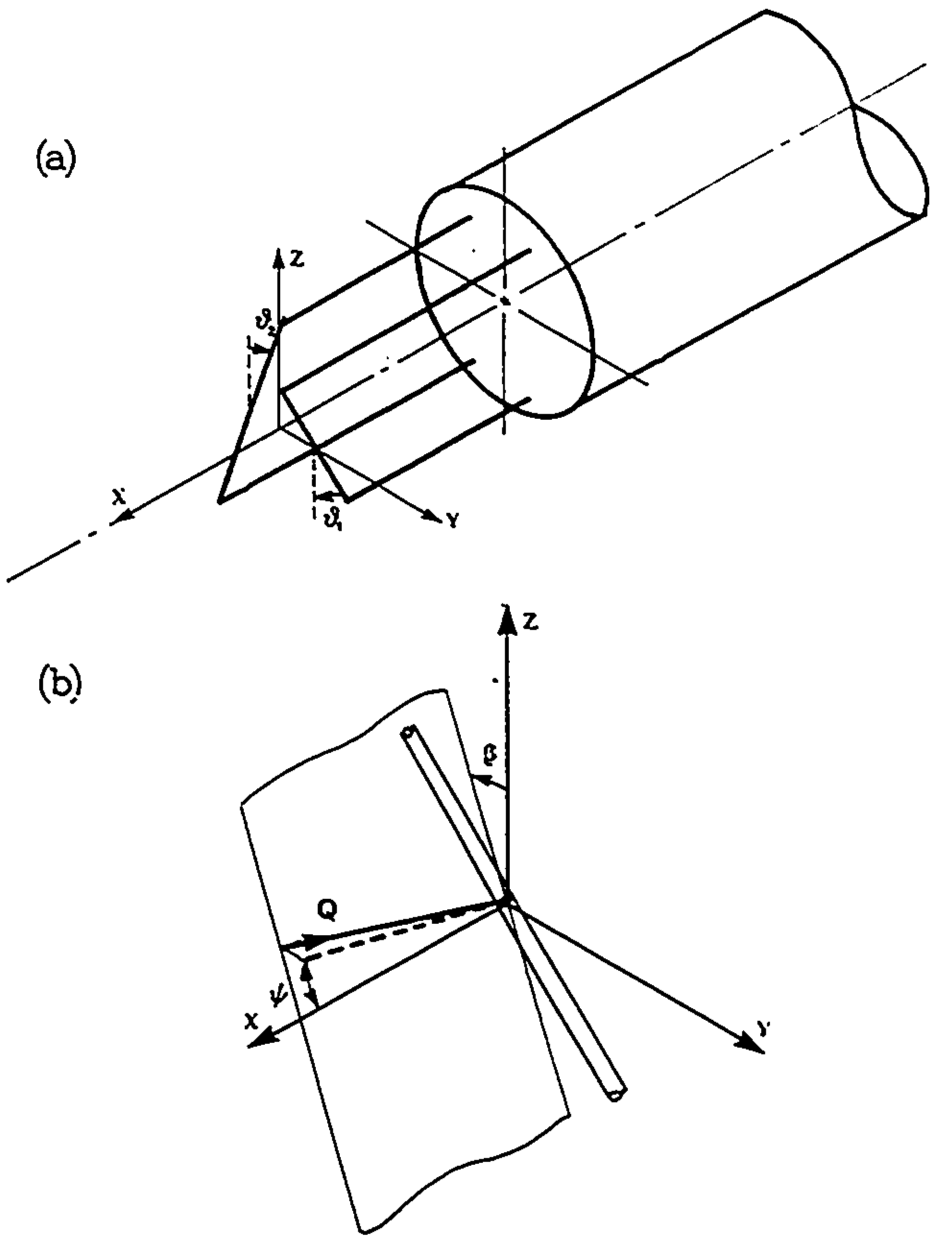

Figure 5.5: Definition of angles of wires; a) wires at angles θ_1 and θ_2 with respect to probe body axis; b) probe body at pitch β and yaw ψ with respect to velocity direction.

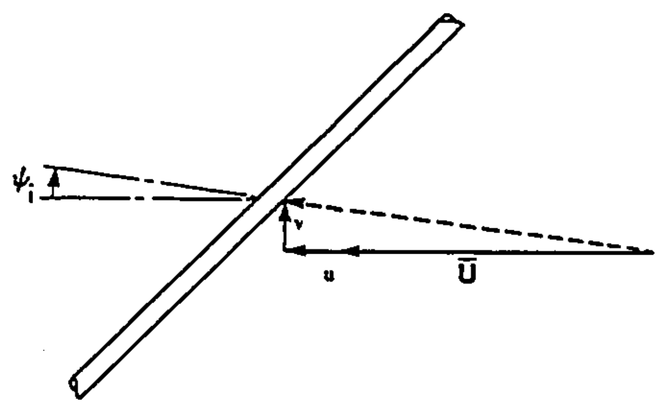

Figure 5.6: Yaw induced by fluctuating transverse velocity component.

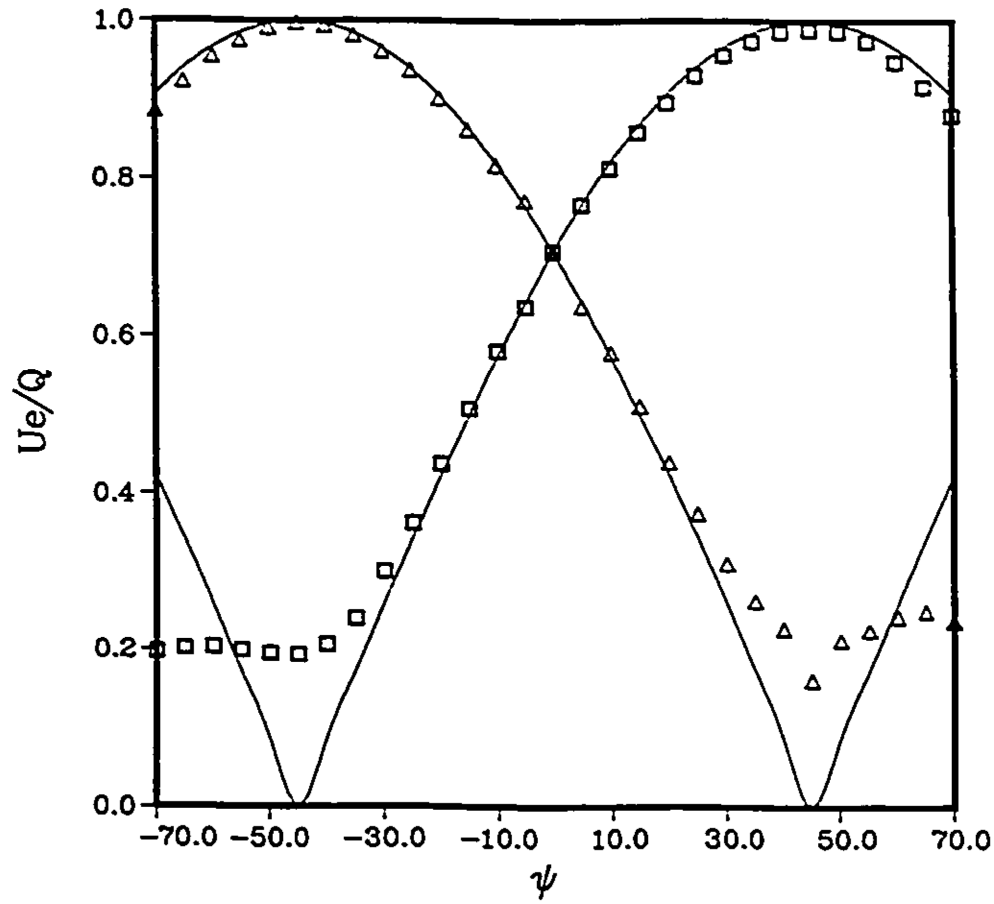

Figure 5.7: Variation of effective cooling velocity with yaw; □, wire 1; △, wire 2;—, equation 5.4 with $h^2 = k^2 = 0.0$.

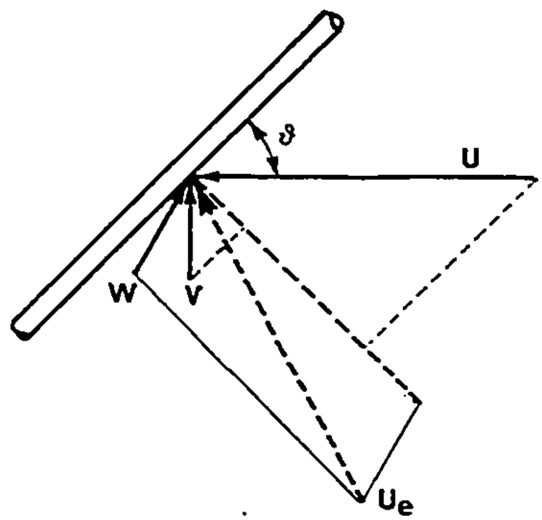

Figure 5.8: Effective cooling velocity.

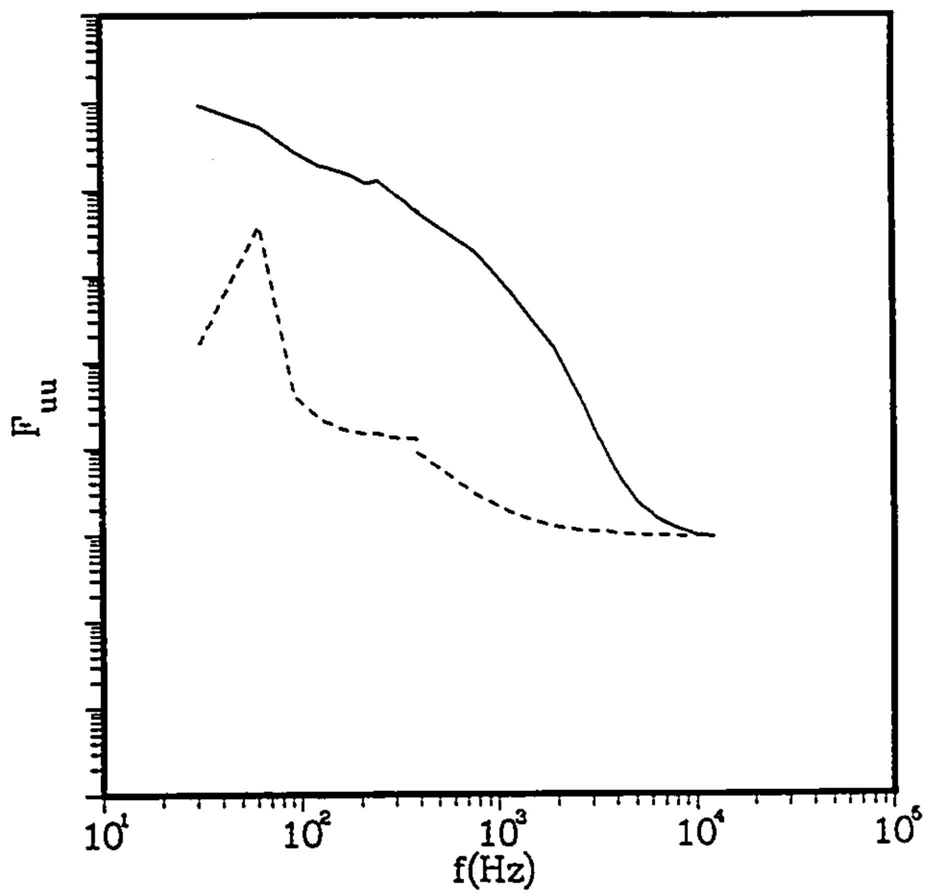

Figure 5.9: Streamwise spectra in wind tunnel; —, shear generator inserted; - - -, without shear generator.

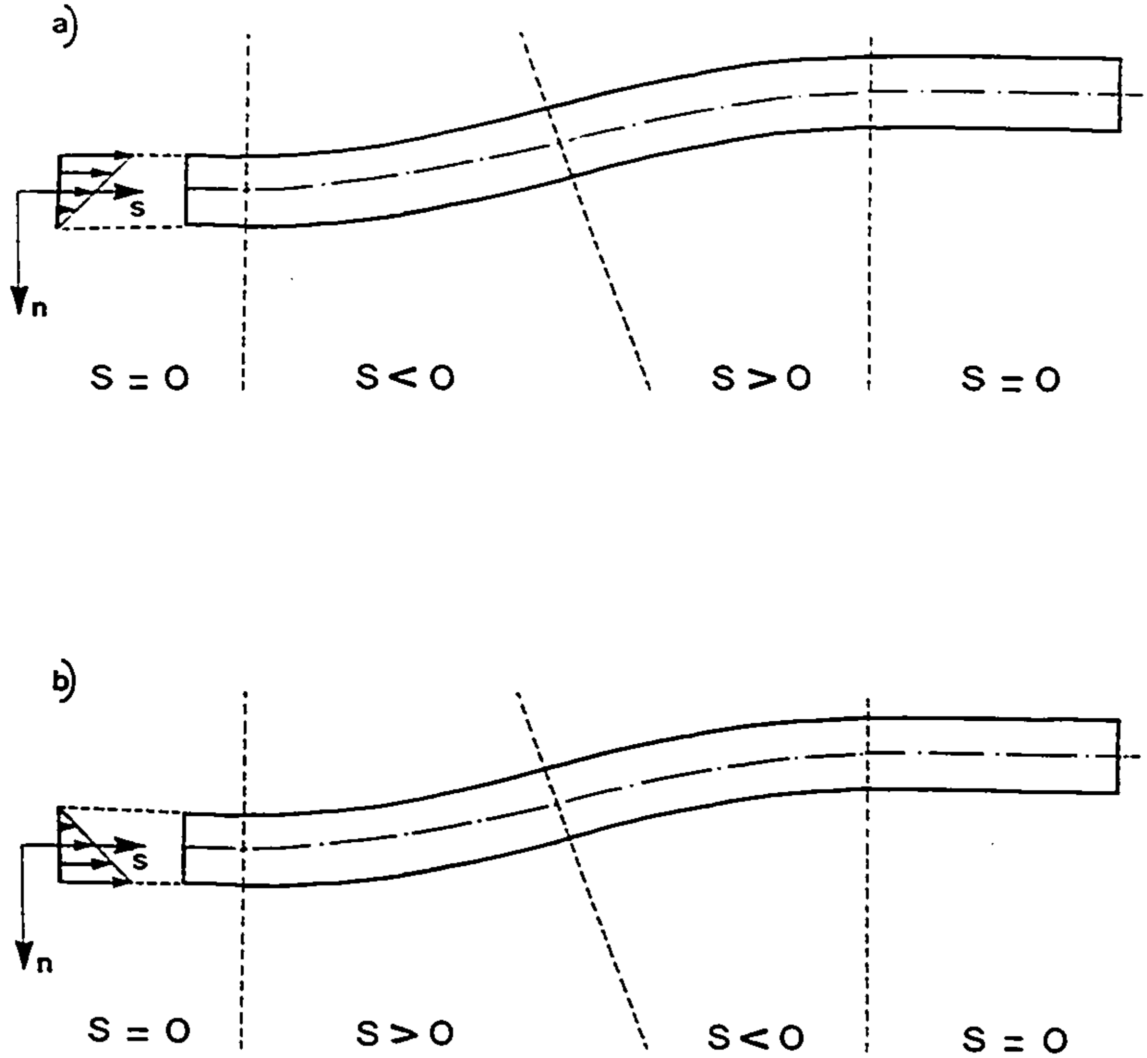

Figure 6.1: Flow configurations: a) configuration NE; b) configuration PE.

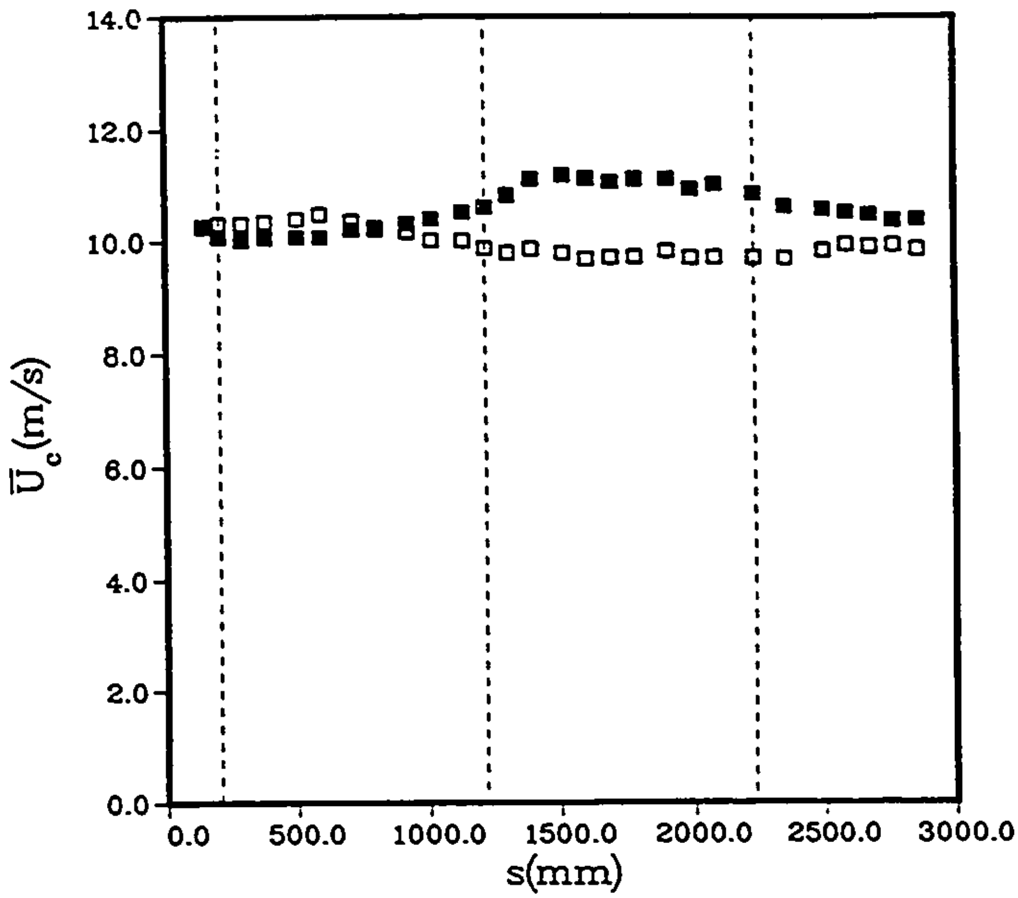

Figure 6.2: Streamwise centerline velocity along the test section; ■, NE; □, PE; vertical lines indicate positions of curvature change.

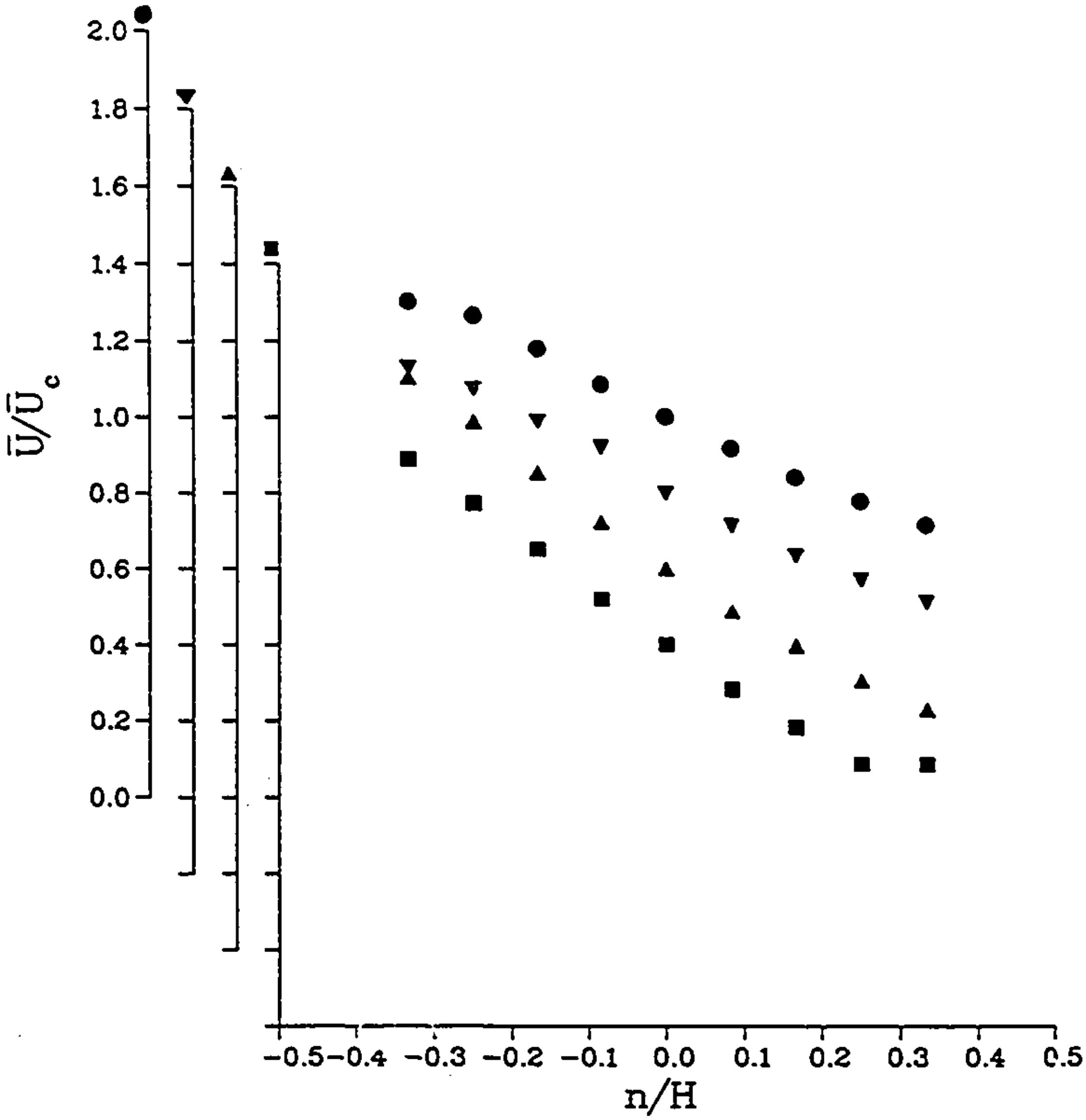

Figure 6.3: Transverse streamwise velocity profiles for case NE; ■, s=143mm; ▲, s=713mm; ▼, s=1692mm; ●, s=2592mm.

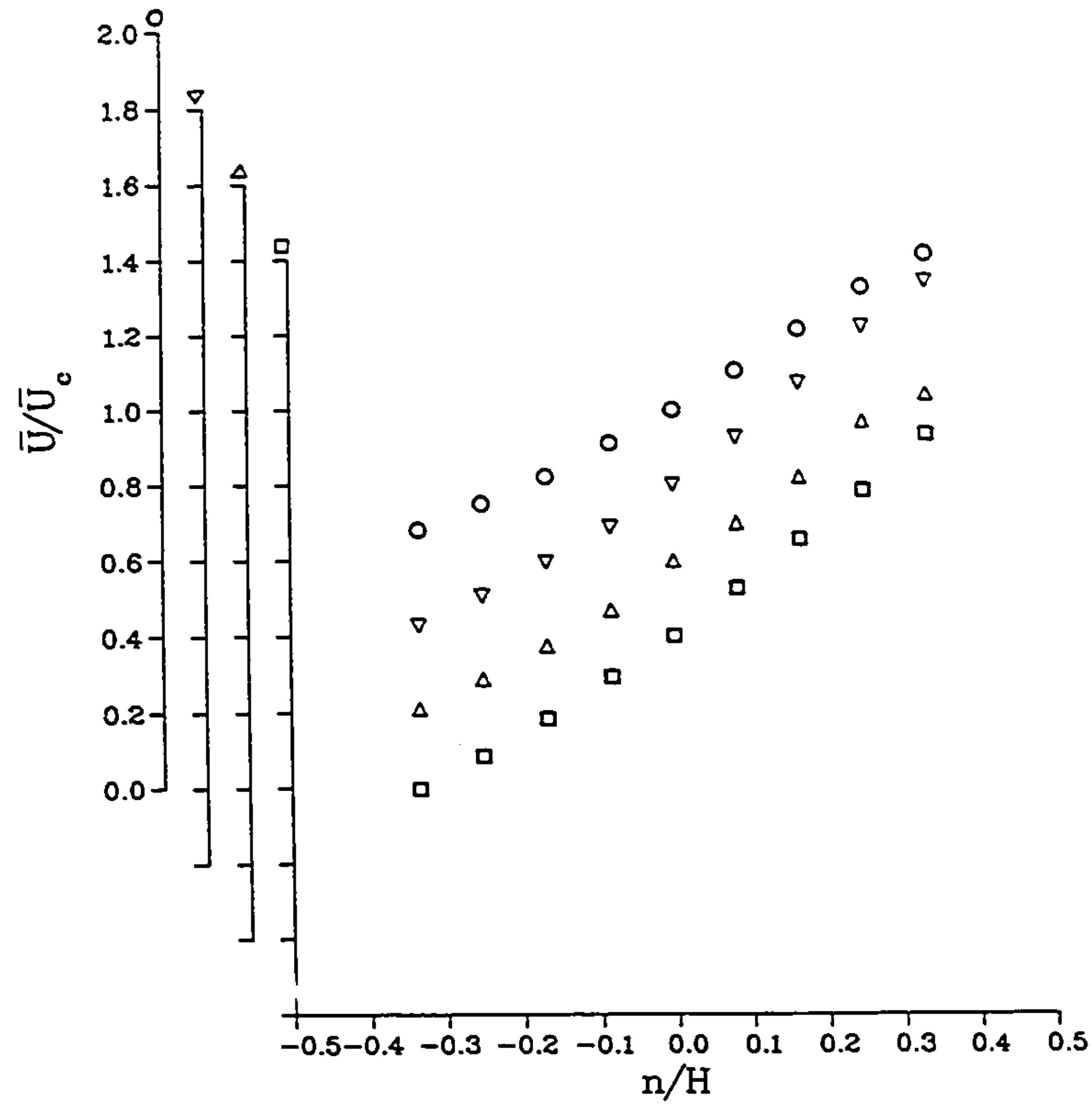

Figure 6.4: Transverse streamwise velocity profiles for case PE; □, s=143mm; △, s=713mm; ▽, s=1692mm; ○, s=2592mm.

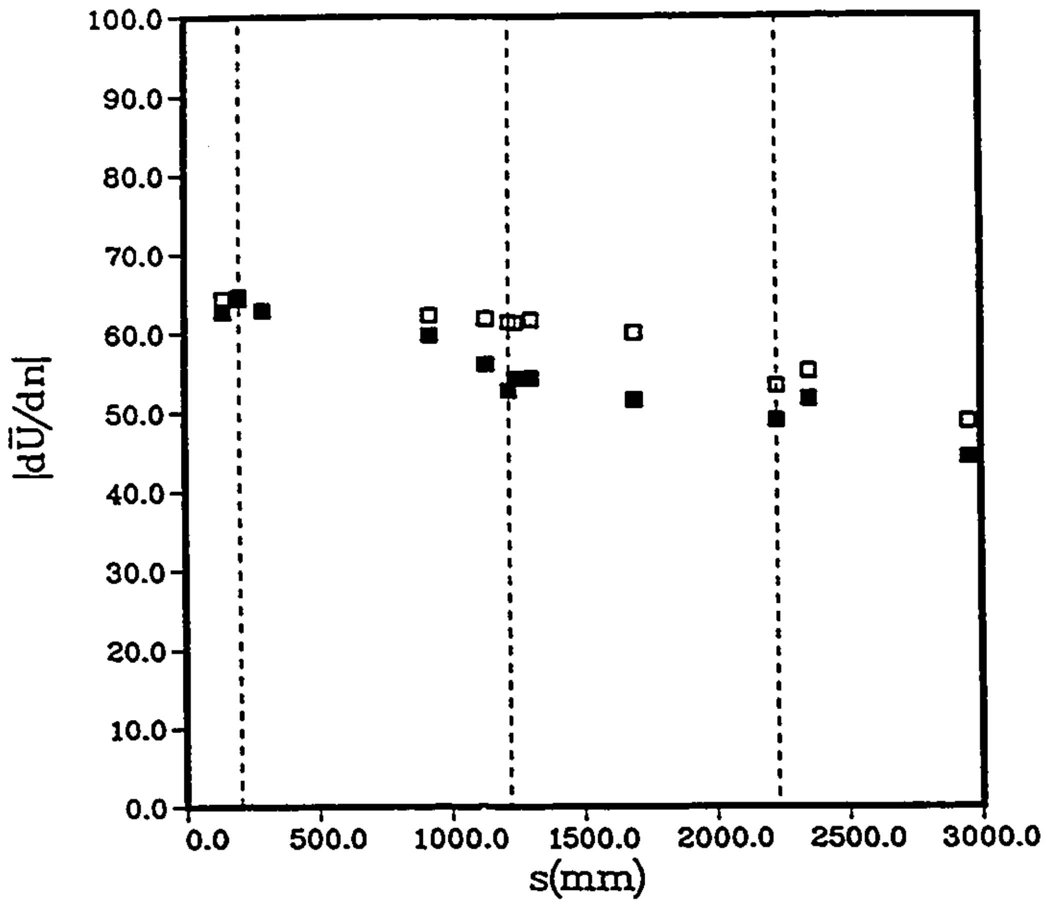

Figure 6.5: Variation of mean shear rate along section; ■, NE; □, PE.

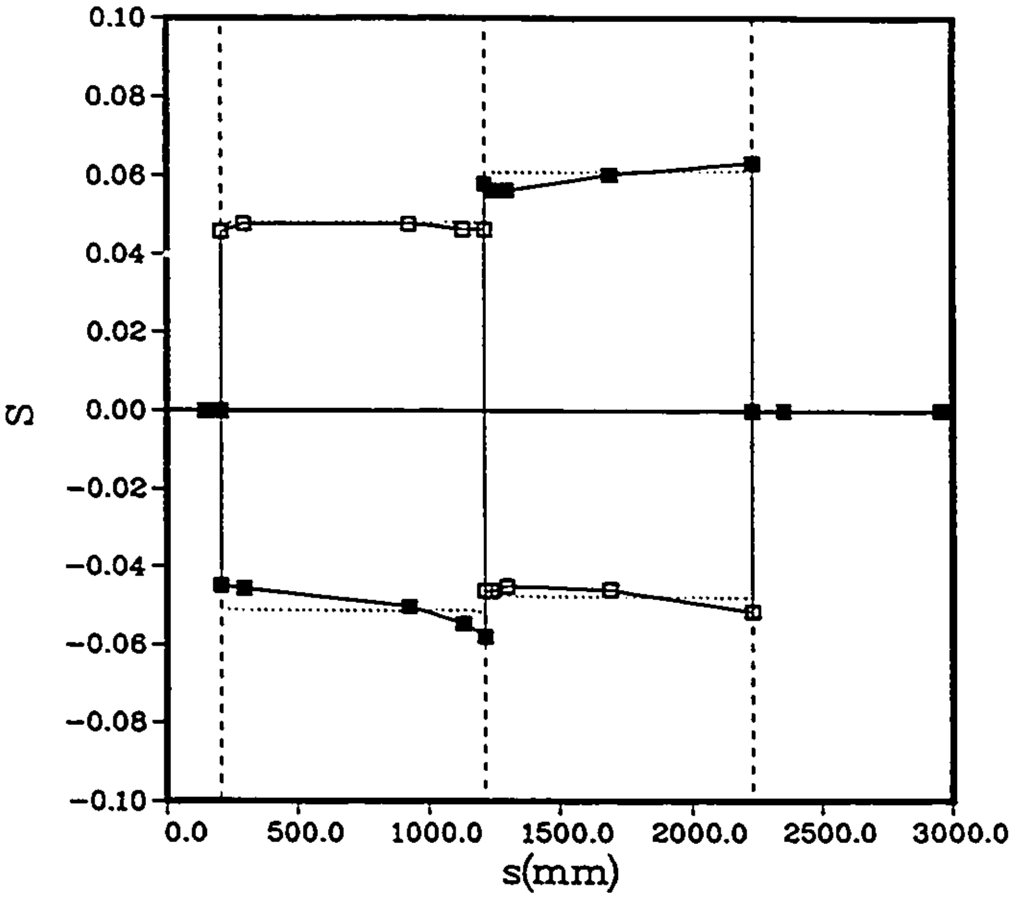

Figure 6.6: Variation of curvature parameter along section; ■, NE; □, PE; ....., average values.

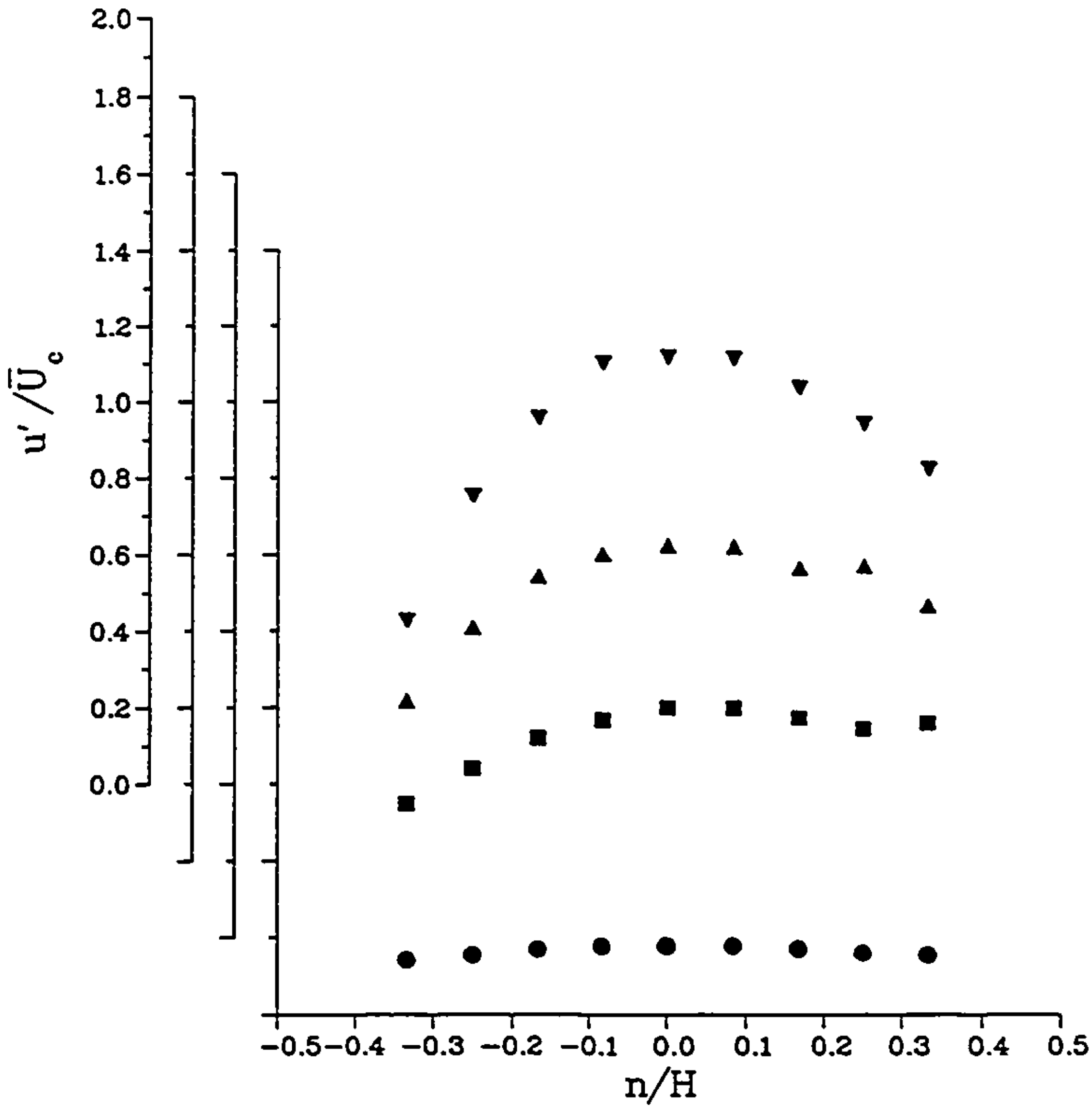

Figure 6.7: Transverse profiles of streamwise turbulence intensity for case NE (symbols as in Figure 6.3).

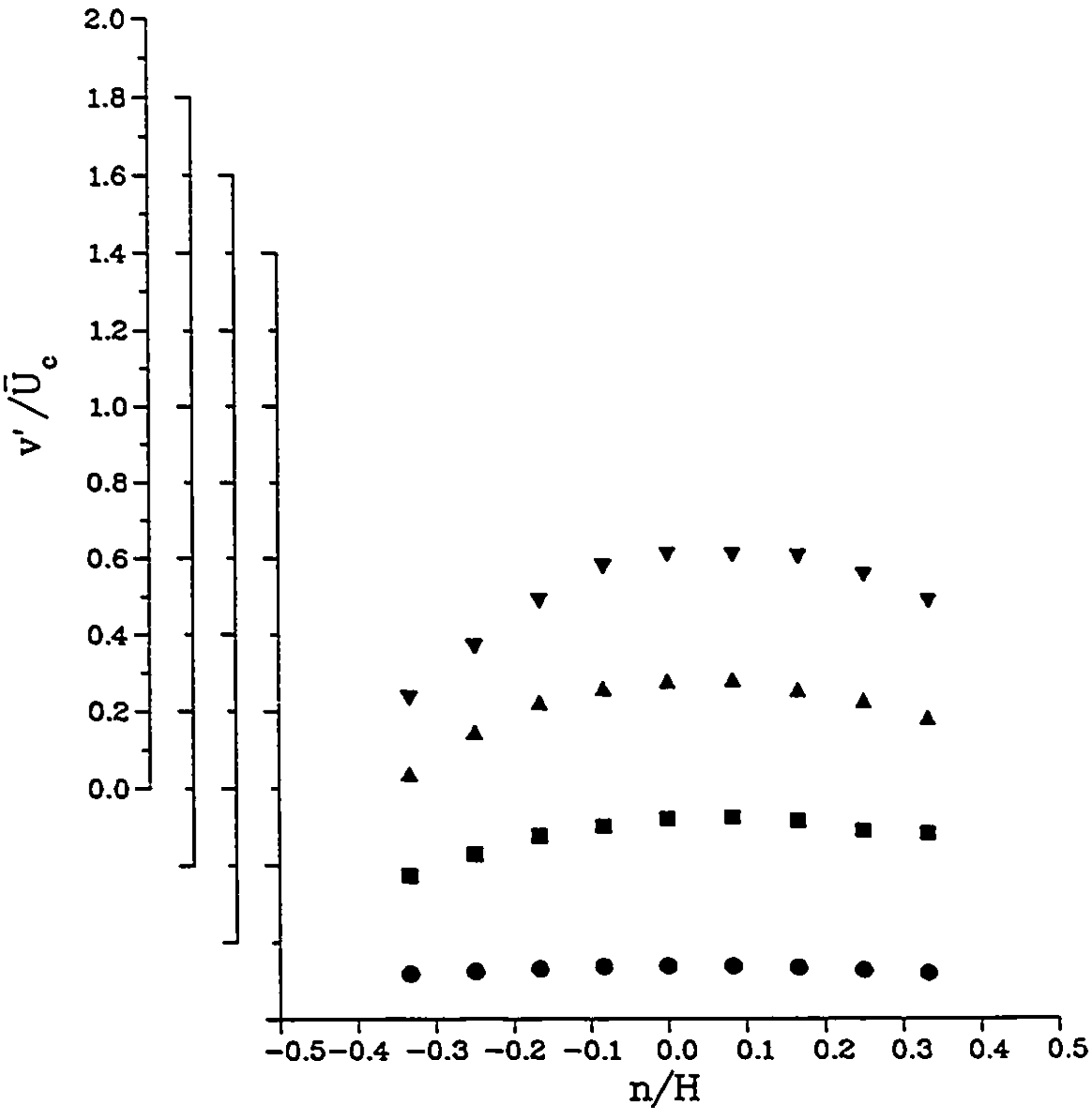

Figure 6.8: Transverse profiles of transverse turbulence intensity for case NE (symbols as in Figure 6.3).

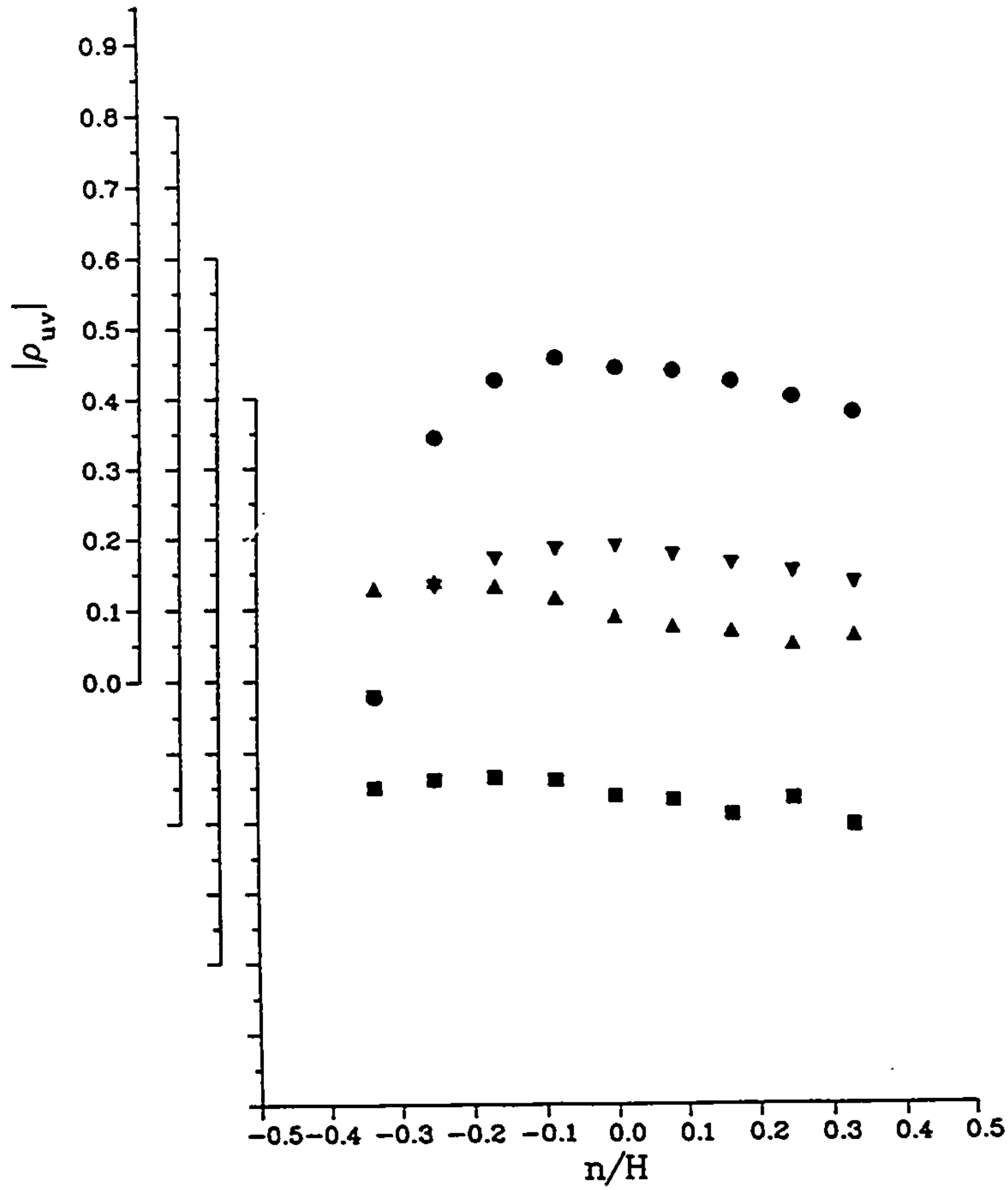

Figure 6.9: Transverse profiles of shear stress correlation coefficient for case NE (symbols as in Figure 6.3).

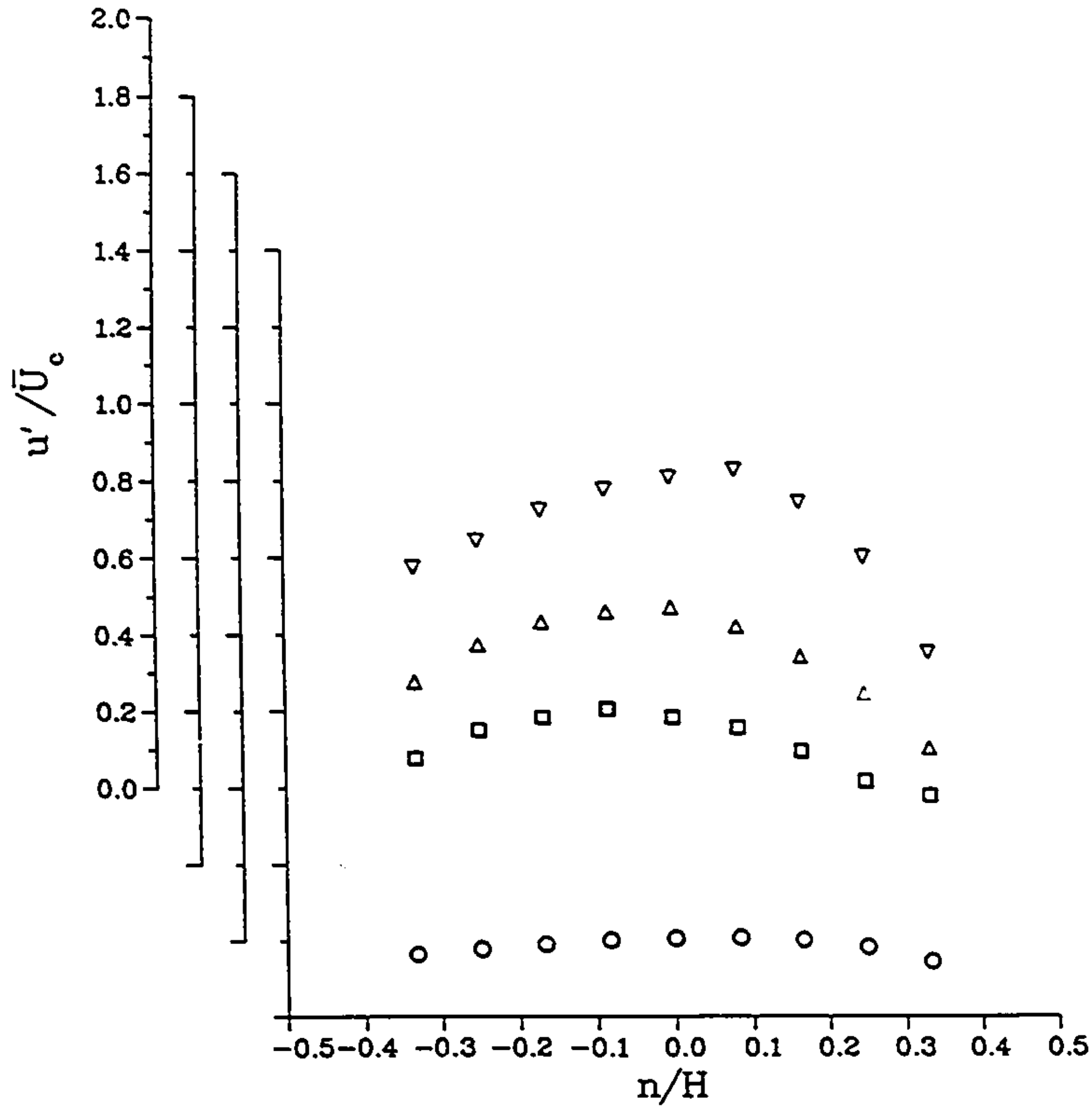

Figure 6.10: Transverse profiles of streamwise turbulence intensity for case PE (symbols as in Figure 6.4).

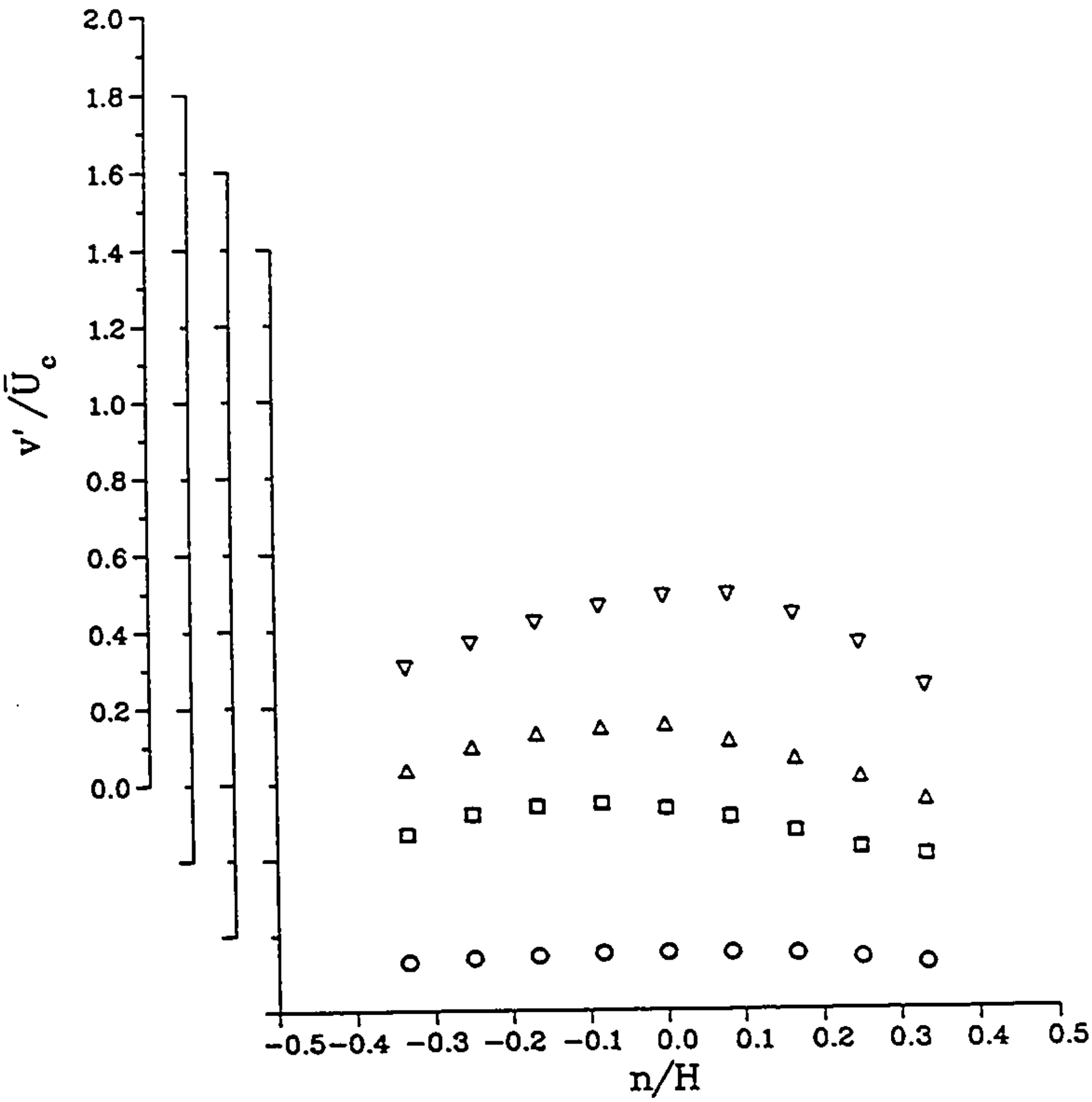

Figure 6.11: Transverse profiles of transverse turbulence intensity for case PE (symbols as in Figure 6.4).

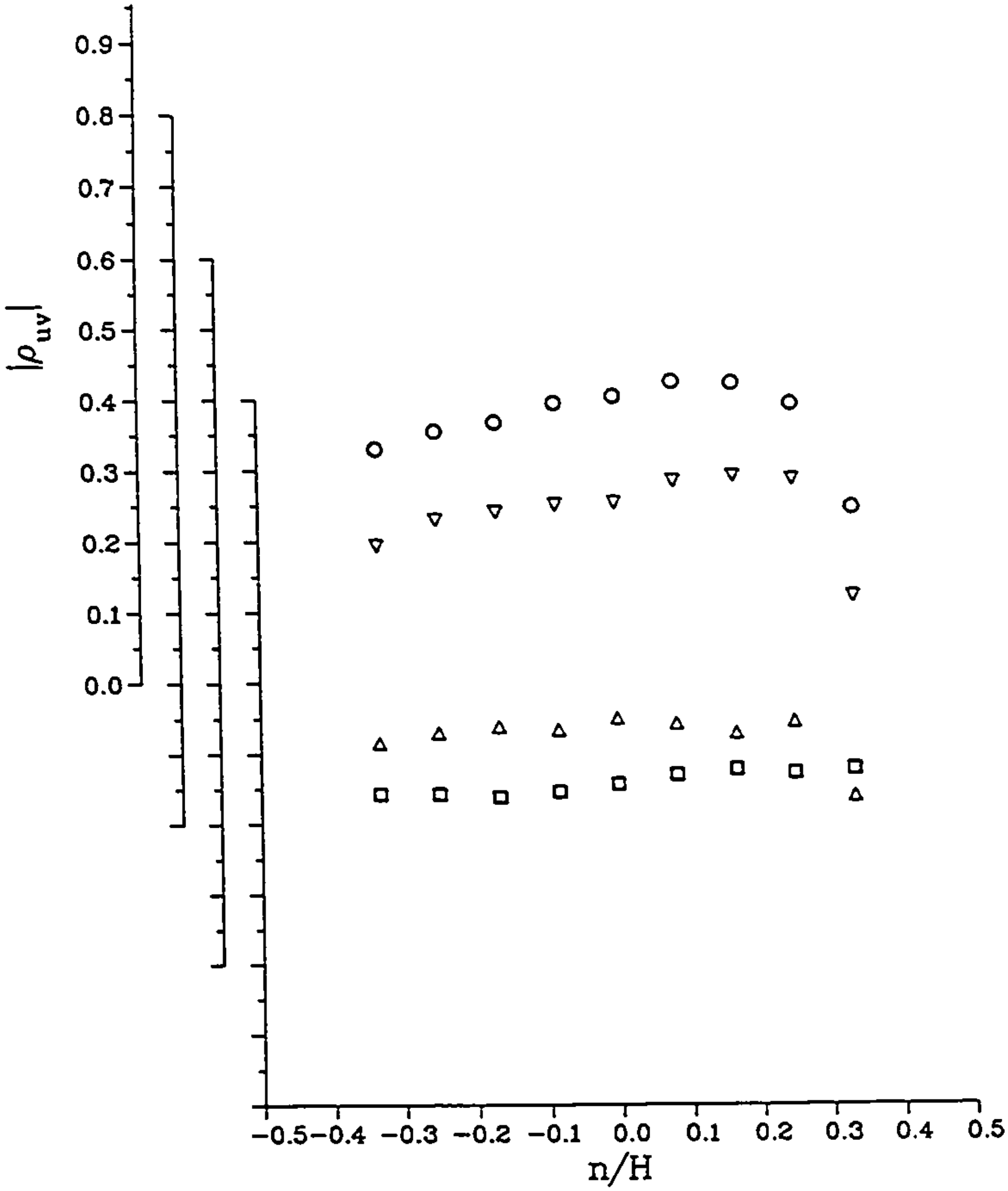

Figure 6.12: Transverse profiles of shear stress correlation coefficient for case PE (symbols as in Figure 6.4).

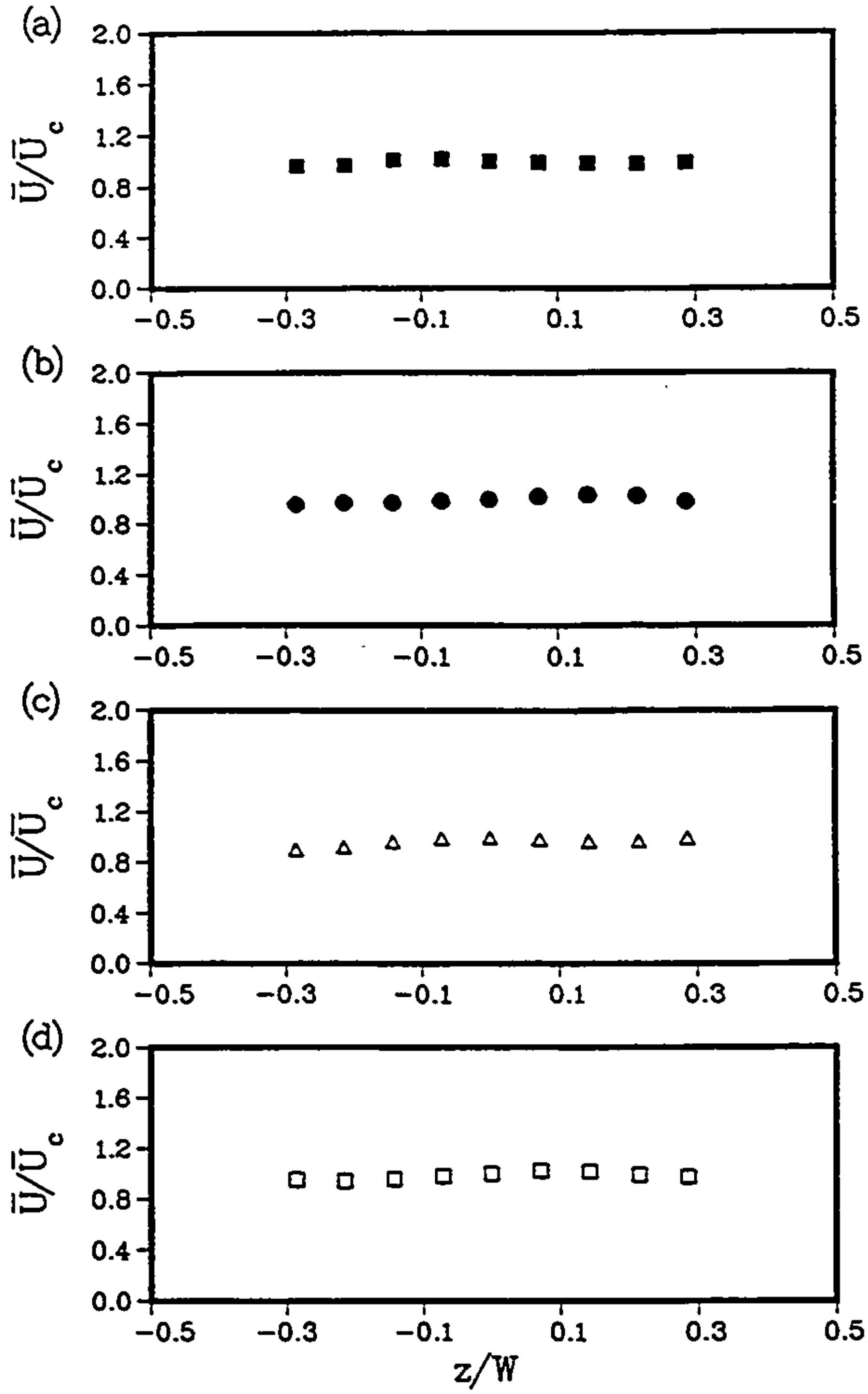

Figure 6.13: Spanwise variation of streamwise mean velocity at n=0; a) s=143mm, case NE; b) s=2862mm, case NE; c) s=143mm, case PE; d) 2862mm, case PE.

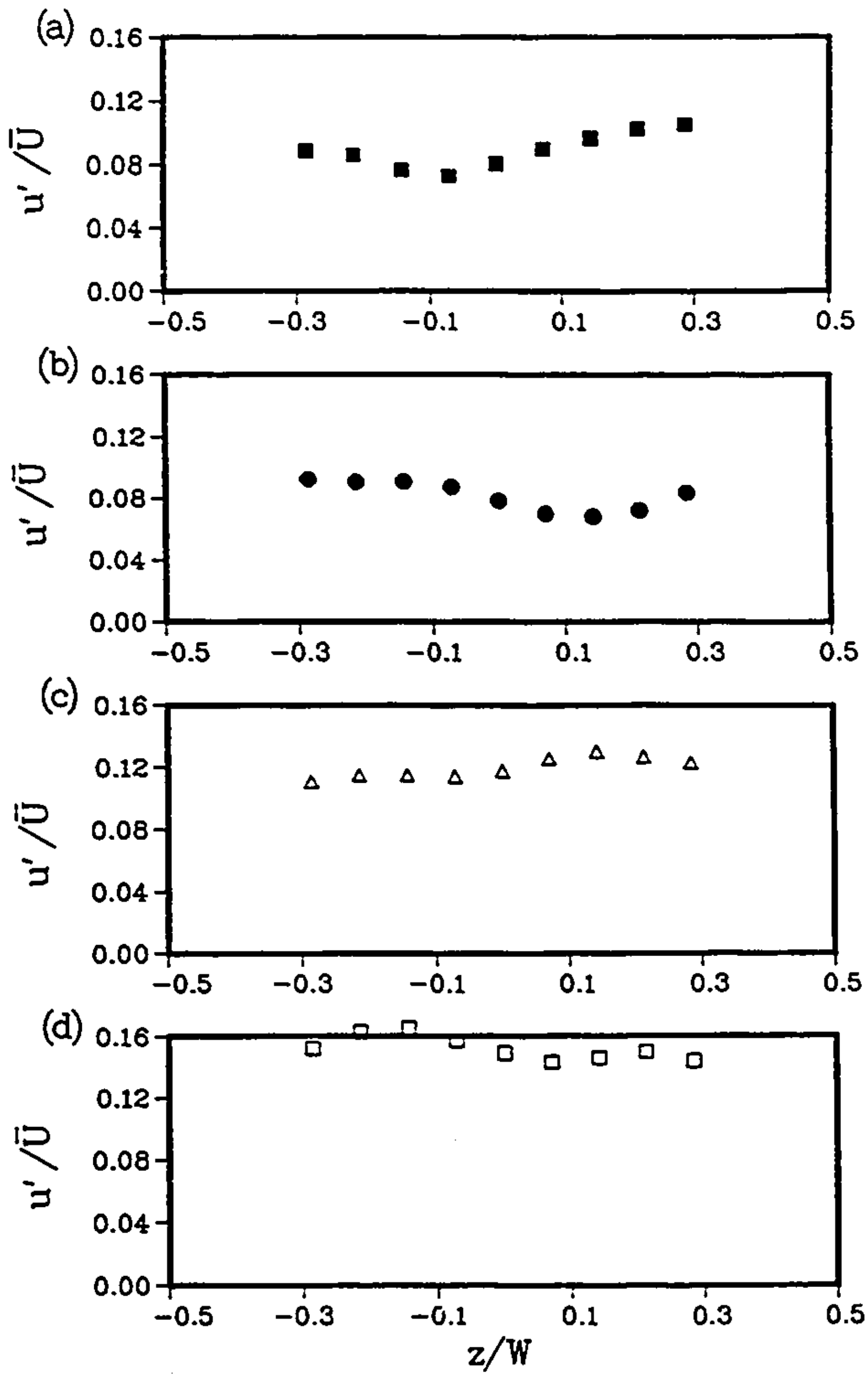

Figure 6.14: Spanwise variation of streamwise turbulence intensity at n=0; a) s=143mm, case NE; b) s=2862mm, case NE; c) s=143mm, case PE; d) 2862mm, case PE.

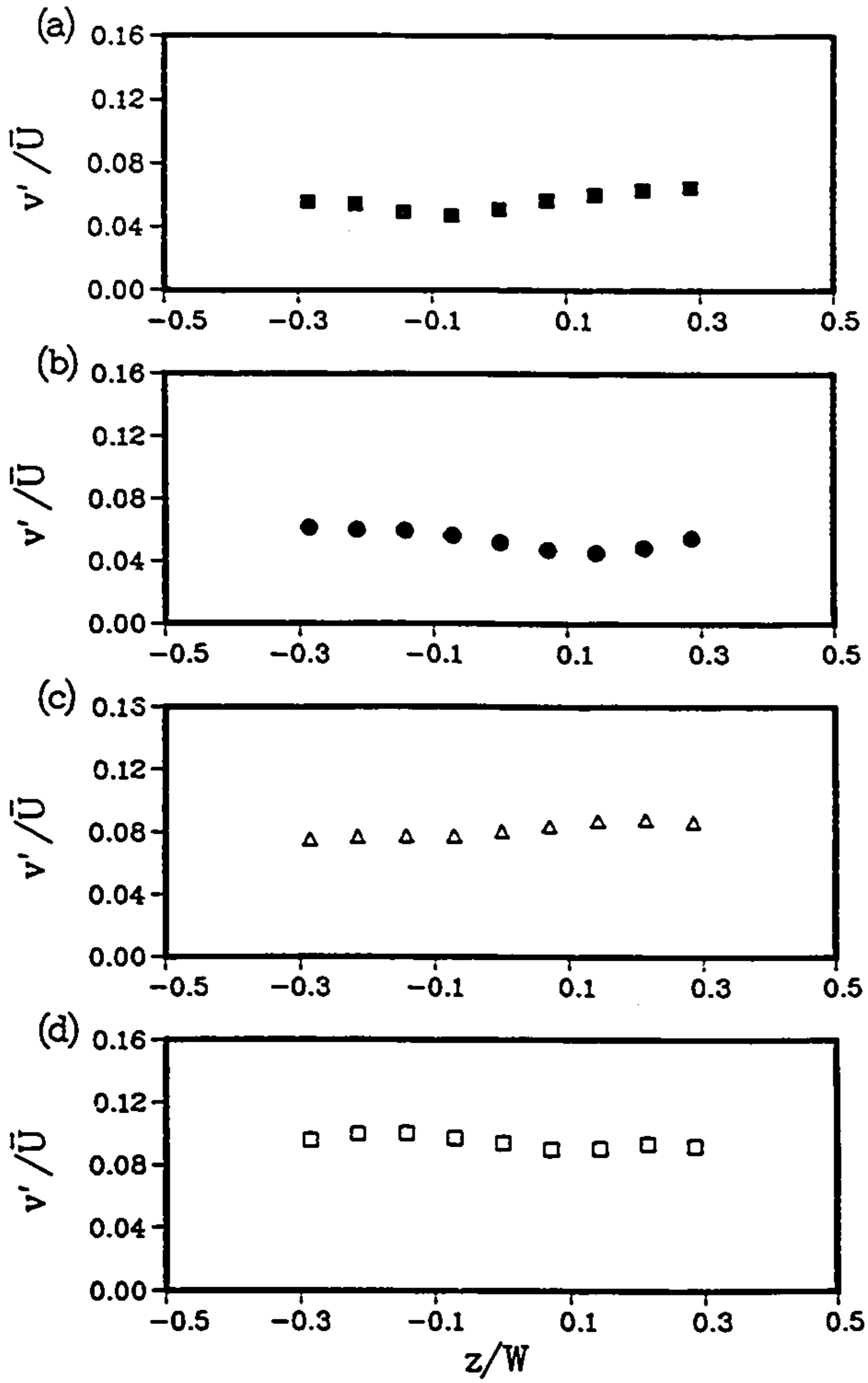

Figure 6.15: Spanwise variation of transverse turbulence intensity at n=0; a) s=143mm, case NE; b) s=2862mm, case NE; c) s=143mm, case PE; d) 2862mm, case PE.

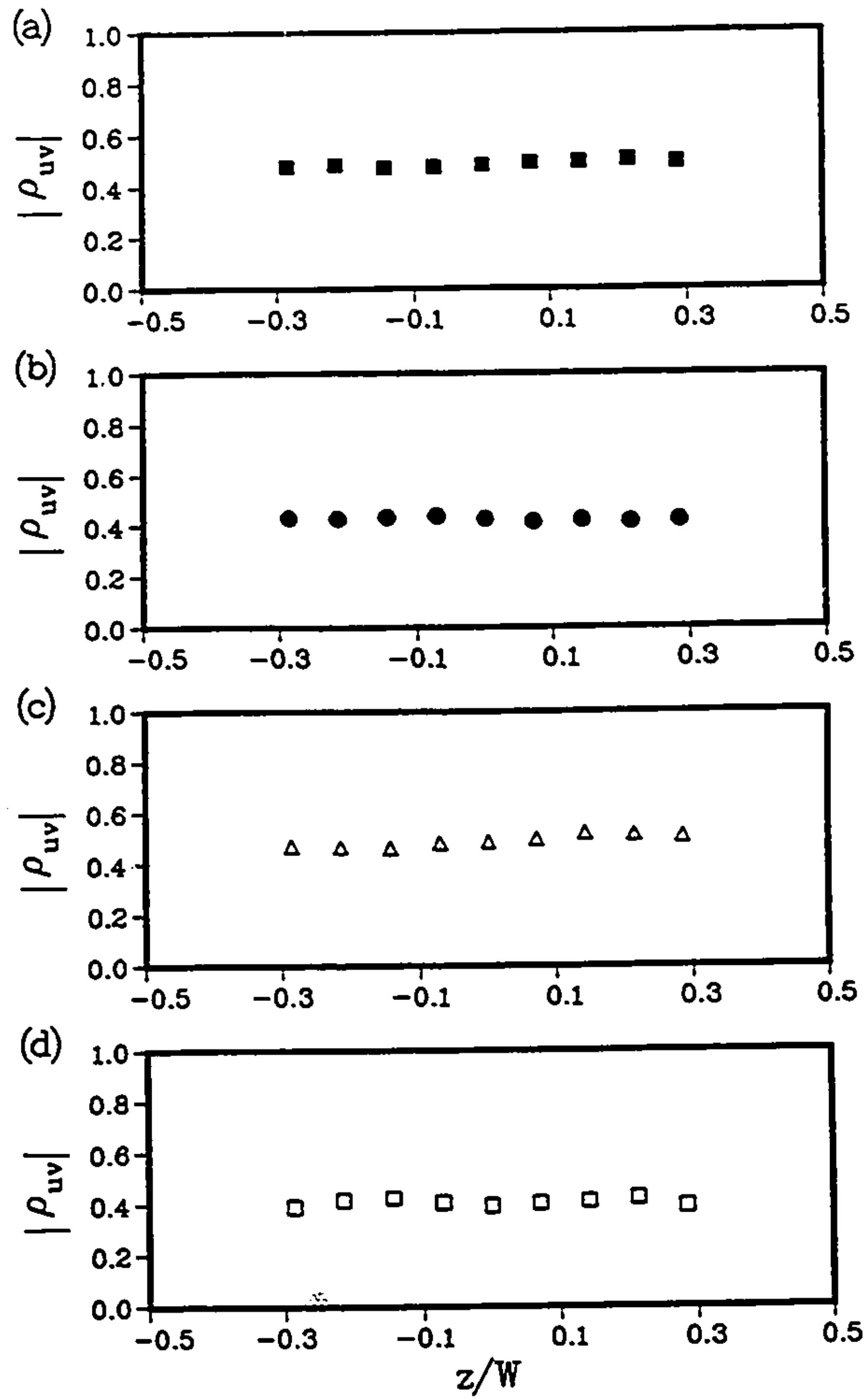

Figure 6.16: Spanwise variation of correlation coefficient at n=0; a) s=143mm, case NE; b) s=2862mm, case NE; c) s=143mm, case PE; d) 2862mm, case PE.

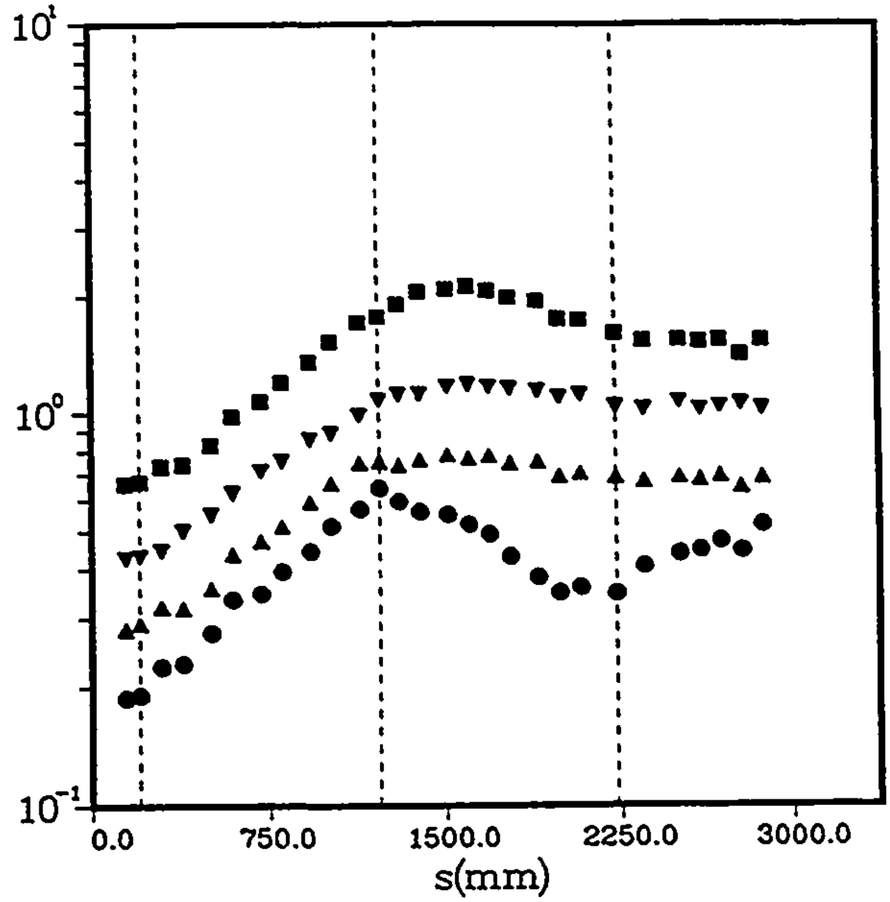

Figure 6.17: Development of Reynolds stresses along section, for case NE; ■, $\overline{u^2}$; ▲, $\overline{v^2}$; ▼, $\overline{w^2}$;●, $\mid \overline{uv} \mid (m^2/s^2)$.

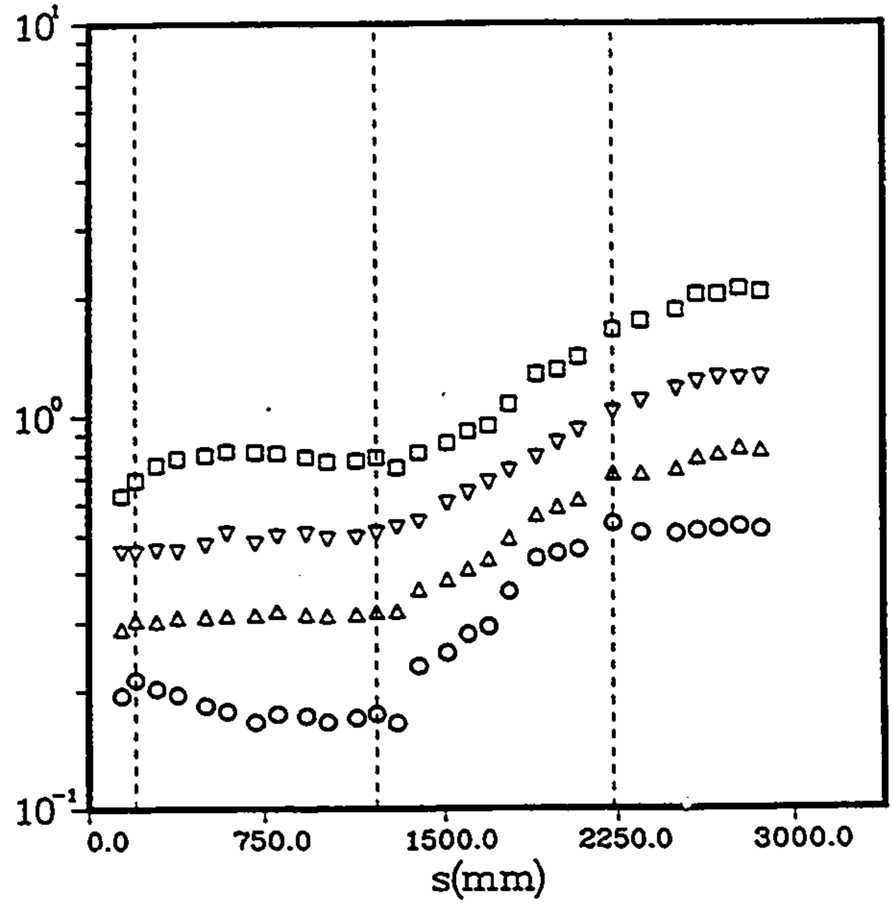

Figure 6.18: Development of Reynolds stresses along section, for case PE; □, $\overline{u^2}$; △, $\overline{v^2}$; ▽, $\overline{w^2}$;○, $|\ \overline{uv}\ |\ (m^2/s^2)$.

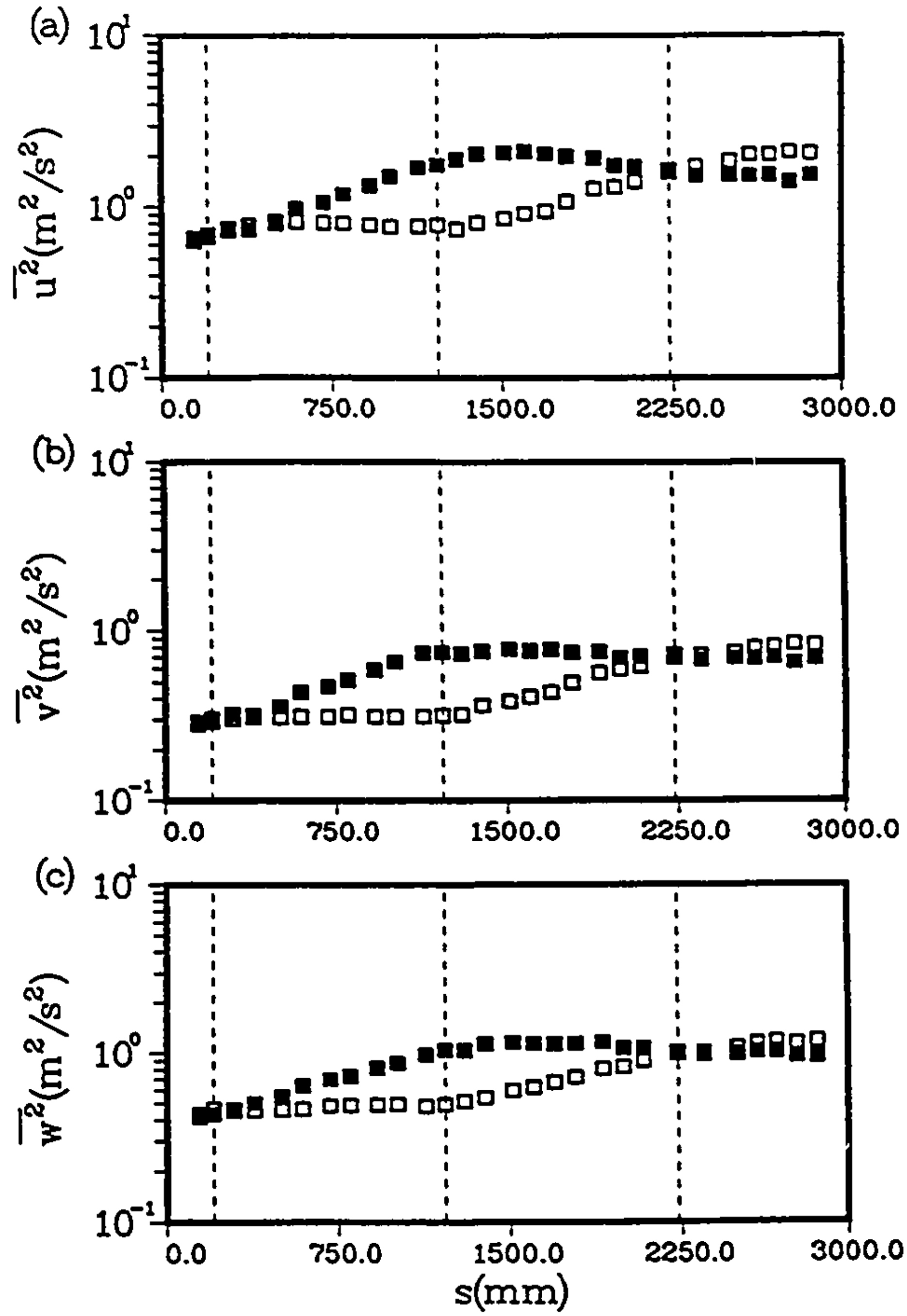

Figure 6.19: Comparison of Reynolds normal stresses development along section for NE and PE cases; ■, NE; □, PE; a) $\overline{u^2}$, b) $\overline{v^2}$, c) $\overline{w^2}$.

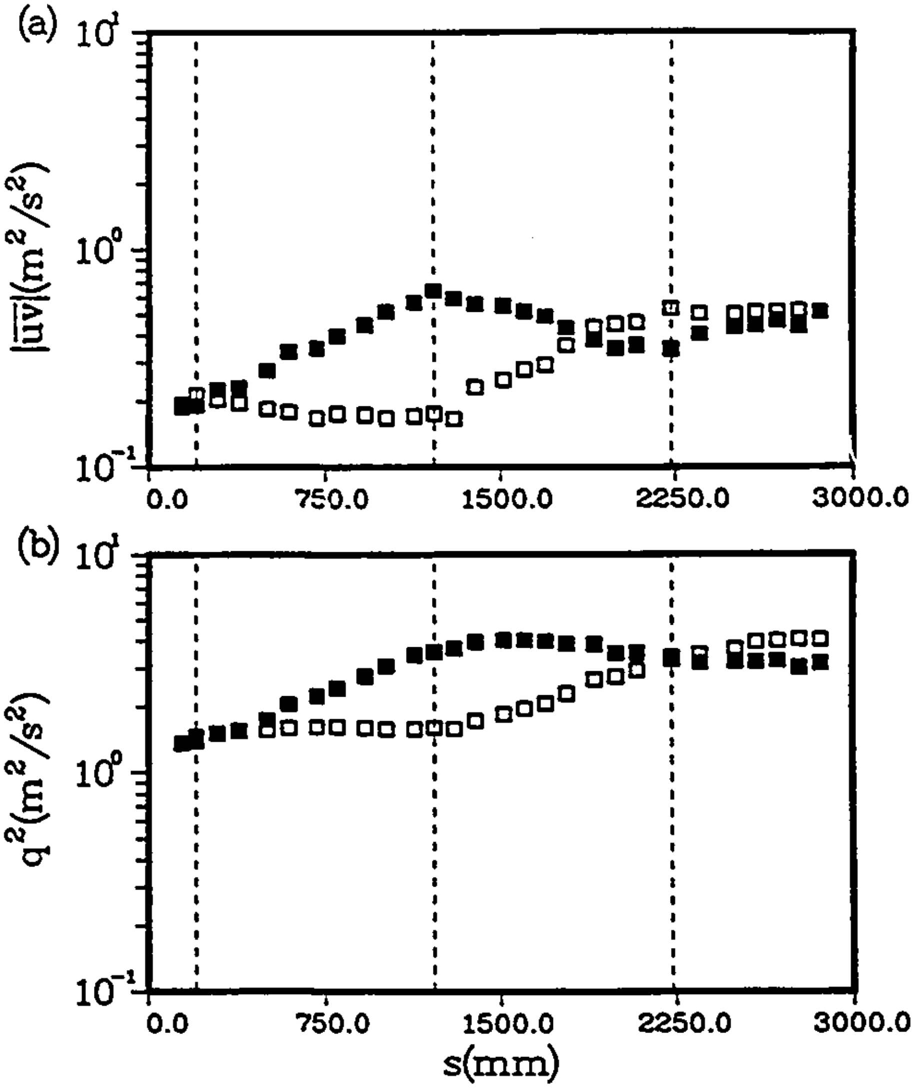

Figure 6.20: Comparison of kinetic energy and Reynolds shear stress development along section for NE and PE cases; ■, NE; □, PE; a) q^2, b) $\overline{uv}$.

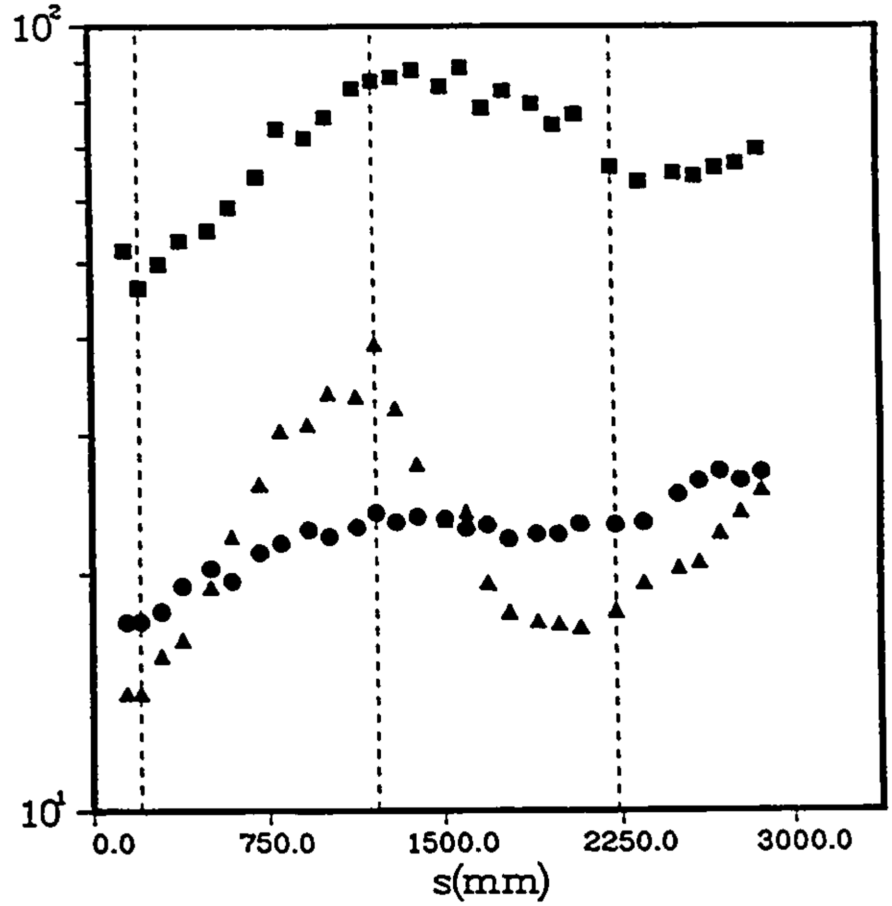

Figure 6.21: Development of integral length scales along section, for case NE; ■, L_{uu}; ▲, L_{vv}; ●, $L_{ww}(mm)$.

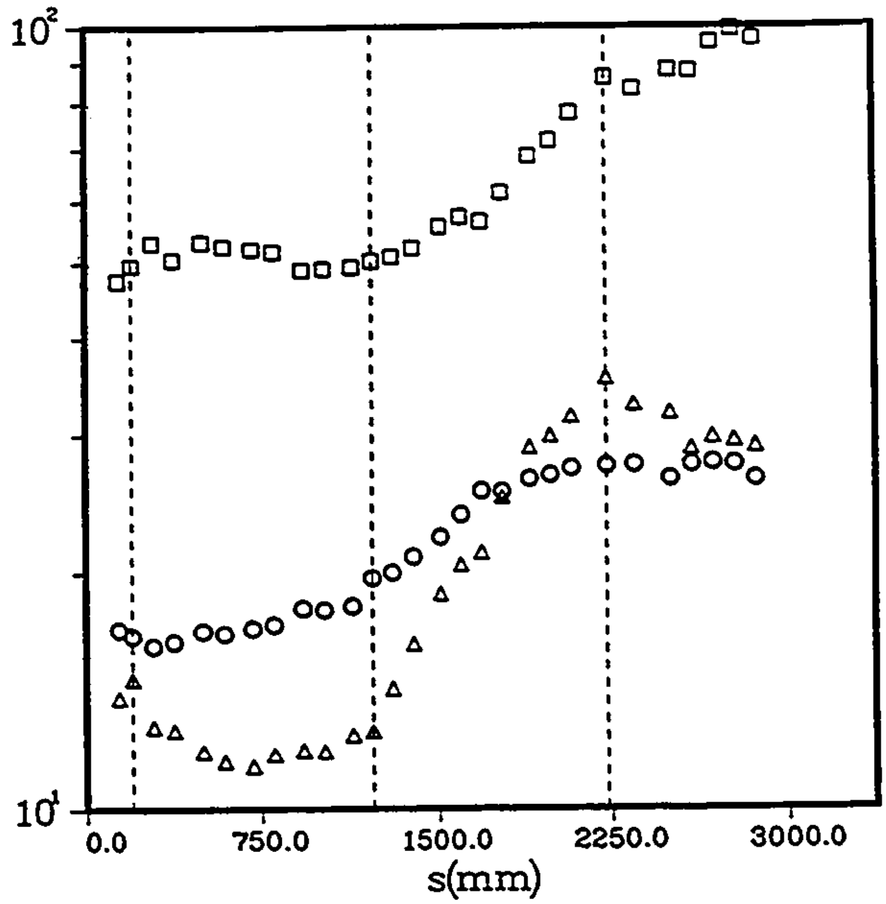

Figure 6.22: Development of integral length scales along section, for case PE; □, L_{uu}; △, L_{vv}; ∘, $L_{ww}(mm)$.

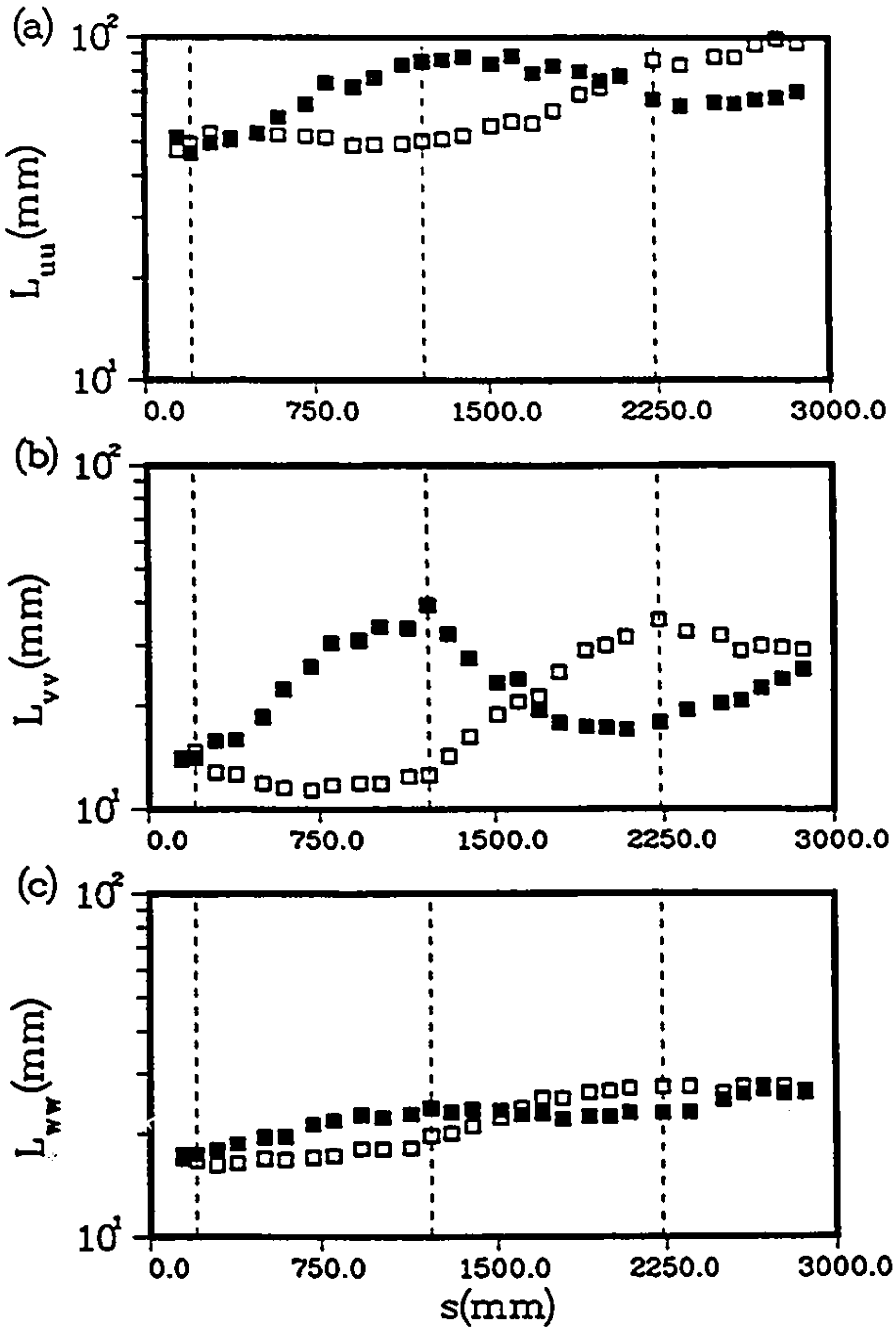

Figure 6.23: Comparison of development of integral length scales for NE and PE cases along section; ■, NE; □, PE; a) L_{uu}; b) L_{vv}; c) L_{ww}.

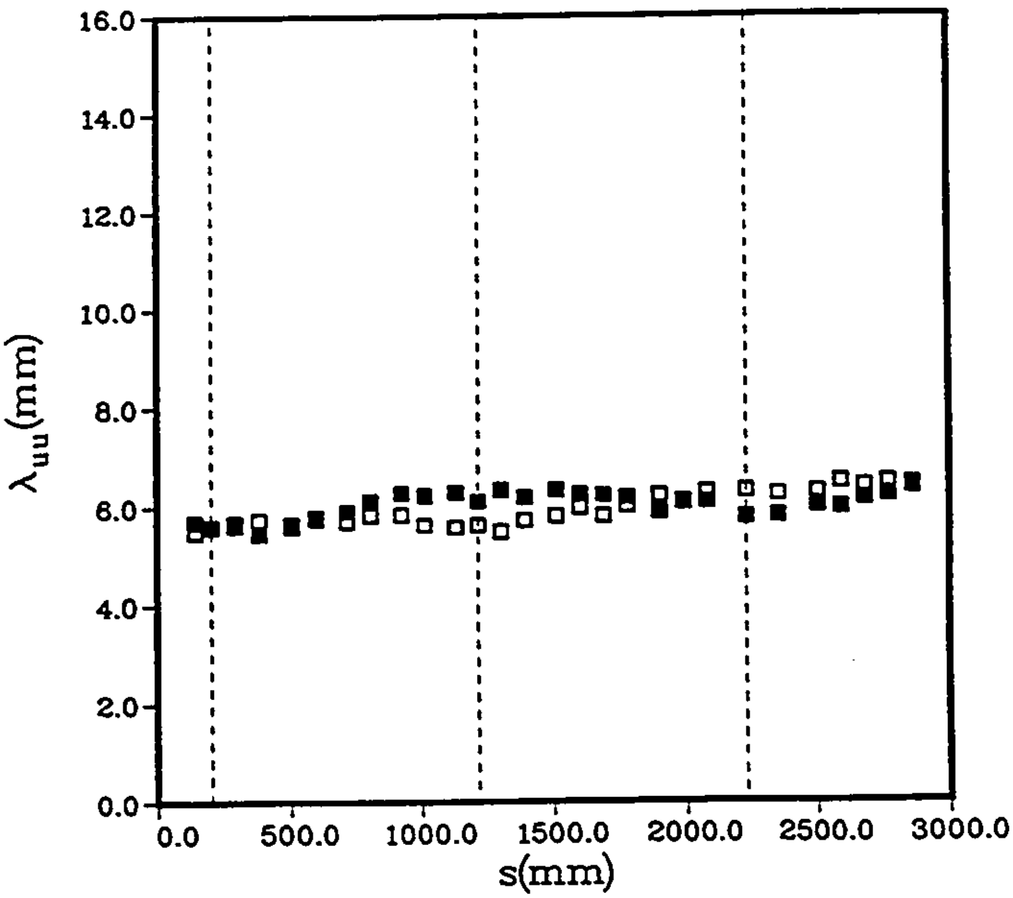

Figure 6.24: Streamwise Taylor microscale development along section; ■, NE; □, PE.

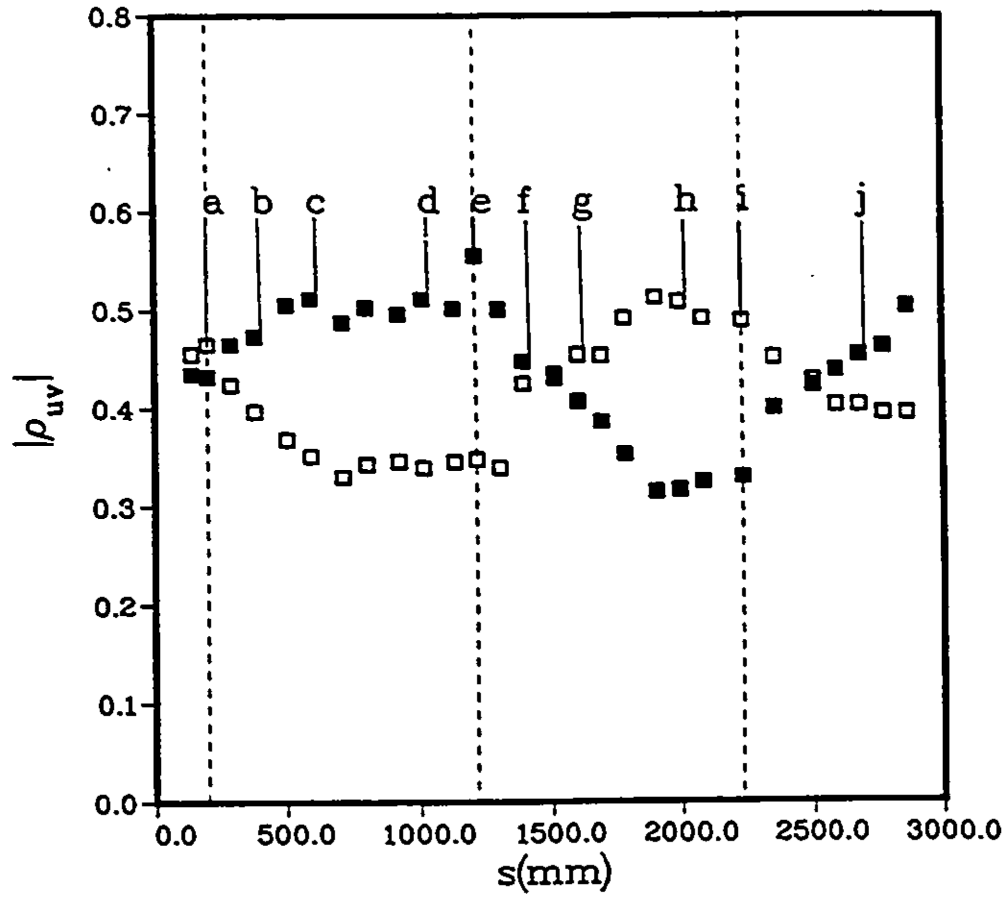

Figure 6.25: Streamwise development of correlation coefficient along section; ■, NE; □, PE; a, b, c, d, e, f, g, h, i, j, positions of spectral measurements.

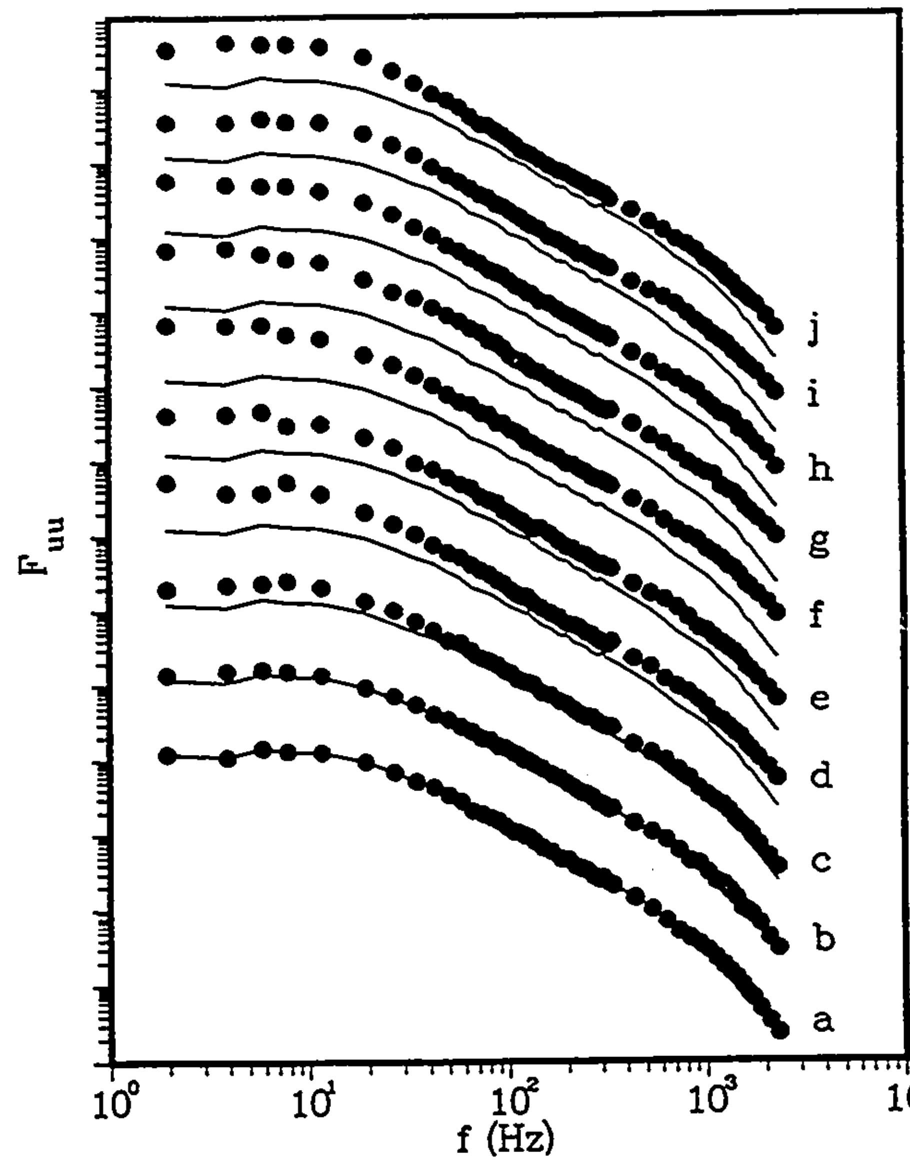

Figure 6.26: Streamwise development of streamwise one-dimensional frequency spectra along section for case NE; •, measurements; —, spectra at a, b, c, d, e, f, g, h, i, j positions specified in Figure 6.25; spectra are staggered by one decade.

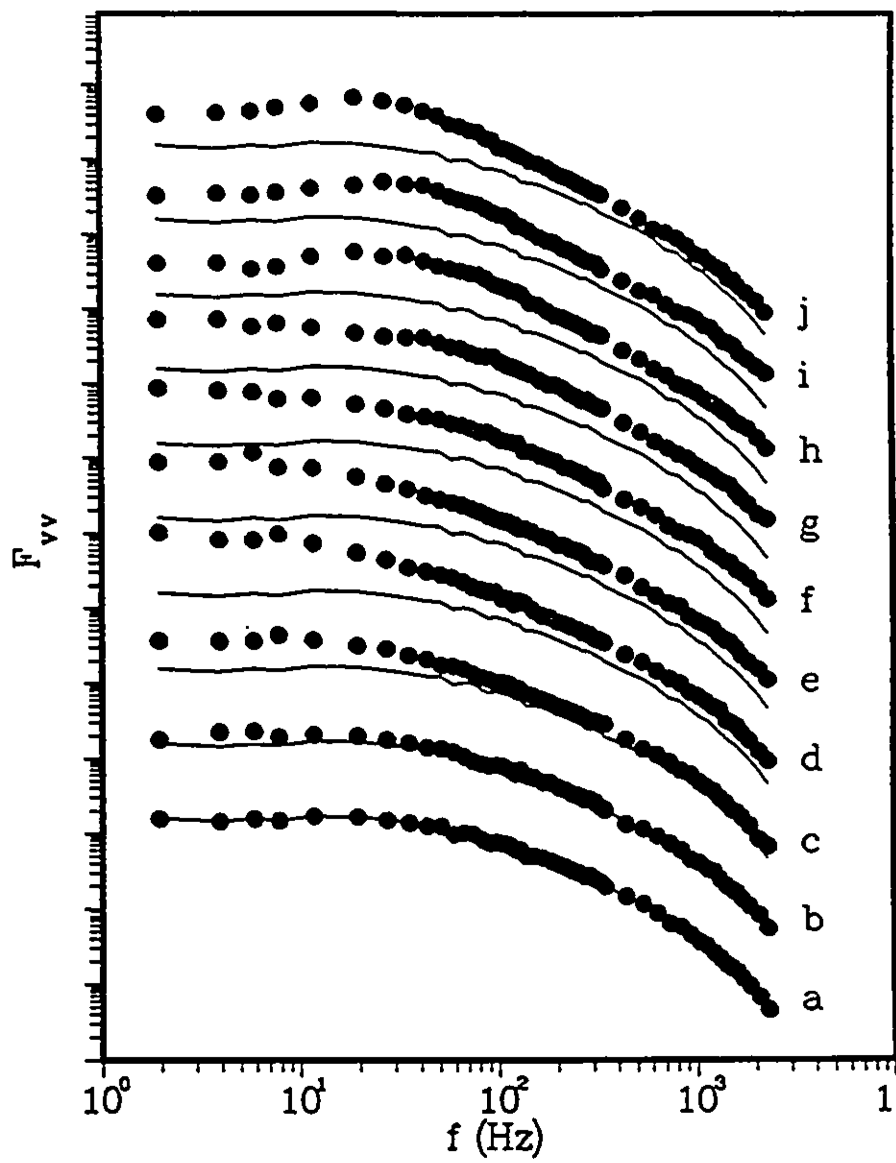

Figure 6.27: Streamwise development of transverse one-dimensional frequency spectra along section for case NE; (see Figure 6.26).

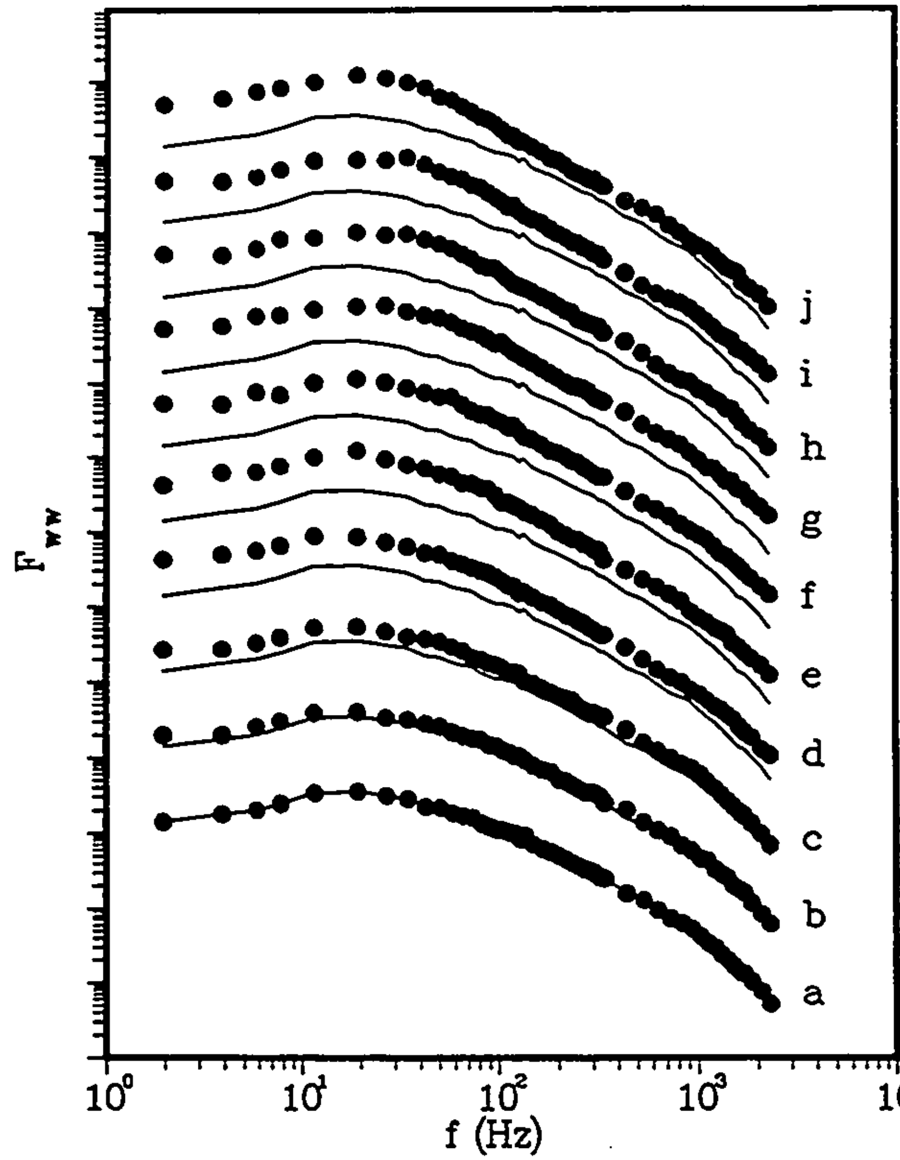

Figure 6.28: Streamwise development of spanwise one-dimensional frequency spectra along section for case NE; (see Figure 6.26).

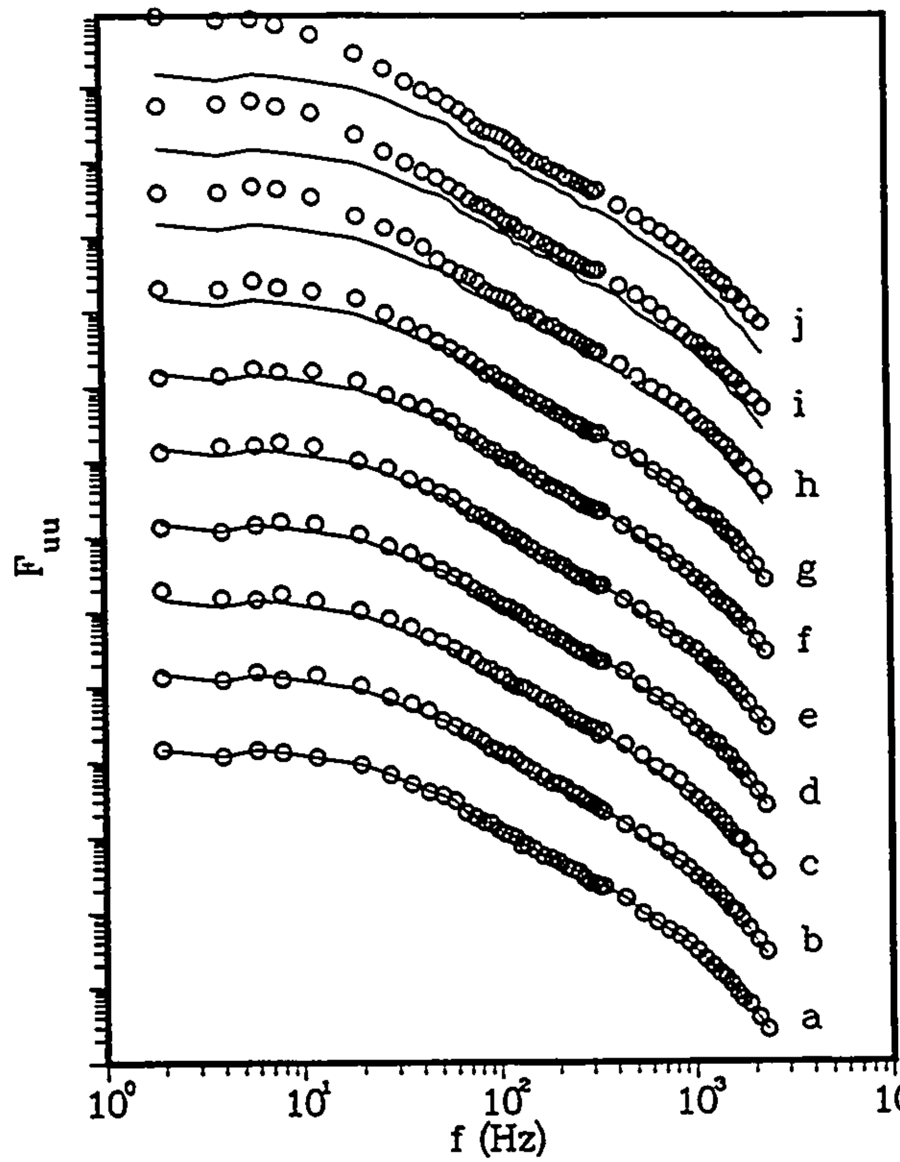

Figure 6.29: Streamwise development of streamwise one-dimensional frequency spectra along section for case PE; o, measurements; —, spectra at a; a, b, c, d, e, f, g, h, i, j positions specified in Figure 6.25; spectra are staggered by one decade.

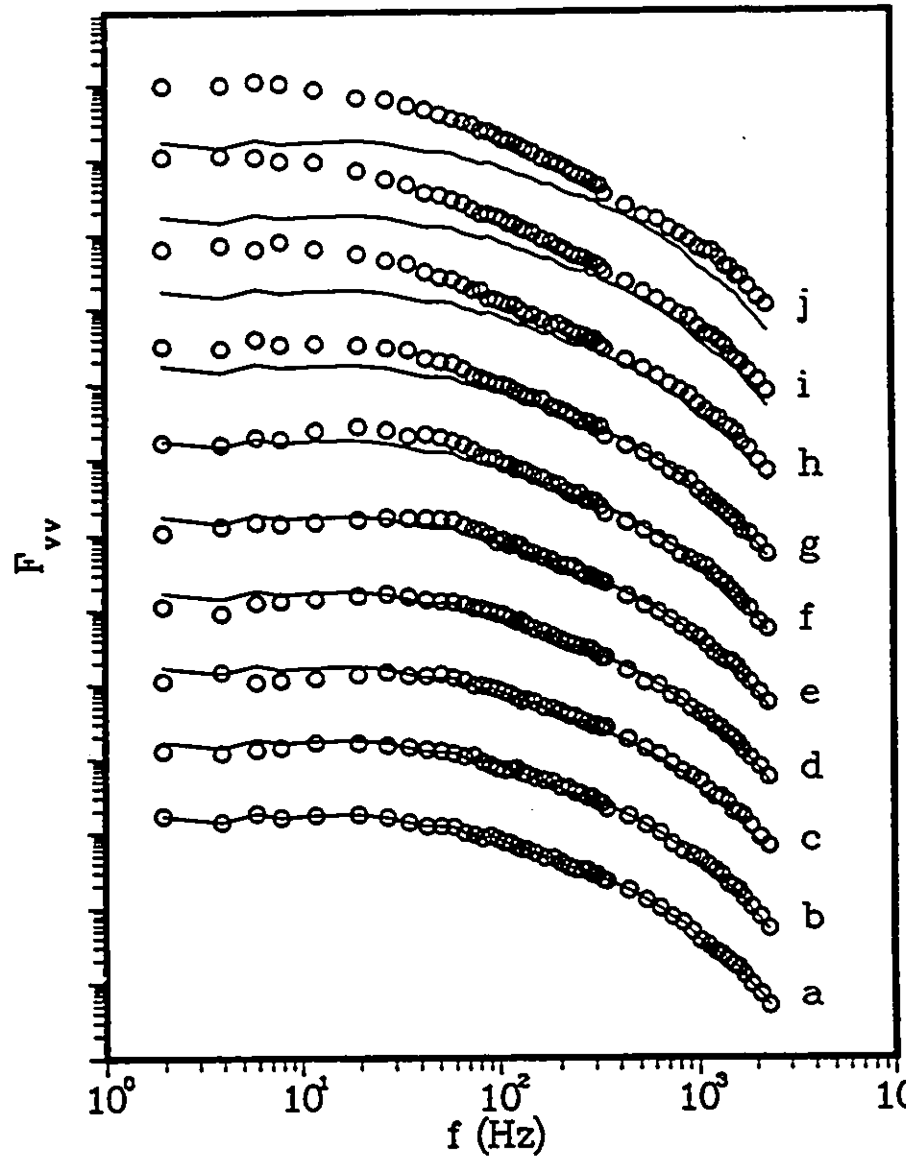

Figure 6.30: Streamwise development of transverse one-dimensional frequency spectra along section for case PE; (see Figure 6.29).

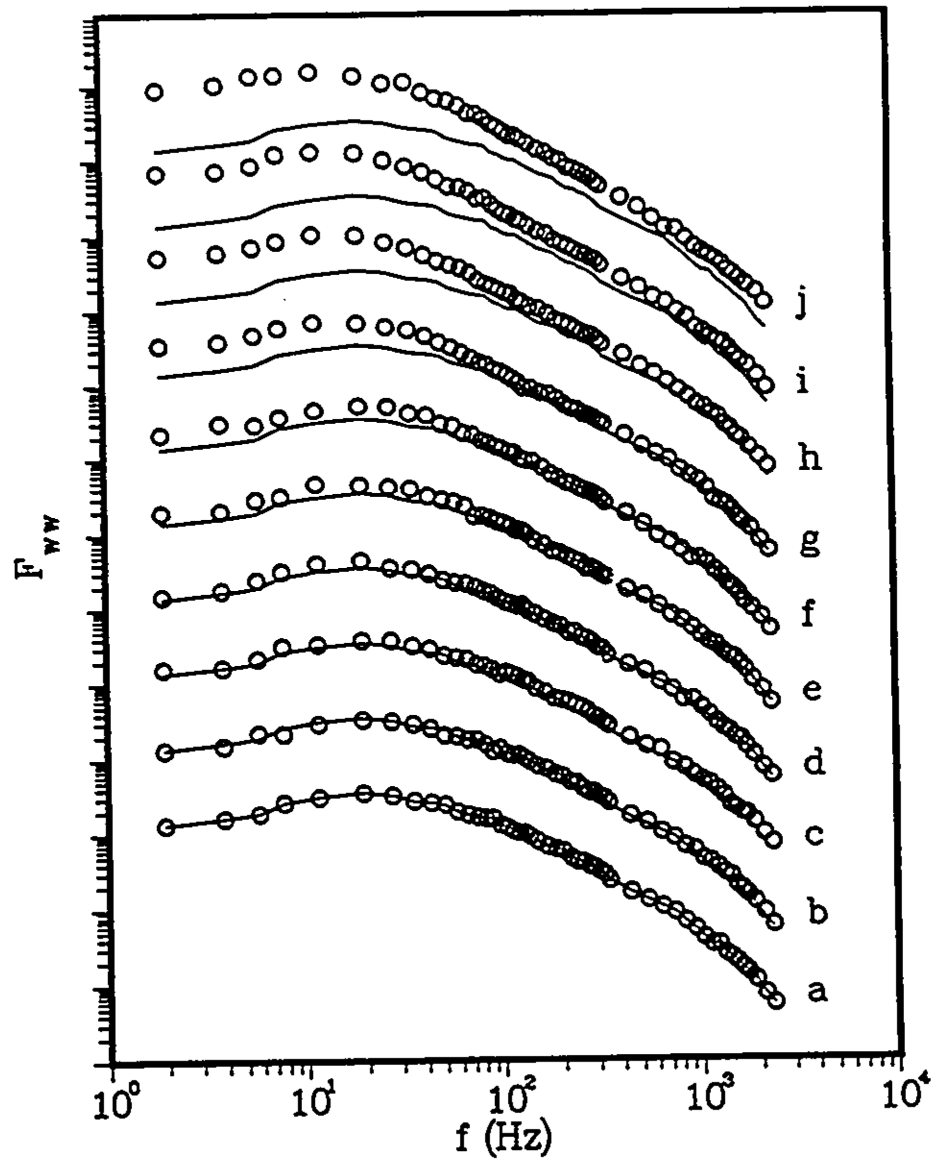

Figure 6.31: Streamwise development of spanwise one-dimensional frequency spectra along section for case PE; (see Figure 6.29).

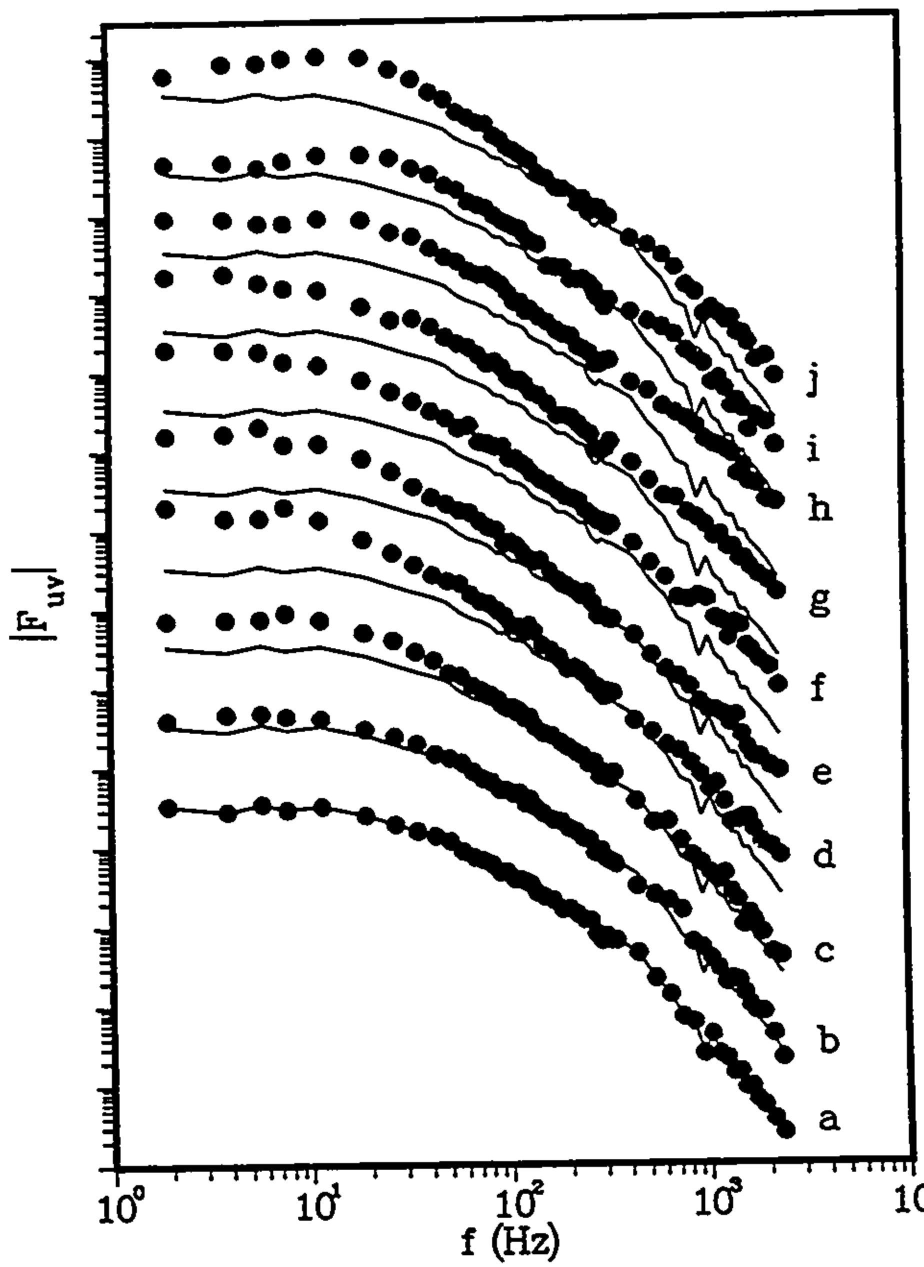

Figure 6.32: Streamwise development of one dimensional frequency cross spectra along section for case NE; (see Figure 6.26).

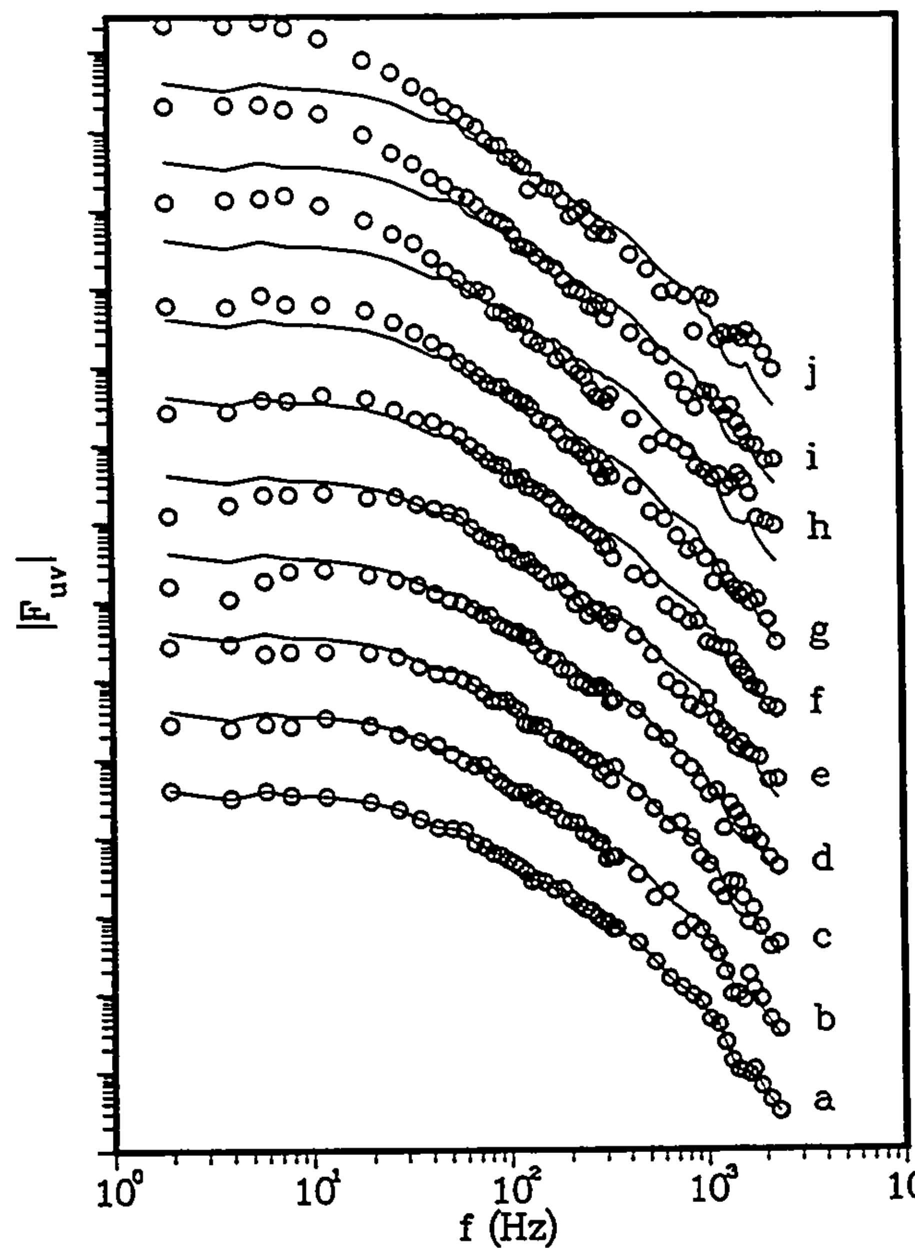

Figure 6.33: Streamwise development of one dimensional frequency cross spectra along section for case PE; (see Figure 6.29).

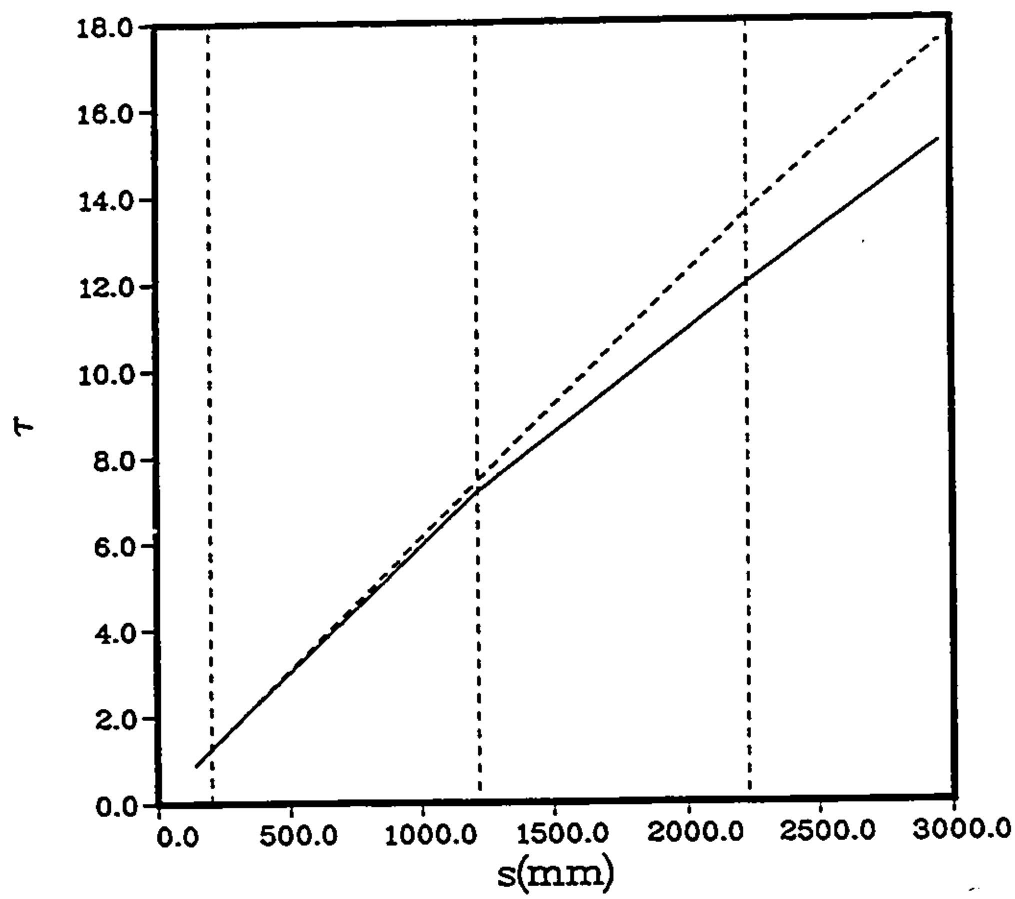

Figure 7.1: Total strain versus streamwise distance; — — ——, NE; — — —, PE.

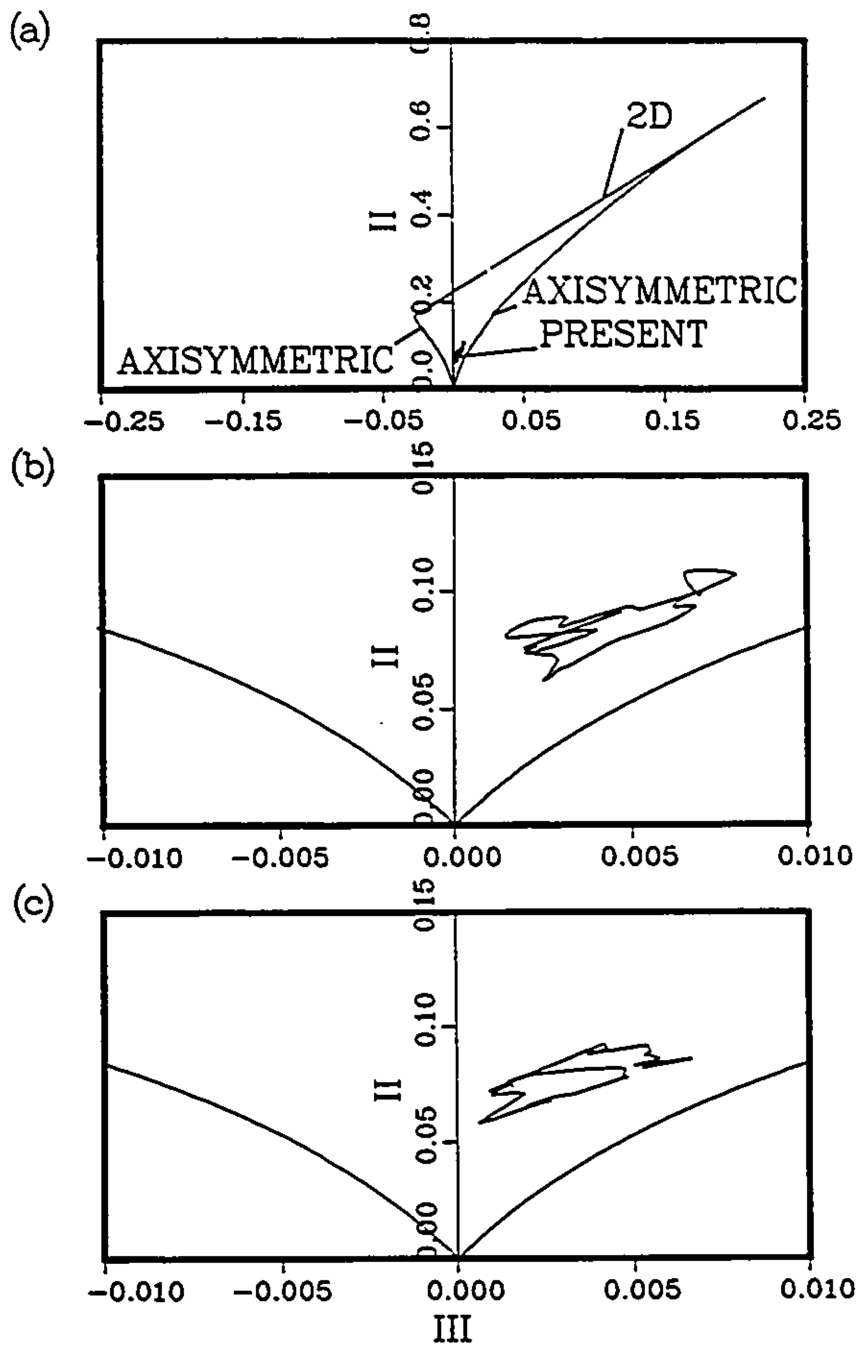

Figure 7.2: Variation of second and third invariants of anisotropy tensor; a) comparison to axisymmetric and 2D turbulence; b) case NE; c) case PE.

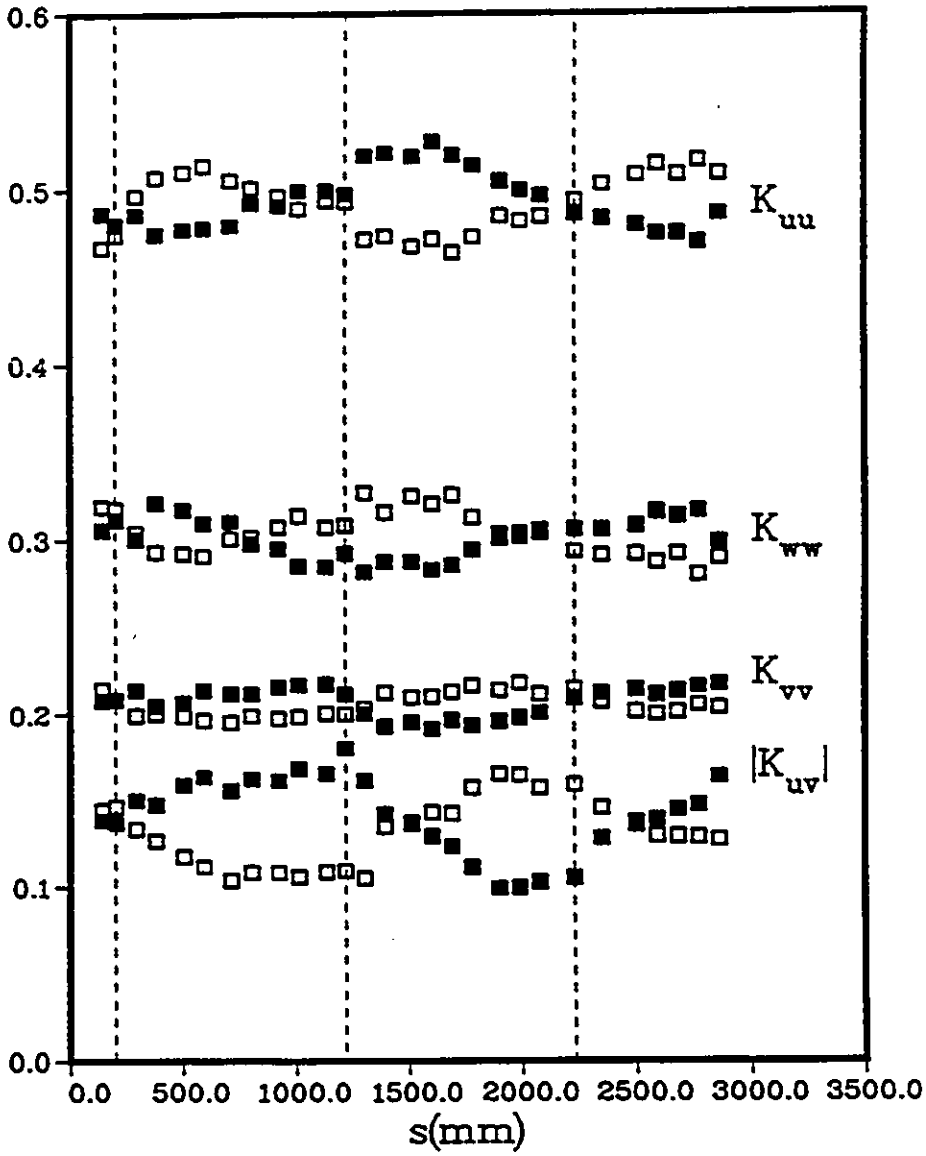

Figure 7.3: Structural tensor components along double curved section; ■, *NE*; □, *PE*.

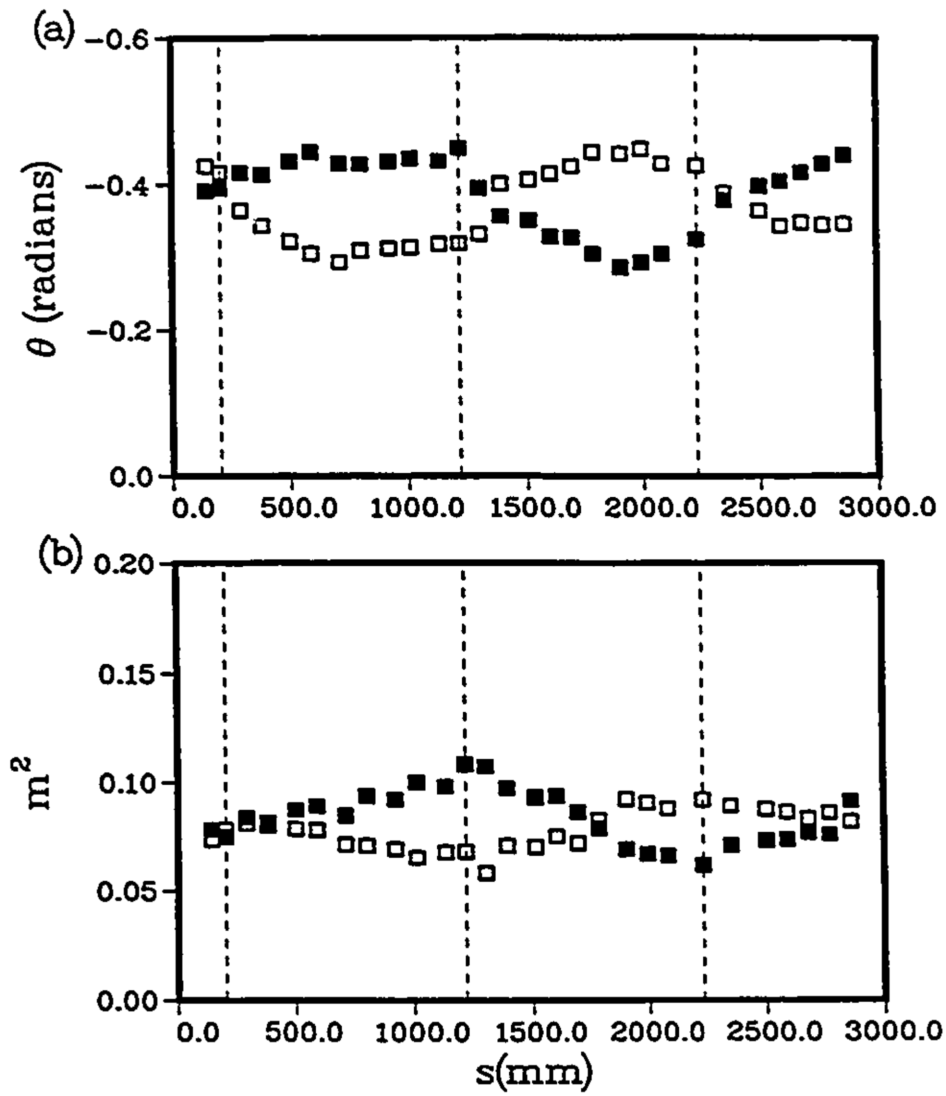

Figure 7.4: a) Development of angle of maximum normal stresses; b) Development of the anisotropy scalar. ■, NE; □, PE.

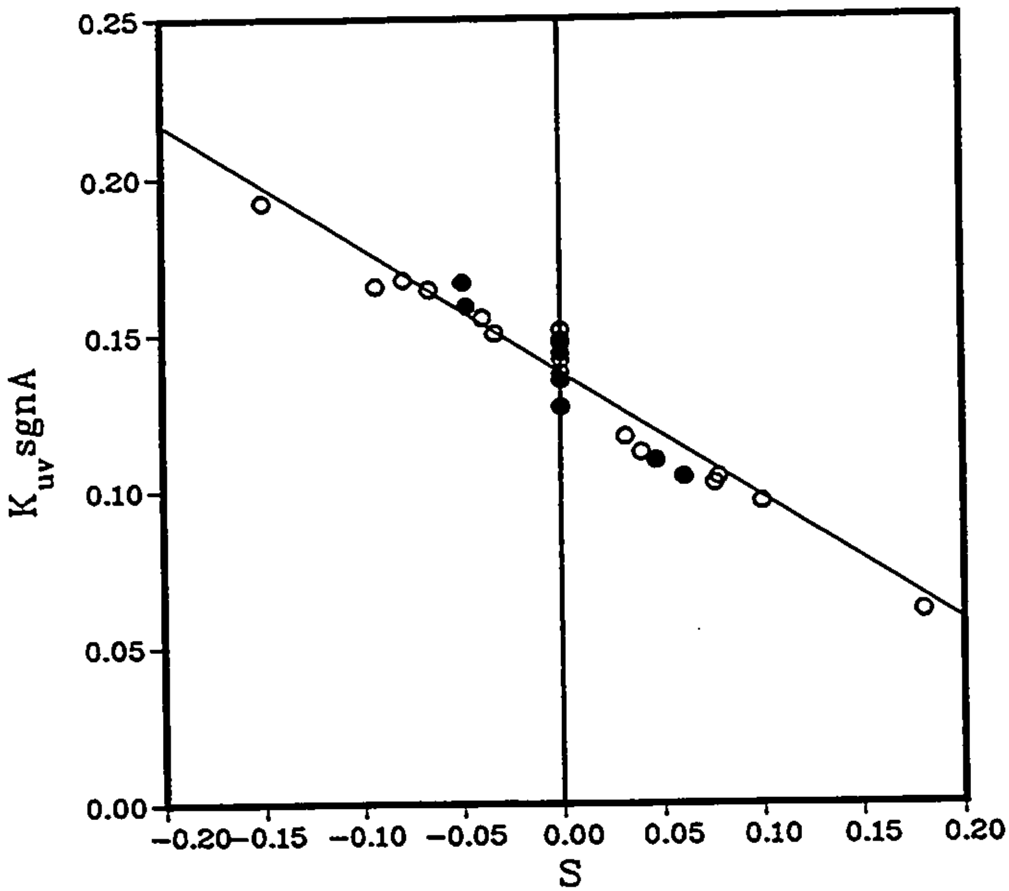

Figure 7.5: Variation of structural parameter with curvature shear parameter; o, $HT1$; •, Present measurements;—, equation 7.7.

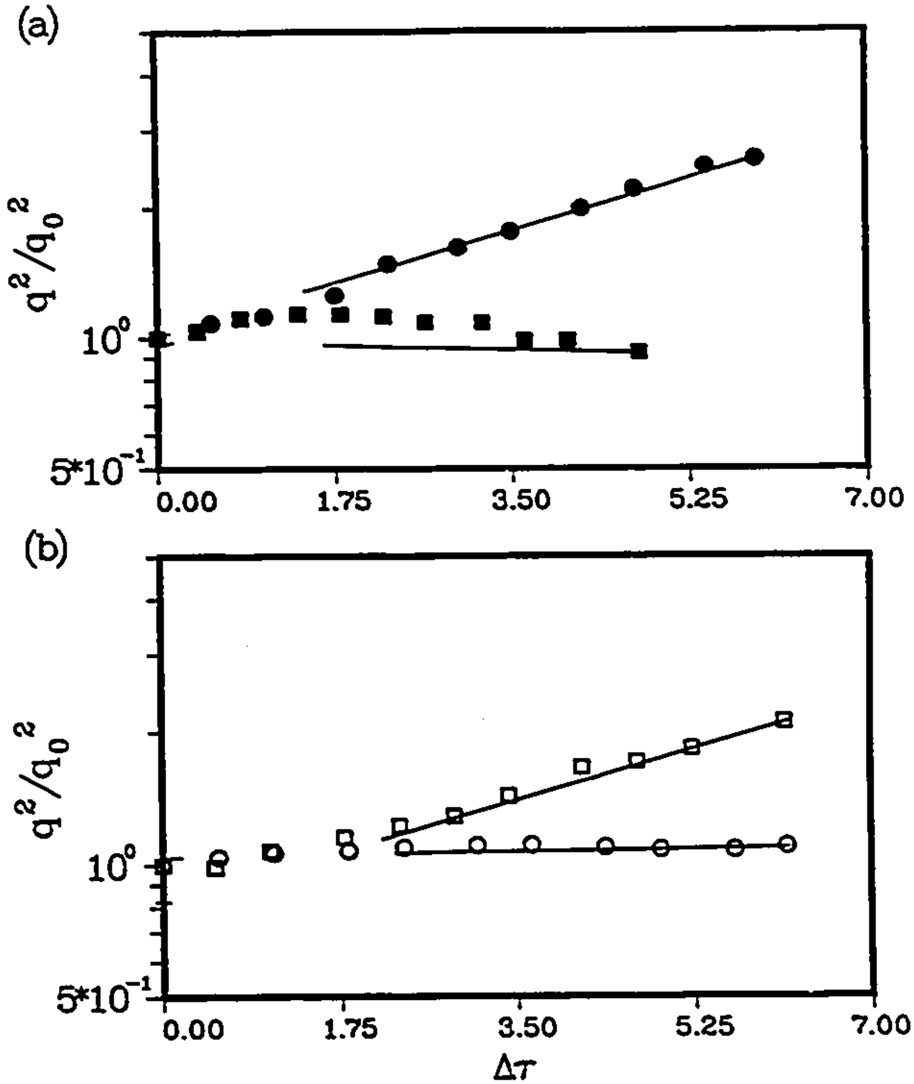

Figure 7.6: Kinetic energy development; a) Case NE: •, $S = -.049$; □, $S = .061$; b) Case PE: ○, $S = .047$; □, $S = -.0472$; —, slope obtained from equation 7.9.

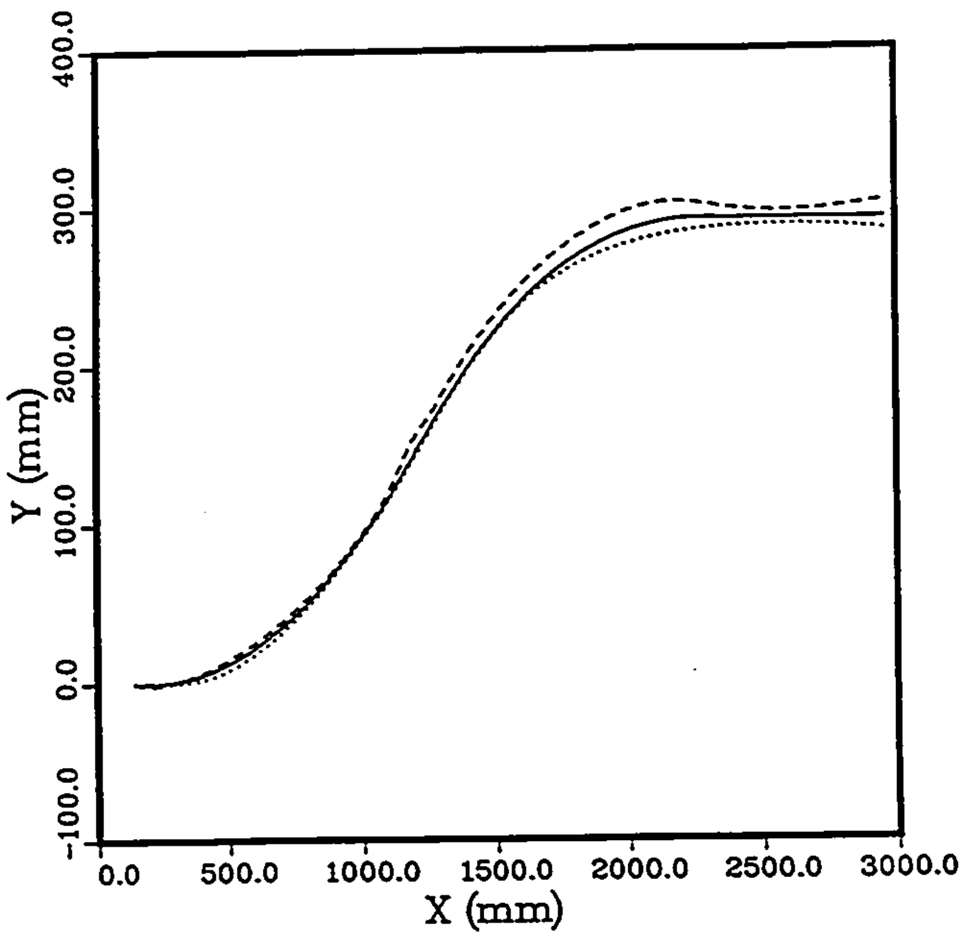

Figure 7.7: Deviation of central streamline; - - - NE; ..... PE; —— geometric centerline.

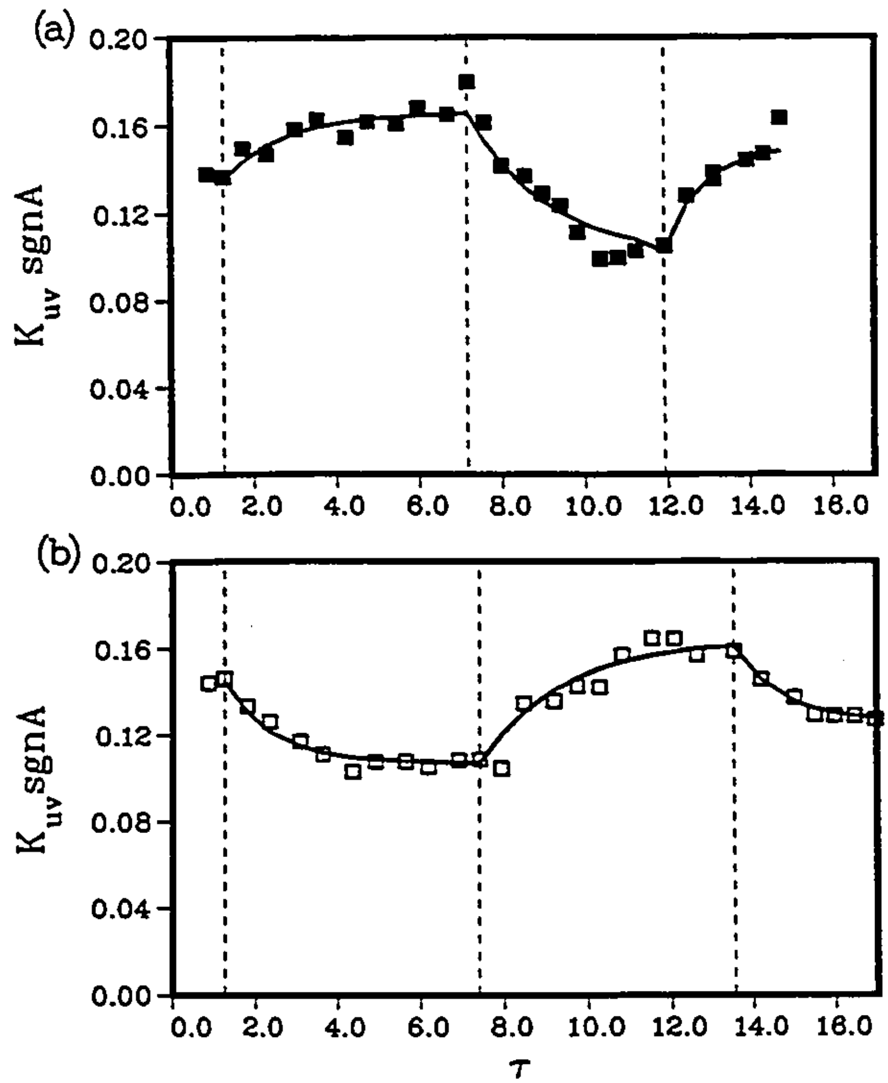

Figure 7.8: Reynolds shear stress structural parameter development and adjustment along section; ——, equation 7.10; ■, □, measurement points; a) case NE; b) case PE.

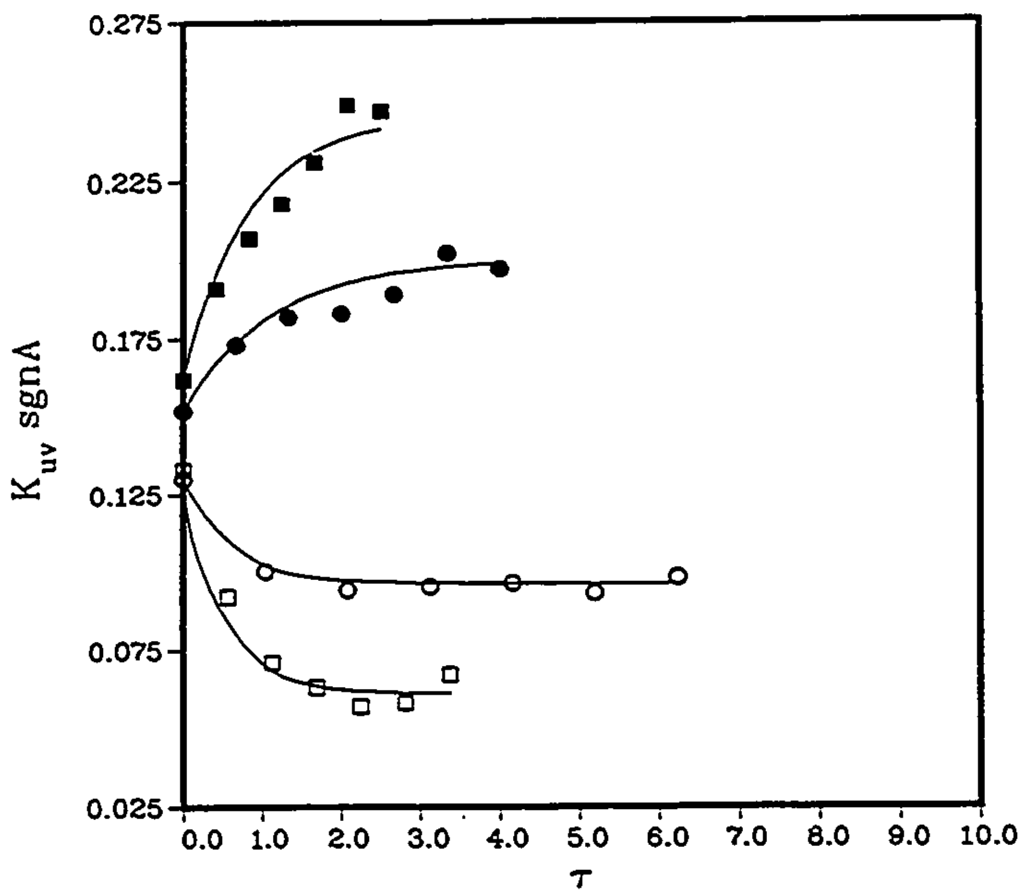

Figure 7.9: Reynolds shear stress structural parameter development and adjustment (Measurements of HT1); ◻, S=.18 and T=0.5; o, S=0.10 and T=0.6; ◻, S=-0.15 and T=1.1; ◻, S=-0.25 and T=0.9.

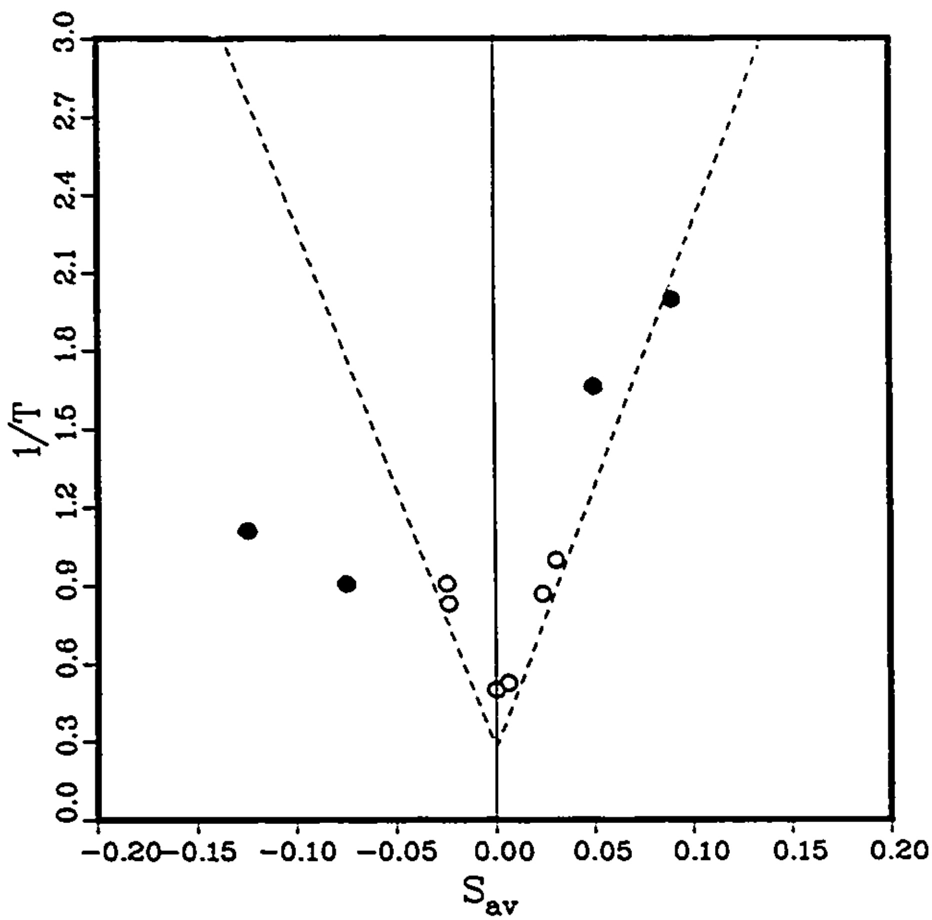

Figure 7.10: Variation of time scale of adjustment with curvature parameter; o present measurements; —— equation 7.18; •, HT1.

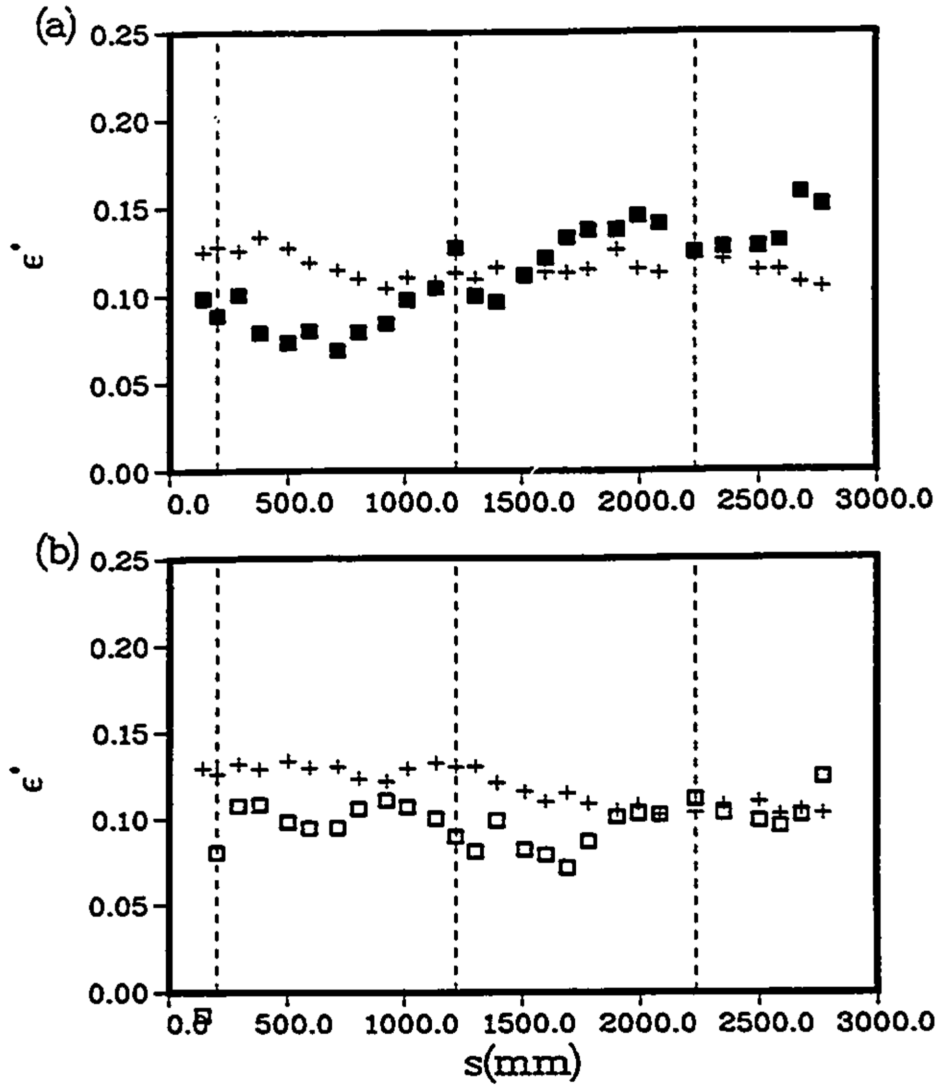

Figure 7.11: Development of dissipation; +, from isotropic relation; ■, □, from energy balance; a) case NE; b) case PE.

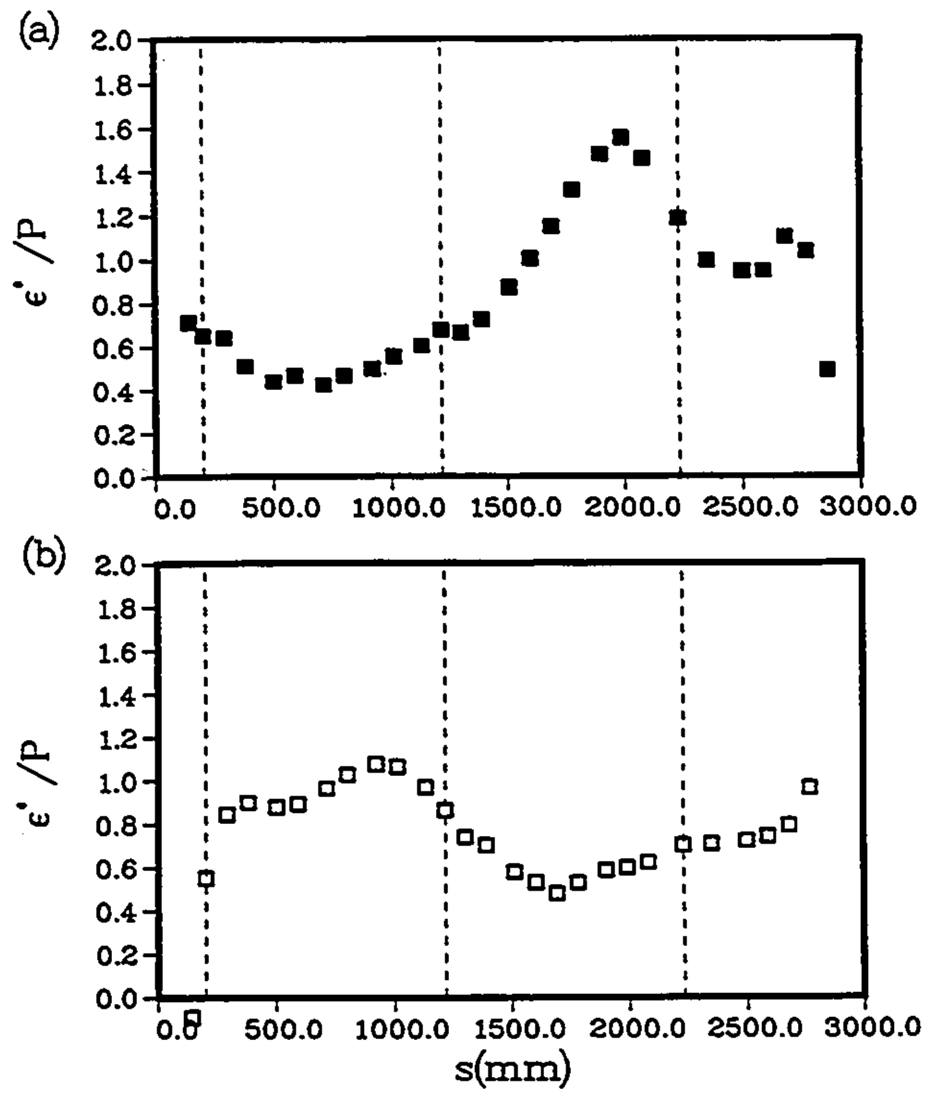

Figure 7.12: Development of dissipation to production ratio; a) case NE; b) case PE.

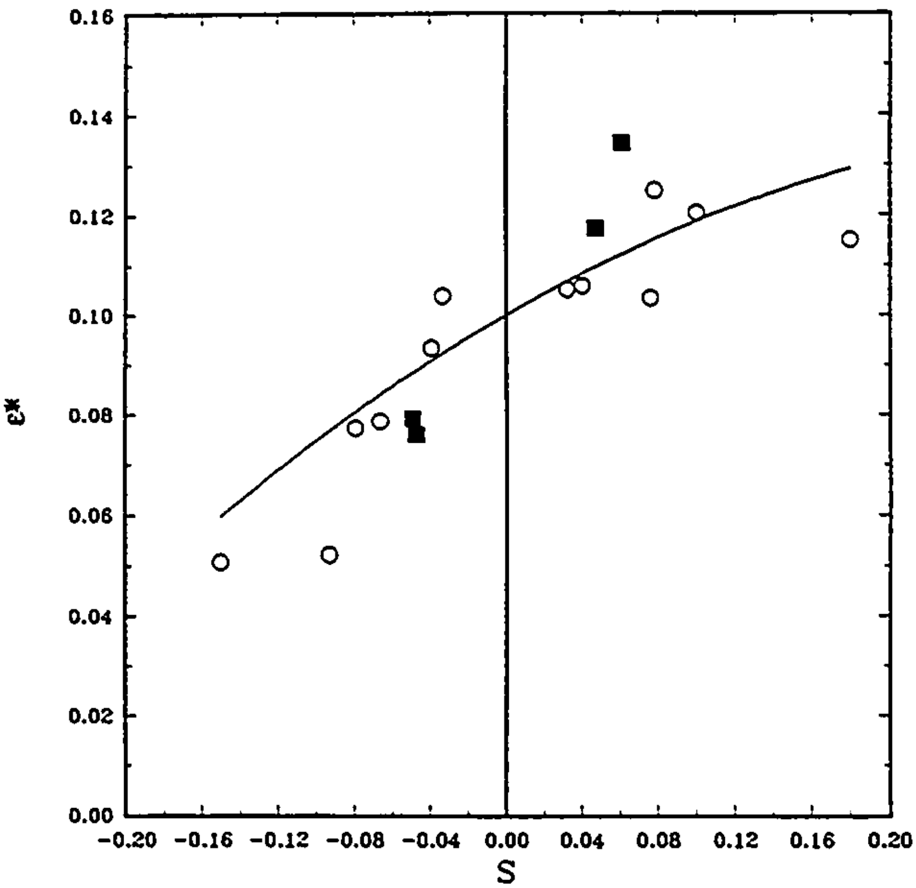

Figure 7.13: Variation of dissipation with curvature parameter; ■, present measurements; o, HT1; —, equation 7.21.

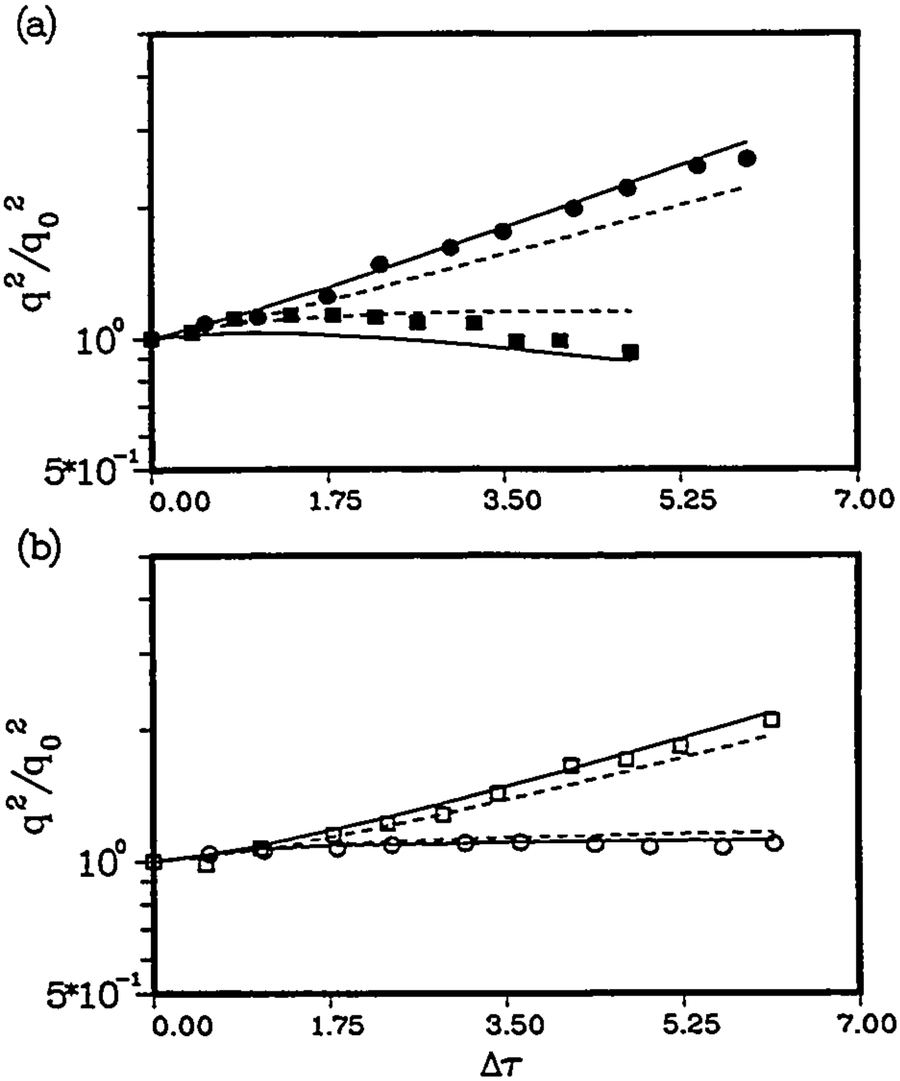

Figure 7.14: Kinetic energy development; a) Case NE: •, S=-.049; ■, S=.061; - - - -, equation 7.22, $\epsilon^* = 0.1$; ——, equation 7.22, $\epsilon^* = f(S)$; b) Case PE: ○, S=.047; □, S=-.0472; - - - -, equation 7.22 $\epsilon^* = 0.1$; ——, equation 7.22 $\epsilon^* = f(S)$.

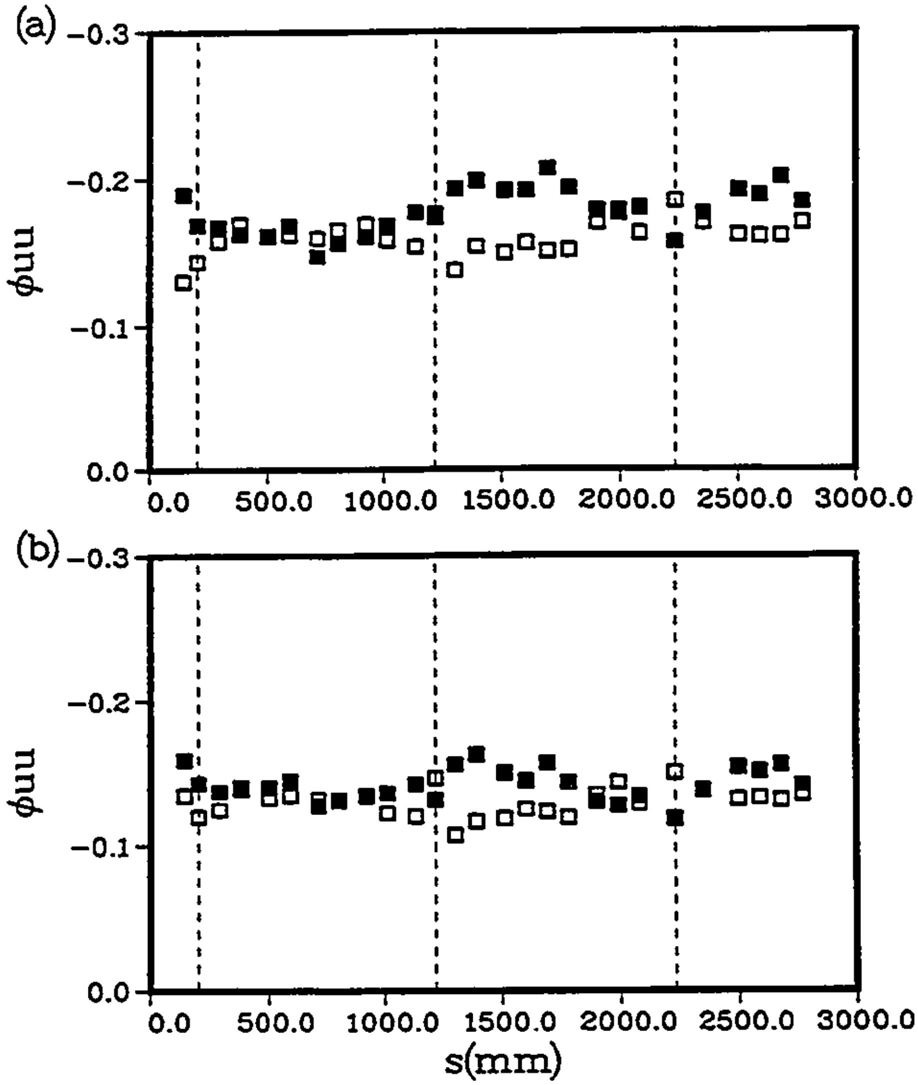

Figure 7.15: Development of the streamwise pressure strain covariance; □, NE; □, PE; a) assuming isotropy of dissipation; b) assuming anisotropy of dissipation equal to anisotropy of Reynolds stresses.

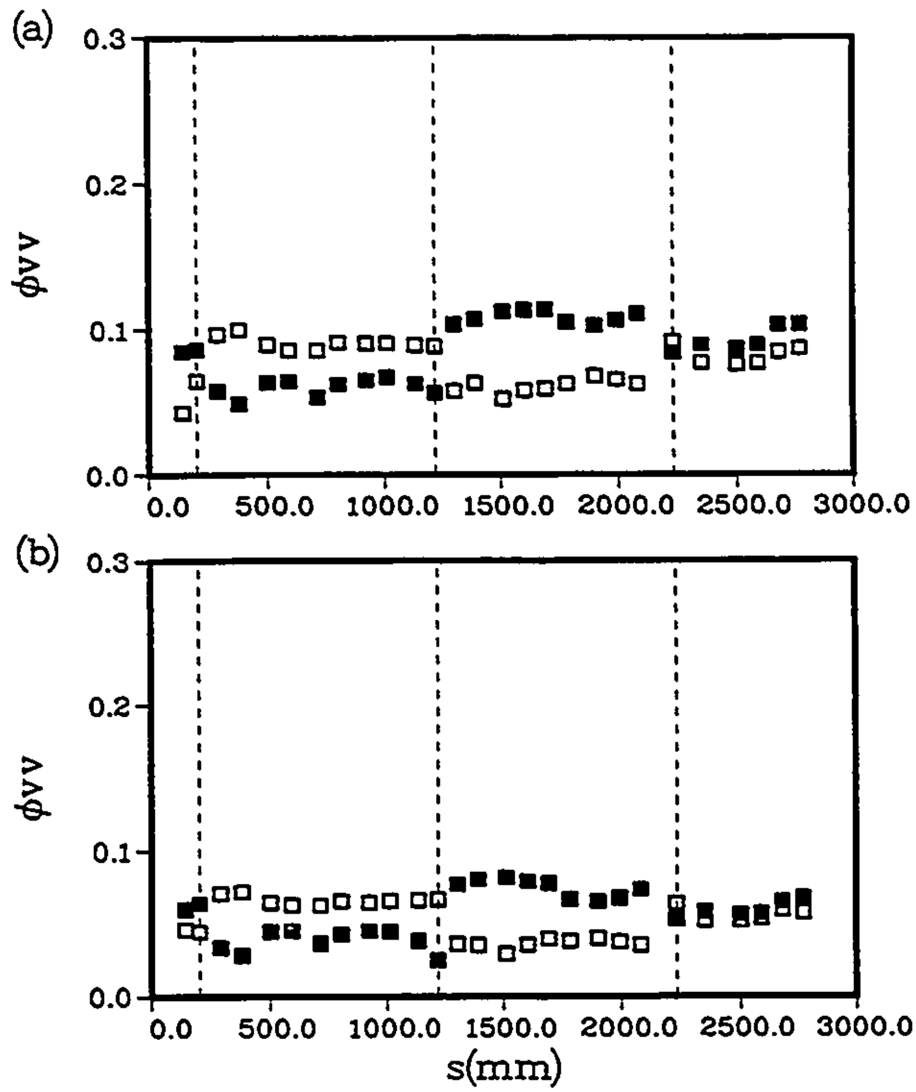

Figure 7.16: Development of the transverse pressure strain covariance; □, *NE*; □, *PE*; a) assuming isotropy of dissipation; b) assuming anisotropy of dissipation equal to anisotropy of Reynolds stresses.

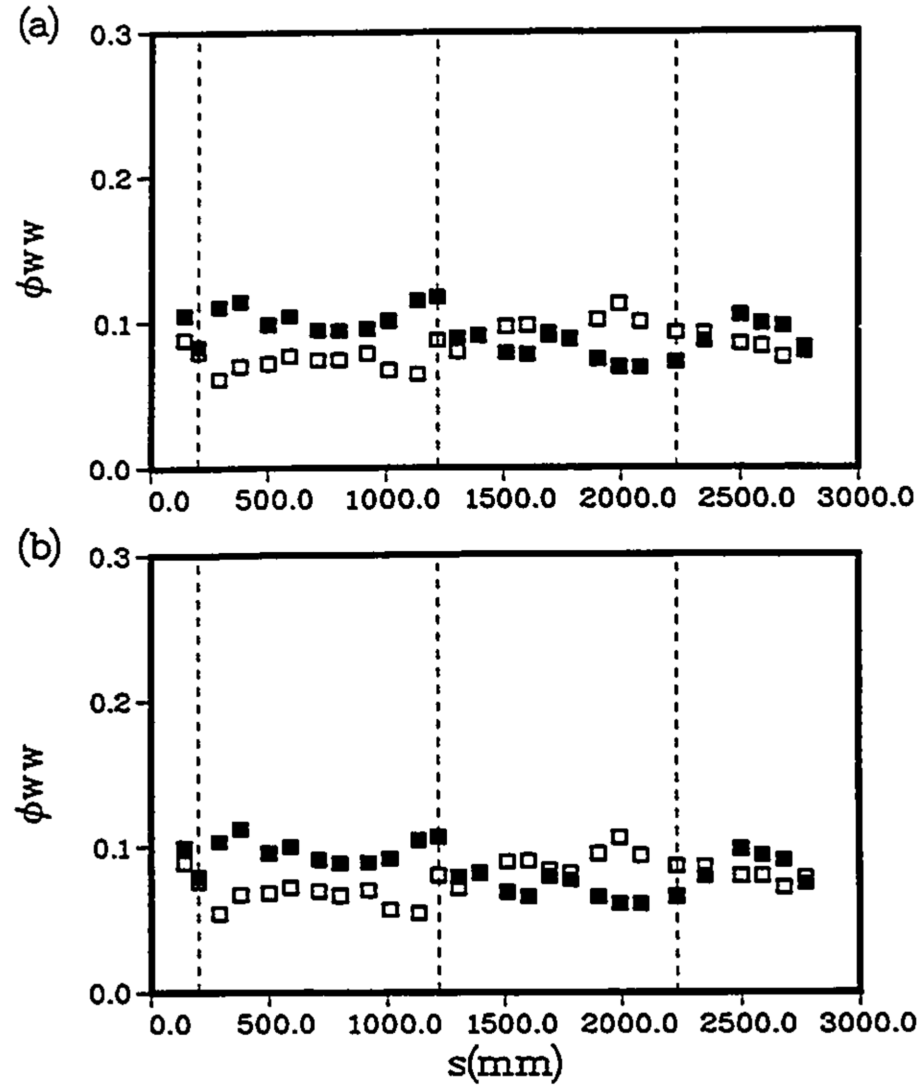

Figure 7.17: Development of the spanwise pressure strain covariance; □, NE; □, PE; a) assuming isotropy of dissipation; b) assuming anisotropy of dissipation equal to anisotropy of Reynolds stresses.

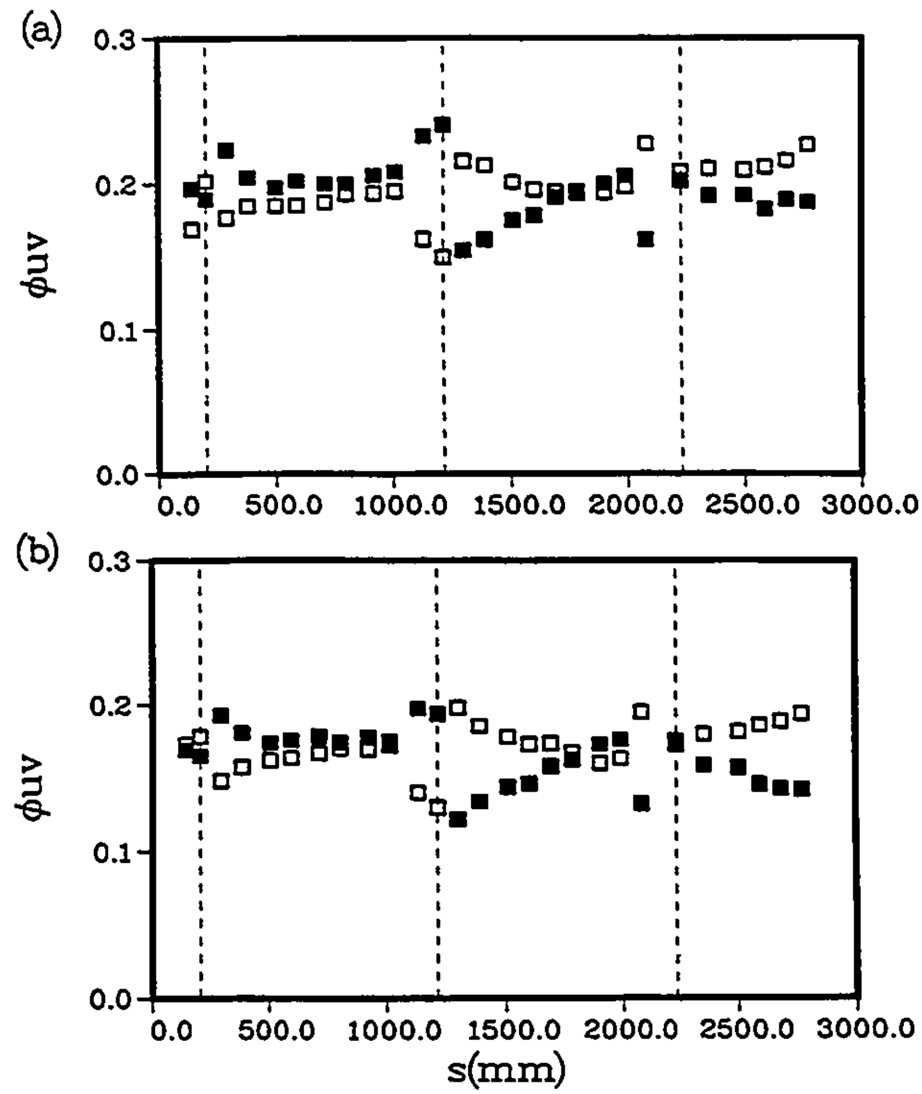

Figure 7.18: Development of the streamwise-transverse pressure strain covariance; □, NE; □, PE; a) assuming isotropy of dissipation. b) assuming anisotropy of dissipation equal to anisotropy of Reynolds stresses.

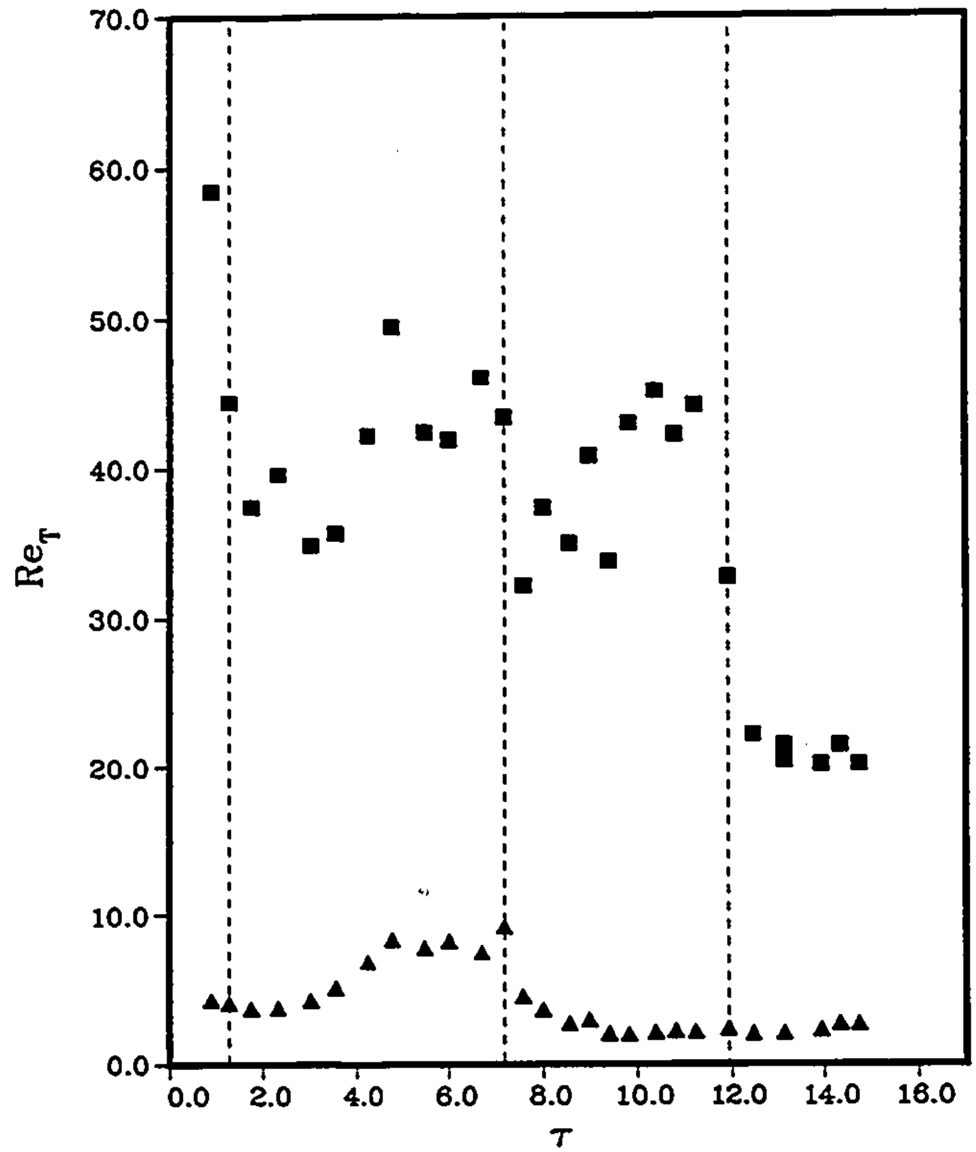

Figure 7.19: Variation of the effective Reynolds number Re_T for case NE; ■, Re_t based on L_{uu}; Δ, Re_t based on L_{vv}.

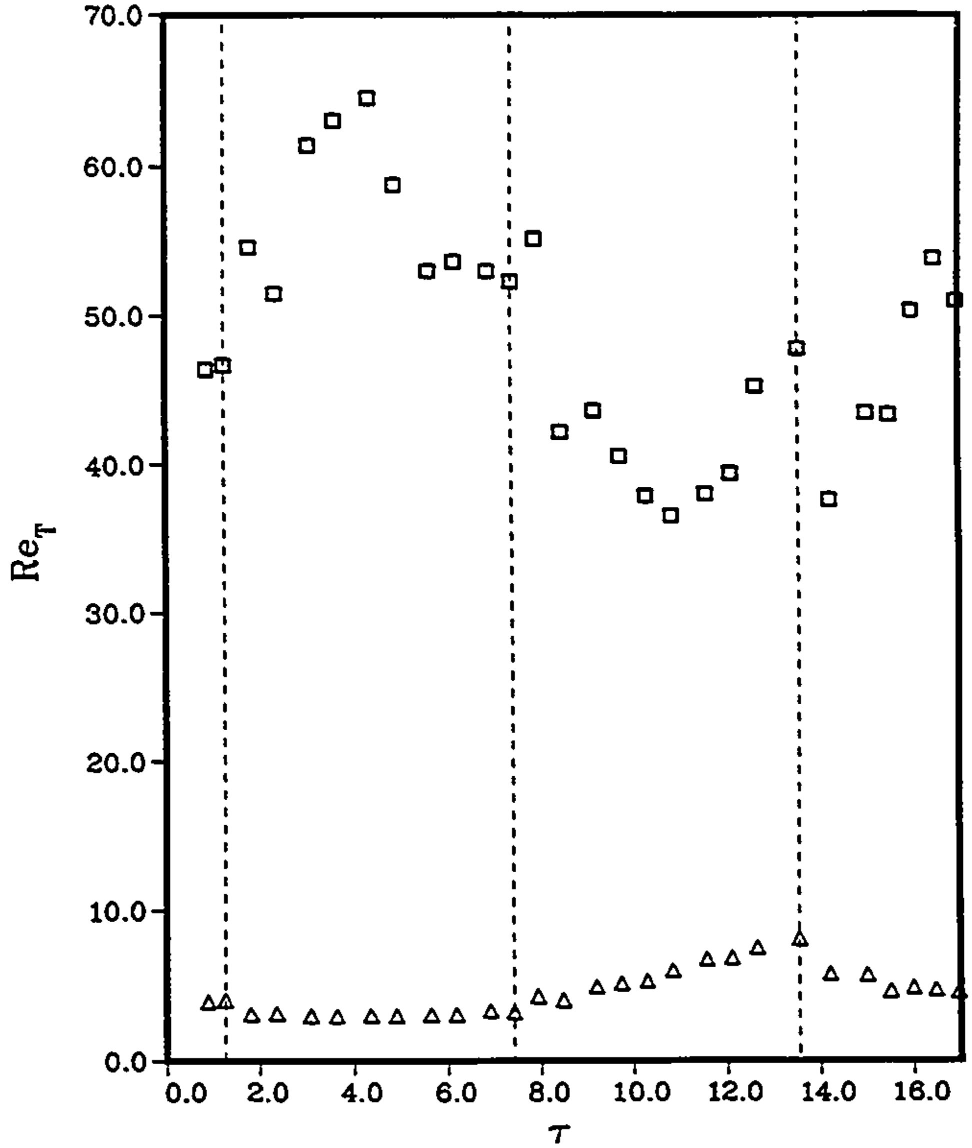

Figure 7.20: Variation of the effective Reynolds number Re_T for case PE; □, Re_t based on L_{uu}; △, Re_t based on L_{vv}.

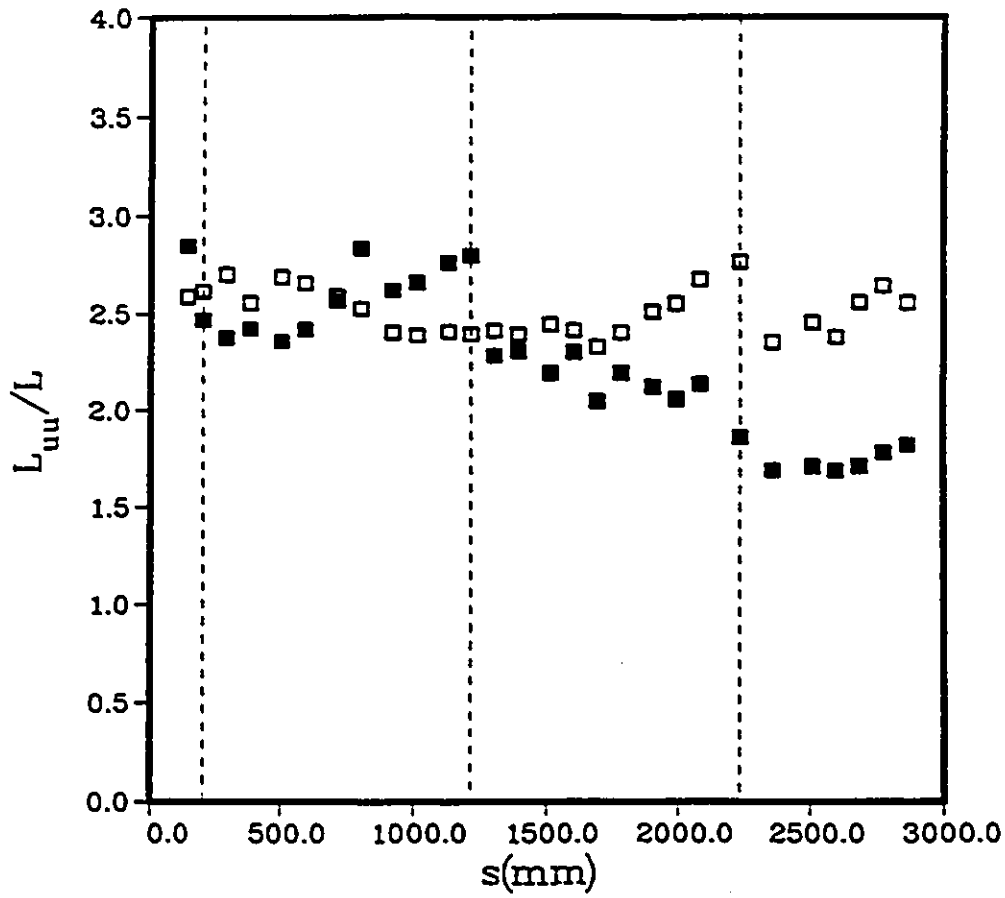

Figure 7.21: Variation of $\frac{L_{uu}}{L}$; ■, NE case; □, PE case.

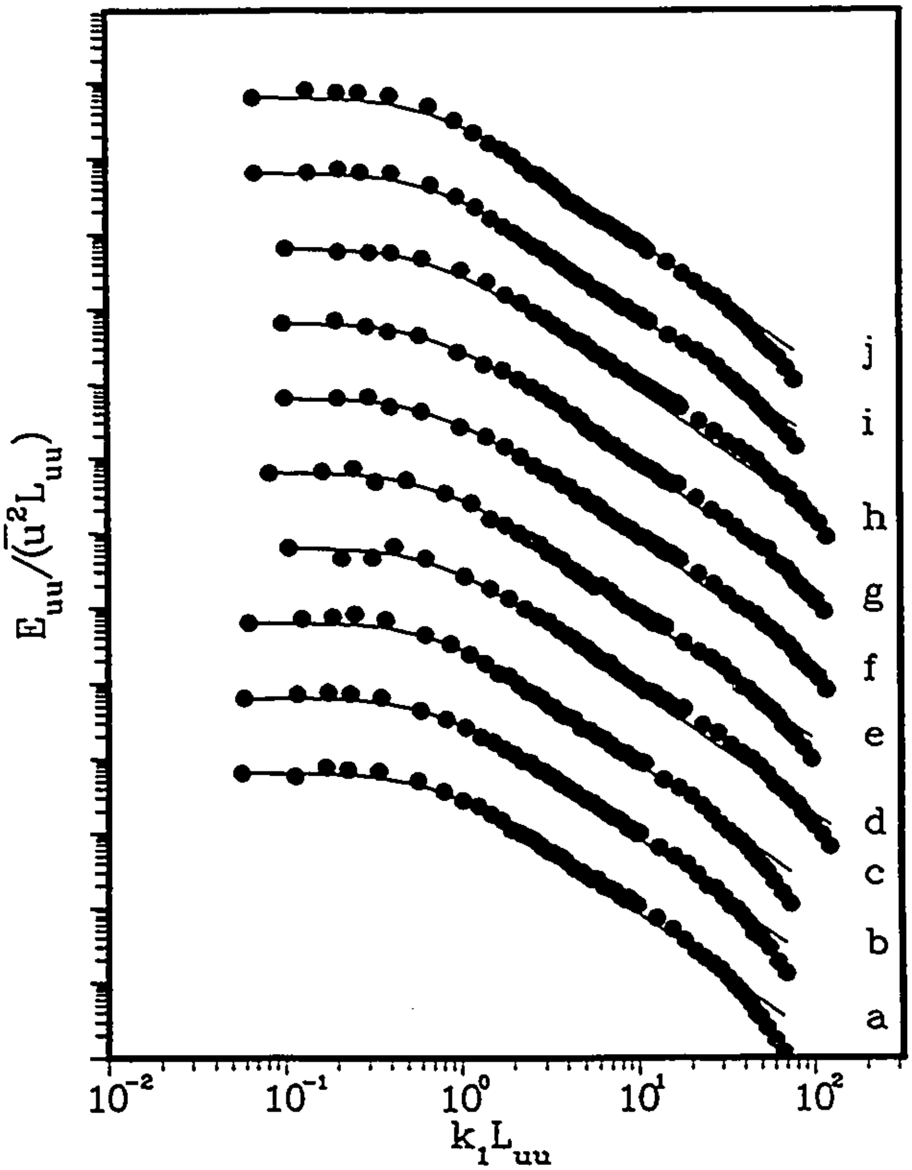

Figure 7.22: Streamwise development of nondimensional streamwise one dimensional wave spectra along section for case NE; o, measurement points; —, isotropic spectra; a, b, c, d, e, f, g, h, i, j positions specified in Figure 6.25. Spectra are staggered by one decade.

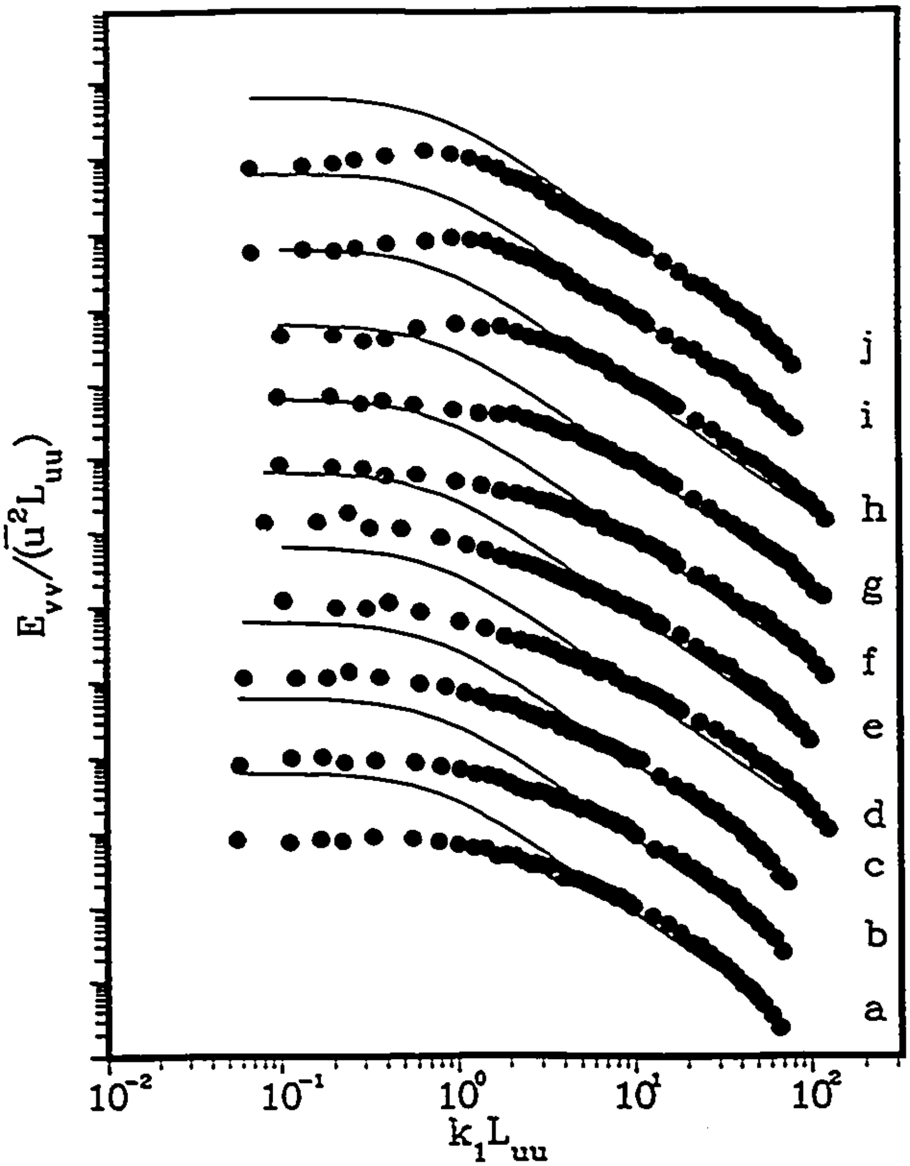

Figure 7.23: Streamwise development of nondimensional transverse one dimensional wave spectra along section for case NE (see Figure 7.22).

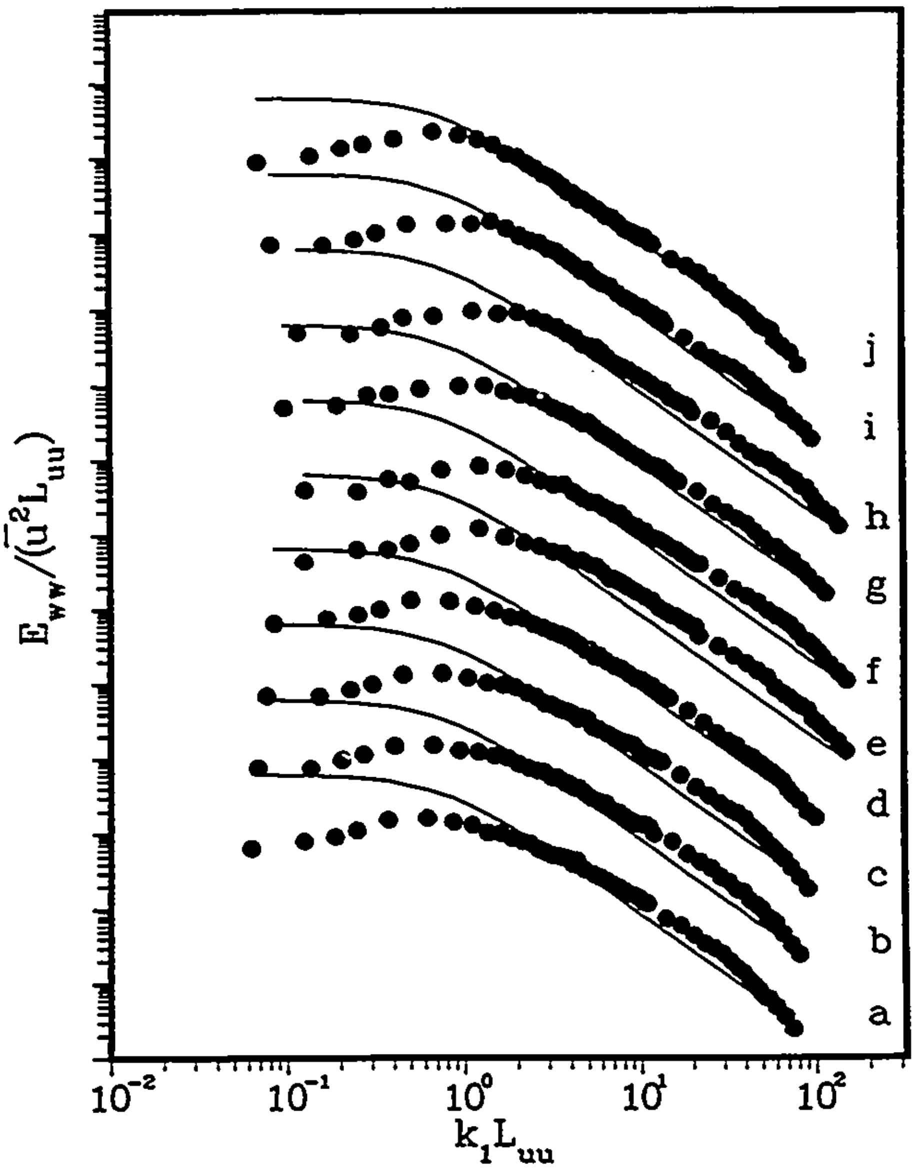

Figure 7.24: Streamwise development of nondimensional spanwise one dimensional wave spectra along section for case NE (see Figure 7.22).

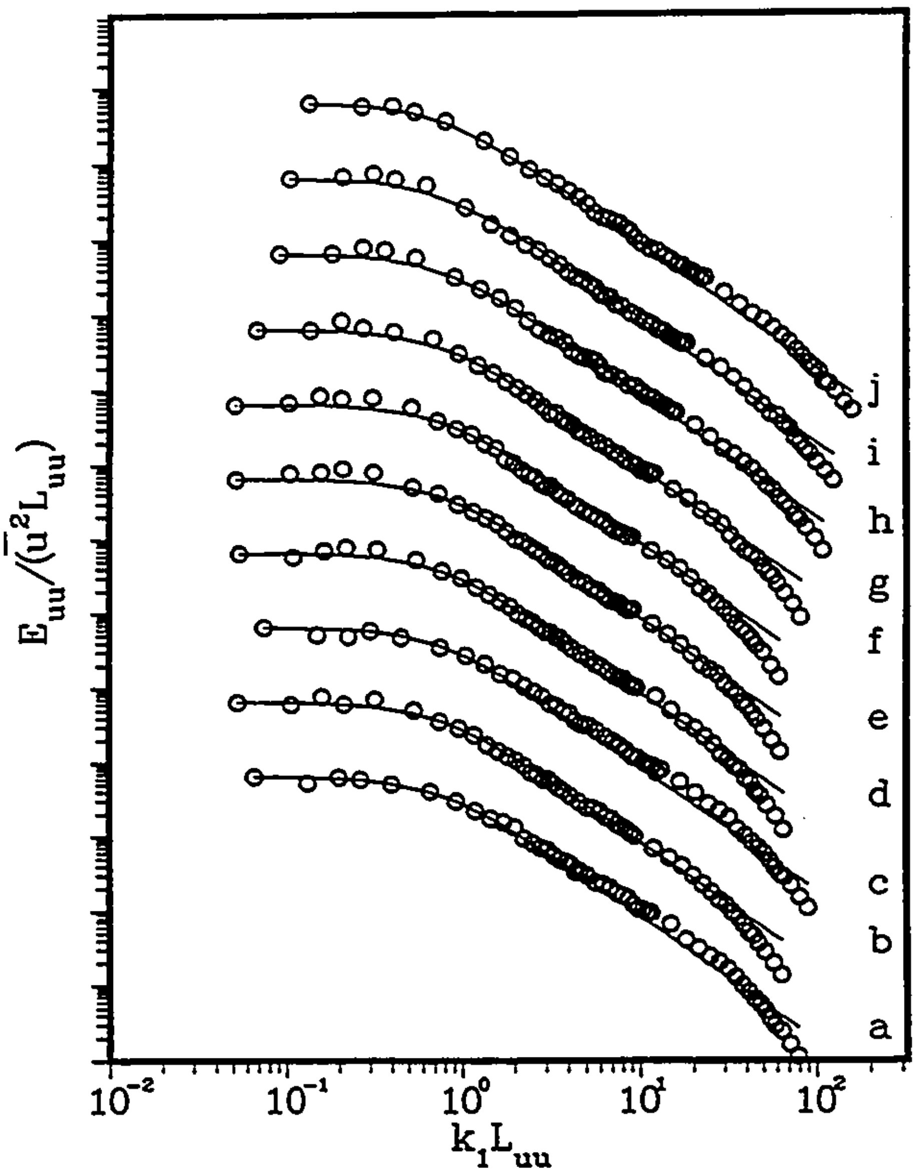

Figure 7.25: Streamwise development of nondimensional streamwise one dimensional wave spectra along section for case PE; o, measurement points; —, isotropic spectra; a, b, c, d, e, f, g, h, i, j positions specified in Figure 6.25. Spectra are staggered by one decade.

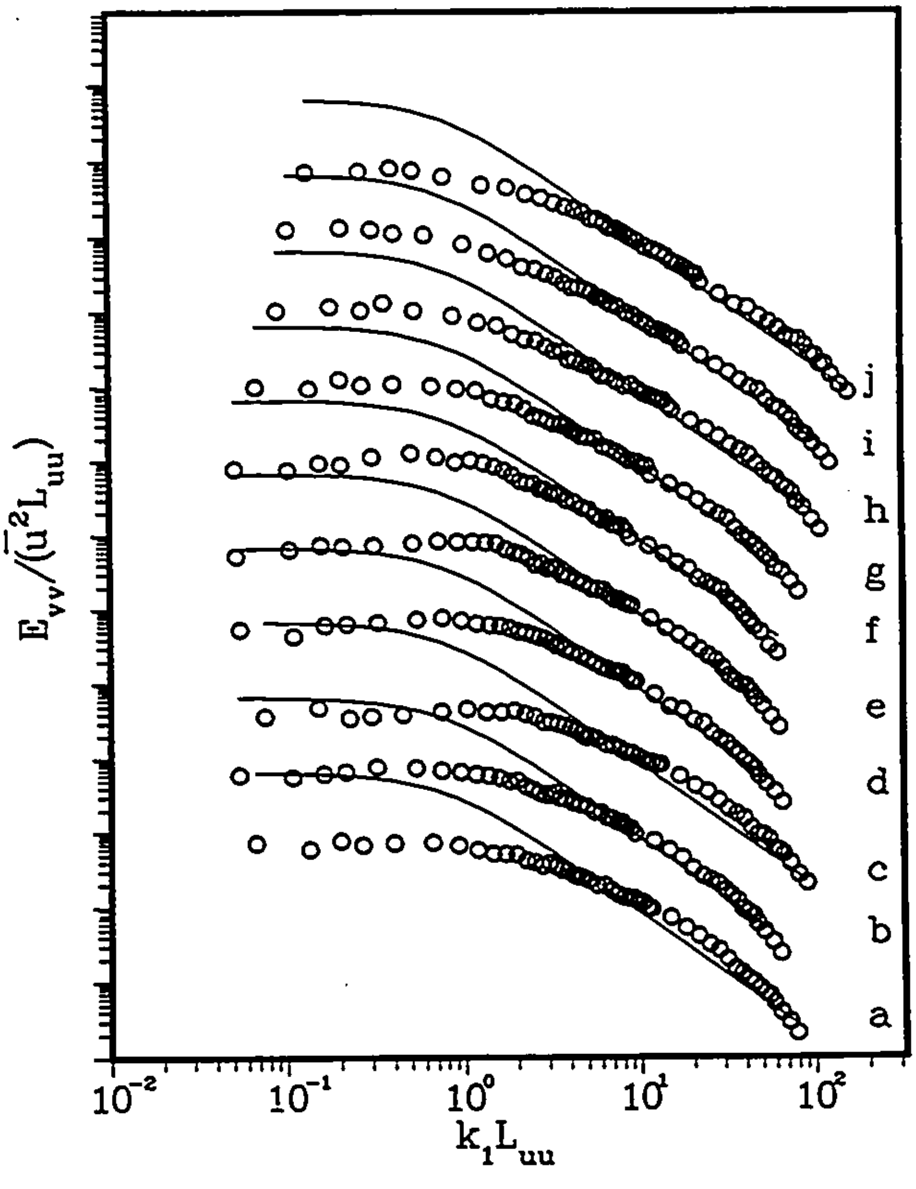

Figure 7.26: Streamwise development of nondimensional transverse one dimensional wave spectra along section for case PE (see Figure 7.25).

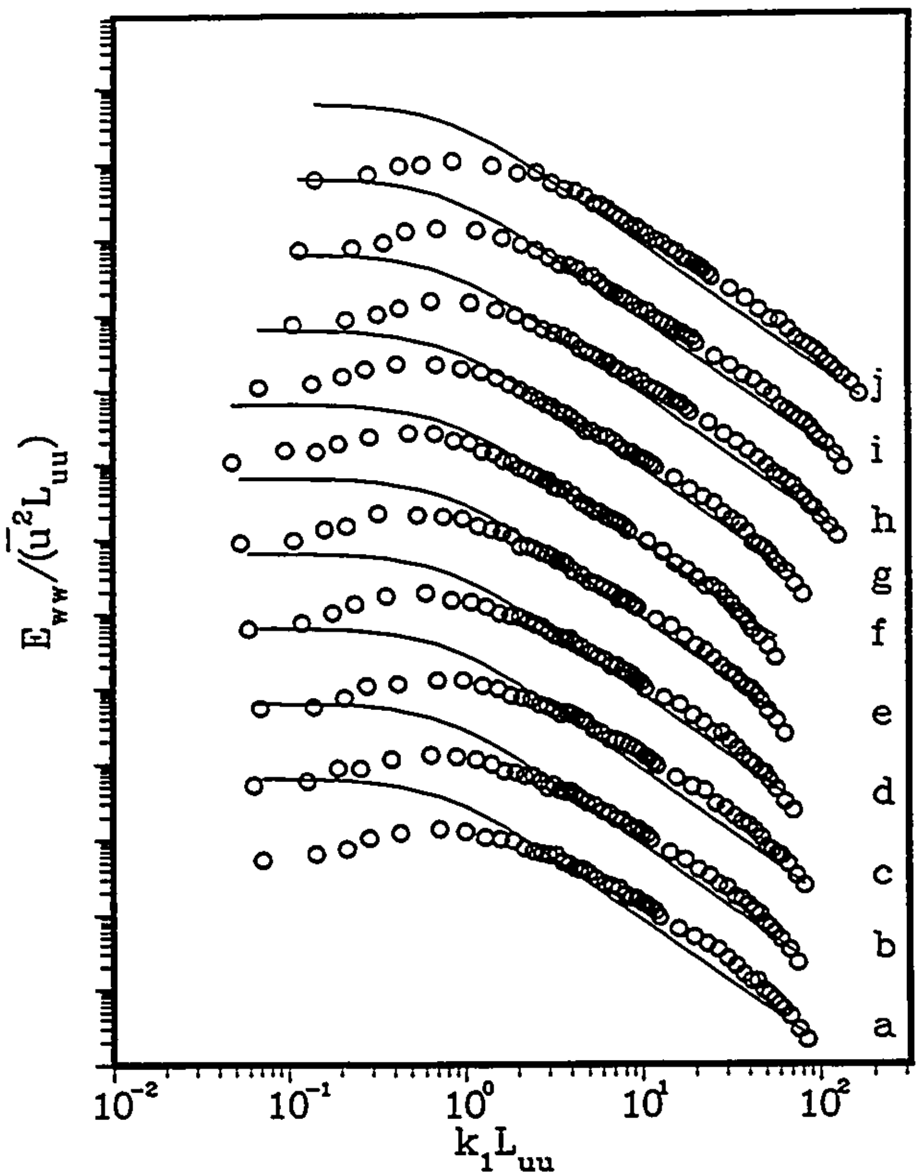

Figure 7.27: Streamwise development of nondimensional spanwise one dimensional wave spectra along section for case PE (see Figure 7.25).

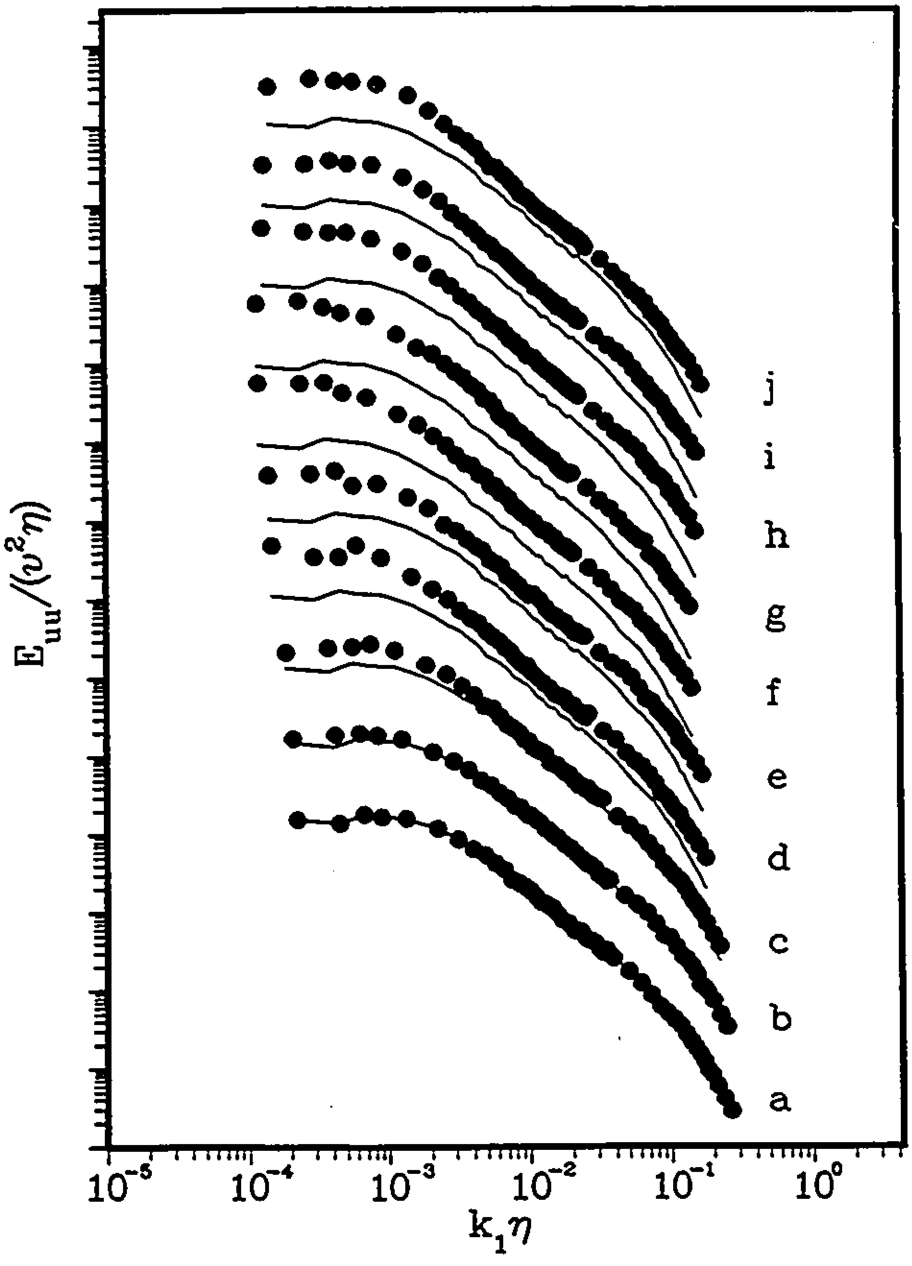

Figure 7.28: Streamwise development of streamwise one dimensional wave spectra nondimensionalized with Kolmogoroff scales for case NE; •, measurement points; a, b, c, d, e, f, g, h, i, j positions specified in Figure 6.25; —, spectra at position a. Spectra are staggered by one decade.

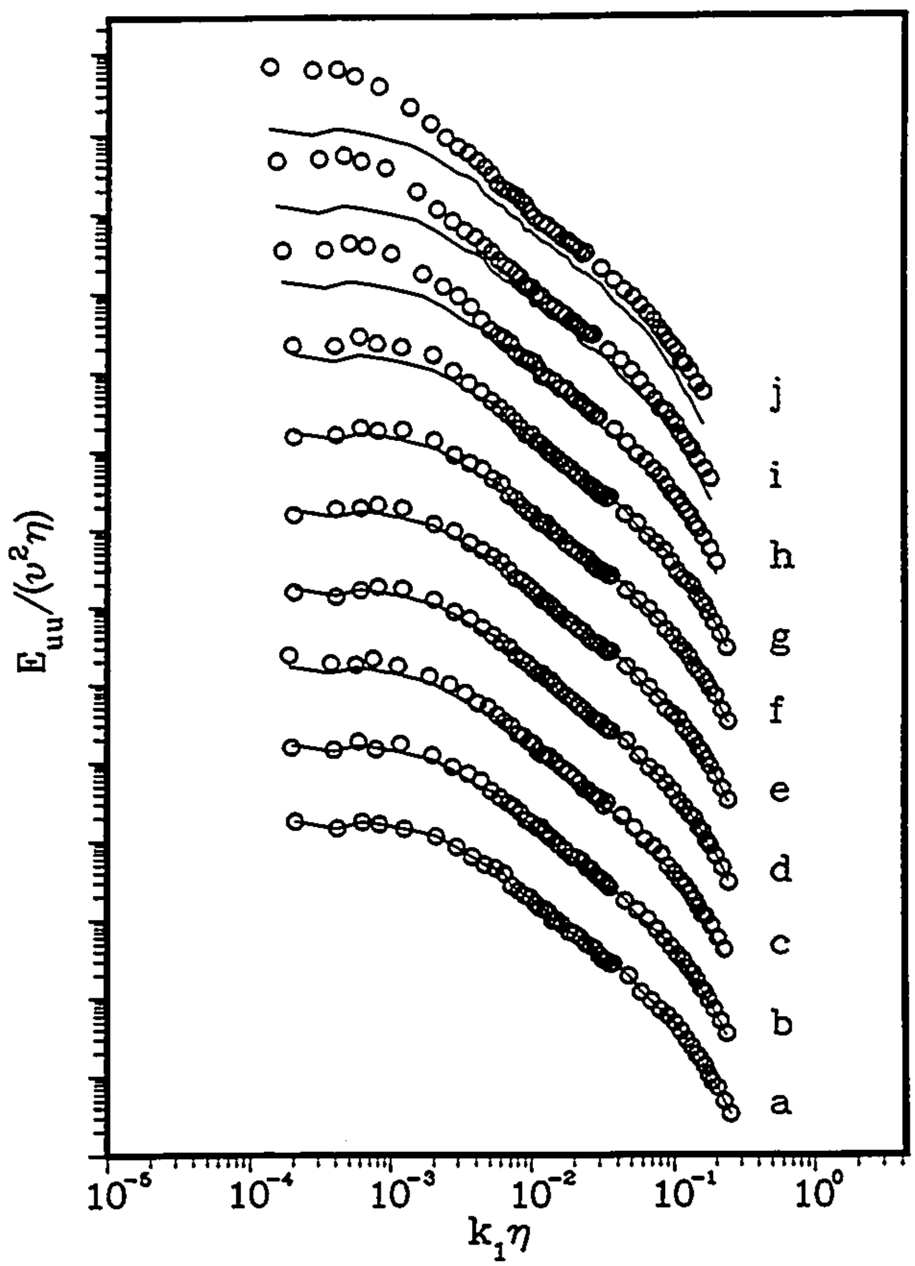

Figure 7.29: Streamwise development of streamwise one dimensional wave spectra nondimensionalized with Kolmogoroff scales for case PE; o, measurement points; a, b, c, d, e, f, g, h, i, j positions specified in Figure 6.25; —, spectra at position a. Spectra are staggered by one decade.

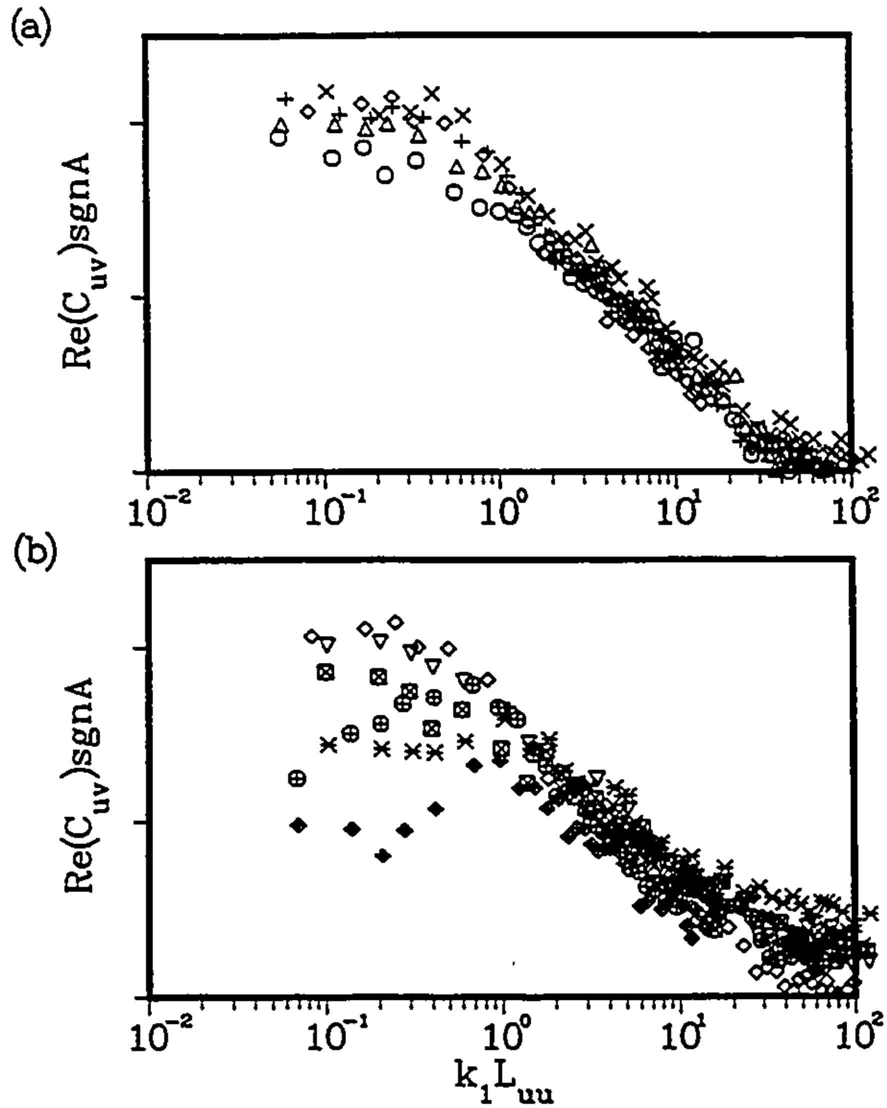

Figure 7.30: Streamwise development of coherence function for case NE; ○,a; △,b; +,c; ×,d; ◇,e; ▽,f; ⊠,g; ⋇,h; ◆,i; ⊕,j (positions specified in Figure 6.25); a) S=-0.049; b) S=0.061.

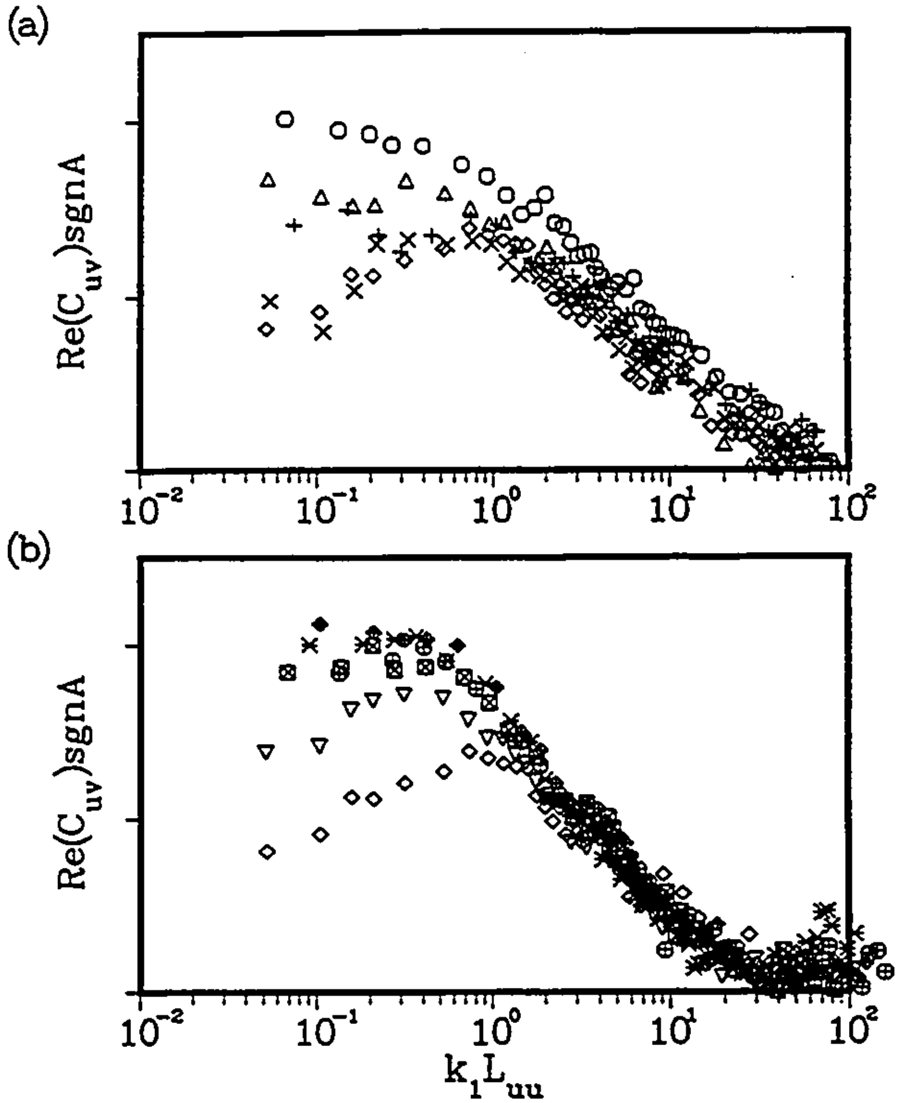

Figure 7.31: Streamwise development of coherence function for case PE; ○,a; △,b; +,c; ×,d; ◇,e; ▽,f; ⊠,g; ⋇,h; ◆,i; ⊕,j (positions specified in Figure 6.25); a) S=0.047; b) S=-0.0472.

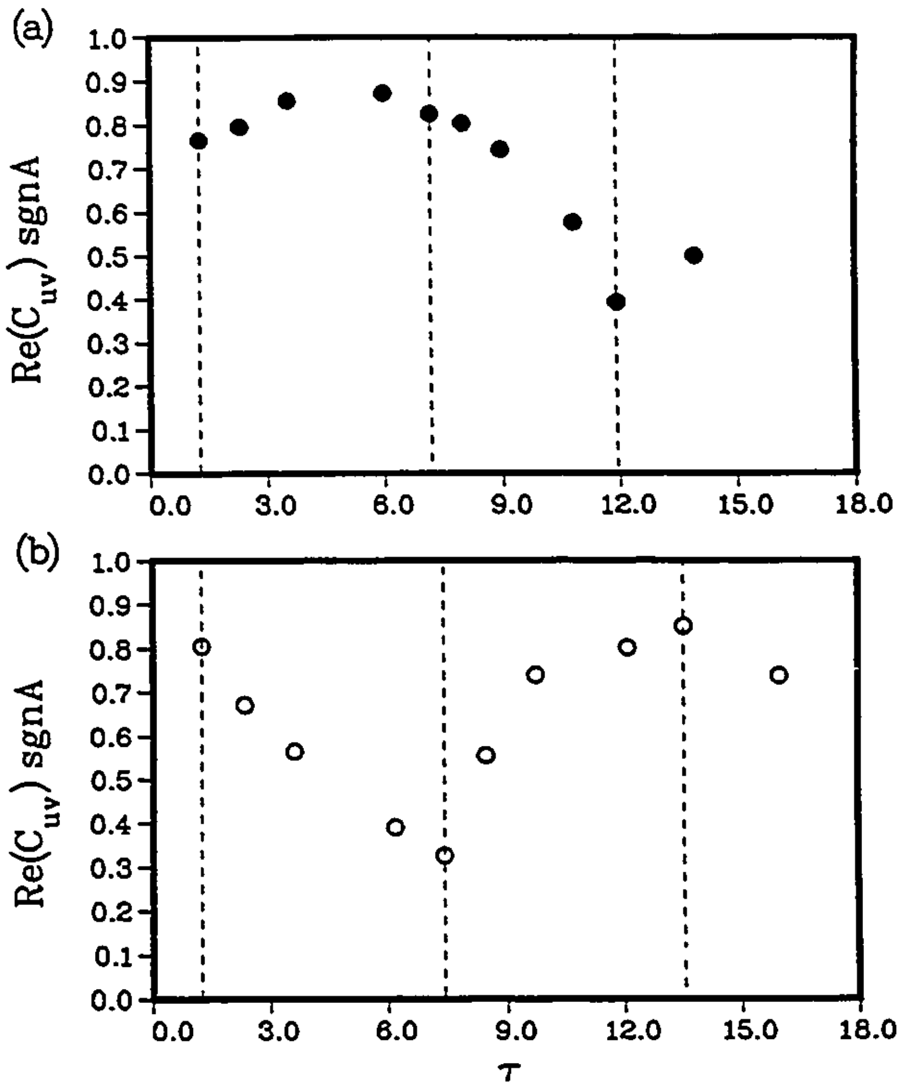

Figure 7.32: Streamwise development of coherence function of large scales; a) case NE; b) case PE.

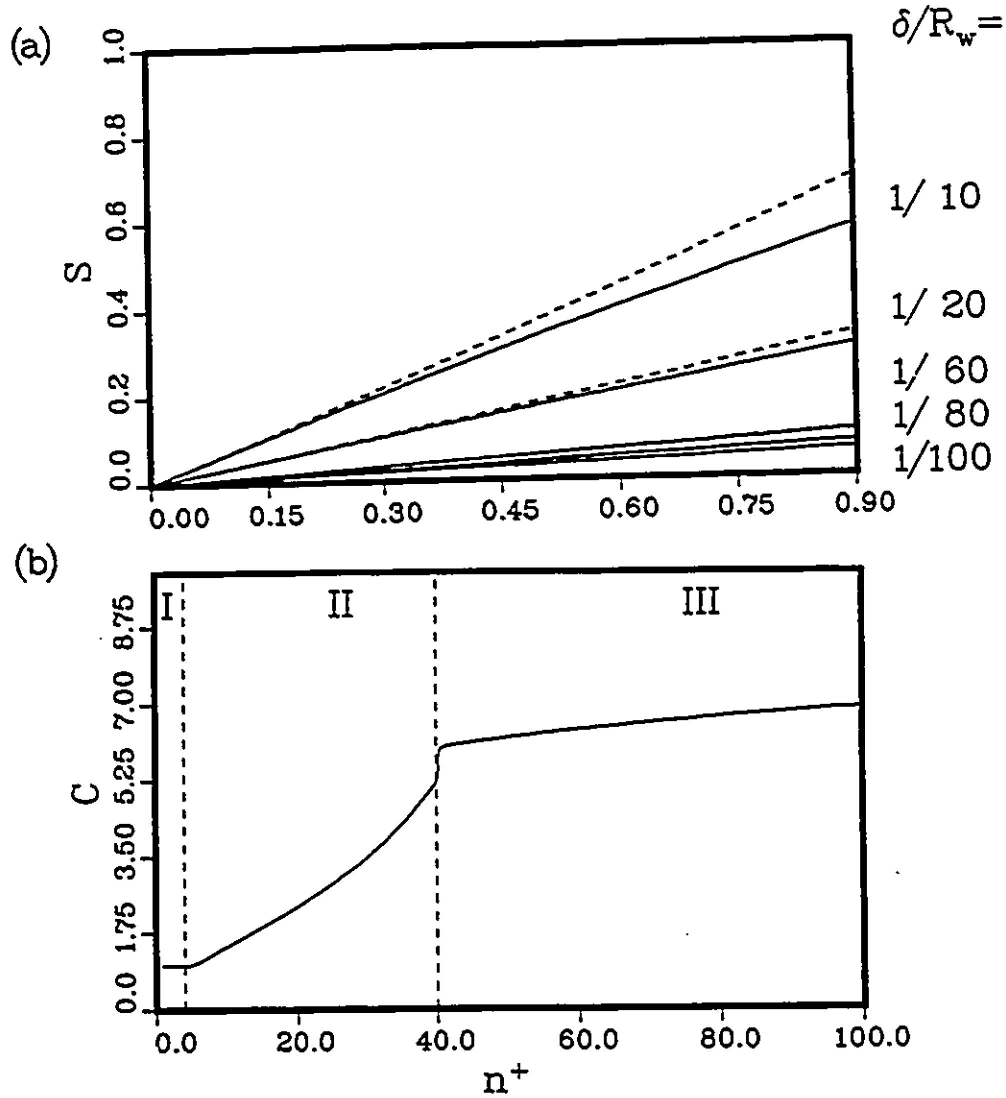

Figure 8.1: Transverse variation of curvature parameter in curved turbulent boundary layers; a) Curvature parameter obtained from power law; —, convex; - - -, concave; b) Coefficient C obtained from law of the wall; I, laminar sublayer; II, ubufferlayer; III,outer region.

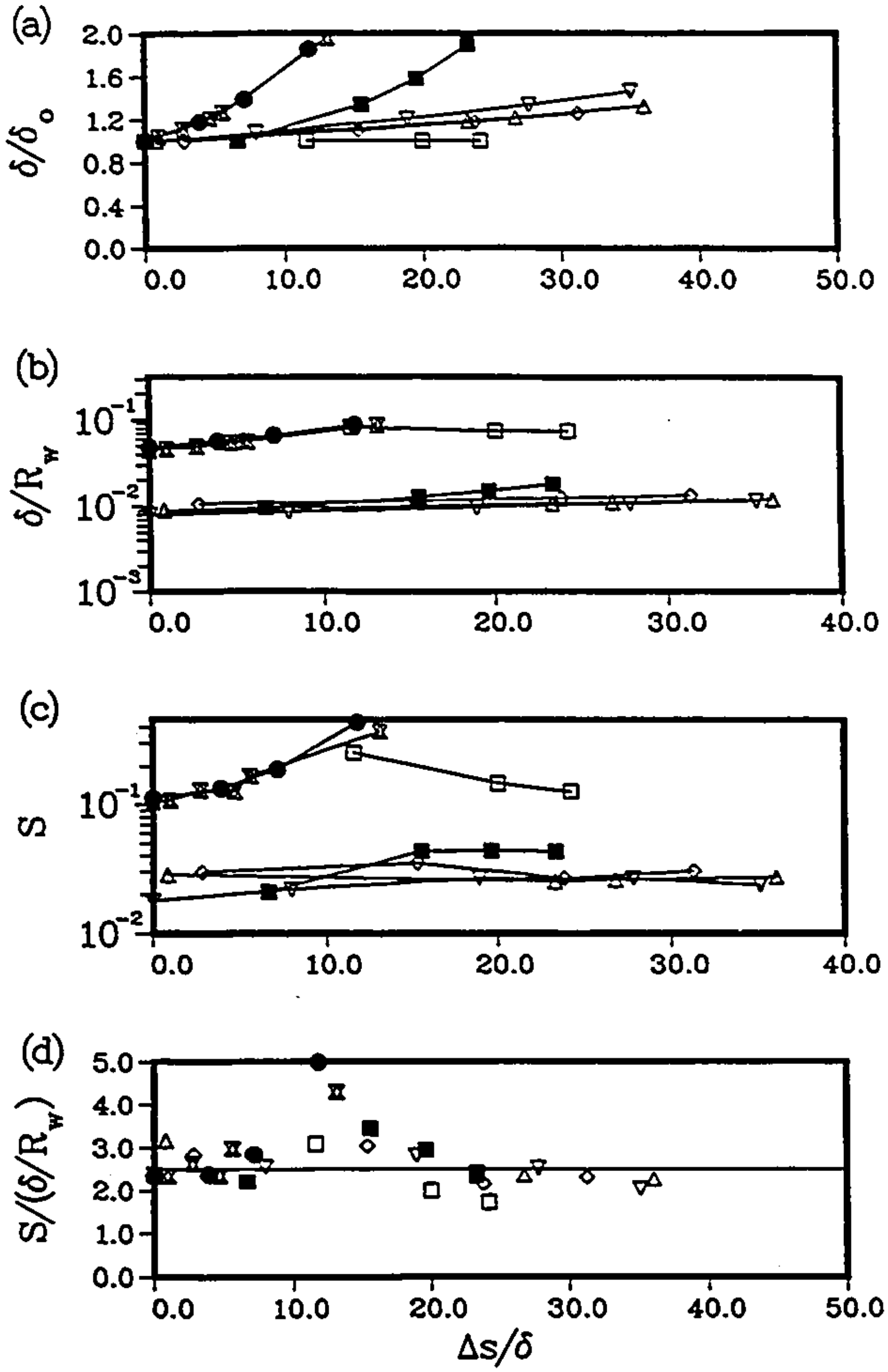

Figure 8.2: Streamwise variation of mean properties in curved turbulent boundary layer; **convex boundary layers:** △ , Meroney and Bradshaw (1975); □ , So and Mellor (1973); ◇ , Muck, Hoffmann and Bradshaw (1985); ▽, Gibson et al. (1984); **concave boundary layers:** ■ Meroney and Bradshaw (1975); ●, Barlow and Johnston (1988); ⧗, Shizawa and Honami (1983); a) nondimensional boundary layer thickness; b) boundary layer thickness to wall radius of curvature ratio; c) curvature parameter; d) $\frac{S}{\frac{\delta}{R_w}}$.

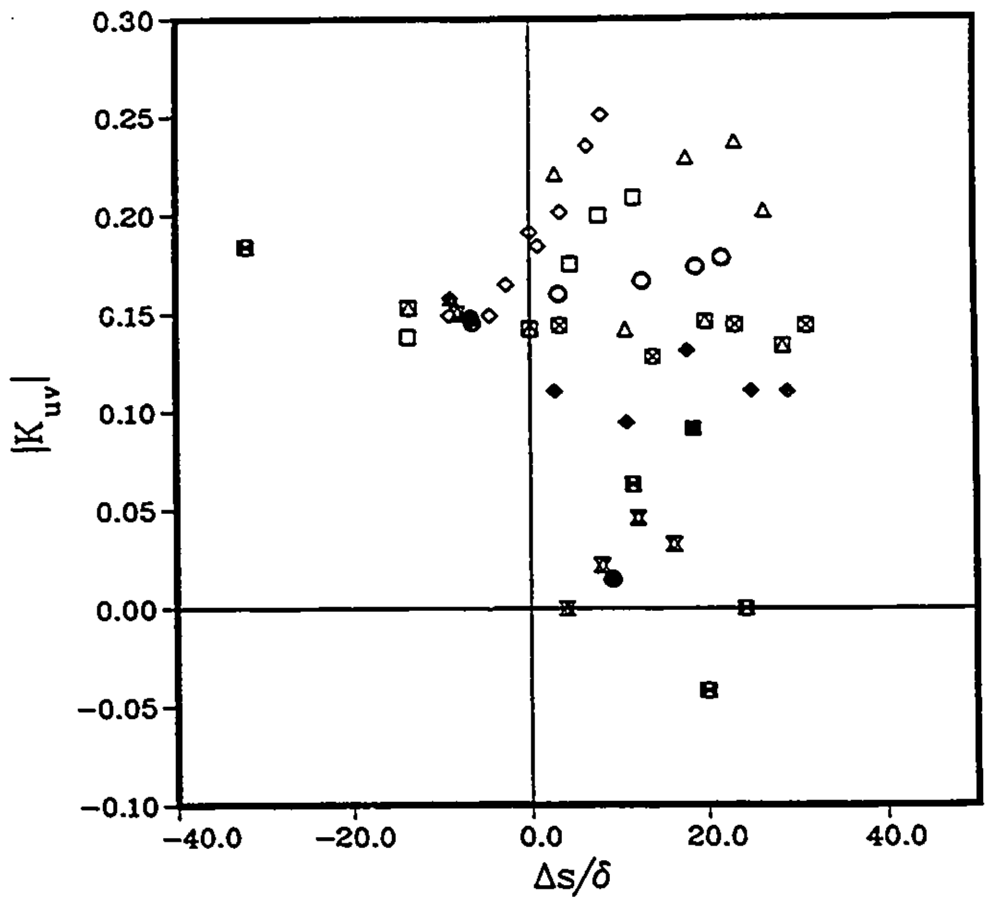

Figure 8.3: Streamwise development of Reynolds shear stress structural parameter of outer region of curved turbulent boundary layers; **Convex boundary layers:** ■ ●, Gillis and Johnston (1983); ⧗, Gillis and Johnston (1980); ⊟, So and Mellor (1973); ◆, Ramaprian and Shivaprasad (1978); ⊠, Gibson et al. (1984); ⊠, Muck Hoffmann and Bradshaw (1985); **Concave boundary layers:** △, Ramaprian and Shivaprasad (1978); ◇, Shizawa and Honami (1983 and 1985); □, Barlow and Johnston (1988a); ○, Hoffmann Muck and Bradshaw (1985).

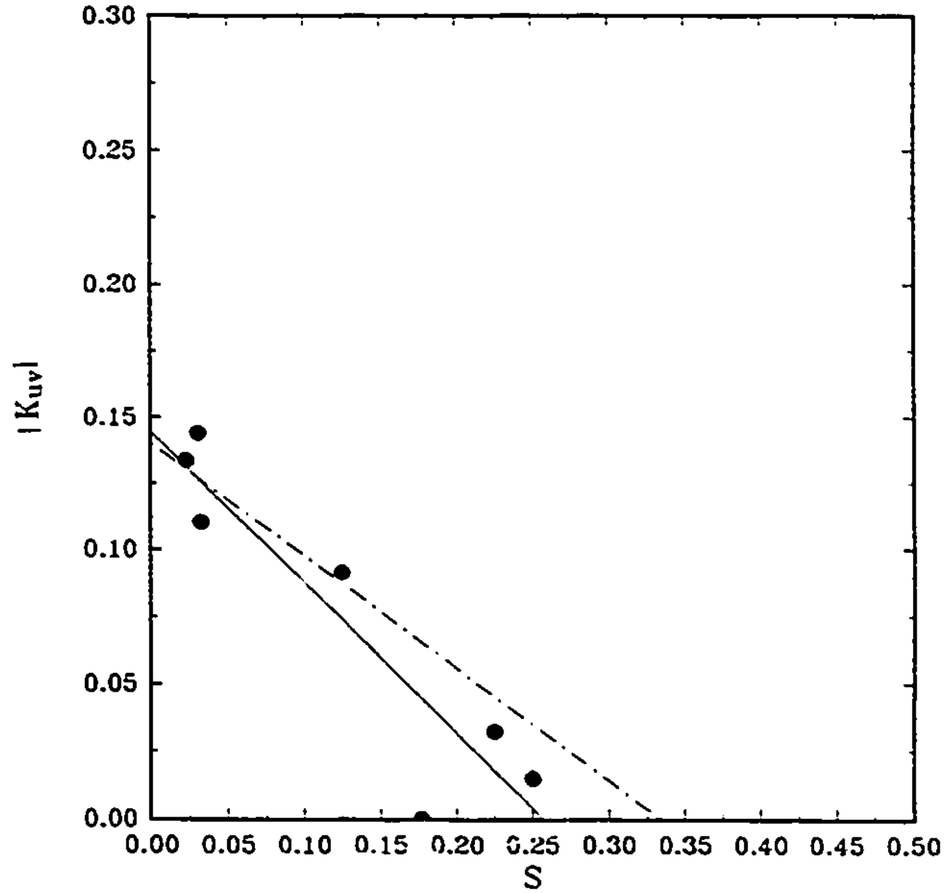

Figure 8.4: Variation of shear stress structural parameter for convex boundary layers; ——, equation 7.7; —·—·, equation 8.12; •, asymptotic values from measurements reported in literature for convex turbulent boundary layers.

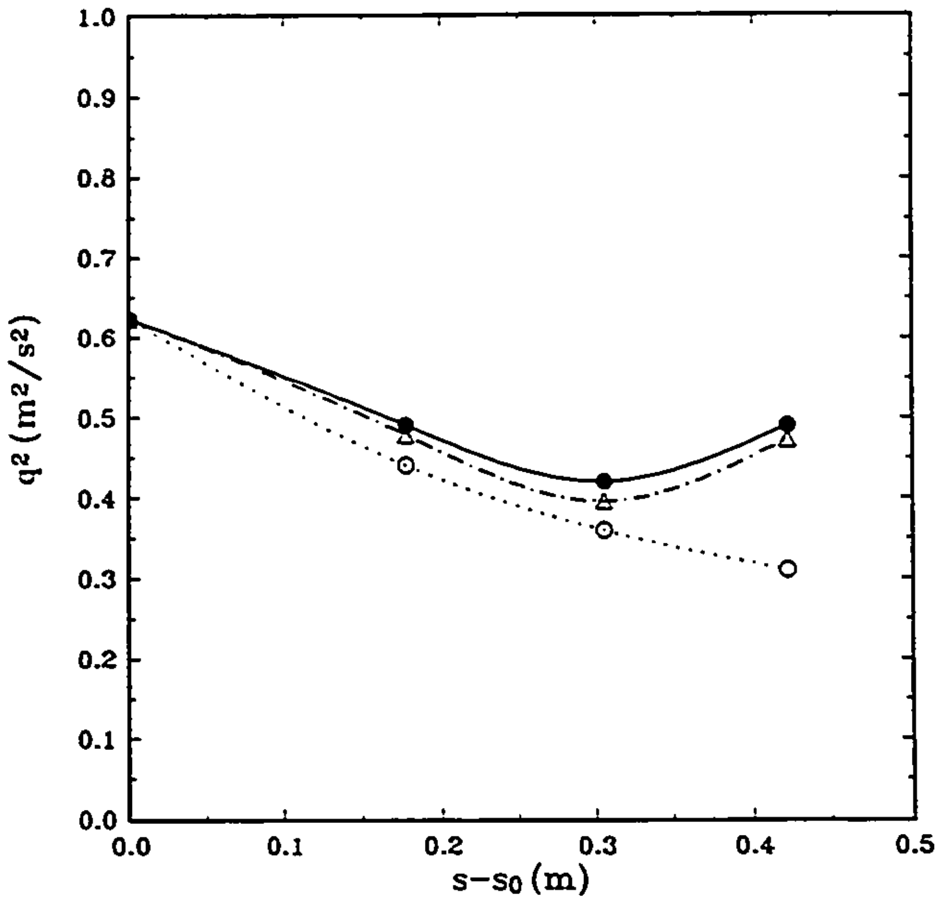

Figure 8.5: Kinetic energy development in outer region of convex turbulent boundary layer (form Gillis and Johnston, 1980); •, measurement points; o , equation 8.14; △ , predictions using nearly homogeneous uniformly sheared flow equations.

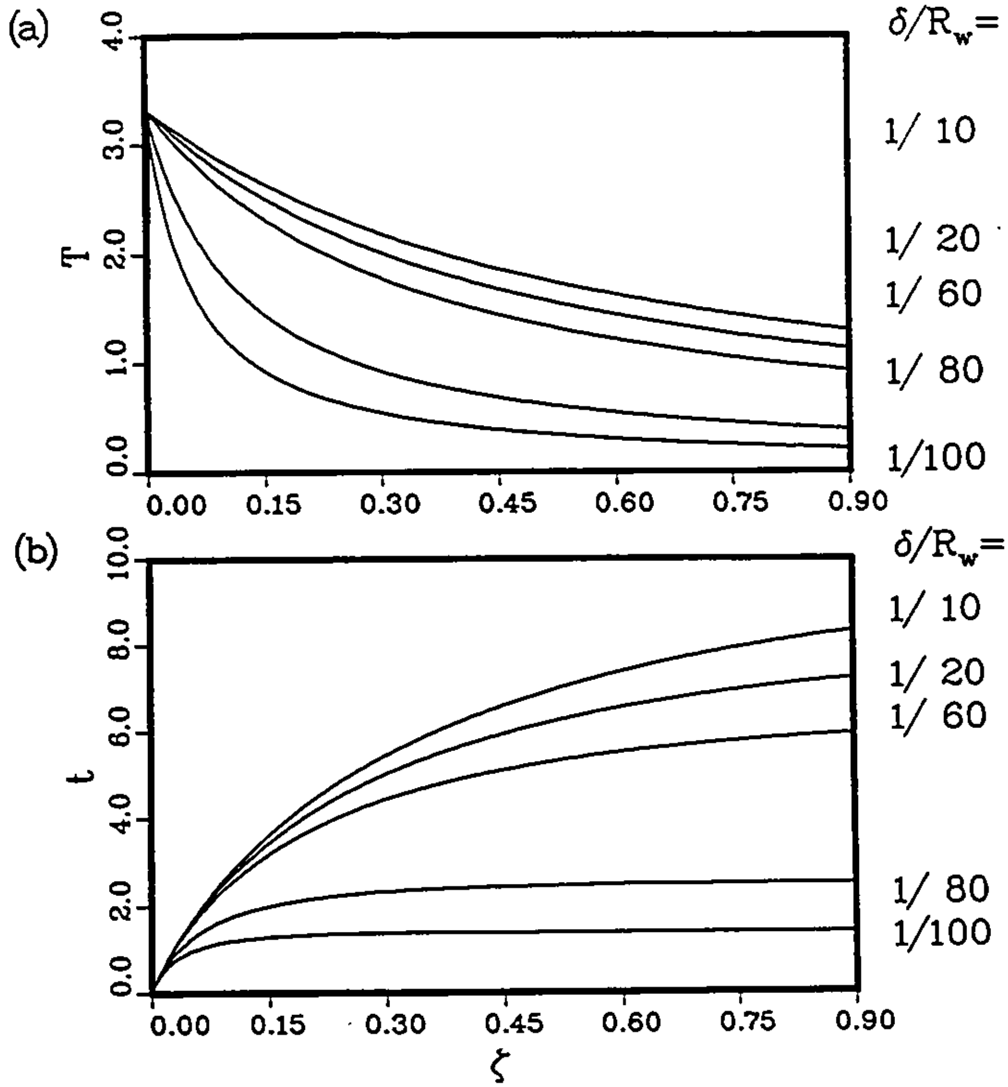

Figure 8.6: Rate of adjustment across a convex boundary layer; a) time constant, T; b) actual time, t.

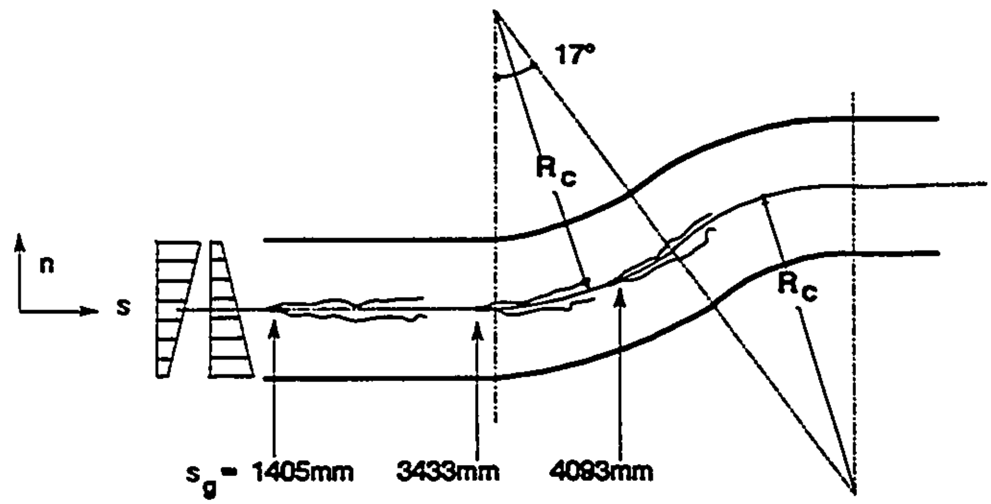

Figure 12.1: Placement of ribbon in straight and curved sections.

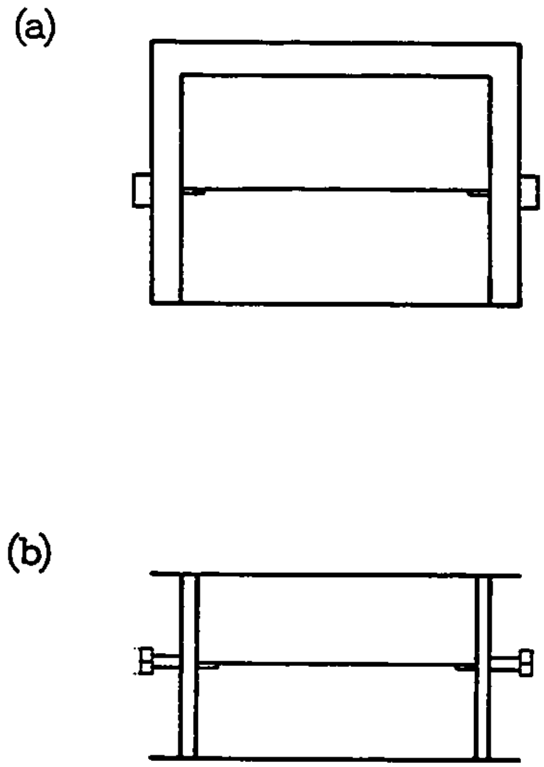

Figure 12.2: Ribbon mounting; a) in straight section; b) in curved section.

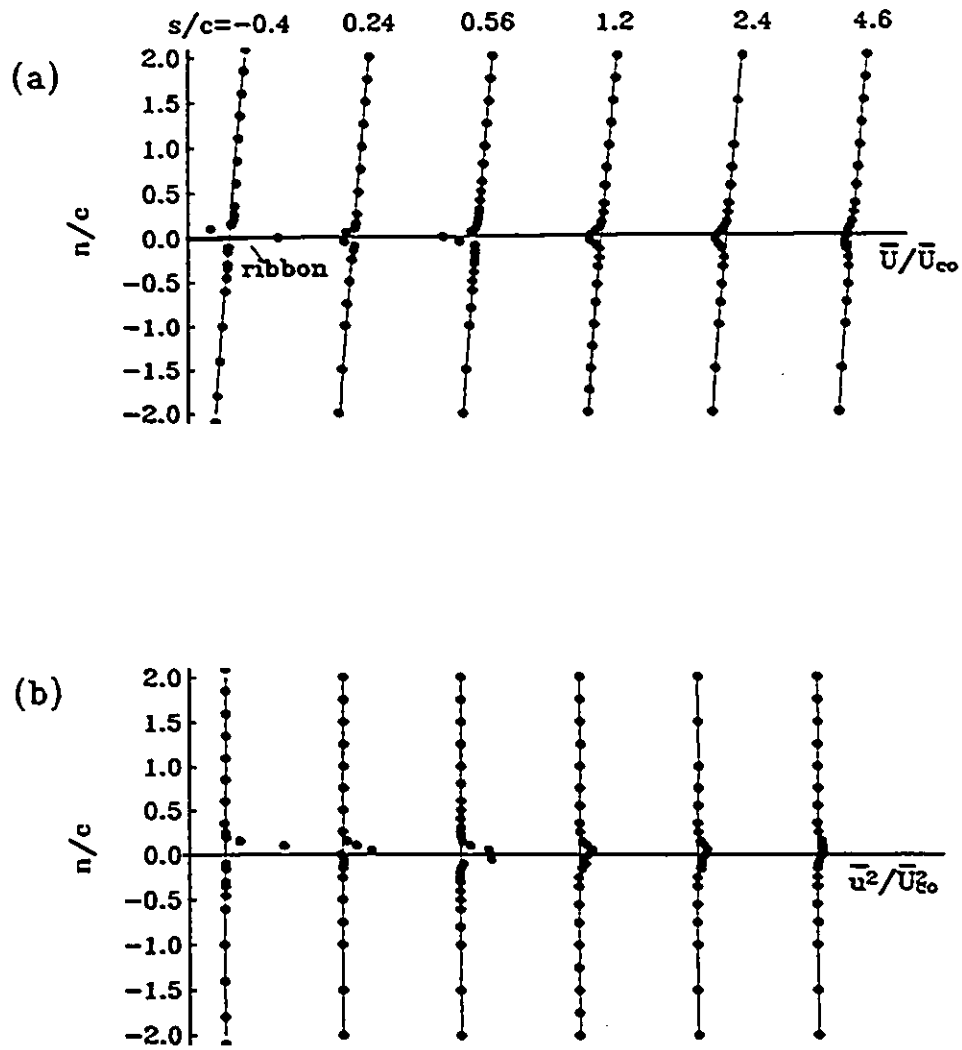

Figure 13.1: Single wire measurements close to ribbon in rectilinear shear flow; a) Streamwise mean velocity; b) Streamwise Reynolds stresses; •, manipulated profiles; —, nonmanipulated profiles.

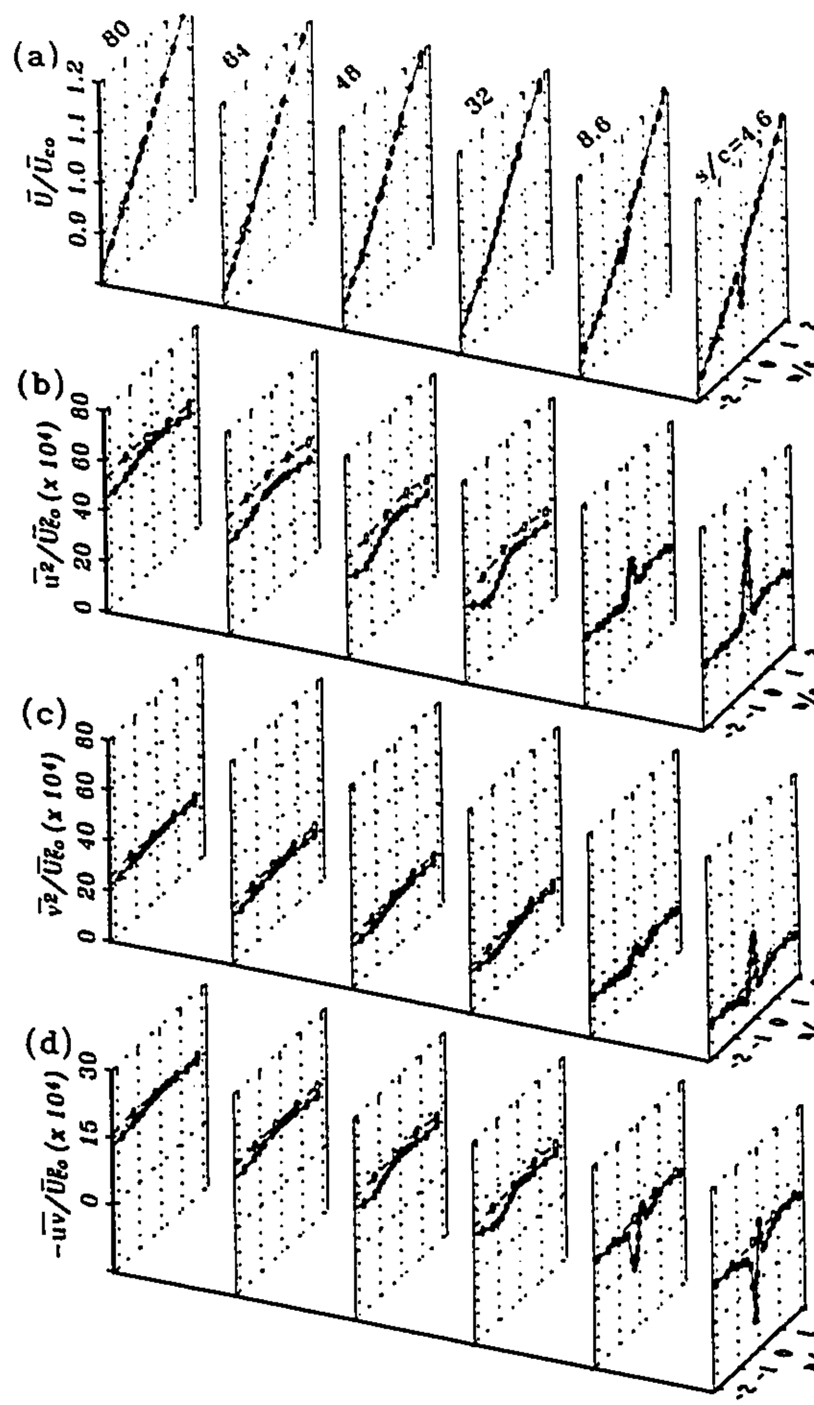

Figure 13.2: Transverse profiles of mean velocity and Reynolds stresses behind ribbon in rectilinear shear flow; a) $\overline{U}$; b) $\overline{u}^2$; c) $\overline{v}^2$; d) $-\overline{uv}$; •, manipulated profiles; o, nonmanipulated profiles.

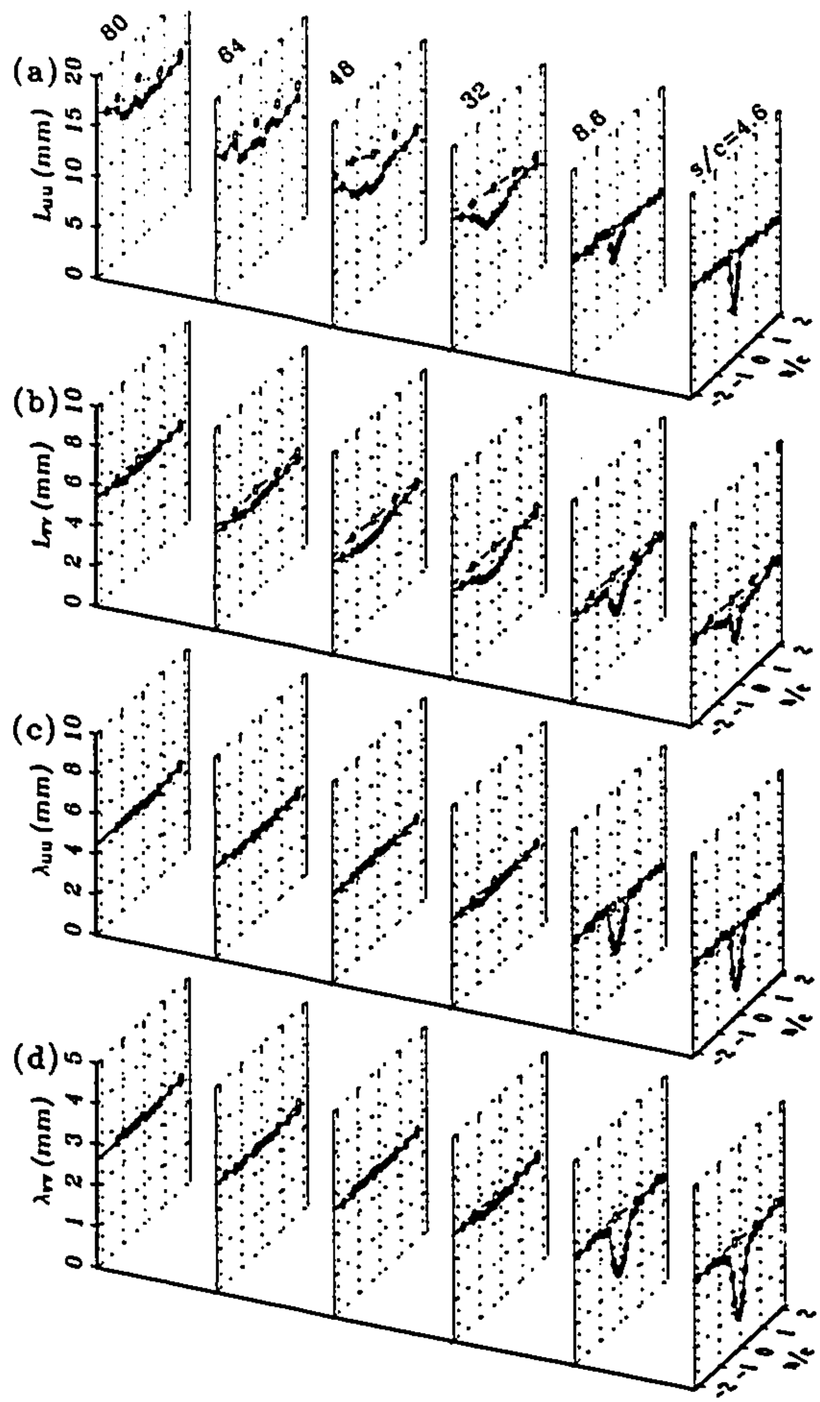

Figure 13.3: Transverse profiles of length scales behind ribbon placed in rectilinear shear flow; a) L_{uu}; b) L_{vv}; c) λ_{uu}; d) λ_{vv}; •, manipulated profiles; o, nonmanipulated profiles.

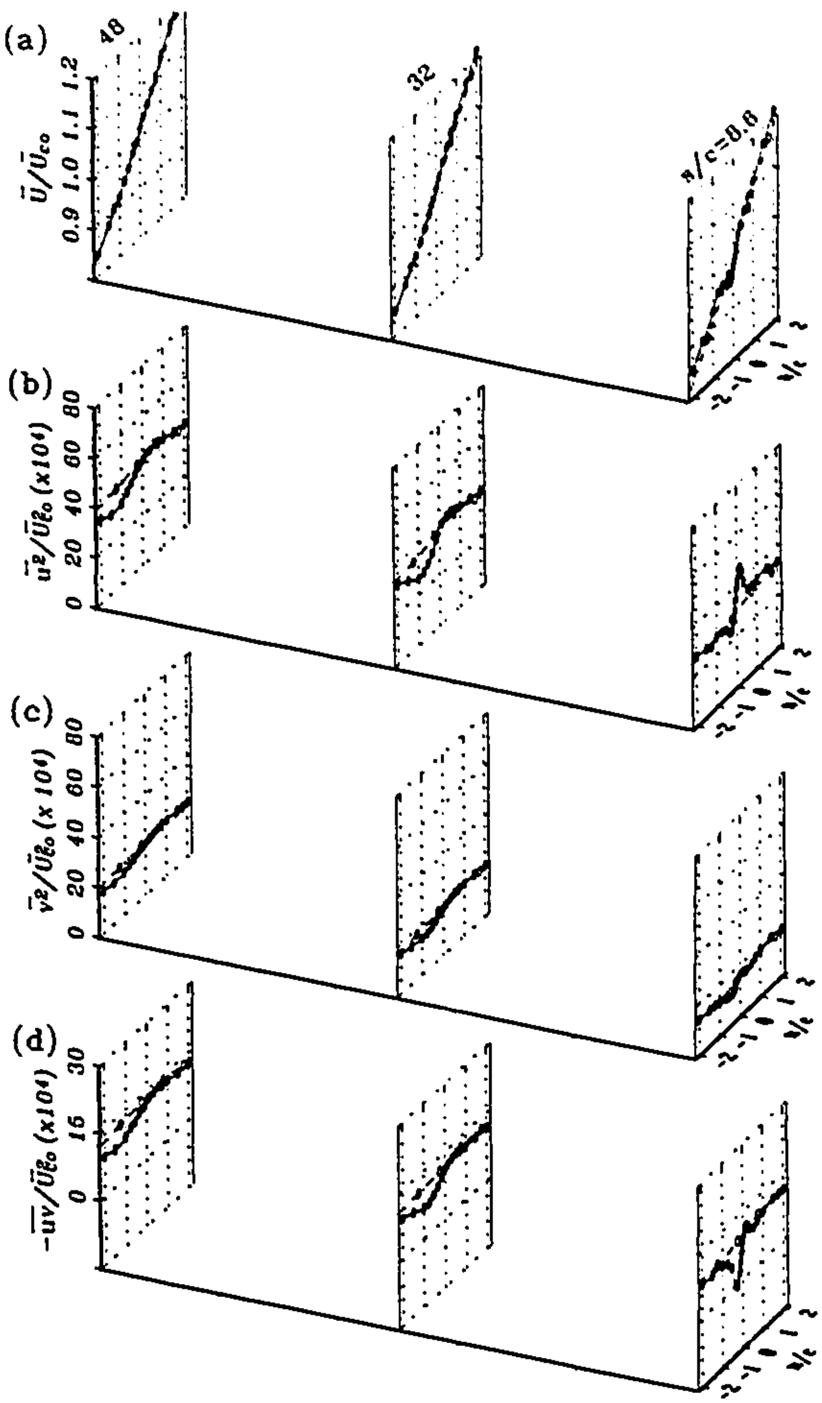

Figure 13.4: Transverse profiles of mean velocity and Reynolds stresses behind ribbon placed at positive angle of attack in rectilinear shear flow. a) $\overline{U}$; b) $\overline{v}^2$; c) $\overline{u}^2$; d) $-\overline{uv}$; •, manipulated profiles; o, nonmanipulated profiles.

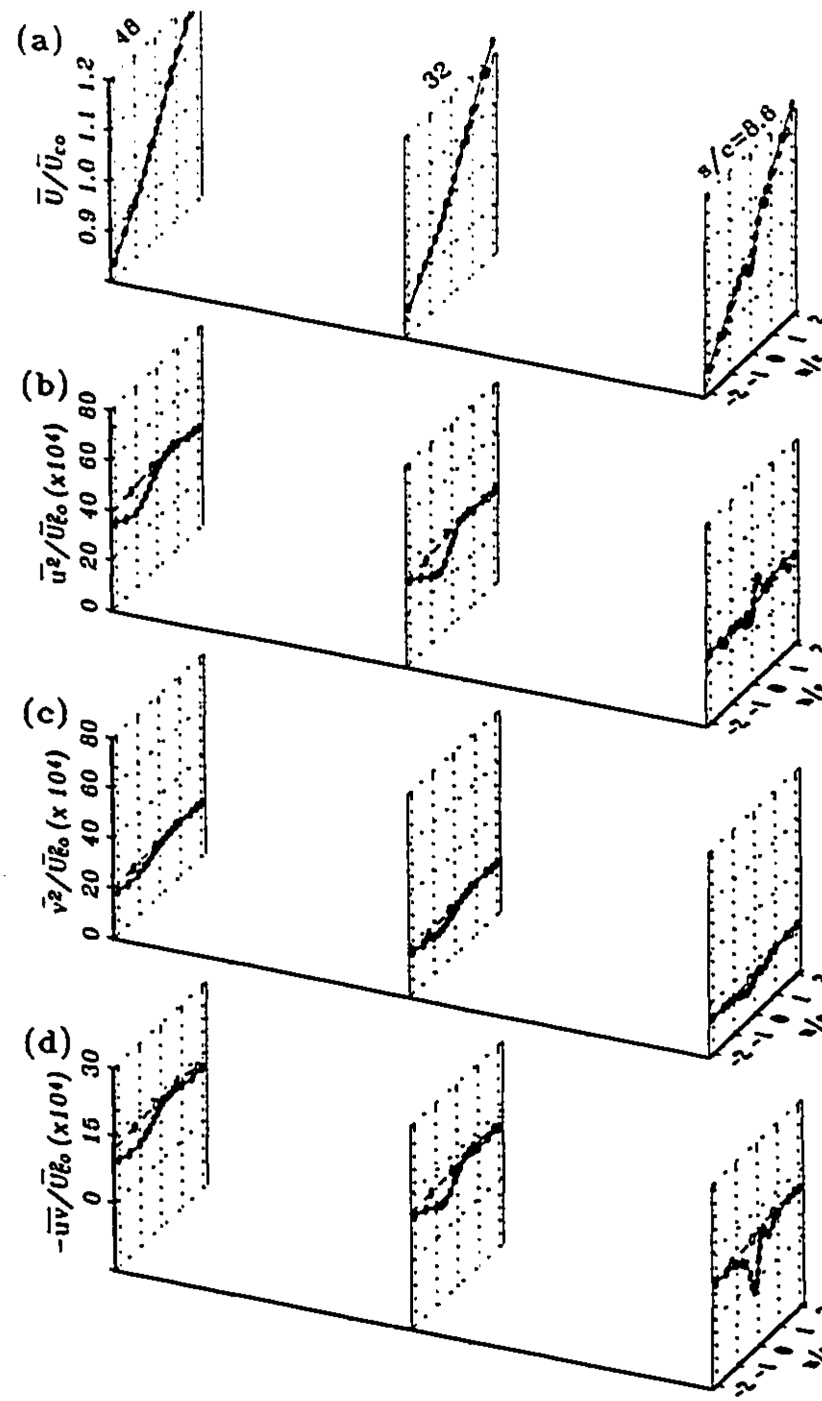

Figure 13.5: Transverse profiles of mean velocity and Reynolds stresses behind ribbon placed at negative angle of attack in rectilinear shear flow; a) $\overline{U}$; b) $\overline{v}^2$; c) $\overline{u}^2$; d) $-\overline{uv}$; •, manipulated profiles; o, nonmanipulated profiles.

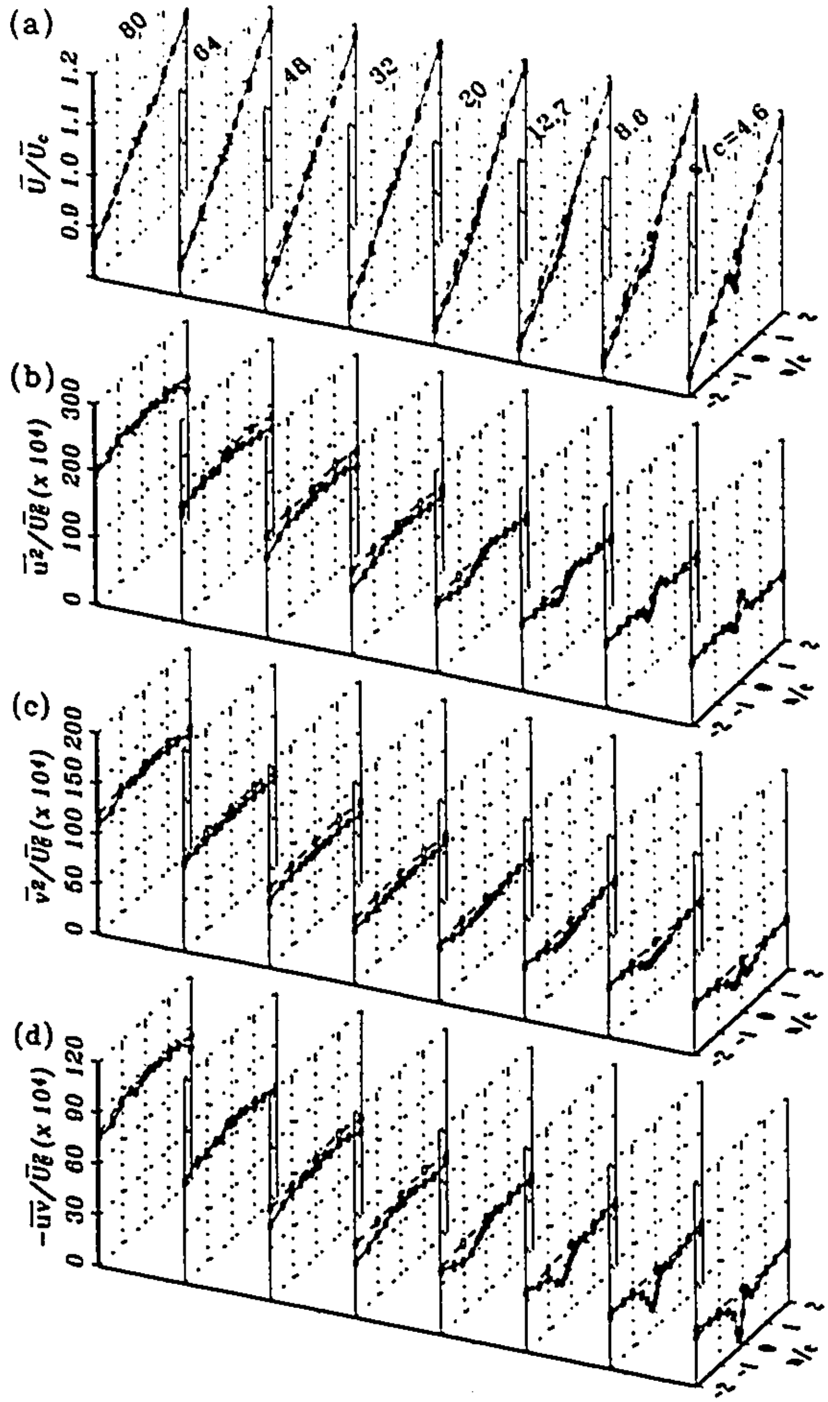

Figure 13.6: Transverse profiles of mean velocity and Reynolds stresses behind ribbon placed in destabilized shear flow; a) $\overline{U}$; b) $\overline{u}^2$; c) $\overline{v}^2$; d) $-\overline{uv}$; •, manipulated profiles; o, nonmanipulated profiles.

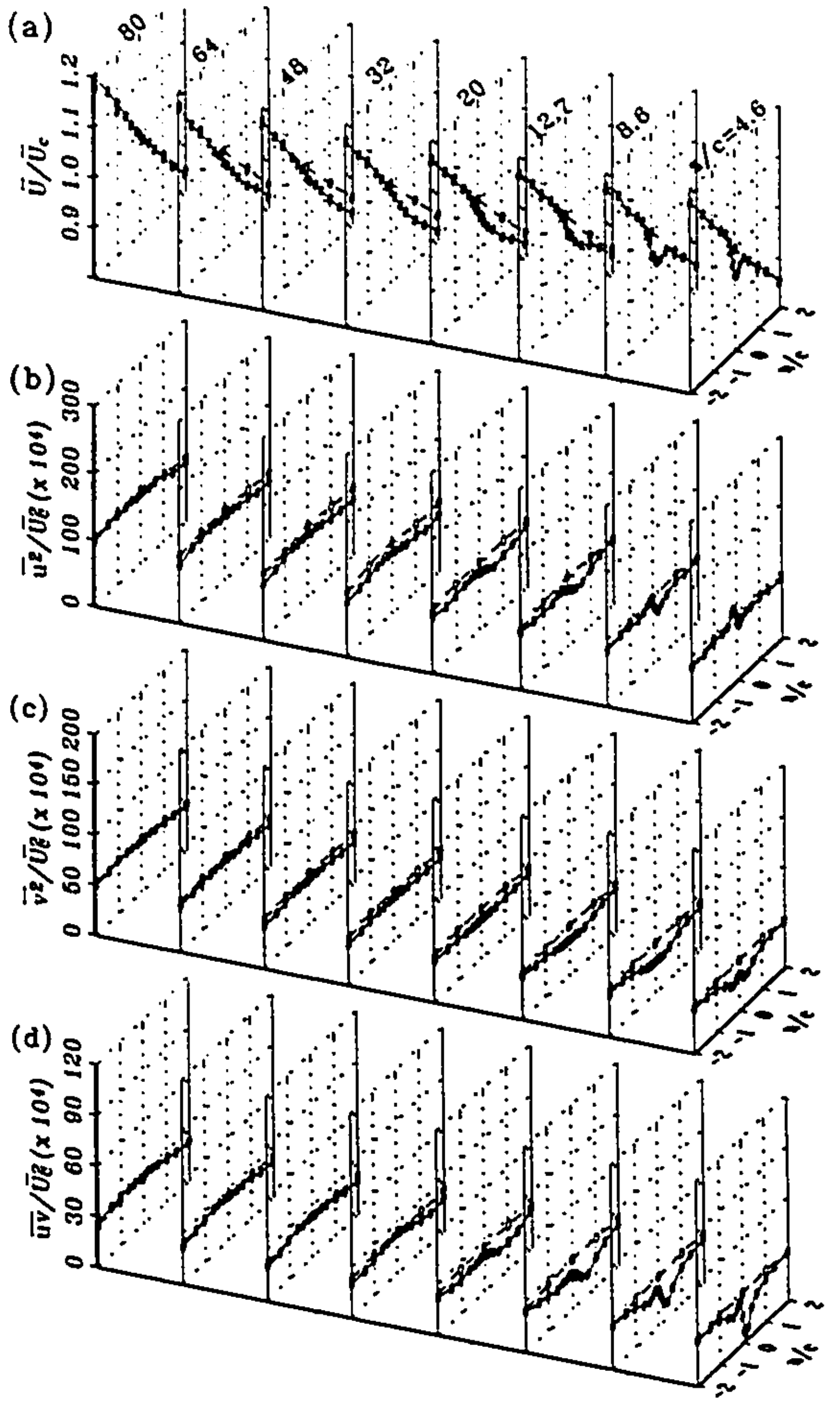

Figure 13.7: Transverse profiles of mean velocity and Reynolds stresses behind ribbon placed in stabilized shear flow; a) $\overline{U}$; b) $\overline{u^2}$; c) $\overline{v^2}$; d) $\overline{uv}$; •, manipulated profiles; o, nonmanipulated profiles.

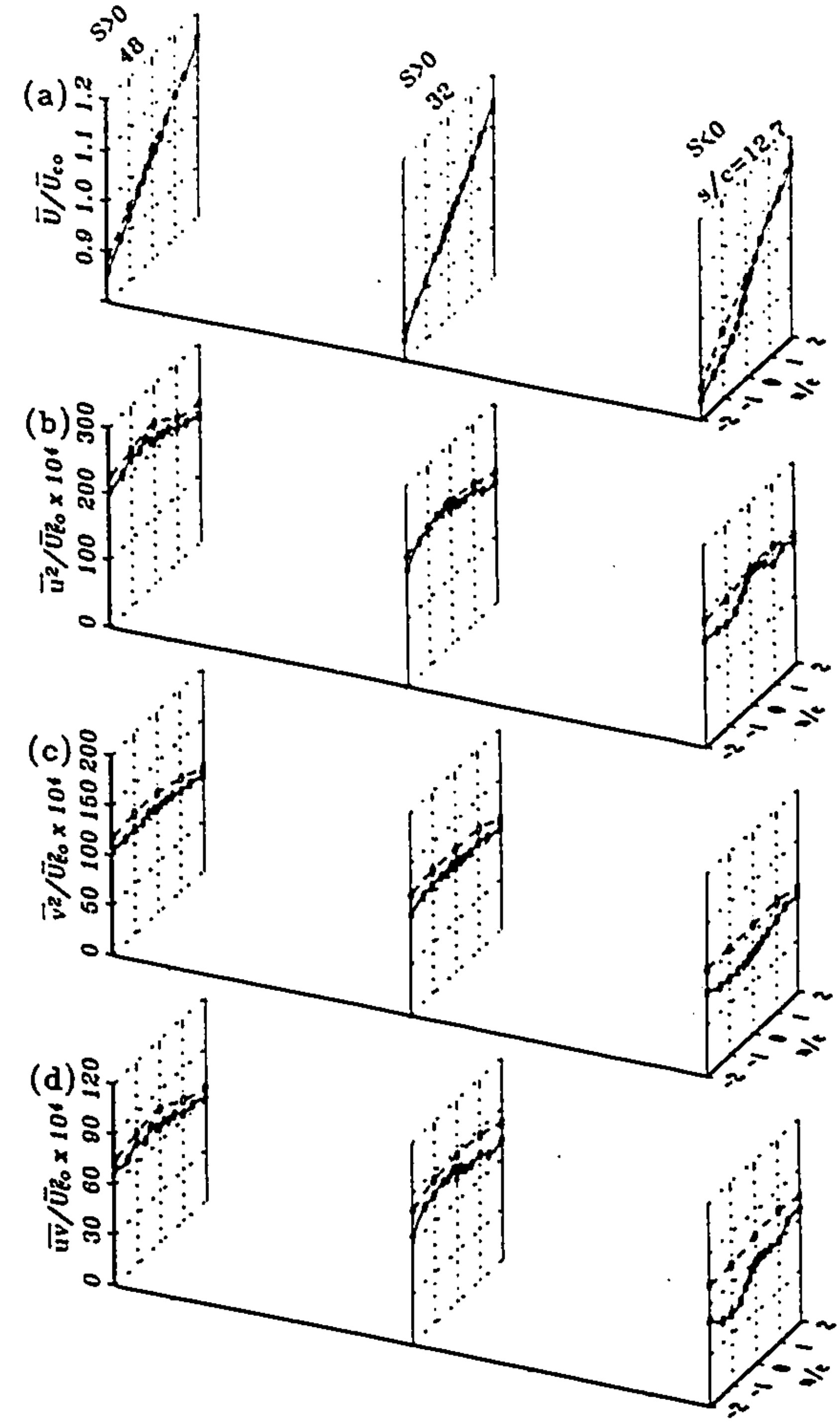

Figure 13.8: Transverse profiles of mean velocity and Reynolds stresses behind ribbon placed in curved flow with reversing curvature ($S < 0, S > 0$); a) $\overline{U}$; b) $\overline{u}^2$; c) $\overline{v}^2$; d) $-\overline{uv}$; •, manipulated profiles; o, nonmanipulated profiles.

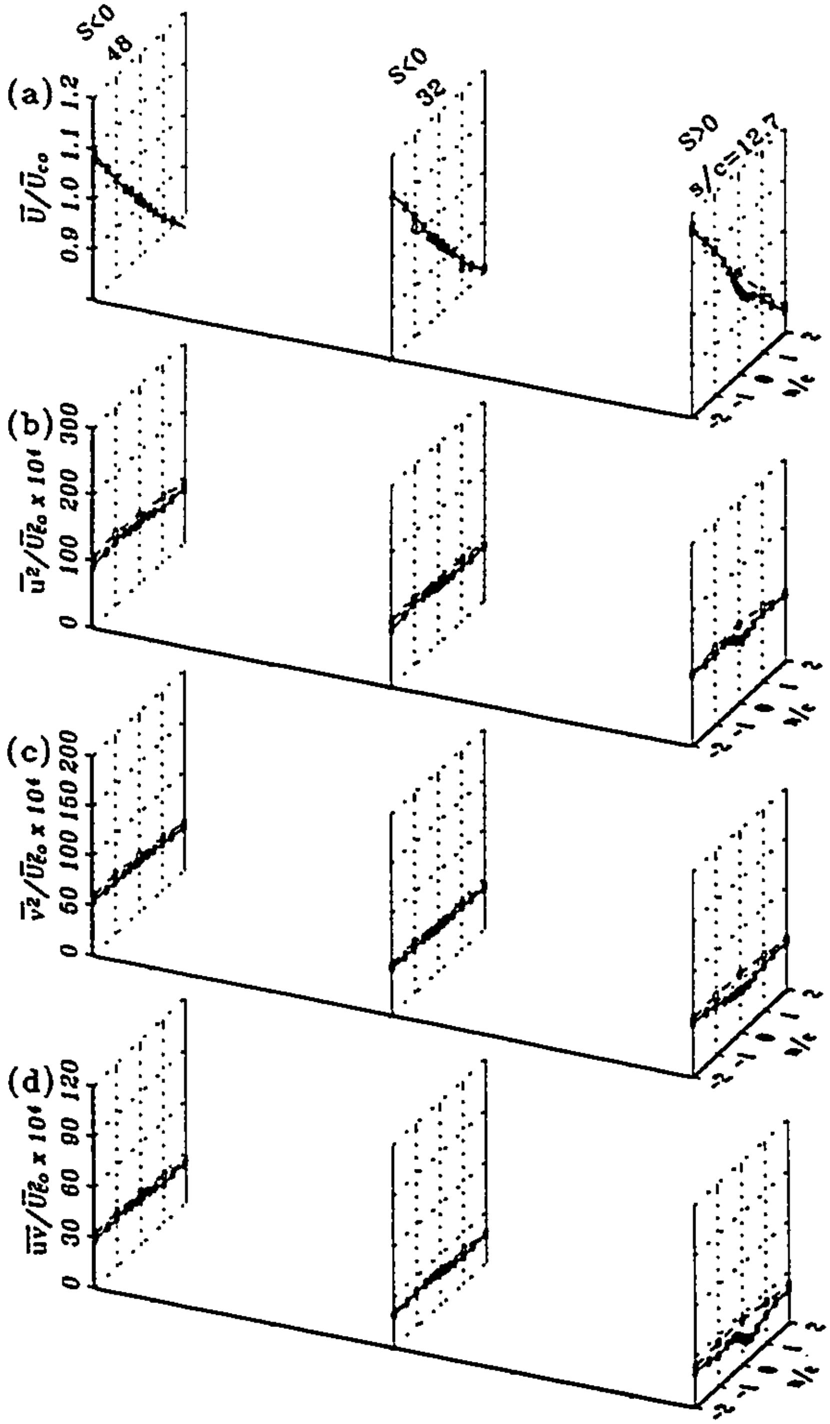

Figure 13.9: Transverse profiles of mean velocity and Reynolds stresses behind ribbon placed in curved flow with reversing of curvature ($S > 0, S < 0$); a) $\overline{U}$; b) $\overline{u}^2$; c) $\overline{v}^2$; d) $\overline{uv}$; •, manipulated profiles; o, nonmanipulated profiles.

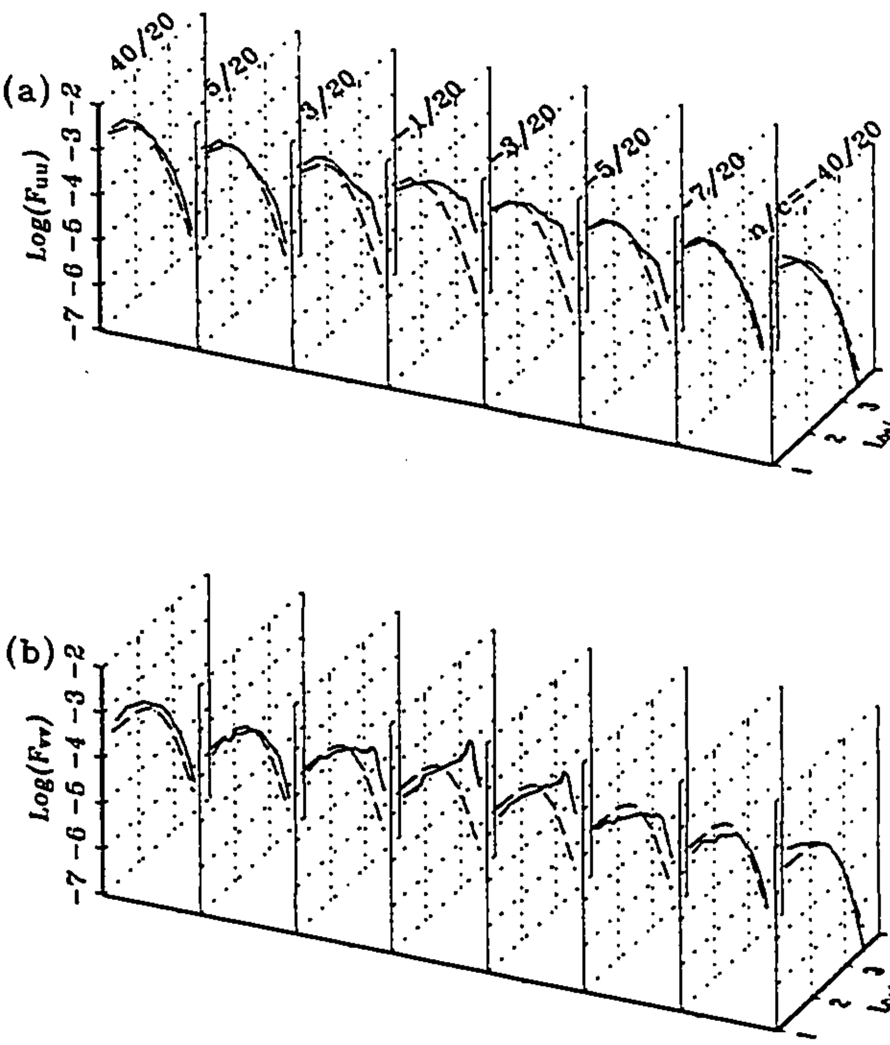

Figure 13.10: Frequency power spectras at $\frac{x}{c} = 4.6$ behind ribbon placed in rectilinear shear flow; a) F_{uu}; b) F_{vv}; ——, manipulated flow; - - - -, nonmanipulated flow.

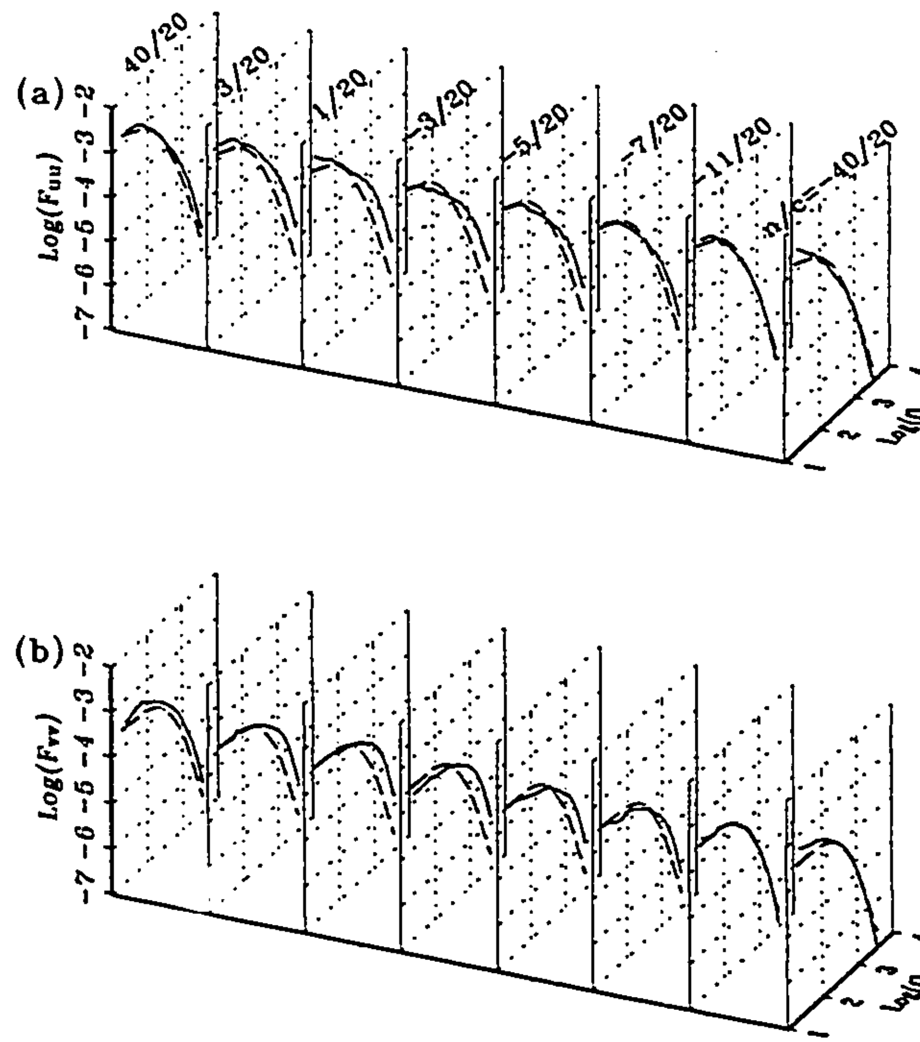

Figure 13.11: Frequency power spectras at $\frac{s}{c} = 8.6$ behind ribbon in rectilinear shear flow; a) F_{uu}; b) F_{vv}; ——, manipulated flow; - - - -, nonmanipulated flow.

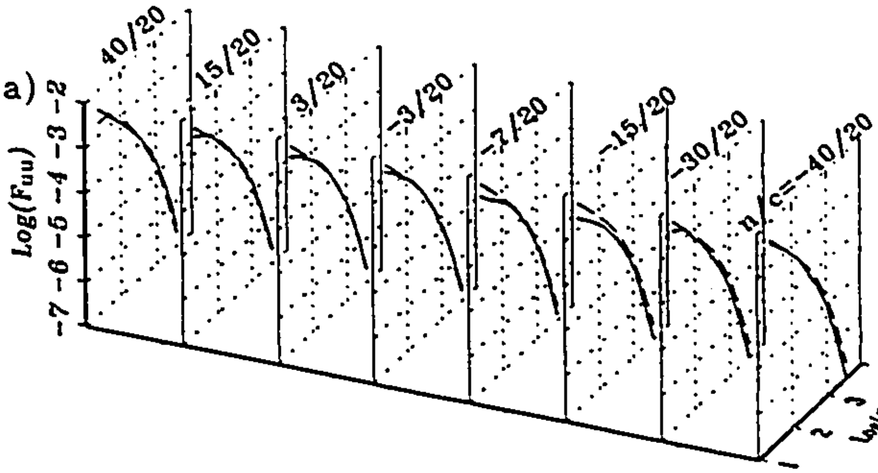

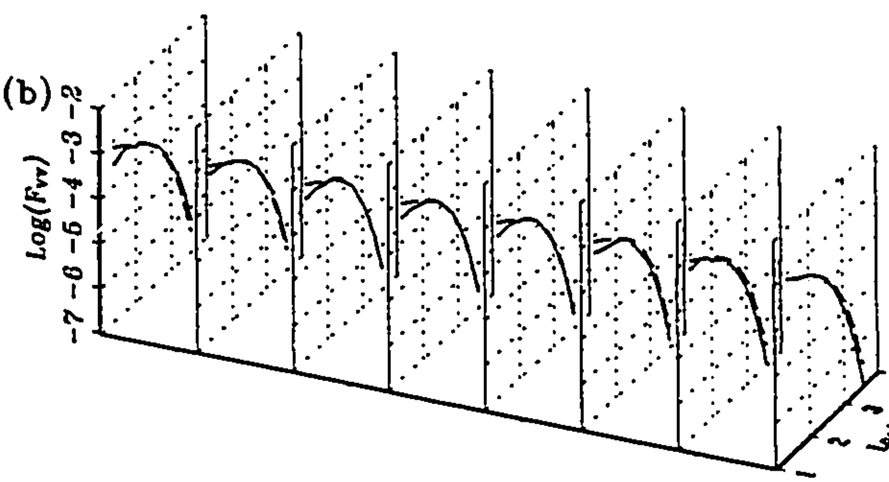

Figure 13.12: Frequency power spectras at $\frac{x}{c} = 32$ behind ribbon in rectilinear shear flow; a) F_{uu}; b) F_{vv}; ——, manipulated flow; - - - -, nonmanipulated flow.

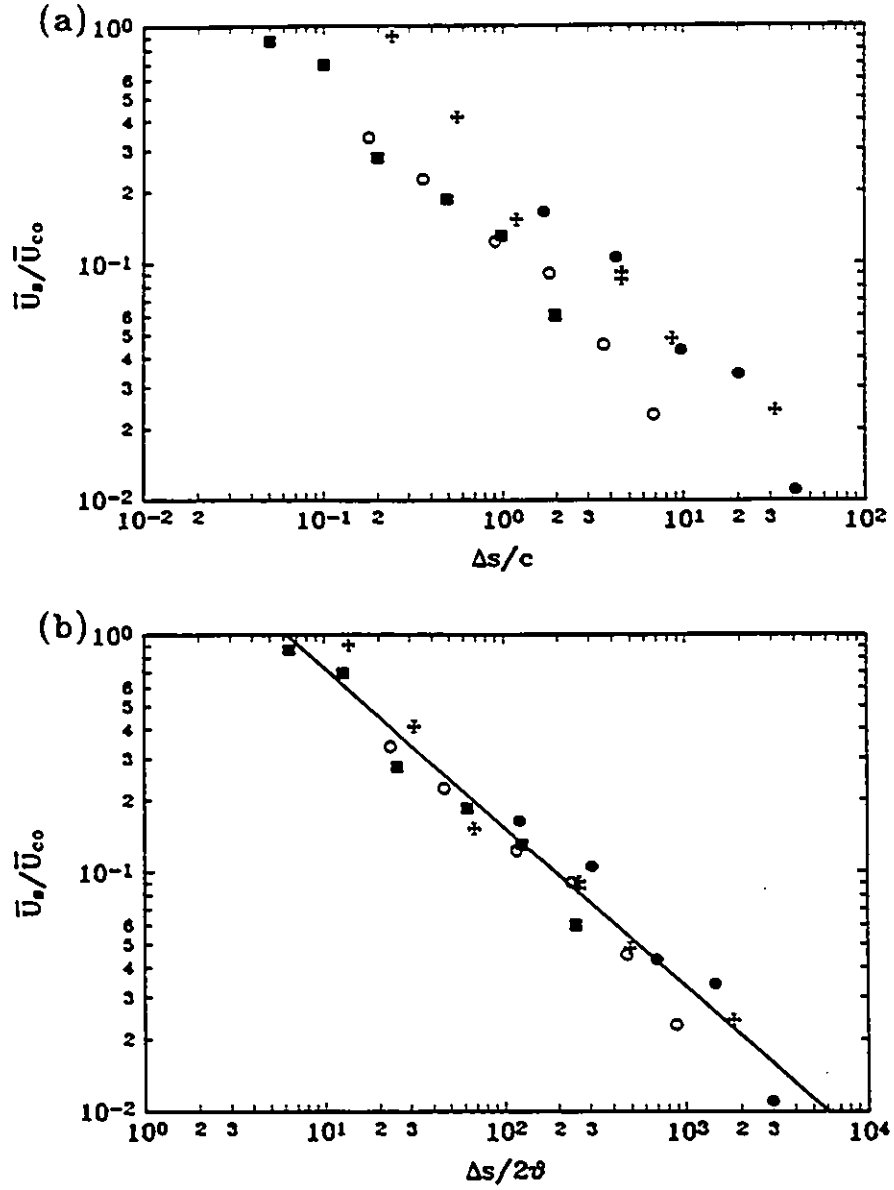

Figure 14.1: Streamwise development of velocity deficit; +, present measurements; •, Blackwelder and Chang (1986); o,Lemay (1989); ■ Coustols, Cousteix and Belanger(1987); —, power law fitted to all data.

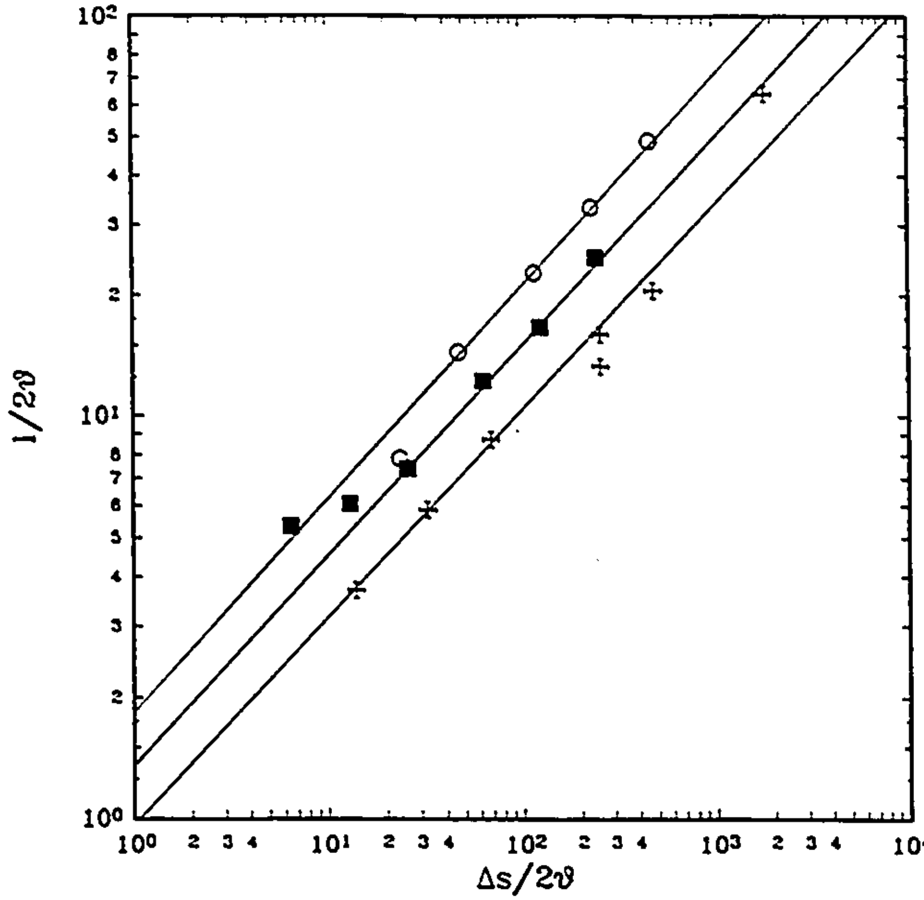

Figure 14.2: Streamwise development of wake half width; +, present measurements; o,Lemay (1989); ■ Coustols, Cousteix and Belanger(1987); —, interpolated line through presented data.

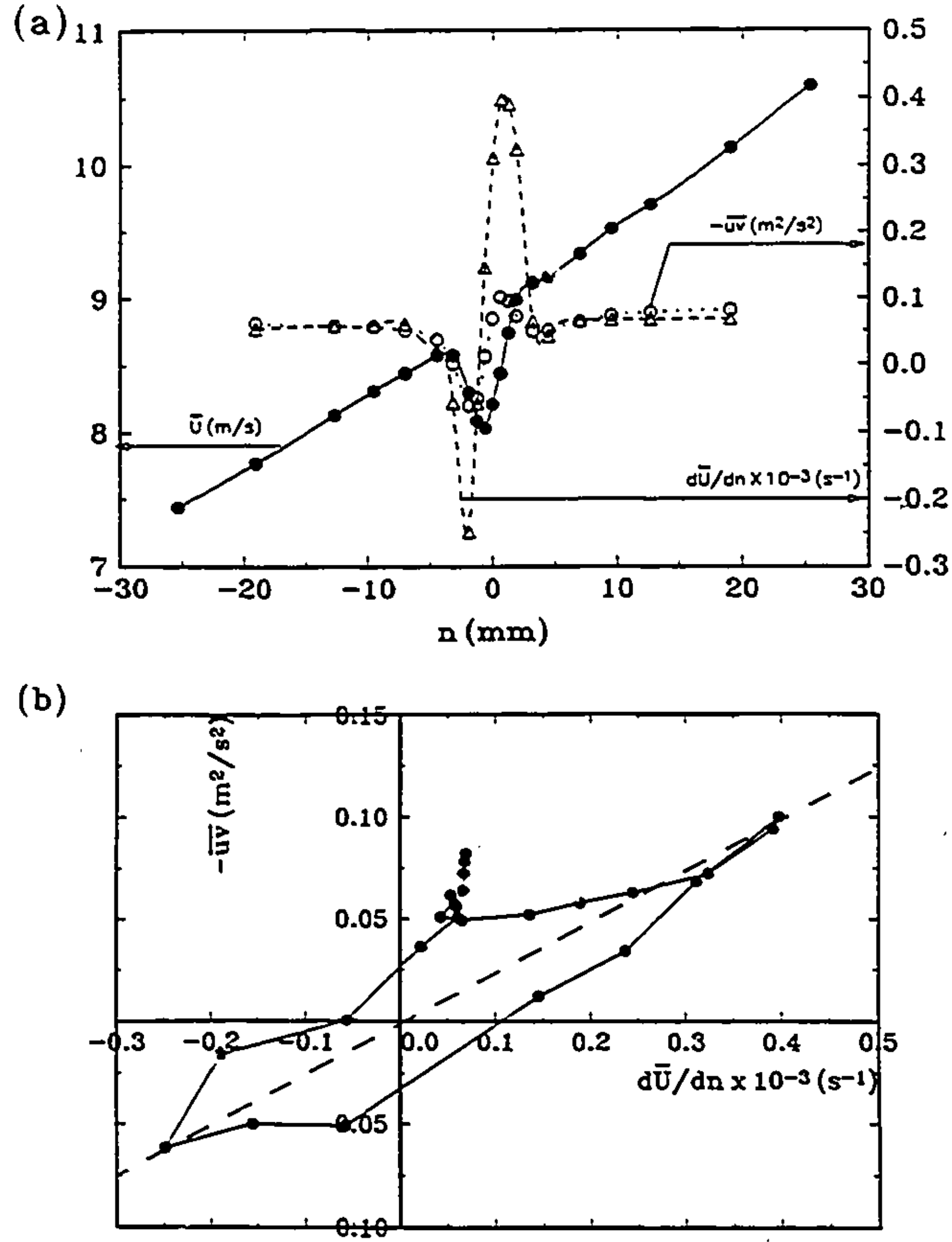

Figure 14.3: Variation of Reynolds shear stress at $\frac{s}{c} = 4.6$ behind ribbon in rectilinear shear flow; a) across the wake (also shown mean velocity and velocity gradient); b) with the mean velocity gradient.

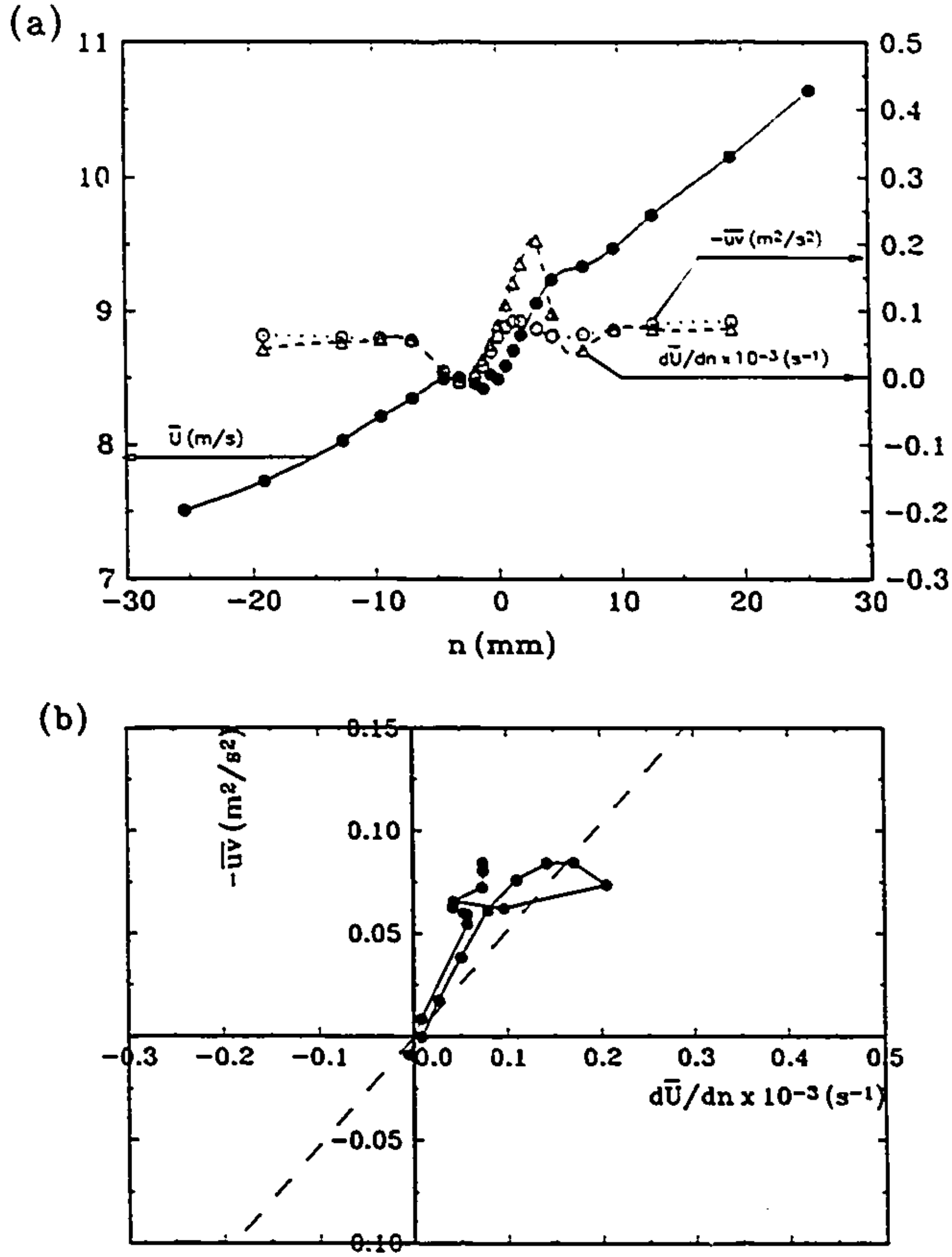

Figure 14.4: Variation of Reynolds shear stress at $\frac{x}{c} = 8.6$ behind ribbon in rectilinear shear flow; a) across the wake (also shown mean velocity and velocity gradient); b) with the mean velocity gradient.

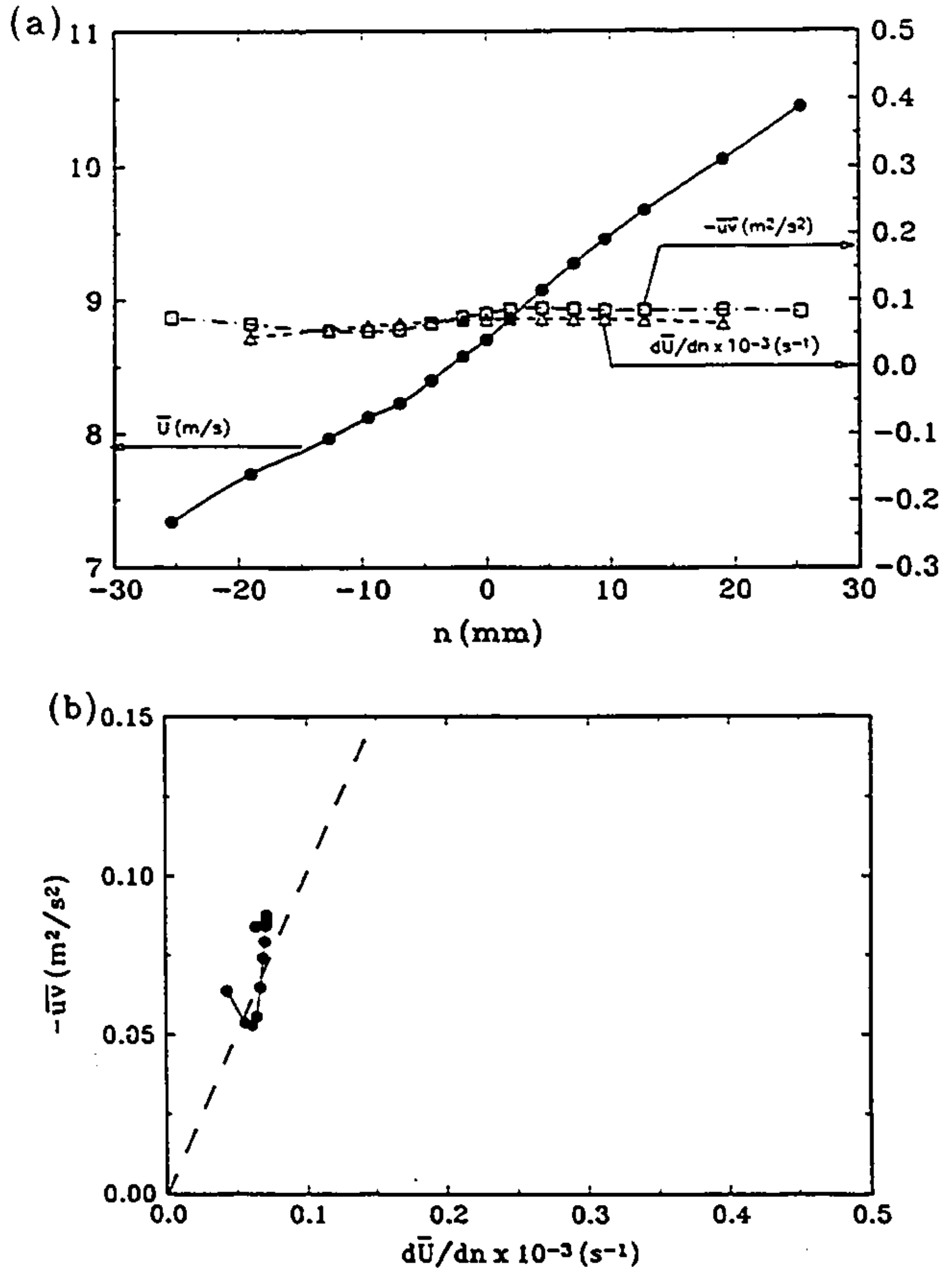

Figure 14.5: Variation of Reynolds shear stress at $\frac{s}{c} = 32$ behind ribbon in rectilinear shear flow; a) across the wake (also shown mean velocity and velocity gradient); b) with the mean velocity gradient.

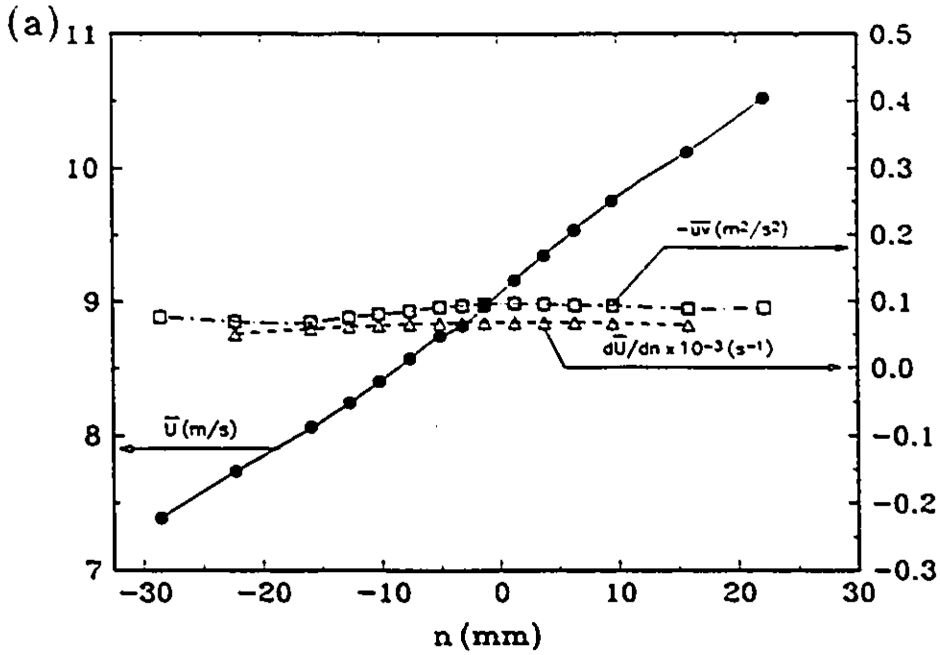

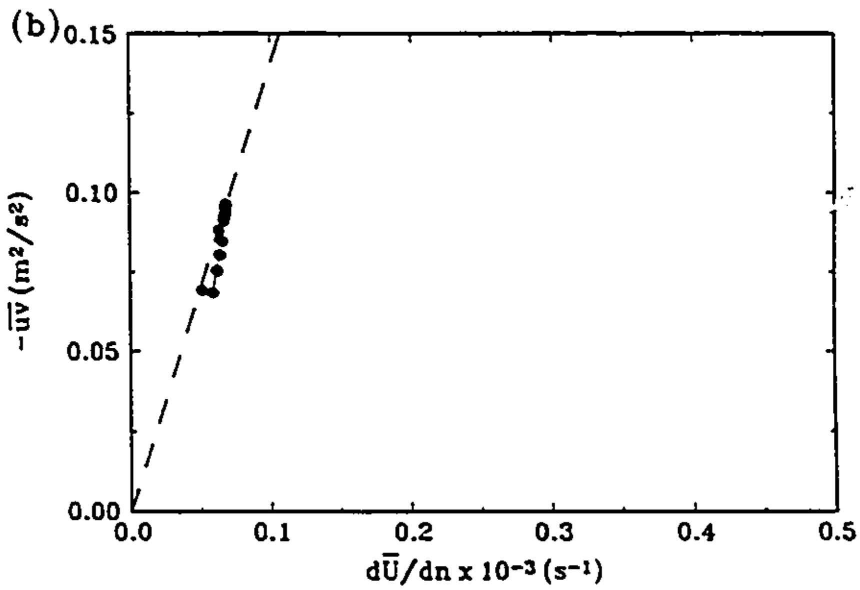

Figure 14.6: Variation of Reynolds shear stress at $\frac{x}{c} = 48$ behind ribbon in rectilinear shear flow; a) across the wake (also shown mean velocity and velocity gradient); b) with the mean velocity gradient.

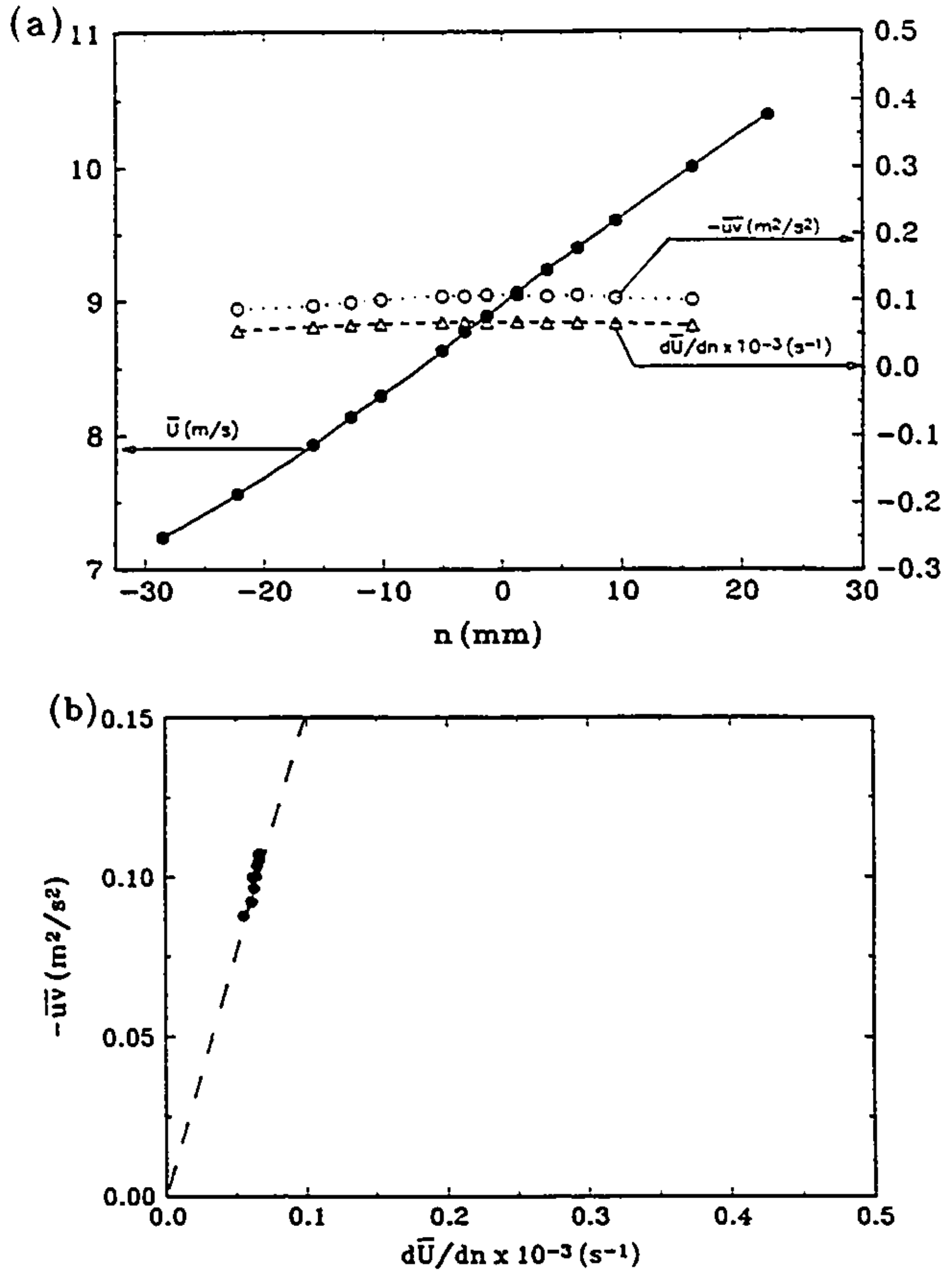

Figure 14.7: Variation of Reynolds shear stress at $\frac{s}{c} = 64$ behind ribbon in rectilinear shear flow; a) across the wake (also shown mean velocity and velocity gradient); b) with the mean velocity gradient.

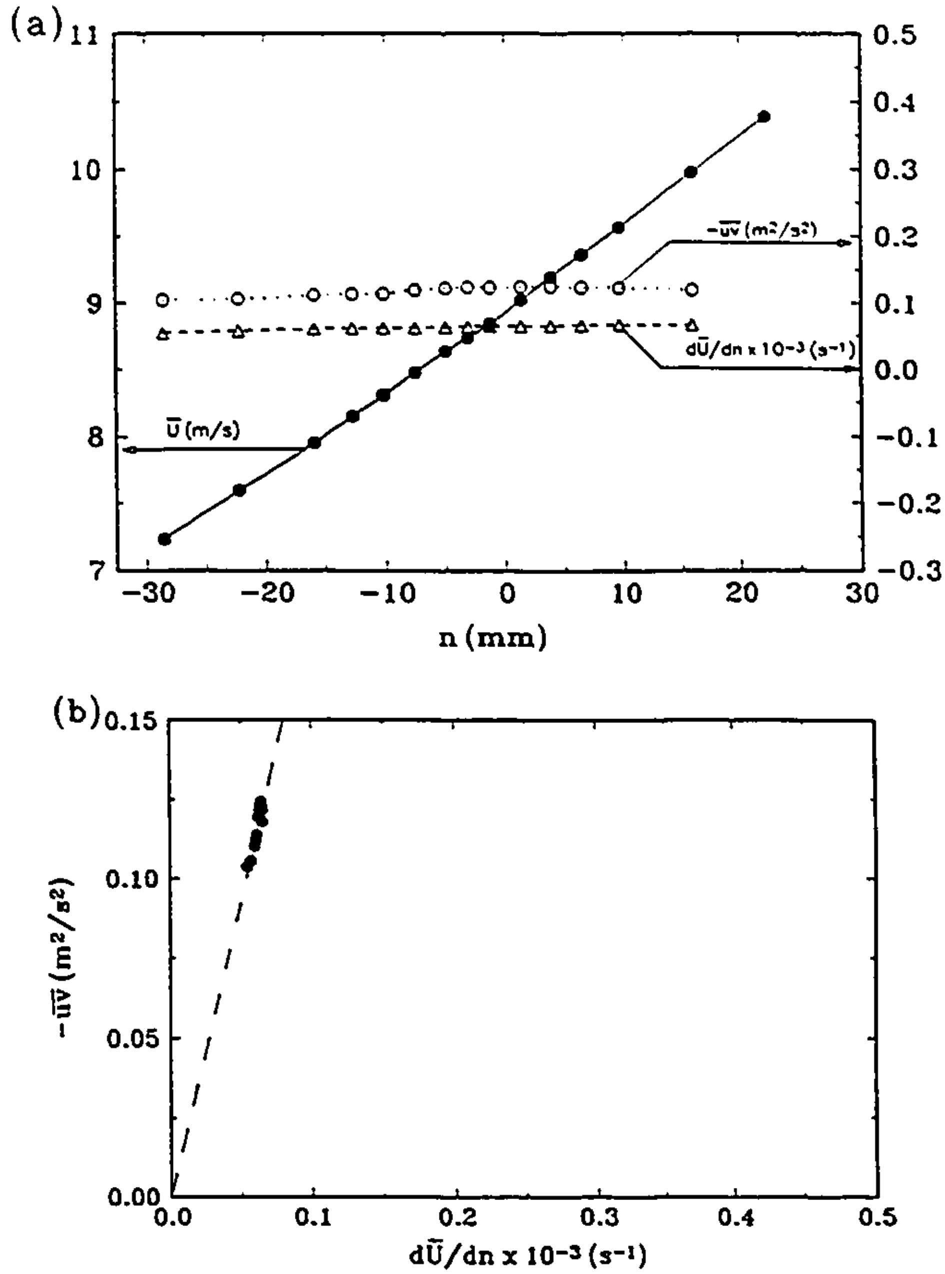

Figure 14.8: Variation of Reynolds shear stress at $\frac{x}{c} = 80$ behind ribbon in rectilinear shear flow; a) across the wake (also shown mean velocity and velocity gradient); b) with the mean velocity gradient.

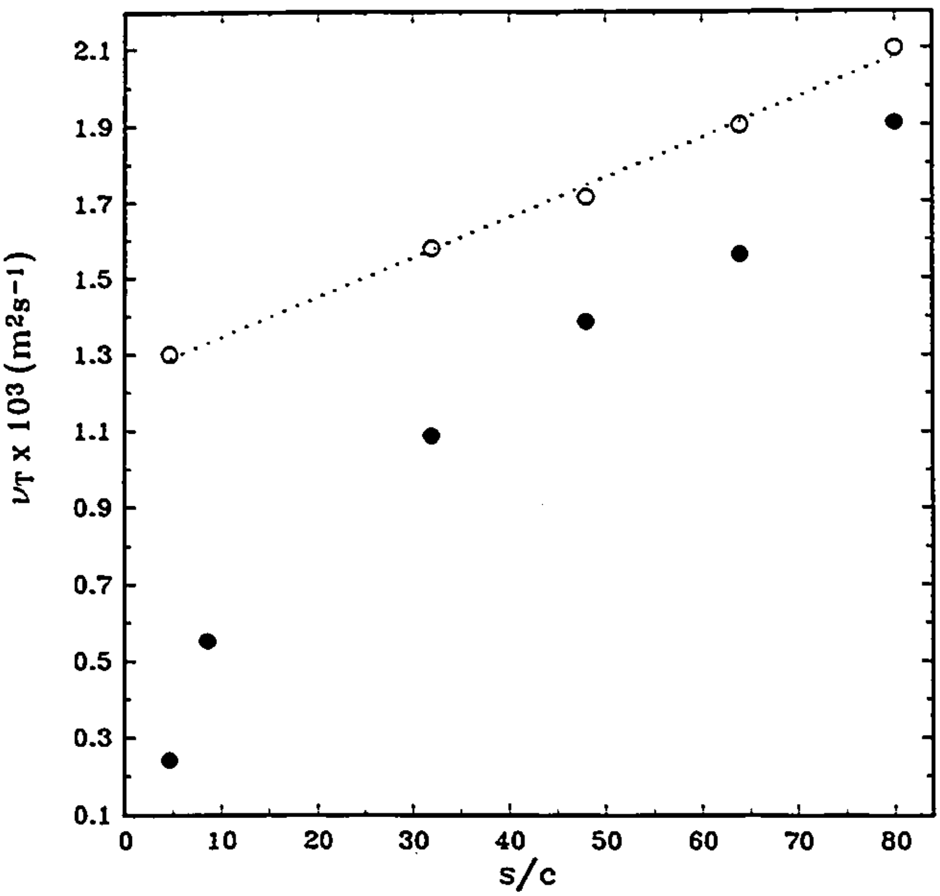

Figure 14.9: Streamwise variation of average eddy viscosity; •, in wake of ribbon; o, in nonmanipulated flow.

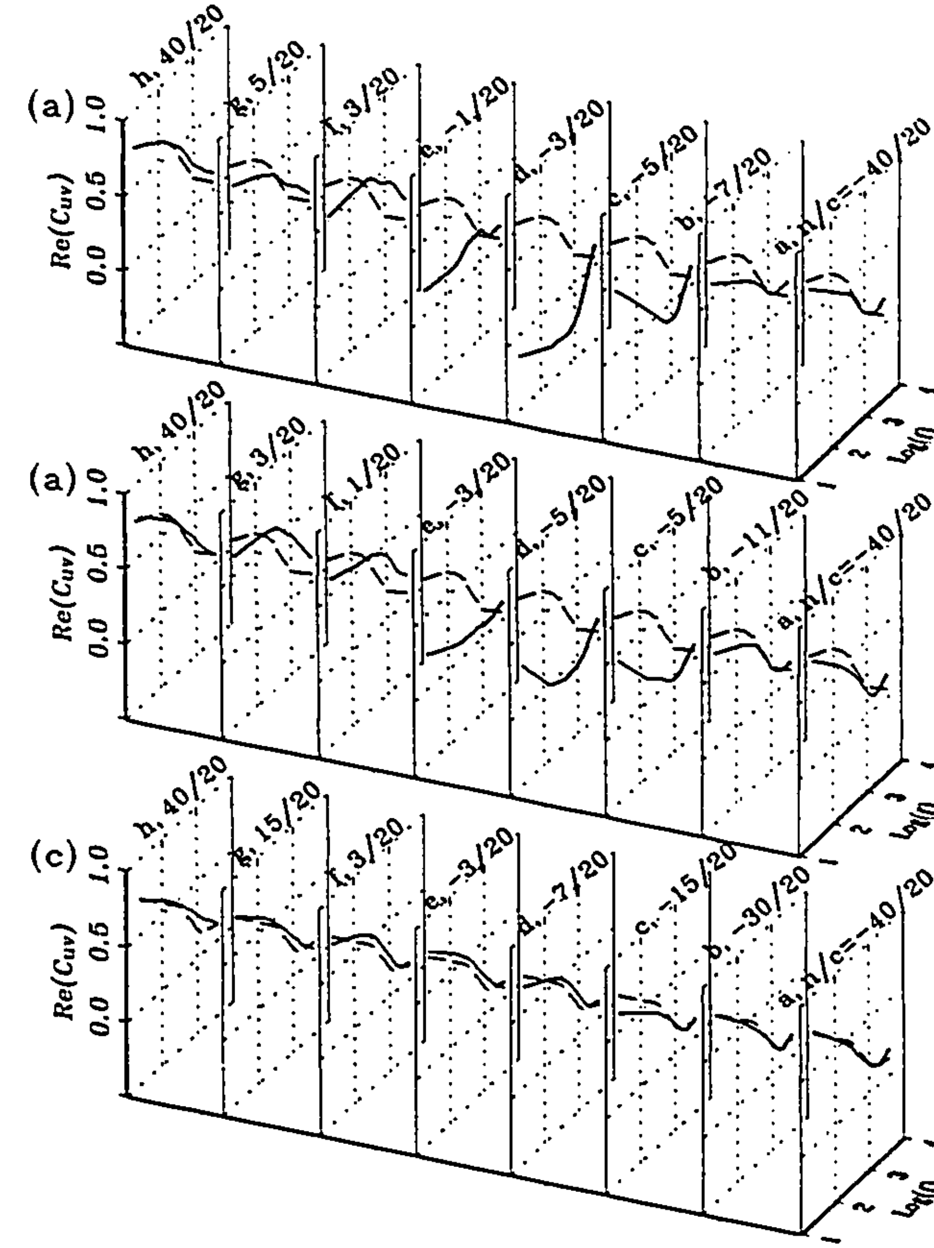

Figure 14.10: Coherence function in behind ribbon in rectilinear shear flow; a) $\frac{s}{c} = 4.6$; b) $\frac{s}{c} = 8.6$; c) $\frac{s}{c} = 32$; —, without the ribbon; ..... with ribbon.

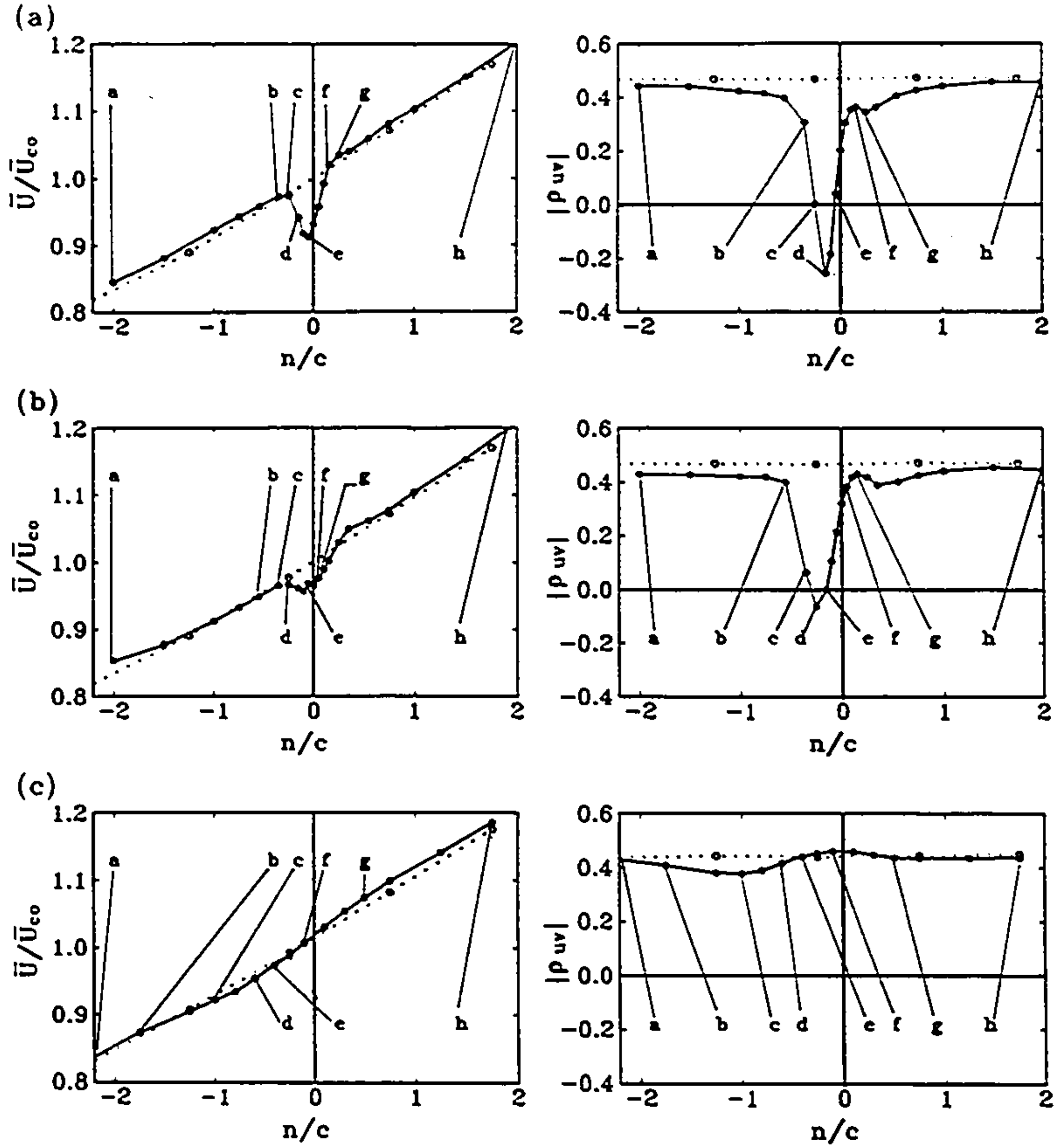

Figure 14.11: Mean velocity and correlation coefficient profiles behind ribbon in rectilinear shear flow; a) $\frac{s}{c} = 4.6$; b) $\frac{s}{c} = 8.6$; c) $\frac{s}{c} = 32$; ——, without the ribbon; ..... with ribbon.

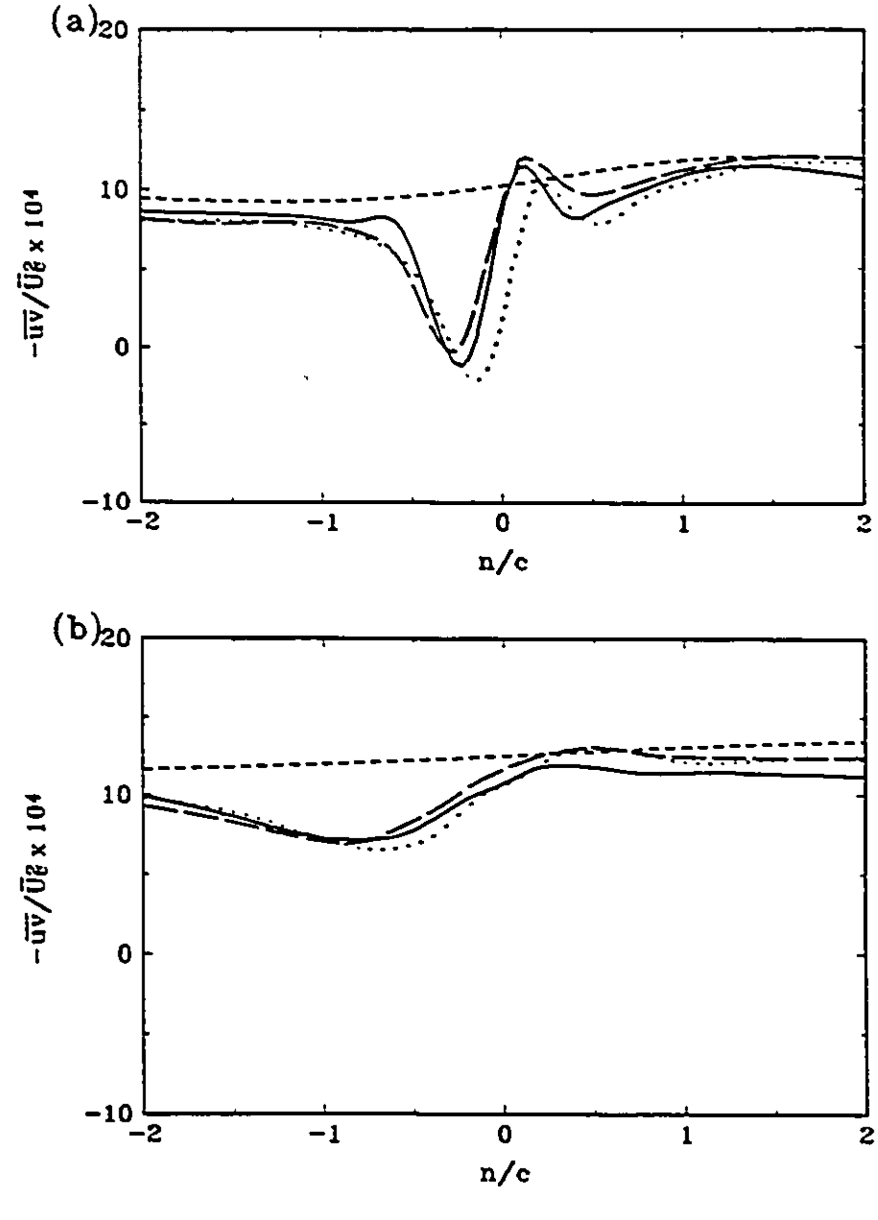

Figure 14.12: Effect of ribbon inclination on the shear stress in behind ribbon in rectilinear shear flow; - - - -, without the ribbon; ——, with the ribbon ($\alpha = 0$); ...., with ribbon ($\alpha < 0$); – – –, with ribbon ($\alpha > 0$).

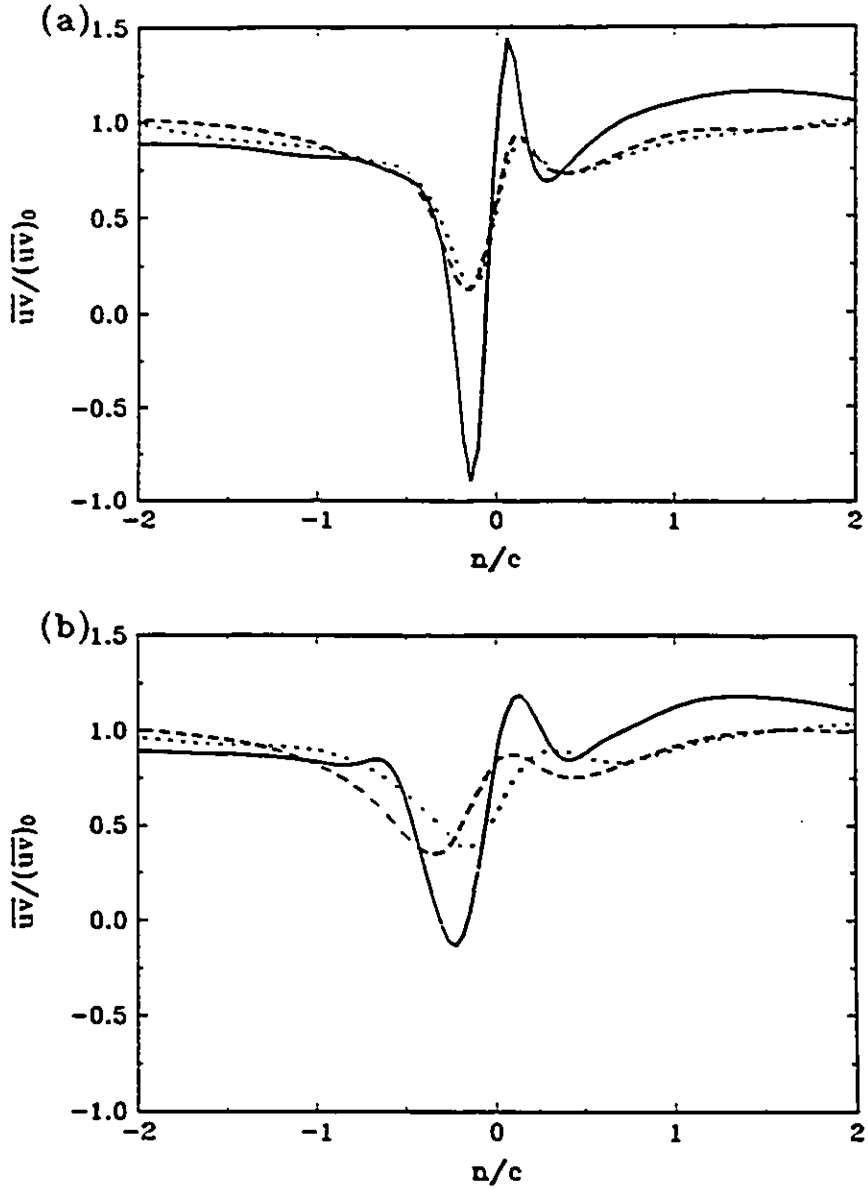

Figure 14.13: Comparison of the turbulent shear stresses in the straight and curved wakes; ——, S=0; ....., S < 0; - - - - ,S > 0.

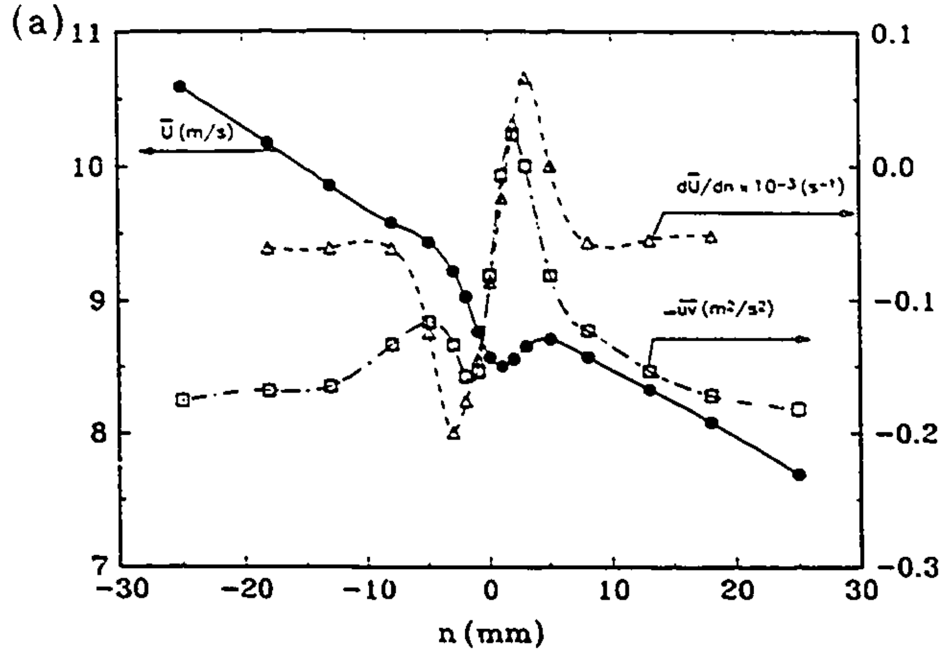

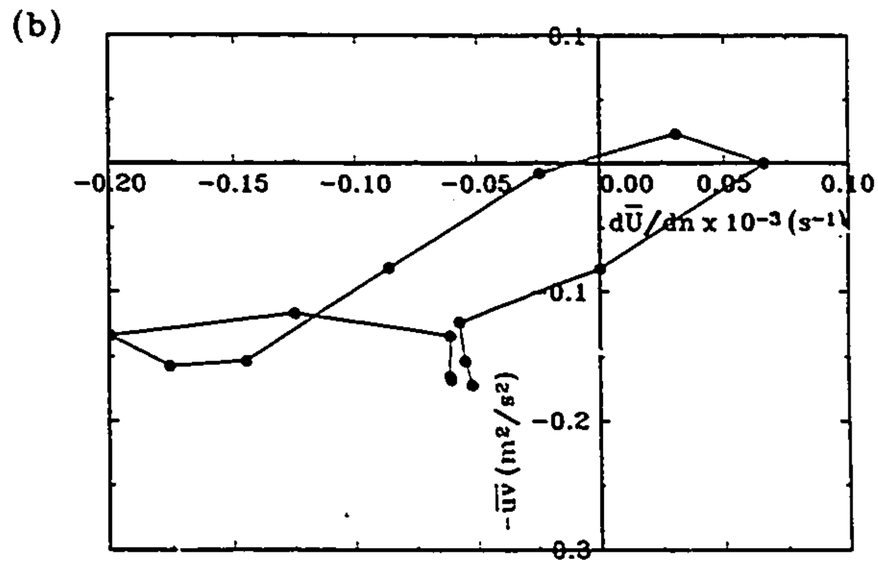

Figure 14.14: Variation of Reynolds shear stress at $\frac{s}{c} = 4.6$ in curved wake (S>0); a) across the wake (also shown mean velocity and velocity gradient); b) with the mean velocity gradient.

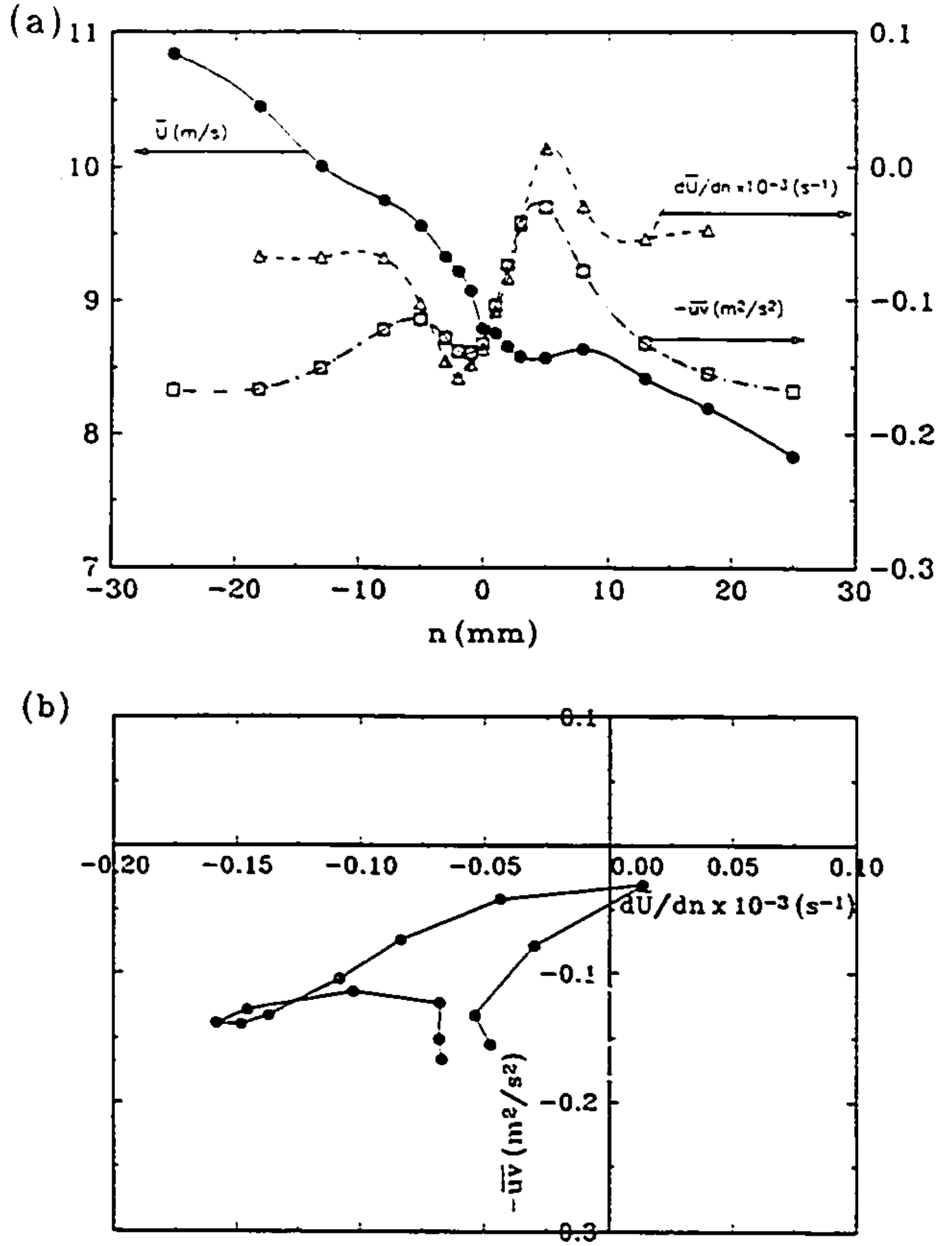

Figure 14.15: Variation of Reynolds shear stress at $\frac{s}{c} = 8.6$ in curved wake (S>0); a) across the wake (also shown mean velocity and velocity gradient); b) with the mean velocity gradient.

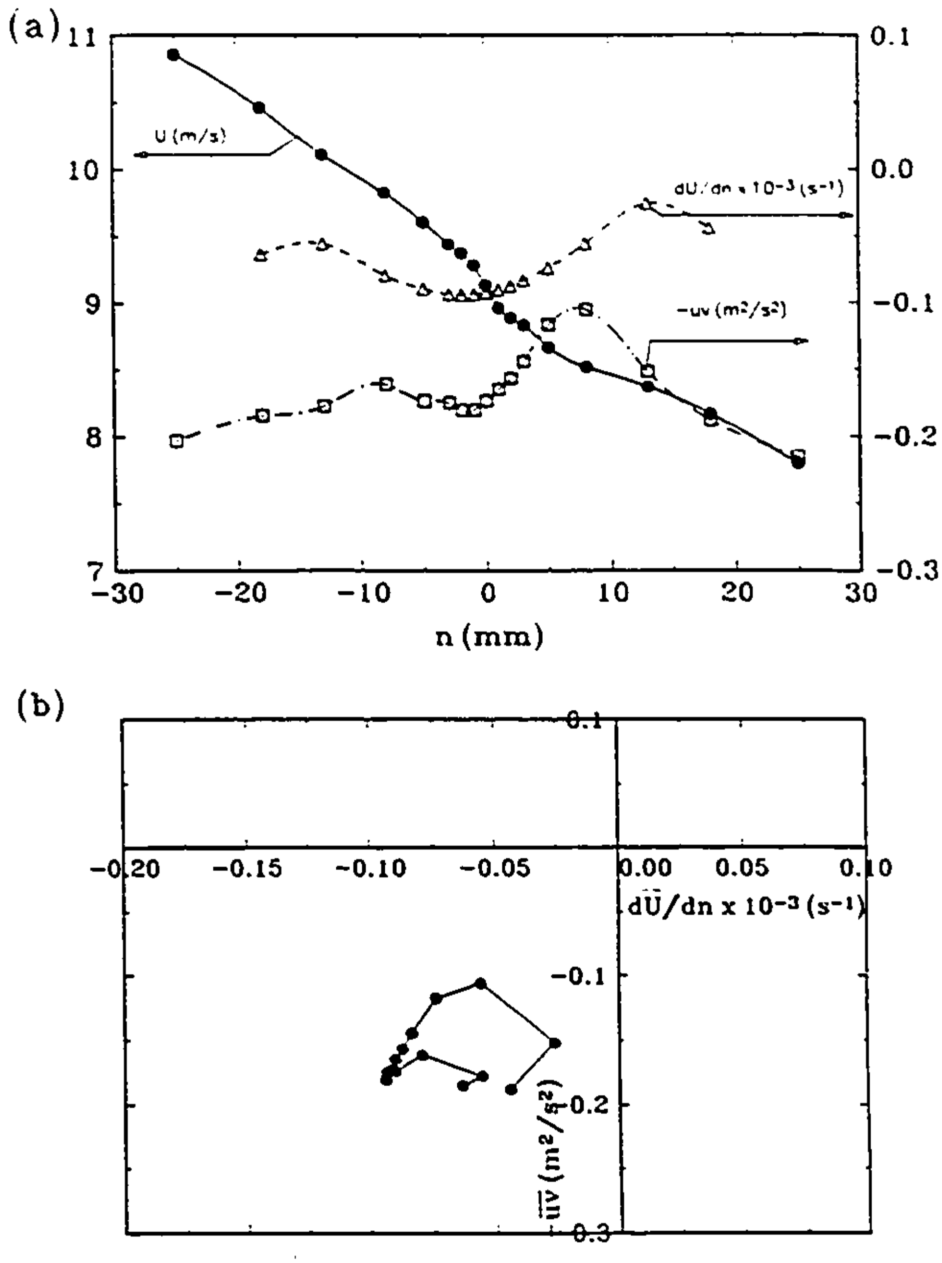

Figure 14.16: Variation of Reynolds shear stress at $\frac{s}{c} = 12.6$ in curved wake (S>0); a) across the wake (also shown mean velocity and velocity gradient); b) with the mean velocity gradient.

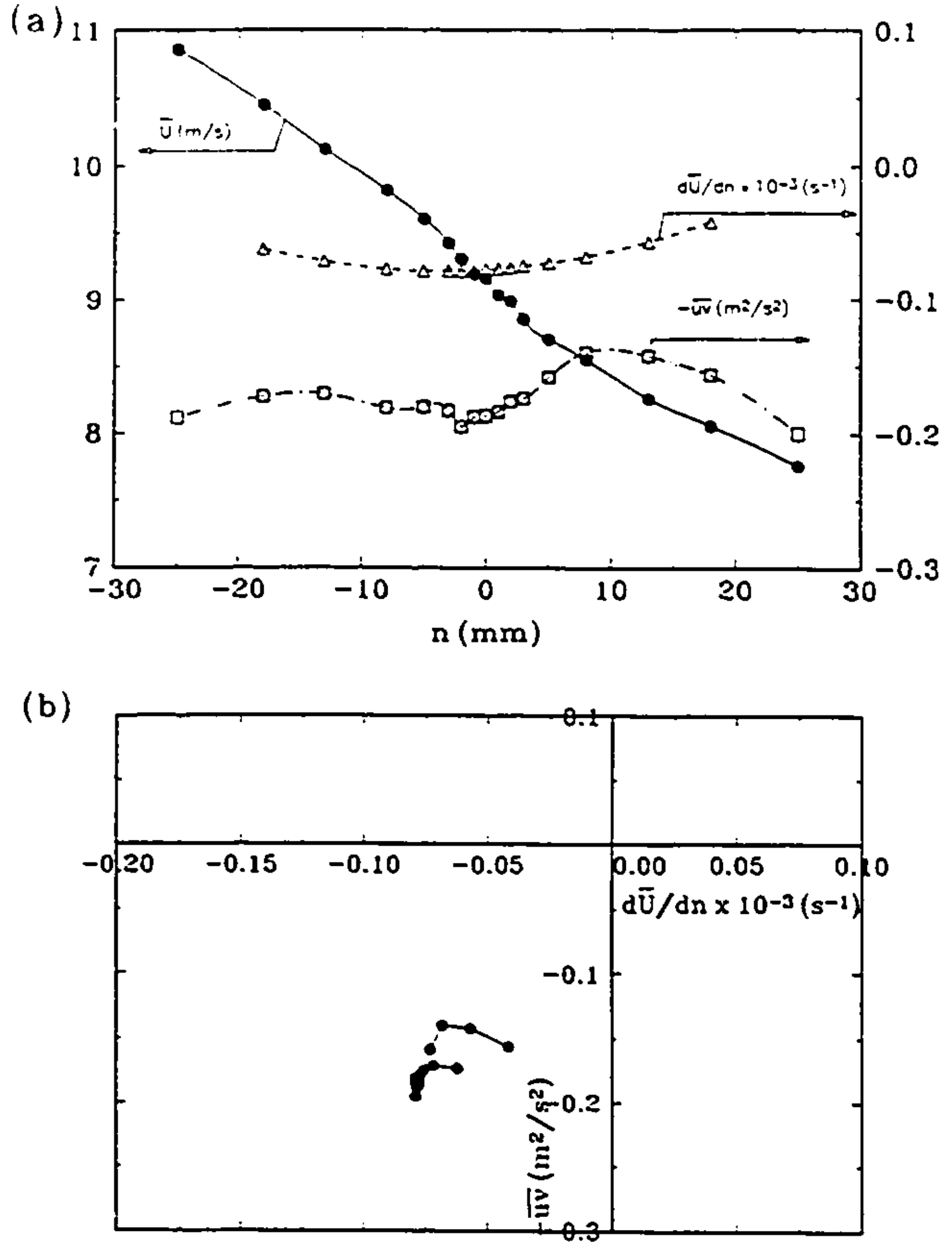

Figure 14.17: Variation of Reynolds shear stress at $\frac{s}{c} = 16$ in curved wake (S>0); a) across the wake (also shown mean velocity and velocity gradient); b) with the mean velocity gradient.

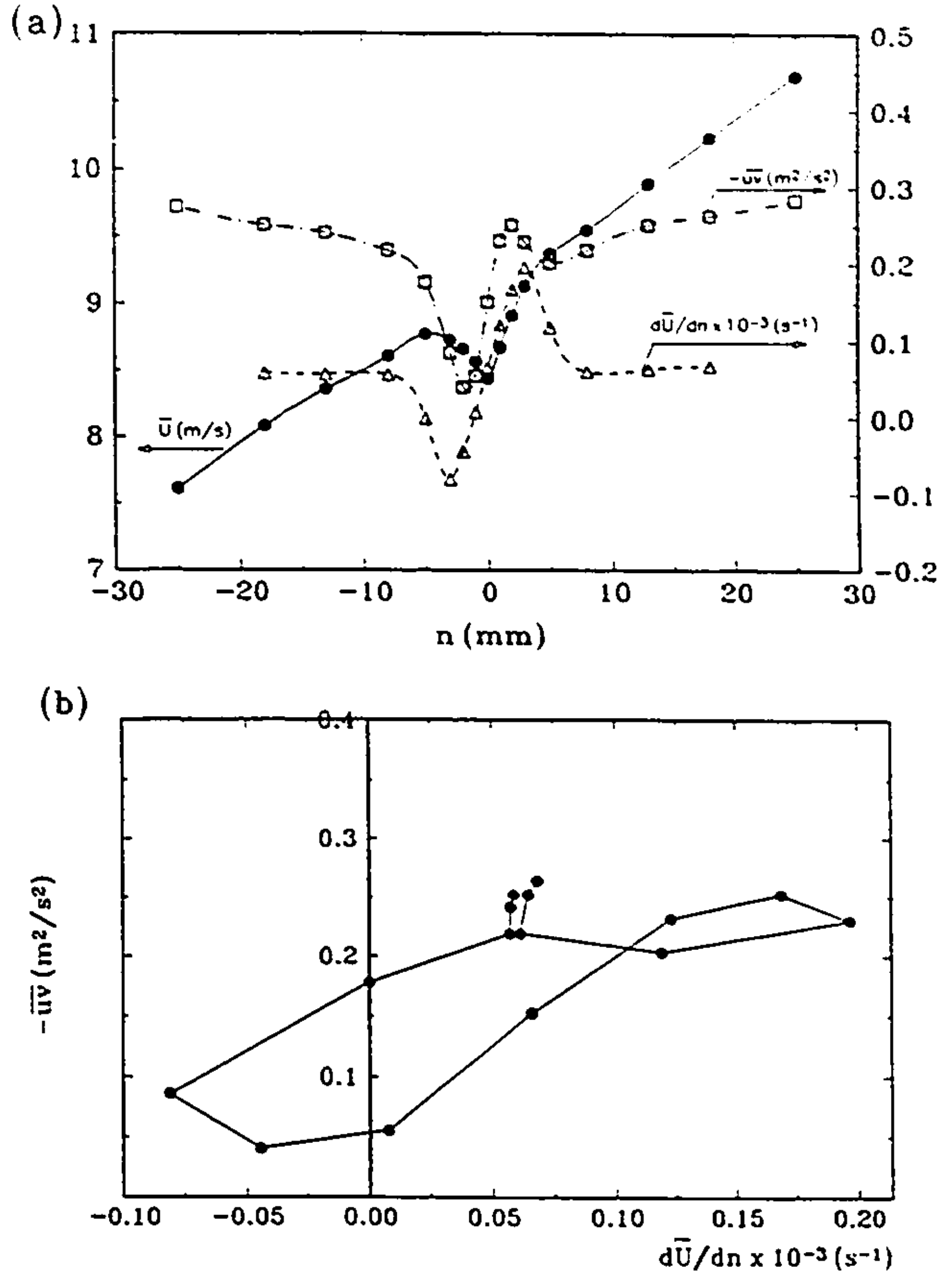

Figure 14.18: Variation of Reynolds shear stress at $\frac{s}{c} = 4.6$ in curved wake (S<0); a) across the wake (also shown mean velocity and velocity gradient); b) with the mean velocity gradient.

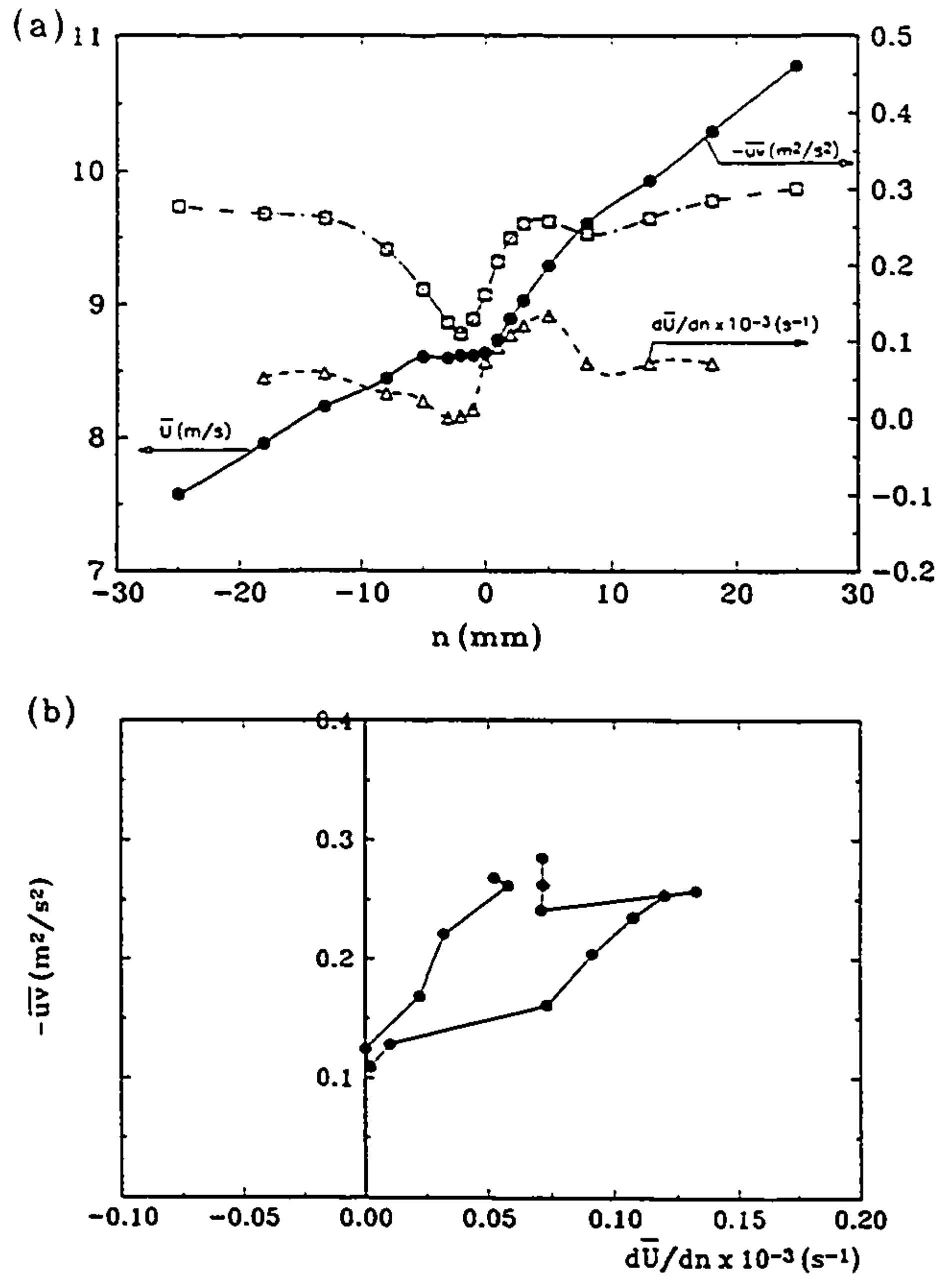

Figure 14.19: Variation of Reynolds shear stress at $\frac{s}{c} = 8.6$ in curved wake (S<0); a) across the wake (also shown mean velocity and velocity gradient); b) with the mean velocity gradient.

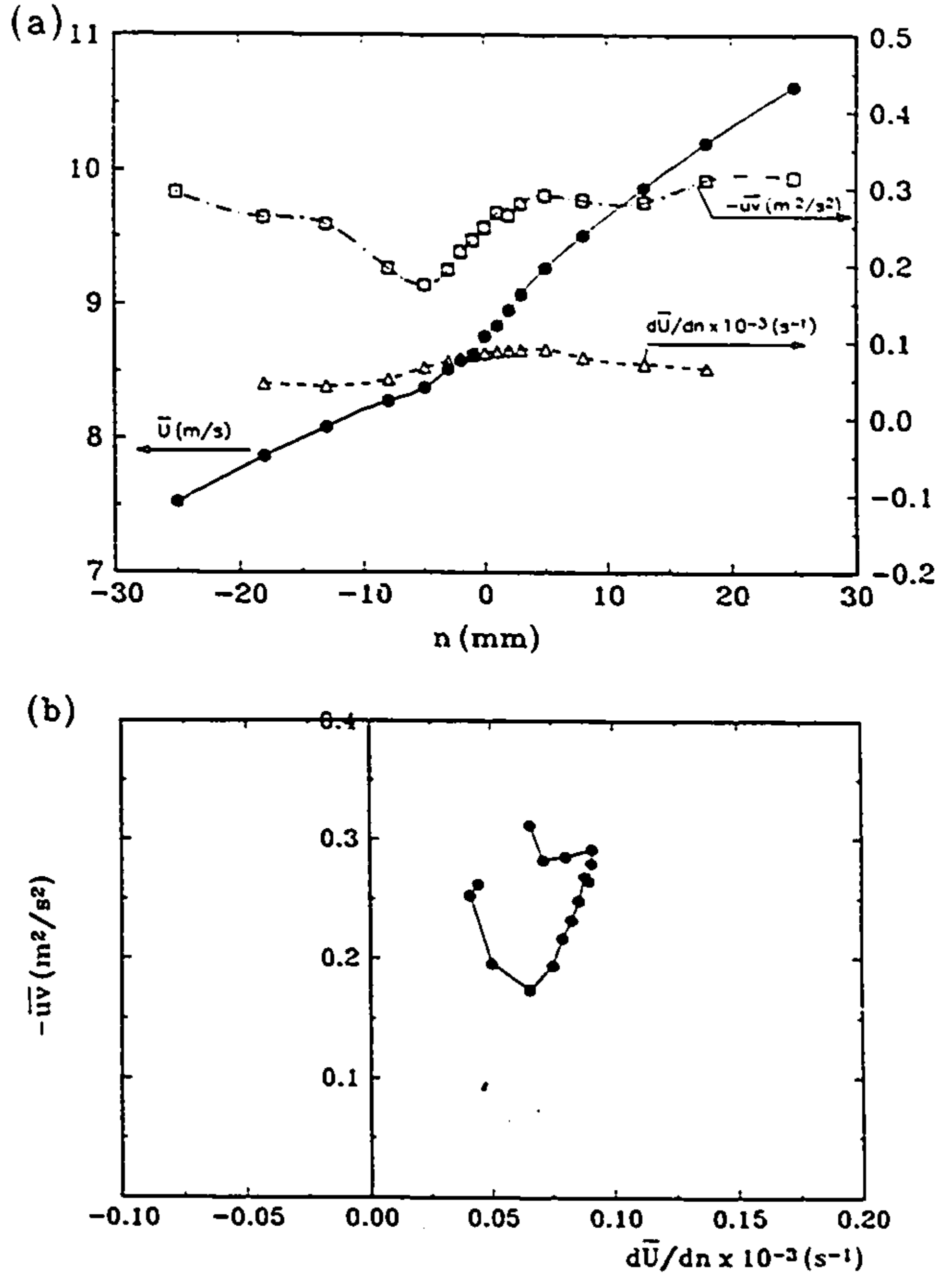

Figure 14.20: Variation of Reynolds shear stress at $\frac{s}{c} = 12.6$ in curved wake (S<0); a) across the wake (also shown mean velocity and velocity gradient); b) with the mean velocity gradient.

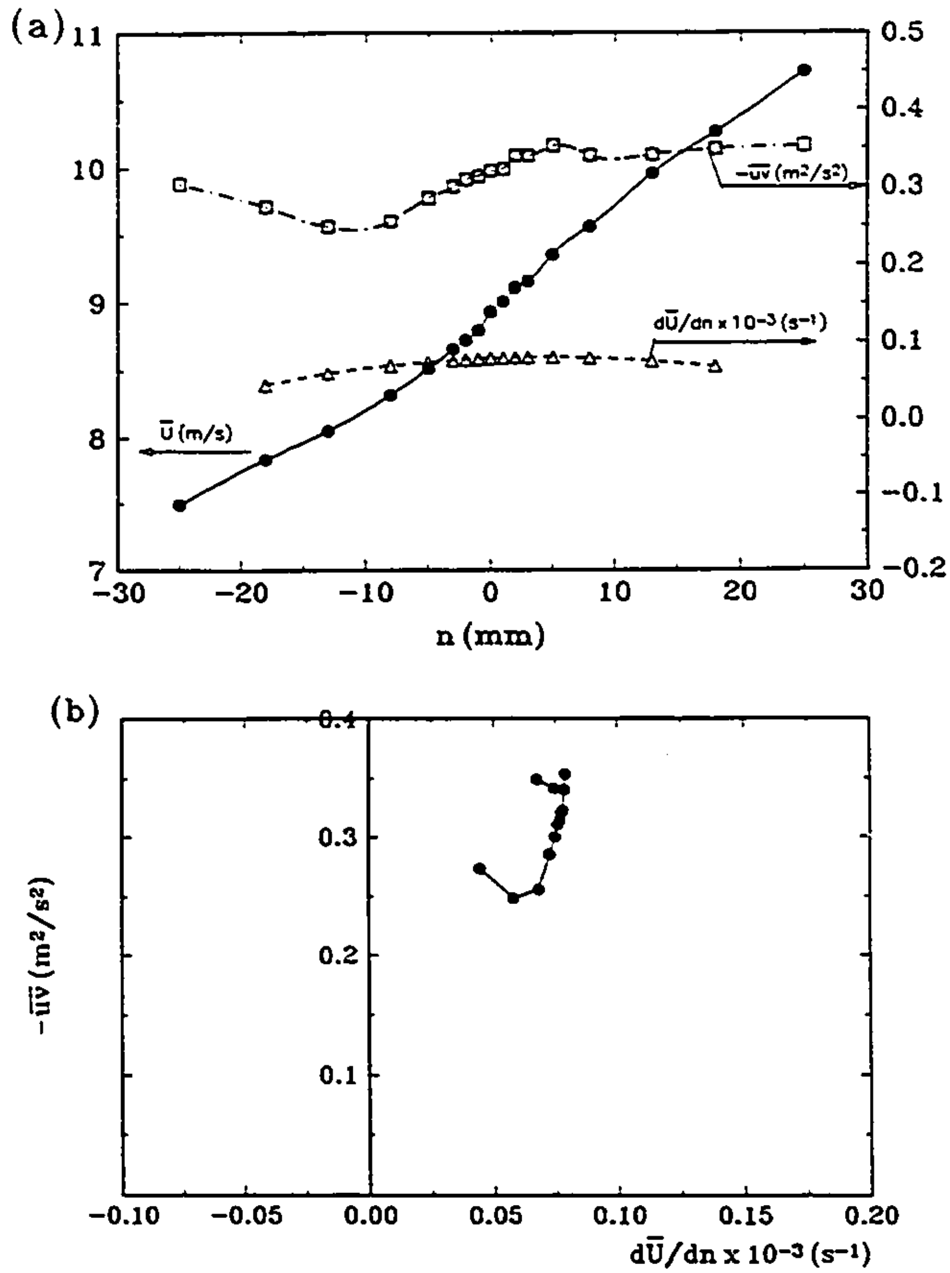

Figure 14.21: Variation of Reynolds shear stress at $\frac{s}{c} = 16$ in curved wake (S<0); a) across the wake (also shown mean velocity and velocity gradient); b) with the mean velocity gradient.